Inclusion of Hydro-Mechanical Behaviour of Discrete Fracture Networks in Coupled Reservoir Geomechanical Simulations

by

Abel Sánchez Juncal

A thesis submitted in partial fulfillment of the requirements for the degree of

Doctor of Philosophy

in

Geotechnical Engineering

Department of Civil and Environmental Engineering
University of Alberta

Abstract

Discontinuities are one of the most prominent features of the Earth's upper crust, these are the result of the action of different geological, mechanical, thermal and chemical activities over millions of years. The term rock mass was created to describe the in situ medium containing intact rock material and rock structures such as joints, faults, fractures, veins, bedding planes and folds. Traditionally, rock masses are considered as a continuous, homogeneous, isotropic and linear elastic material in engineering practice. However, they commonly occur as discontinuous, inhomogeneous, anisotropic and non-elastic materials in nature. Although it is well known that discontinuity networks influence the flow and geomechanical behaviour of fractured reservoirs, their effect and impact on deformability and permeability properties are not usually taken into account in complex reservoir simulations. Therefore, the determination of hydraulic and geomechanical properties is of great importance in characterization of rock mass formations. Inclusion of fracture patterns described by discrete fracture networks (DFN) in coupled reservoir geomechanical simulations is necessary to capture the influence of discontinuities in the reservoir life cycle operations.

A coupling methodology is presented here to include the hydro-mechanical behavior of fracture networks in coupled reservoir geomechanical simulations whereby several commercial simulators are involved and linked together following an explicit sequential coupling scheme built into a coupling simulation platform developed by the reservoir geomechanics research group (RGRG) at the University of Alberta. A porosity correction strategy based on the fixed stress split method has been implemented in the sequential scheme. The generalized tensorial form of the Biot effective stress coefficient, disregarded in most numerical coupling methods, is rigorously included in the thermo-poromechanical coupling formulation. The small and large scale structural

features present in the reservoir such as joints and major faults are represented by a DFN. The complex fluid flow processes are captured by the reservoir flow simulator, CMG – STARS. A continuum geomechanical simulator, Itasca – FLAC^{3D}, is used to calculate deformation changes due to new stresses induced by changes in temperature and pore pressure in the reservoir at each simulation stage. A virtual rock mass numerical laboratory, VRM lab, is developed by means of a discontinuum geomechanical simulator, Itasca – 3DEC, to determine through a numerical homogenization process the hydraulic and mechanical equivalent anisotropic properties for the characterization of the equivalent continuum representative of the fractured rock formation. During the numerical simulation, the equivalent permeability, anisotropic elastic parameters as well as the Biot effective stress coefficient tensor can be updated at specific simulation stages in all the fractured reservoir discretization regions or only in those where the change in the effective stress field reaches a certain tolerance to account for effect of pore pressure changes developed during the activities of the reservoir production operations. The explicit sequential coupling scheme implemented in the RGRG coupling platform and the mechanical and hydraulic modules of the VRM lab have been compared and successfully verified against analytical solutions. This research shows the importance of conducting reliable equivalent characterizations of fractured media and properly modelling the effect of material anisotropy in thermo-poromechanical coupled simulations, which is required to correctly model stress-sensitive reservoirs involving anisotropic porous formations. The methodology presented here has the goal of providing some insights in the influence of geomechanics in the overall behaviour and management of fractured porous formations sensitive to stress changes.

Preface

All research completed in this thesis is an original work by Abel Sánchez Juncal. The design, formulation and code corresponding to the virtual rock mass laboratory, VRM lab, implemented in 3DEC have been fully developed by me. I have personally developed, coded and implemented the anisotropic thermo-poromechanical formulation of the explicit sequential coupling scheme presented here, in the numerical coupling platform developed by the reservoir geomechanics research group, RGRG, at the University of Alberta. The RGRG coupling platform has been developed and updated during the course of this research by Dr. Nathan Deisman and myself. Dr. Deisman is responsible of coding the main controlling RGRG platform interface, involving the reservoir and geomechanical grid generation, CMG simulator linkages, and permeability and porosity update implementations for isotropic formations; while I developed and coded the FLAC3D linkages and all the formulation to input changes in stress due to changes imposed from the flow simulator, as well as the porosity correction strategy based on the fixed stress split method included in the aforementioned explicit sequential coupling scheme for anisotropic porous media. The verification cases have been selected and conducted by myself as well as the design and analysis of all the numerical simulations presented in this study. All the files, subroutines and functions coded for developing the VRM lab and the RGRG coupling platform have been deposited in the RGRG digital archive. Contact the RGRG for more information about the developed software. The research described herein was performed under full supervision of Prof. Richard J. Chalaturnyk. No part of this thesis has been previously published.

Dedicated to my wife Paula
and to my son Nicolás
"per aspera ad astra"

Acknowledgments

I would like to thank first of all to my wife Paula for her love and unconditional support during all these years. You are the best team I could ever have! To my parents Carmen del Pilar and Benito, who taught me that one can never know too much. Also, to my parents in law Carmen and Antonio, who always supported and treated me as one of their own.

I wish to express my sincere appreciation and gratitude to my supervisor Prof. Richard J. Chalaturnyk for his support, trust and guidance through this long journey. The guidance of the supervisory committee members Prof. C. Derek Martin and Prof. Nicholas Beier is warmly appreciated.

To my dear friends Dr. Ehab Hamza, Dr. Alireza Rangriz Shokri, Mr. Keivan Khaleghi, Dr. Stephen Talman, Dr. Hossein Akbarzadeh Kasani, and colleagues of the reservoir geomechanics research group for sharing with me endless discussions and beautiful moments: Dr. Nathan Deisman, Mr. Jacob Brandl, Dr. Juan Arias, Dr. Alireza Khani, Dr. Bo Zhang, Dr. Alireza Moghadam and to Hope Walls.

Last but not least, I want to thank my friend and colleague Dr. Diego Mas Ivars, who during our period working together at Itasca Consultants AB encouraged me to pursue this research.

Table of Contents

List of Tables

List of Figures

1 Introduction

Most rock masses of the Earth's upper crust have undergone multiple geological processes involving significant mechanical, thermal and chemical activities over millions of years (Hudson et al. 1997). Different scales of geological structures and discontinuities such as folds, veins, bedding planes, faults and joints originate mainly from these geological processes. The presence of discontinuities is therefore one of the most prominent features of the rock masses (Peng et al. 2007). Rock masses generally occur in nature as systems of rock materials containing or being separated in discrete bodies by rock structures, where the term rock material refers to the intact rock between discontinuities, and the rock structure describes the nature and distribution of the structural features (Brady et al. 2004).

It is well known that heterogeneities and discontinuities induce anisotropic deformability in rock masses. However, these are commonly considered as continuum homogeneous isotropic and linear-elastic materials in engineering analyses. This assumption may introduce significant errors in estimating the deformation and stress distribution of anisotropic rock masses in which the medium should be treated as discontinuum inhomogeneous anisotropic and non-elastic (Barla 1974; Hudson et al. 1997). In addition, discontinuities generally affect the permeability and fluid flow behaviour of fractured porous formations. Thus, natural fractures commonly present in hydrocarbon reservoirs, especially in unconventional resources, may have a significant impact on the formation performance. Consequently, an efficient reservoir management should assume all formations as fractured unless any other assumption or treatment is proven more appropriate (Narr et al. 2006; Liu et al. 2012).

Although discontinuities generally influence the geomechanical and hydraulic behaviour of fractured reservoirs, including explicitly all the structural features in reservoir geomechanical coupled simulations is either inefficient or unfeasible in terms of practical computational time and memory requirements. In these cases, it is necessary to reduce the number of fractures,

incorporating only the critical ones with respect to the fractured formation response and disregarding all the rest (Hart 1993; Itasca 2016). To overcome this issue, the discontinuum fractured rock mass is often replaced by an equivalent continuum material able to capture the effect of all the fractures in the *in situ* media. In general, the equivalent continuum properties are estimated using homogenization and upscaling techniques based on empirical, analytical or numerical methods. Among them, the numerical approach has the advantage of accounting for the nonlinear behaviour and interaction effect of complex fracture patterns. It is worth noting that despite this capability, the numerical methods have been traditionally used in two-dimensional analyses, being recently used more often in three-dimensional cases.

The inclusion of fracture patterns in reservoir geomechanical simulations may help in a better understanding of the overall reservoir performance. Nevertheless, the characterization of extensive fractured porous formations is still not a simple task. The difficulty arises from the impossibility of performing large scale field tests (Lorig et al. 2010). Thus, a reservoir geomechanical coupling methodology including a numerical homogenization tool for three dimensional fractured porous media is proposed here, with the aim of capturing the effect of complex fracture networks present in natural and engineered fractured reservoirs through hydraulic and mechanical equivalent parameters determined for the equivalent continuum representation of the fractured porous formation.

1.1 Background

The operations developed during the production of a reservoir usually involve deformation, fluid flow and thermal processes which are coupled together; that is, one process affects the initiation and progress of another (Tsang 1991). The degree of coupling interaction will depend on the features and nature of the rock mass, being more significant in those reservoirs sensitive to stress changes. In order to capture the thermo-hydro-mechanical physical interaction and with the progressive enhancement of computational capabilities, several numerical simulation techniques have been developed and applied to coupled problems such as, oil and gas production, geothermal

energy, geological nuclear waste disposal and carbon sequestration (Jing & Hudson 2002; Rutqvist 2017).

The hydro-mechanical coupling comprises two main components: volume coupling which considers changes in pore volume due to changes in stress; and coupling through flow properties which accounts for changes in permeability induced by stress changes (Settari et al. 1998). Analogous, the phenomena involved in coupling fluid flow and geomechanics can be divided in *direct* (Wang 2000) and *indirect* (Rutqvist et al. 2003) hydro-mechanical couplings. The direct hydro-mechanical couplings occur through deformation and pore-fluid interactions, such as, fluid pressure changes induced by changes in stress; or changes in the volume of the porous medium due to changes in fluid pressure. The indirect hydro-mechanical couplings involve changes in hydraulic and mechanical material properties due to changes in stress and fluid pressure, respectively. In general, while the direct couplings are significant in soft and low-permeability rocks and soils, the indirect couplings are more important in fractured rock masses (Rutqvist et al. 2003). Tsang (1991) presented an overview of the different types of coupled processes that may occur in rock fractures.

Discontinuities may be explicitly included in coupled hydro-mechanical numerical models (e.g. Noorishad et al. 1982; Karimi-Fard et al. 2004; Zandarin 2010; Jin et al. 2017), however this approach is more suitable for local or small scale numerical analyses containing a low number fractures. On the other hand, the equivalent continuum representation of the fractured porous formation is often the most practical approach for large scale coupled simulations (Rutqvist et al. 2003); thus, it is not necessary to deal with large computational times and to generate complex meshes to include fracture intersections. During the past decades several homogenization and upscaling procedures have been proposed to evaluate the equivalent properties for the hydraulic and mechanical continuum characterization of rock masses.

Salamon (1968) derived the overall elastic moduli of a homogeneous equivalent continuum representative of a stratified rock mass, consisting of homogeneous, transversely isotropic strata

with random thickness and elastic properties. Following the same approach, Gerrard (1982) calculated the equivalent properties of a system consisting of homogeneous orthorhombic strata. Fossum (1985) obtained the effective isotropic elastic properties for a rock mass containing a system of randomly oriented persistent fractures. Amadei and Goodman (1983) introduced the concept of an equivalent orthotropic continuum for a body containing three orthogonal joint sets. Additionally, closed-form solutions for rock masses with two (Yoshinaka & Yamabe 1986) and three (Huang et al. 1995) intersecting non-orthogonal fully persistent joint sets were derived. Moon (1987) extended the elastic theory of two-material composites to estimate the overall elastic properties of well-jointed rock masses by the sequential addition of joints to an updated rock mass properties matrix until the complete inclusion of all the joints (Pariseau & Moon 1988). Based on the effective medium theory, Oda (1982) introduced a symmetric crack tensor accounting for geometrical parameters of the rock structure to estimate the equivalent permeability tensor (Oda 1985), and compliance matrix of the rock mass (Oda 1986). Stietel et al. (1996) used the Oda's work to derive the equivalent hydraulic and mechanical properties of a two-dimensional fractured system. The validity of the formulation was assessed by performing numerical tests with the UDEC code, developed for two-dimensional numerical analyses of discontinuum media (Itasca 2000). Cui et al. (2016) provided an analytical solution for the equivalent elastic compliance tensor of a rock mass with multiple persistent joint sets introducing a joint deformation tensor, which consists in a modified version of the Oda's crack tensor. They used the three-dimension distinct element code, 3DEC (Itasca 2016) to show the validity of the proposed solution. Later, Jiang et al. (2017) extended the previous work to include non-persistent joints sets.

Even though the previous analytical approaches are well suited for simple and regular fracture geometries, it is worth noting that they generally neglect the nonlinear behaviour and the effect of fracture interactions. To overcome these limitations, several researchers have used numerical methods to determine the equivalent continuum characterization and the representative elementary volume (REV) of a rock mass; where the REV can be defined as the minimum volume beyond which, all equivalent constitutive properties remain largely constant with increasing the

sampling volume (Bear 1972; Long et al. 1982; Mas Ivars et al. 2001; Min et al. 2004a). Long et al. (1982) developed a numerical finite element code to determine the equivalent permeability tensor and the REV of two-dimensional samples with random fracture networks. Their samples were assigned boundary conditions to induce a linear gradient in the flow region with two constant heads. They measured the hydraulic conductivity in models at different scales with several flow orientations, assuming the rock material as impervious and the validity of the cubic law. Long et al. (1982) concluded that the equivalent permeability of a fractured system can be properly determined as long as the mass balance is constant and the anisotropic permeability tensor describes and ellipse. On the other hand, Pouya and Fouché (2009) argued that the permeability tensor of a discontinuous heterogeneous material is symmetric and definite positive, in other words, it represents an ellipsoid; and consequently, in the cases in which Long et al. (1982) could not find an ellipse, the reason is simply because the REV was not met (Pouya & Fouché 2009).

Mas Ivars et al. (2001) developed a methodology based on the distinct element method (DEM) (Cundall 1971) to estimate the 2D equivalent elastic parameters of a rock mass containing fully persistent joint sets with UDEC. This method was extended to determine the possible existence of a REV, the equivalent mechanical properties (Min et al. 2003) and the permeability tensor following the Long's procedure (Min et al. 2004a) of fractured rock masses including a discrete fracture network (DFN). The simulations it these DFN-DEM methodology consisted in modelling the fractured rock mass, assuming the rock material as elastic with several realizations of stochastic DFN models at different scales and orientations. Min et al. (2004b) investigated the effect of nonlinear normal deformation and shear dilation of fractures in the stress-dependent permeability of rock masses under several load conditions. They observed channeling effects of fluid flow in fractures with high mobilization of shear dilation. Thoraval et al. (2004) conducted a similar study using three-dimensional samples with 3DEC and a fracture network generator. Min et al. (2012) compared the equivalent mechanical properties of 2D and 3D models using UDEC and 3DEC respectively. It was found that while the Young's modulus is overestimated in the two-dimensional analysis, the Poisson's ratio depends on the orientation of the UDEC cross-section —

built by cutting through the 3DEC model— in which the fractures are assumed infinite and perpendicular to the model plane. Mas Ivars et al. (2011) used the synthetic rock mass (SRM) method (Pierce et al. 2007) to estimate the strength and deformation characteristics of fractured rock masses in mine scale analyses. The SRM simulates the rock mass as an assembly of bonded spheres with and embedded DFN, allowing for block breakage, observation of deformation, fragmentation and fracture propagation.

Bagheri (2006) developed a dual porosity reservoir simulator iteratively coupled with a geomechanical module to account for the stress influence on the fluid flow and fracture permeability tensor of deformable fractured reservoirs. They used an empirical constitutive model for joints (Bandis et al. 1983) and the analytical formulation by Huang et al. (1995) to estimate the equivalent continuum properties. Gu and Chalaturnyk (2010) presented a reservoir-geomechanical coupled simulation with the application of analytical permeability and porosity models in coalbed methane recovery processes. In their study, the coal matrix and orthogonal cleats are simulated with an equivalent continuum elastic medium model capturing the anisotropy in the permeability and mechanical parameters. Based in the concept of multiple interacting continua (Pruess & Narasimhan 1985), Rutqvist et al. (2013) presented a linked multicontinuum and crack tensor approach (Oda, 1986) to calculate the upscaled effective properties, such as permeability and elastic tensors for coupling geomechanics, fluid flow, and solute transport in fractured rock simulations.

Deisman et al. (2009) introduced a simulation approach to account for geomechanical effects in fractured reservoirs sensitive to stress changes. Their envisioned coupling scheme links four numerical simulators: a reservoir simulator to represent complex flow processes; a continuum geomechanical simulator to determine the deformation and change in effective stress due to changes in reservoir temperature, pore pressures and fluid volumes; a discontinuum simulator based on the SRM approach to capture changes in apertures, fracture propagation and acoustic emission; and a DFN simulator to generate the rock mass structure and to estimate the equivalent permeability and porosity from fracture apertures and new induced fracture generation. They

proposed to estimate the new mechanical and flow properties when a certain change in effective stress is reached. Thus, new equivalent continuum properties can be updated and fed into their respective simulators; and the models are sequentially cycled again. This previous work has motivated the study proposed here.

1.2 Problem Statement

The hydro-mechanical behaviour of discontinuities may have an important effect in the fluid flow and deformability response of fractured porous formations; however, in general, their influence is not taken into account in conventional reservoir geomechanical coupled simulations. That is mainly because the explicit inclusion of all the structural features present in highly fractured reservoirs in hydro-mechanical coupled numerical simulations usually results in high demanding computational power, large memory requirements and prohibitive simulation times. These issues are common in numerical codes for modelling large discontinuum media with explicit fractures.

In addition, the empirical and analytical homogenization or upscaling techniques available to estimate the equivalent continuum properties of rock masses generally disregard the effect of fracture interactions and nonlinear fracture deformations. Also, they are usually restricted to fractures with particular shapes and geometry. Therefore, a methodology capable of determining the hydro-mechanical equivalent continuum properties of a fractured porous formation through numerical homogenization must be developed with the aim of including the influence of fractures represented by a DFN in large reservoir geomechanical coupled simulations.

1.3 Hypothesis and objectives

The geomechanical and fluid flow behaviour of fractured porous formations where the structural features are represented by a discrete fracture network can be captured with acceptable accuracy through an equivalent continuum representative of the rock mass, input for large reservoir geomechanical coupled simulations. The permeability and anisotropic deformability equivalent

parameters can be determined by direct measurement on numerical specimens including the rock structure tested in a virtual rock mass (VRM) numerical laboratory.

This research has the main objective of developing a methodology to include the hydraulic and mechanical effects of discrete fracture networks in reservoir geomechanical coupled simulations, taking into account the inherent capabilities (limitations and advantages) of the involved commercial software. The coupling strategy and methodology are based on the envisioned approach presented by Deisman et al. (2009) where several simulators are linked together following an explicit iterative sequential coupling scheme. The coupling approach involves a reservoir flow simulator and two geomechanical simulators, one for large scale continuum simulations and the other for small and meso-scale discontinuum media. The reservoir flow simulator is used to obtain changes in temperature and pore pressure developed during the complex fluid flow processes. The continuum geomechanical simulator is necessary to determine deformations induced by changes in temperature and pore pressure in the reservoir at each simulation stage. The discontinuum geomechanical simulator is used as a virtual rock mass numerical laboratory (VRM lab) to determine the hydraulic and mechanical equivalent continuum properties representative of the discontinuum material at the desired scale.

1.4 Proposed Methodology

The methodology to capture the hydraulic and mechanical effect of discrete fracture networks in reservoir geomechanical coupled simulations involves numerical modelling techniques including a flow simulator coupled with a continuum geomechanical simulator; and the development of a numerical virtual rock mass laboratory to determine the equivalent properties for the hydro-mechanical continuum characterization of the fractured porous formation.

The Itasca's code FLAC^{3D} (Itasca 2013) is proposed as continuum geomechanical simulator. The commercial code, STARS (CMG 2018) is proposed as reservoir flow simulator. The VRM laboratory is developed in 3DEC (Itasca 2016) with the capability of performing

mechanical and fluid flow numerical tests to determine the hydro-mechanical equivalent continuum parameters of the discretization regions of the fractured reservoir. These homogenized permeability and anisotropic elastic parameters may be updated at specific coupling simulation stages in those fractured regions where the change in the effective stress field reaches a certain tolerance.

1.5 Organization of the thesis

The thesis has been structured such that each chapter can be read as a stand-alone paper; however, all of them are fundamental to understand this research. The thesis consists of five chapters:

- The first chapter presents a brief introduction covering the background and problem statement, a summary of the hypothesis and research objectives, as well as the proposed methodology in this study. The outline of the thesis is also included herein.

- The second chapter presents an explicit sequential coupling scheme for accurately modelling the thermo-poromechanical behaviour of anisotropic porous formations in complex reservoir geomechanical simulations. The validation of the coupling scheme against analytical solutions is also presented.

- The third chapter introduces the mechanical module of the virtual rock mass numerical laboratory, VRM lab, for determining the equivalent orthotropic continuum parameters of a fractured porous formation through a numerical homogenization procedure. The VRM mechanical lab is verified in this chapter against the analytical Oda's crack tensor approach.

- The fourth chapter presents a coupling strategy and methodology proposed for the inclusion of the hydro-mechanical behavior of discrete fracture networks in

reservoir geomechanical simulations of fractured porous formations through numerical homogenization of rock mass discontinuum regions using the VRM laboratory. Additionally, the VRM hydraulic lab developed to determine the full equivalent permeability tensor of fractured regions is also introduced and verified in this chapter.

- The last chapter provides the summary and conclusions of this study, and recommendations for future research.

2 Sequential coupling of reservoir and geomechanical simulators for anisotropic porous media with Biot coefficient tensor

2.1 Summary

A sequentially coupled method is introduced for modelling the thermo-poromechanical behaviour of anisotropic porous media in complex reservoir geomechanical simulations. The method is implemented in a numerical coupling platform whereby the reservoir (CMG – STARS) and geomechanical (Itasca – FLAC^{3D}) simulators are sequentially coupled. The porosity correction coupling strategy is based on the fixed stress split method, given that this scheme enjoys excellent stability and convergence properties. The formulation rigorously includes the generalized tensorial form of the Biot effective stress coefficient, neglected in most numerical coupling techniques. The capabilities of the coupling method to accurately simulate the interactions between thermal, fluid flow and mechanical processes developed in anisotropic media are verified against analytical solutions of the one-dimensional consolidation problem for isotropic and anisotropic materials, the thermal consolidation and the Mandel's problem for transversely isotropic porous media. Additionally, the anisotropic effect of the Biot tensor and the symmetry plane orientation has been studied. The results demonstrate the importance of correctly modelling the effect of material anisotropy in thermo-poromechanical coupled simulations. This study shows that the methodology presented here is required to correctly model stress-sensitive reservoirs involving anisotropic porous formations.

2.2 Introduction

Understanding the behaviour of a porous medium filled with a fluid has been of great importance in many areas of engineering (de Boer 2000). Based on experimental observations, Terzaghi (1923, 1925) proposed a one-dimensional consolidation theory capable of describing the progressive settlement of fully saturated soils, when a uniform distributed surcharge is suddenly

applied. This theory was developed for deformational analyses of laterally constrained soil bodies, under the assumptions of incompressible fluid and solid constituents. Making use of the generalized Hooke's law, Biot (1941) derived a linear theory of isotropic poroelasticity consistent with the coupled interaction between the mechanical and fluid flow processes that take place during the three-dimensional consolidation of saturated porous solids. Biot reformulated these poroelastic equations for anisotropic elastic and viscoelastic materials (Biot 1955, 1956a), thermoelasticity (Biot 1956b), propagation of stress waves (Biot 1962) and nonlinear elasticity cases (Biot 1973). Gassmann (1951) studied the hydro-mechanical coupling problem from a micromechanical perspective through an ideal porous medium model (Cheng 2016), in which the solid phase is assumed microscopically homogeneous and isotropic, while the porous material can be anisotropic and heterogeneous at the macroscopic scale. Later, Biot and Willis (1957) introduced a more general model by removing these previous micromechanical conditions (Cheng 2016), and they included a physical interpretation of the poroelastic coefficients, as well as the suggested methods for their measurement. Following these pioneering works, different researchers contributed to clarifying the physical meaning of the poroelastic constitutive parameters, introducing alternative formulations (e.g., Geertsma 1957; Verruijt 1969; Nur & Byerlee 1971; Rice & Cleary 1976; Zimmerman et al. 1986). This early theoretical framework settled the foundation for a large variety of emergent engineering applications (Cheng 1997; Castelletto et al. 2015). Detournay and Cheng (1993) provided a comprehensive review of the development of the classic poroelasticity theory. A significant contribution to the study of the influence of pore fluids on the mechanical behaviour of porous materials was made by Coussy (1995), who developed a theory based on the fundamental principles of mechanics and thermodynamics of open continua. This poromechanics theory was subsequently extended to cover unsaturated thermoporoelastic, poroplastic, chemoelastic processes and other phenomena related to the physical chemistry and mechanics of porous media (Coussy 2004, 2010). Although traditional problem-solving usually relies on analytical solutions, most are not suitable enough for analyzing complex problems in engineering practice (Cheng 2016). Furthermore, the progressive enhancement of computational capabilities has contributed to the application of the theory of poromechanics in multiple numerical

modelling techniques. Many of these numerical methods have been successfully applied to a diverse range of geoengineering fields such as oil and gas production, geothermal energy, geological nuclear waste disposal and carbon sequestration, among others (Jing & Hudson 2002; Rutqvist 2017).

The strategies to couple flow and mechanics in numerical simulations are commonly divided into fully and sequentially coupled methods (Kim 2018a). The fully coupled, or monolithic, formulation solves the governing equations simultaneously at each time step in a unified flow-mechanical simulator, adopting, in general, an implicit coupling scheme. This algorithm ensures the unconditional stability and convergence of the solution provided that the coupled problem is mathematically well-posed. However, the scheme entails a high computational cost associated with the software development and demanding memory requirements for solving large systems of equations (Kim et al. 2012), making the sequential approach more appealing for large scale simulations. The sequentially coupled method splits the governing equations into subsystems to be solved in separate software modules, in which the information is exchanged following a staggered solution procedure (Felippa & Park 1980). This method has the advantage of being able to incorporate robust commercial codes in the sequential coupling scheme. Typically, two verified numerical simulators are linked together through an interface, one for solving the complex thermal and fluid flow processes and another for dealing with the geomechanical response of the system. The modular attribute of this approach allows for using separate numerical domains with different grid sizes and spatial discretization at each simulator (Tran et al. 2009). The sequential coupling schemes can be classified in explicitly and implicitly coupled solutions (Gu & Chalaturnyk 2005; Deisman et al. 2009). In the explicit sequentially coupled approach, the flow and mechanical coupling parameters are updated and transferred between simulators, once at the end of each time step or simulation stage, that is, after a certain simulation time interval (Zandi et al. 2010). On the other hand, the implicit sequential coupling method entails the iteration of the coupling variables at every time step until a convergence criterion is satisfied. The sequential scheme is expected to produce the same results as the fully coupled solution, as long as the

convergence tolerance is tight enough (Dean et al. 2006; Kim et al. 2011). However, contrary to the fully coupled approach, the unconditional stability and convergence of the solution are not always guaranteed. Kim (2010) studied the numerical stability and convergence of four implicit sequential coupling strategies for splitting the equations of poromechanics in oil reservoir simulations. These split methods can be divided into fixed-strain and fixed-stress when the flow sub-problem is solved first, followed by the mechanical solution and, in drained and undrained splits, when the flow solution is calculated after the mechanical solution. It was found that only the fixed-stress and undrained methods have unconditional numerical stability; however, the fixed-stress split is recommended over the undrained scheme because it provides a faster convergence rate (Kim et al. 2011). A more rigorous analysis of the stability and convergence of the undrained and fixed-stress split methods was conducted by Mikelić and Wheeler (2013). Further studies have shown the convergence of the fixed-stress method for multirate iterative coupling schemes (Almani et al. 2016), multiscale iterative coupling schemes (Dana et al. 2018) and heterogeneous problems (Both et al. 2017). The fixed-stress split strategy has become a popular sequential coupling scheme, being recently extended and used in several coupling problems (e.g., Kim et al. 2013; Kim 2018a, 2018b; Gaspar & Rodrigo 2018; Borregales et al. 2019; Delgado et al. 2019).

In conventional reservoir simulations, the effect of geomechanical deformations is usually taken into account through a pore compressibility factor (Gutierrez & Lewis 1998; Mainguy & Longuemare 2002). This approach does not simulate the complex mechanical behaviour that occurs during oil production activities in stress sensitive reservoirs. Therefore, Settari and Mourits (1994, 1998) proposed a sequential coupling scheme, where the thermal and fluid flow equations are solved first in the reservoir simulator while keeping the mean total stress constant (fixed); then, new temperatures and pore pressures are updated in the geomechanical simulator to determine the resultant strain field. The predicted reservoir porosity is corrected with the calculated porosity in the geomechanical solution, and the thermal and pore compressibility parameters are updated for the next simulation step. This method was found to be very robust; in fact, it essentially follows the same algorithm as the fixed-stress split scheme. On a similar basis, Tran et al. (2004) presented

a more rigorous formulation to determine and update the reservoir porosity as a function of the mean total stress, pore pressure and temperature. Mainguy and Longuemare (2002) studied other sequential strategies where the porosity correction is estimated not only in terms of the mean total stress but also as a function of the pore volume and volumetric strain. They concluded that the pore compressibility can be used as a parameter to improve the stability and convergence of sequentially coupled schemes (Mainguy & Longuemare 2002; Kim et al. 2011). Later, several authors have implemented the fixed-stress split method by employing a porosity correction strategy to model thermo-poromechanical processes in sequentially coupled simulations, given that this approach revealed excellent stability and convergence properties (Kim et al. 2012, 2015; Blanco-Martín et al. 2017; Garipov et al. 2018; Sangnimnuan et al. 2018).

The rock formation is usually treated as isotropic in the coupled solution of reservoir geomechanical simulations. In some cases, when the anisotropy becomes significant, a stress-strain constitutive relation for anisotropic materials is included in the coupling formulation. However, even though the porous material is assumed anisotropic, the Biot effective stress coefficient is still considered a scalar in the equations of poroelasticity. Several studies have revisited Biot's anisotropic poroelastic equations (Biot 1955) in the framework of micromechanics, showing that the generalized anisotropic form of the Biot coefficient is a second-order tensor (Carroll 1979; Thompson & Willis 1991; Cheng 1997; Gao et al. 2017). Moreover, the behaviour of fluid-filled anisotropic porous media through analytical and fully coupled solutions have been studied, revealing that neglecting the effect of anisotropy may yield erroneous or misleading results (Abousleiman et al. 1996; Cui et al. 1996a; Cui et al. 1996b; Hoang & Abousleiman 2012; Cheng 2016; Giot et al. 2018). Recently, the fixed-stress split method was proved to be numerically convergent for the case of anisotropic poroelasticity with Biot effective stress tensor (Dana & Wheeler 2018). Thus, a sequentially coupled method is developed here with the purpose of rigorously including the Biot effective stress coefficient tensor (Biot tensor in the following) in a porosity correction strategy, based on the fixed-stress split scheme, for modelling thermo-poroelastic coupled processes in complex reservoir geomechanical simulations.

2.3 Coupling Methodology

The sequential coupling method presented here involves two commercial codes, STARS and FLAC^{3D}, which are required for modelling the complex thermal and fluid flow processes, and mechanical deformations occurring during reservoir operations. STARS is a steam, thermal, and advanced processes reservoir simulator developed by Computer Modelling Group Ltd. (CMG), which has been widely used over the last decades, becoming a standard multi-phase and multi-component simulator in the oil and gas industry. This software has been designed to simulate simple and highly complex thermal recovery processes, injection of gases, polymers and other chemical additives, advanced well completions, and electrical heating, among other capabilities (Goulet et al. 2009; CMG 2018). The fast lagrangian analysis of continua in three-dimensions, FLAC^{3D}, is a geomechanical modelling software developed by Itasca Consulting Group Inc., which has been extensively used in many geoengineering applications and intended for the mechanical analysis of three-dimensional problems. It follows an explicit finite volume formulation that makes it a robust numerical tool for simulating the nonlinearity and complex plastic behaviour, and even the total collapse of soils and rock formations. The FLAC^{3D} documentation includes several verification problems where the code has been validated and compared against analytical solutions (Itasca 2013). Here, the proposed sequential scheme has been built into a coupling platform developed by the reservoir geomechanics research group (RGRG) at the University of Alberta. The main purpose of the RGRG coupled simulation platform is to serve as the interface for linking both simulators together. That is, it generates the numerical grids for the flow and mechanical models, populates the simulators, as well as managing the exchange and storage of coupling parameters throughout the sequential simulation process.

One of the important factors to take into account when coupling commercial simulators is accessibility to the internal variables of each software. The geomechanical code, FLAC^{3D}, has embedded a useful programming language, FISH, which allows the user to define subroutines to access and manipulate almost all the internal data through predefined intrinsic functions (Itasca 2013). On the other hand, STARS provides access to many simulation parameters; however, due

to consistency purposes, the manipulation of the internal variables is limited to the recurrent input data available in the code. In particular, STARS allows the user to input a new reference porosity, volumetric thermal expansion coefficient, and pore space compressibility of the formation, in a porosity function, to take into account the effect of mechanical deformations during the thermal and fluid flow simulation (CMG 2018). This porosity function and subroutines coded in FISH are used to sequentially couple STARS and FLAC^{3D} through the RGRG coupling platform.

2.3.1 Thermo-Poromechanical Constitutive Relations

The porous medium is considered as an open thermodynamic system composed of a deformable skeleton and an interstitial fluid, representing two superimposed continua. The skeleton is assumed anisotropic having the interconnected porous space within the solid matrix saturated by a single phase fluid. All deformations are assumed small in such a way that the infinitesimal strain theory applies. Compressive stresses and strains are considered negative. The coupling formulation is based on the thermoporoelastic theory presented in Coussy (1995, 2004, 2010). Following Coussy's formalism, the constitutive equations of anisotropic thermoporoelasticity for the porous material are written in the incremental form as:

$$d\sigma_{ij} = C_{ijkl} d\varepsilon_{kl} - b_{ij} dp - C_{ijkl} \alpha_{kl} dT \tag{2.1}$$

$$\frac{dm_f}{\rho_f} = b_{ij} d\varepsilon_{ij} + \frac{1}{M} dp - 3\alpha_m dT \tag{2.2}$$

where σ_{ij} is the total stress tensor; ε_{kl} is the strain tensor; p is the pore pressure; T is the temperature; m_f is the current Lagrangian fluid mass content per unit of initial volume; ρ_f is the fluid mass density; C_{ijkl} is the drained elastic stiffness tensor of the skeleton; b_{ij} is the Biot tensor; α_{kl} is the linear thermal expansion coefficient tensor of the skeleton; M is the Biot modulus of the porous material, and; α_m is the linear thermal expansion related to the fluid-solid mixture. The inverse of the Biot modulus represents the constrained specific storage coefficient (at constant strain). The relationship between the change in fluid mass content and the fluid mass density, that is, the term at the left-hand side of Eq. (2.2) corresponds to the increment of fluid content ζ in

the classic poroelastic formulations (Wang 2000). The thermoporoelastic tangent properties in Eqs (2.1) and (2.2) have the following general forms (Thompson & Willis 1991; Cheng 1997; Hoang & Abousleiman 2012; Gao et al. 2017),

$$b_{ij} = \delta_{ij} - C_{ijkl} S^s_{klmn} \delta_{mn} \tag{2.3}$$

$$\frac{1}{M} = C_{ijmn} S^s_{mnll} \left(S_{ijkk} + S^s_{ijkk} \right) - \phi S^s_{iikk} + \phi C_f \tag{2.4}$$

$$\alpha_m = \alpha_\phi + \phi \alpha_f \tag{2.5}$$

where δ_{ij} is the Kronecker delta; S_{ijkl} is the drained elastic compliance tensor of the skeleton, (or in case of having the superscript *s*, of the solid matrix); ϕ is the Lagrangian porosity defined as the ratio of the current pore volume to the initial volume; C_f is the fluid compressibility; α_ϕ and α_f are the linear thermal expansion coefficients related to the porosity and fluid respectively. The Einstein summation convention applies; thus, tensor contraction is implied over repeated indices. The drained elastic tensors in the previous equations enjoy full symmetry conditions (minor and major). That is, the symmetry of the stress and strain tensors results in the minor symmetry of the stiffness (or compliance) tensor of the skeleton: $C_{ijkl} = C_{jikl} = C_{jilk} = C_{ijlk}$. The major symmetry condition, $C_{ijkl} = C_{klij}$, comes from the conservation of the elastic strain energy density (Ting 1996). The compliance (or stiffness) tensor of the solid matrix, S^s_{ijkl}, satisfies the same minor and major symmetries as long as the matrix of the skeleton is homogeneous. However, in those cases where the solid matrix is inhomogeneous, the major symmetry is not always guaranteed even though the minor symmetry is met (Thompson & Willis 1991; Gao et al. 2017). Here, the compliance (or stiffness) tensor of the solid phase has been assumed to satisfy the major symmetry condition.

Solving for the strain tensor term in the Eq. (2.1) gives,

$$d\varepsilon_{ij} = S_{ijkl} d\sigma_{kl} + S_{ijkl} b_{kl} dp + \alpha_{ij} dT \tag{2.6}$$

The substitution of Eq. (2.6) in the Eq. (2.2) leads to the equivalent form of the variation of fluid content in terms of the total stress, pore pressure and temperature,

$$\frac{dm_f}{\rho_f} = b_{ij} S_{ijkl} d\sigma_{kl} + \left(b_{ij} S_{ijkl} b_{kl} + \frac{1}{M} \right) dp + \left(b_{ij} \alpha_{ij} - 3\alpha_m \right) dT \tag{2.7}$$

Substituting Eqs. (2.3), (2.4) and (2.5) in the two terms related to the pore pressure and temperature of Eq. (2.7) and simplifying results in the constitutive equation of the change in fluid content, in which the corresponding terms of the fluid-solid mixture are shown separately,

$$\frac{dm_f}{\rho_f} = b_{ij} S_{ijkl} d\sigma_{kl} + \left(S_{iikk} - (1+\phi) S^s_{iikk} + \phi C_f \right) dp + \left(b_{ij} \alpha_{ij} - 3\alpha_\phi - 3\phi\alpha_f \right) dT \tag{2.8}$$

Now, the increment of fluid content related to the saturating fluid can be obtained by differentiating the equation of the current fluid mass content, $m_f = \rho_f \phi$, and dividing by the fluid mass density, as follows:

$$\frac{dm_f}{\rho_f} = d\phi + \phi \frac{d\rho_f}{\rho_f} \tag{2.9}$$

The constitutive equation of the saturating fluid is written as (Coussy 2004):

$$\frac{d\rho_f}{\rho_f} = C_f dp - 3\alpha_f dT \tag{2.10}$$

Substituting Eq. (2.9) in Eq. (2.10) yields:

$$\frac{dm_f}{\rho_f} = d\phi + \phi C_f dp - 3\phi\alpha_f dT \tag{2.11}$$

Finally, combining Eqs. (2.8) and (2.11), and substituting the compliance tensor of the solid matrix for terms with the compliance tensor of the skeleton, results in:

$$d\phi = b_{ij} S_{ijkl} d\sigma_{kl} + \left(S_{iikl} b_{kl} (1+\phi) - \phi S_{iikk} \right) dp + \left(b_{ij} \alpha_{ij} - 3\alpha_\phi \right) dT \tag{2.12}$$

This last constitutive equation shows the general form of the change in Lagrangian porosity related to the anisotropic skeleton, regardless of the saturating pore fluid, that must be included in the sequentially coupled simulation scheme to account rigorously for the effect of mechanical deformations.

2.3.2 Porosity Correction Parameters

The porosity in the STARS simulator corresponds to the reservoir porosity, which is a Lagrangian parameter defined as the current pore volume divided by the initial bulk volume. It can be corrected to include the effect of geomechanics during the reservoir simulation, through the following porosity function defined in terms of pressure and temperature as (CMG 2018),

$$\left(\phi-\phi_r\right)=\phi_r c_p\left(p-p_r\right)-\phi_r c_T\left(T-T_r\right) \tag{2.13}$$

where c_p is the pore compressibility; c_T is the volumetric thermal expansion coefficient, and the subscript, *r*, indicates the reference value corresponding to the last simulation step at which the porosity function was updated. These parameters are assumed to behave linearly during the flow simulation step.

The general form of the porosity variation related to the porous skeleton, Eq. (2.12) can be linearized by assuming the thermoporoelastic tangent properties constant during the simulation time interval $\left[t_n, t_{n+1}\right]$. Comparing this linearized form with the expressions of Eq. (2.13) in the same interval gives the following coupling parameters related to the change in porosity caused by changes in stress, pore pressure and temperature:

$$\Delta\phi_{n+1}=b_{ij}S_{ijkl}\Delta\sigma_{kl_n} \tag{2.14}$$

$$c_{p_{n+1}}=\frac{1}{\phi_n}\left(S_{iikl}b_{kl}\left(1+\phi_n\right)-\phi_n S_{iikk}\right) \tag{2.15}$$

$$c_{T_{n+1}}=\frac{1}{\phi_n}\left(3\alpha_\phi-b_{ij}\alpha_{ij}\right) \tag{2.16}$$

where $\Delta\phi_{n+1}$ is the porosity change due to the increment of the total stress tensors determined from the geomechanical simulations at the two previous consecutive steps, t_n and t_{n-1}, (i.e., $\Delta\sigma_{kl_n} = \sigma_{kl_n} - \sigma_{kl_{n-1}}$). Analogous expressions of this porosity correction have been presented in Settari and Mourits (1994, 1998); and Kim et al. (2012) where the Biot coefficient of the porous material is considered a scalar.

The FLAC^{3D} code operates by default in small-strain mode, in which the coordinates of the nodes are not updated with the computed displacements during the simulation process. In the general calculation sequence embodied in FLAC^{3D}, the stresses are determined from strain rates, which in turn are derived from current nodal velocities. In other words, the displacements are not involved in the numerical solution procedure; however, they are calculated to derive a strain increment tensor based on the model geometry at the time of measurement (Itasca 2013). Since the current volume of the model in the small-strain mode is equal to its initial volume, the strain increment corresponds to a Lagrangian parameter, which is compatible with the definition of the reservoir porosity in STARS. Therefore, it is convenient to express the change in porosity in terms of changes in strain, pore pressure and temperature. Substituting Eq. (2.1) in Eq. (2.14) yields,

$$\Delta\phi_{n+1} = b_{ij}\Delta\varepsilon_{ij_n} - b_{ij}S_{ijkl}b_{kl}\Delta p_n - b_{ij}\alpha_{ij}\Delta T_n \tag{2.17}$$

where the strain increment is computed in the geomechanical module, and the variations in pore pressures and temperatures are calculated in the reservoir simulator; all of them are determined from the two previous consecutive simulation steps, as in the aforementioned total stress change: $\Delta\varepsilon_{ij_n} = \varepsilon_{ij_n} - \varepsilon_{ij_{n-1}}$; $\Delta p_n = p_n - p_{n-1}$; and $\Delta T_n = T_n - T_{n-1}$ (Kim et al. 2012).

2.3.3 Implementation of the Sequential Scheme

The flow and geomechanical coupling scheme between STARS and FLAC^{3D} has been developed based on the fixed-stress split sequential method (Kim 2011). Thus, in the modelling sequence, the main coupling cycle (Figure 2.1) begins with the solution of the thermal and fluid flow sub-problem by STARS, in which the total stress is assumed constant (fixed) during the

simulation. After convergence of the flow problem, the RGRG coupling platform pauses the STARS simulation, and stores pore pressures and temperatures obtained in the reservoir model. Then, the effect of the change in pressure and temperature is included in the geomechanical simulation through a total stress tensor increment calculated as,

$$\Delta\sigma_{ij_{p,T}} = -\left(\delta_{ij} - C_{ijkl}S^{s}_{klmn}\delta_{mn}\right)\Delta p_n - C_{ijkl}\alpha_{kl}\Delta T_n \tag{2.18}$$

where the term in brackets corresponds to the Biot tensor (Eq. (2.3)). This equation shows that the change in pore pressure and temperature may induce shear stresses due to the anisotropy of the porous material; in fact, the stress change is not hydrostatic for anisotropic materials (Carroll 1979; Dana & Wheeler 2018). Before running the mechanical simulation, the stress increments are determined by the RGRG platform (Eq. (2.18)) and added to the stress components in the FLAC^{3D} zones. This approach is based on the logic associated with the automatic total stress update, *config ats,* and *zone-based* features available in FLAC and FLAC^{3D} respectively (Itasca 2011, 2017); whereby the total stresses in the model are updated to account for the effect of pore pressure changes imported from an external source. Blanco-Martín et al. (2017) adopted a similar stress correction approach for isotropic materials. Once the total stress tensors are updated in the elements of the FLAC^{3D} model, the mechanical sub-problem is solved under the assumption of drained conditions. Then, after reaching the mechanical equilibrium state, the RGRG platform pauses the FLAC^{3D} simulator, and the resulting stress and strain increment tensors are stored. The next task consists of determining the pore compressibility, volumetric thermal expansion coefficient and porosity change from Eqs. (2.15), (2.16) and (2.17), respectively. At this point, the platform updates the porosity function in STARS with these new correction parameters, and it is ready to start a new coupling cycle again.

In the simulation procedure conducted by the RGRG platform, the reservoir and geomechanical modules are sequentially coupled in an explicit manner. Hence, following the main coupling cycle, STARS computes the changes in temperature and pore pressure during a simulation time interval; then, new stress increments are added in FLAC^{3D} to calculate the resultant

mechanical deformation induced in the reservoir; and finally, the new coupling parameters are determined and updated in the porosity function. At the end of this simulation stage, several coupling cycles, n_u, involving STARS and FLAC^{3D}, are iterated by setting a simulation time short enough to prevent the fluid transport at each of them. These short time steps are motivated by the consideration that the change in stresses can be treated as instantaneous compared to the pressure diffusion processes occurring in the reservoir. This way, geomechanical effects are included in the simulation, while the fluid mass is conserved after the porosity correction in the short-time cycles. The procedure continues with the computation of another reservoir simulation time interval, followed by the number of short-time iterations, n_u, defined by the user (Figure 2.2). This procedure is repeated until the last reservoir geomechanical simulation stage is computed.

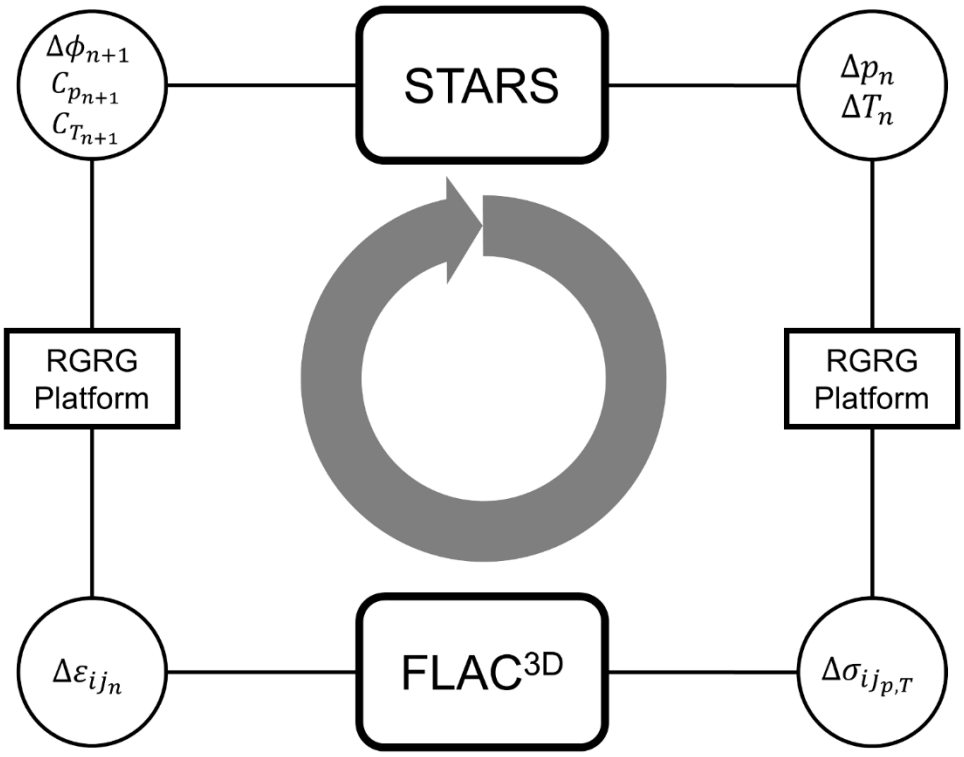

Figure 2.1—Main coupling cycle between STARS and FLAC^{3D} controlled by the reservoir geomechanics research group (RGRG) coupling platform.

During each simulation cycle, the coupling parameters are assumed to behave linearly; however, the incremental form of the constitutive equations allows for choosing suitable time intervals to incrementally simulate the nonlinear response of the system (Thompson & Willis 1991). For the cases with strongly coupled nonlinear processes, the simulation time interval must be short, and the number of short-time iterations large enough, to induce changes in pore pressure, porosity and deformations within an acceptable tolerance, analogous to the convergence criteria used in the implicit sequentially coupled methods.

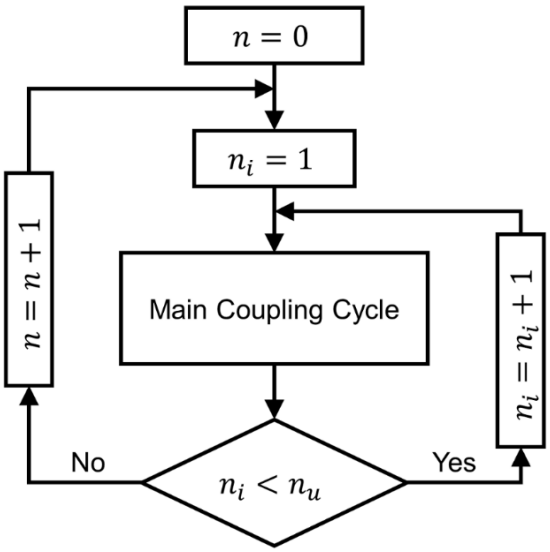

Figure 2.2—Flow diagram for the sequential coupling scheme, showing the number of simulation stages, n, and the short-time iterations, n_u, defined by the user.

2.4 Numerical Results

2.4.1 Terzaghi's Problem

The first case to be analyzed is the classic one-dimensional (1D) consolidation problem (Terzaghi 1923, 1925). This problem has been widely used as a benchmark for testing the validity of numerical coupling methods (Cui et al. 1996a; Kim et al. 2012, 2015; Blanco-Martín et al. 2017). It consists of a 1D column of a fully saturated material, in which an external axial load is suddenly applied on its top boundary. The lateral displacements are constrained to zero and the bottom boundary is fixed in all directions. Only the vertical displacements are freed, allowing the

material to consolidate along the column. The fluid is allowed to flow out through the top boundary while the rest of the boundaries remain impermeable. Figure 2.3 shows the schematic of the classic 1D consolidation problem.

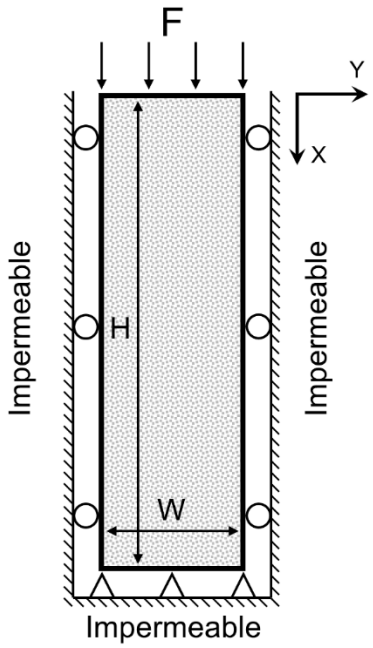

Figure 2.3—Geometry and boundary conditions scheme for the 1D consolidation problem.

2.4.1.1 Isotropic Consolidation

In this case, the column has been modelled with a height, H = 31 m, and a square cross-section of width, W = 1 m. The material is set as isotropic, homogeneous and saturated by a compressible single phase fluid. The solid matrix is set incompressible with respect to the skeleton; therefore, the Biot tensor contracts to the scalar value of one. The temperature is assumed constant and the effect of gravity is neglected. The material and fluid input parameters are summarized in Table 2.1. This problem has also been analyzed in Blanco-Martín et al. (2017). The column is discretized in the reservoir and geomechanical simulators in 31 cubic elements of 1 m edge length (Figure 2.4). The model is at equilibrium with an initial pore pressure of 10 MPa and the compressive total stress field also of 10 MPa. In STARS, the boundaries of the model are unconstrained by default. Thus, to account for the constrained boundary conditions and to improve the convergence of the problem (Kim et al. 2011; Castelletto et al. 2015), the drained compliance

in the porosity correction parameters is replaced by the compliance under oedometric conditions, C^{oedo}. For isotropic materials, C^{oedo} is defined as the inverse of the oedometric bulk modulus of the skeleton: $K^{oedo} = K + 4G/3 = 0.634$ GPa. Additionally, a producer well with bottomhole pressure of 10 MPa is perforated at the top boundary to allow for the fluid drainage (CMG 2018). Figure 2.4 shows the detail of the producer well drilled at the surface of the model.

Table 2.1—Material and fluid properties for the isotropic 1D consolidation problem.

Property	**Value**
Young's modulus E, (GPa)	0.6
Poisson's ratio v, (-)	0.15
Bulk modulus* K, (GPa)	0.286
Shear modulus* G, (GPa)	0.261
Oedometric compliance C^{oedo}, (1/GPa)	1.578
Biot's coefficient b, (-)	1
Biot's modulus M, (GPa)	4.706
Porosity ϕ, (%)	42.5
Fluid compressibility C_f, (1/GPa)	0.5
Fluid viscosity μ, (Pa·s)	0.001
Permeability k, (m^2)	$6.51 \cdot 10^{-15}$

* Bulk and shear modulus are calculated from Young's modulus and Poisson's ratio as: $K = E/(3(1-2v))$ and $G = E/(2(1+v))$ respectively.

At the beginning of the simulation, a constant load of 10 MPa is applied on the top boundary of the FLAC^{3D} model while keeping the producer well closed in STARS. After the instantaneous undrained pressure rise, the producer is opened (i.e. allowed to flow), and the material consolidates gradually as the fluid flows out of the column. The simulation is divided into several time intervals until 100 days, with two short-time iterations (n_u = 2) at the end of each simulation stage. Figure 2.5a shows the evolution of the pore pressure obtained from the analytical solution and the coupled simulation results of four monitoring points installed at different depths

along the column (X-axis). The analytical and numerical results of the surface settlement are compared in Figure 2.5b. Both plots show that the numerical results are in close agreement with the analytical solution. The slight pressure mismatch between the numerical and analytical solutions observed at the first time stage (0.0025 days) and monitoring point at 0.5 m depth (Figure 2.5a) has been attributed to the local effect of perforating the producer well at the same element of the model (x = 0.5 m) where the pressure is measured (Figure 2.4).

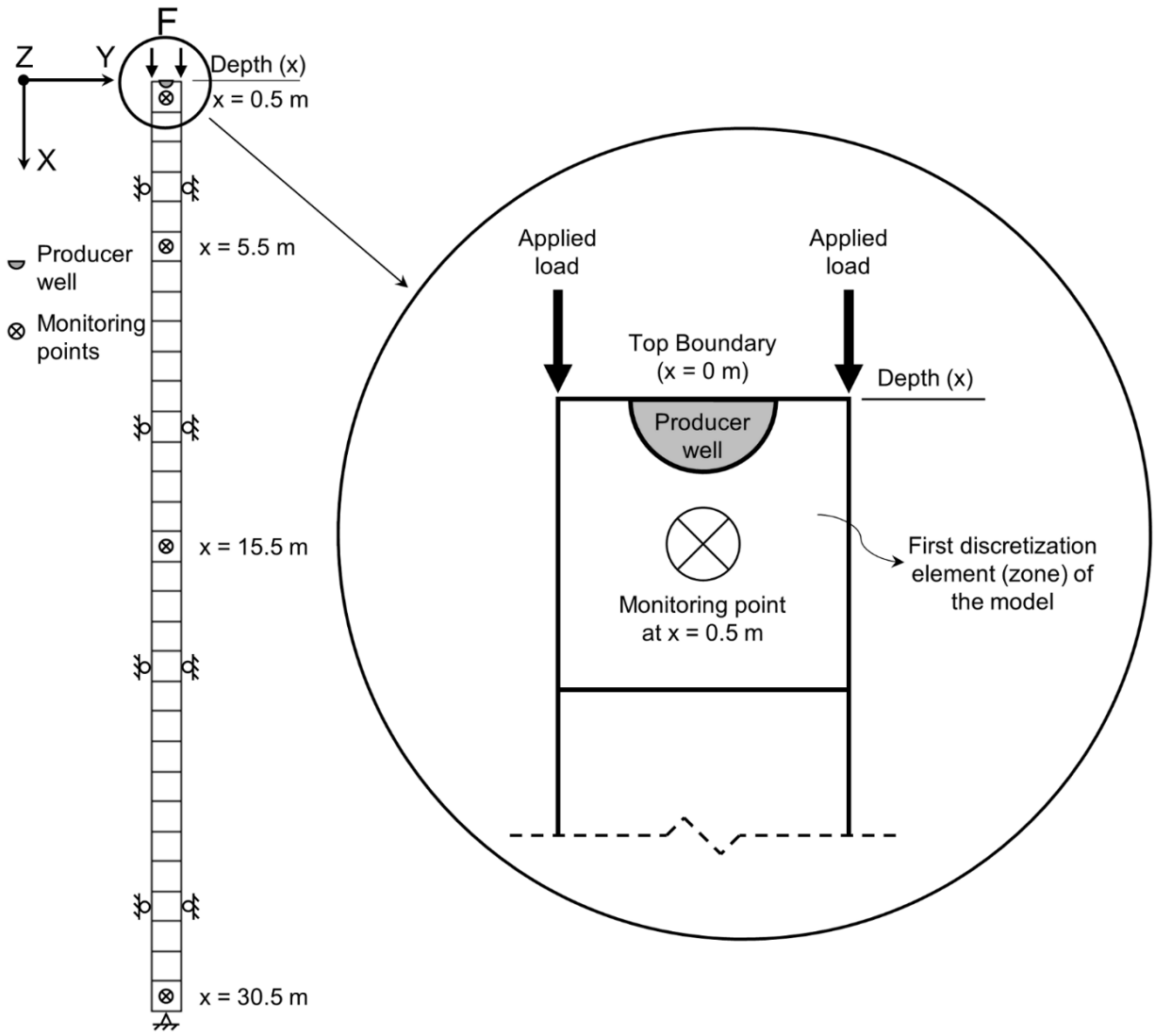

Figure 2.4—Geometry of the 1D consolidation model showing the discretization elements, the producer well drilled at the surface and the pressure monitoring points at the center of four elements at different depths (x). The figure in the circle shows the detail of the first element of the model at the top of the column including the first monitoring point and the producer well excavated at the surface to simulate the flow boundary condition.

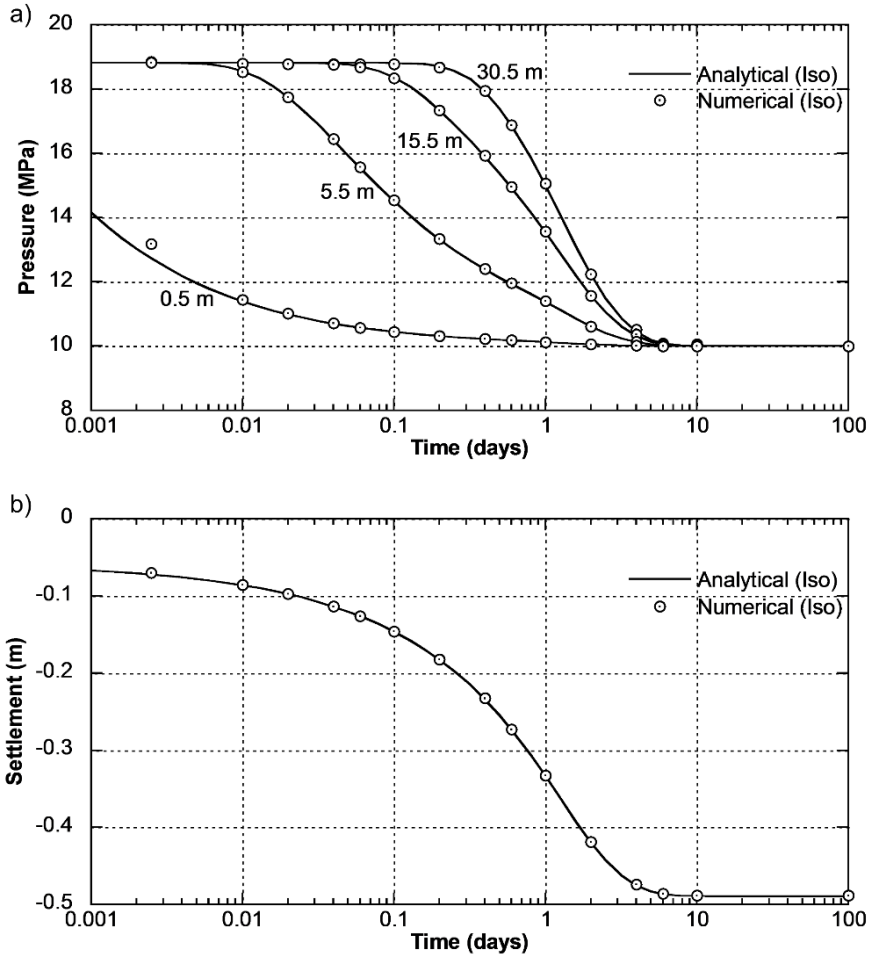

Figure 2.5—Comparison of analytical and numerical results for the isotropic (Iso) case: a) pore pressure measurements at monitoring points; b) settlement at the surface (x = 0 m).

2.4.1.2 Anisotropic Consolidation

The effect of anisotropy on the 1D consolidation problem was studied by Cui et al. (1996a). They extended the analytical solution of the Terzaghi's consolidation problem to account for material anisotropy. Following this previous work (Cui et al. 1996a), a 1D consolidation problem with a transversely isotropic porous medium has been analyzed. In this example, the model geometry, initial conditions and input parameters are the same as the isotropic case. Material anisotropy was induced by setting Poisson's ratio in the plane of isotropy, ν, to 0.15 and in the normal direction, ν', to 0.35. The Young's modulus is set equal in all directions, $E = E' = 0.6$ GPa. The shear modulus in the symmetry plane orientation, G, is calculated to 0.261 GPa (Table 2.1). The independent shear modulus in the normal direction, G', has been estimated to 0.222 GPa

using the approximate formula in the Appendix A (Eq. (A-9)). The plane of isotropy is identified with the horizontal plane (Y-Z), to represent the regular structural features of a standard depositional scenario. Then, the elastic parameters correspond with: $E_x = E_y = E_z = E$; $v_{yz} = v$; $v_{xy} = v_{xz} = v'$; $G_{yz} = G$; $G_{xy} = G_{xz} = G'$. The solid phase is considered incompressible; therefore, the Biot tensor is equal to the identity matrix. In addition, the oedometric compliance along the column (X-axis) is calculated equal to 1.186 GPa^{-1} (Appendix A). The simulation is conducted following the same procedure as in the previous case. The pore pressure and surface settlement determined with the analytical solution (Cui et al. 1996a) are in excellent agreement with the results of the numerical simulation (Figure 2.6).

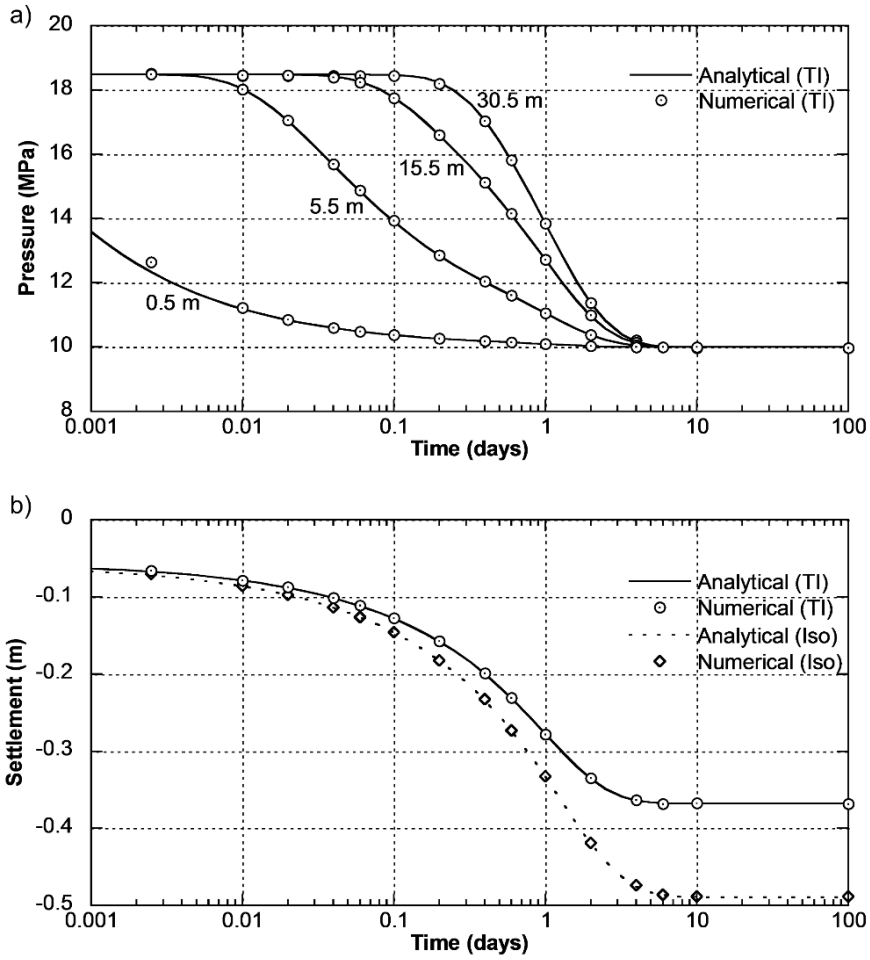

Figure 2.6—Comparison of analytical solution (Cui et al. 1996a) and numerical results for the transversely isotropic (TI) case: a) pore pressure measurements at four monitoring points (0.5, 5.5, 10.5 and 30.5 m depth); b) settlement at the surface (x = 0 m), including the previous results of the isotropic (Iso) settlement.

2.4.1.3 Thermal Consolidation

The following case illustrates the thermo-poroelastic behaviour of a saturated porous medium in the condition of 1D deformation. Selvadurai and Suvorov (2016) proposed an analytical solution to account for the mechanical, hydraulic and thermal effects in the 1D consolidation case. The same geometry and initial conditions have been used to compare to the previous isotropic and anisotropic cases. The Biot tensor coefficients have been set to the scalar value of 0.75 to include the effect of a compressible and isotropic solid matrix in the simulation. The column is assumed fully saturated with water. The permeability value has been decreased four orders of magnitude to induce the dissipation of pore pressure and temperature at the same time interval; this way, the coupling degree of the thermo-poromechanical process developed during the simulation is emphasized. The overall volumetric heat capacity, c_p^*, and thermal conductivity, k_c^*, of the porous medium are calculated to 2912 kJ/(m^3▪°C) and 3.15 W/(m▪°C), respectively, through the approximations: $c_p^* = \phi\rho_f c_f + (1-\phi)\rho_s c_s$ and; $k_c^* = \phi k_{cf} + (1-\phi)k_{cs}$ (Selvadurai & Suvorov 2016). For isotropic materials under drained conditions, the linear thermal expansion of the porous skeleton, α, and the solid matrix, α_s, are equivalent (Coussy 2004). Moreover, the linear thermal expansion coefficient is related to porosity as, $\alpha_\phi = \alpha_s(b-\phi)$. Therefore, Eq. (2.16) can be simplified to: $c_{T_{n+1}} = -3\alpha_s$. Table 2.2 summarizes the material and fluid parameters for the thermal consolidation problem.

Initially, the model is at equilibrium with a pore pressure of 10 MPa and a temperature of 25°C. The lateral and bottom boundaries are thermally insulated, limiting the thermal exchange through the top surface only. Three wells, an injector, a producer, and a heater (CMG 2018), have been perforated at the top boundary of the STARS model, to simulate the boundary conditions of pore pressure and temperature of the surface. These wells have been drilled at the same surface element and location as the producer well of the two previous cases as depicted in Figure 2.4. The injector and producer are both set to operate with a bottomhole pressure of 10 MPa, and the initial temperature of the heater is 25°C.

Table 2.2—Material and fluid properties for the thermal consolidation case.

Property	**Value**
Young's modulus E , (GPa)	0.6
Poisson's ratio v , (-)	0.15
Biot's coefficient b , (-)	0.75
Porosity ϕ , (%)	42.5
Fluid compressibility C_f , (1/GPa)	0.5
Fluid viscosity μ , (Pa·s)	0.001
Permeability k , (m^2)	$6.51 \cdot 10^{-19}$
Solid density ρ_s , (kg/m^3)	2700
Fluid density ρ_f , (kg/m^3)	997
Linear thermal expansion solid α_s , (1/°C)	$0.83 \cdot 10^{-5}$
Linear thermal expansion fluid α_f , (1/°C)	$6.90 \cdot 10^{-5}$
Specific heat capacity solid c_s , (J/(kg·°C))	735
Specific heat capacity fluid c_f , (J/(kg·°C))	4180
Thermal conductivity solid k_{cs} , (W/(m·°C))	5
Thermal conductivity fluid k_{cf} , (W/(m·°C))	0.64

The simulation starts with the three wells closed. Then, the heater is set to 75°C to create a temperature increment of 50°C. This sudden change in temperature induces thermal stresses, causing an undrained pore pressure increase along the column, and heaving of the top boundary. Once the temperature reaches the constant value of 75°C in the entire model, the injector and producer wells are opened and, the temperature of the heater is reduced to its initial value of 25°C to permit the progressive dissipation of pore pressure and temperature through the surface. The temperature and pore pressure evolution obtained from the analytical solution (Selvadurai & Suvorov 2016) and the numerical simulation are compared in Figure 2.7a and Figure 2.7b.

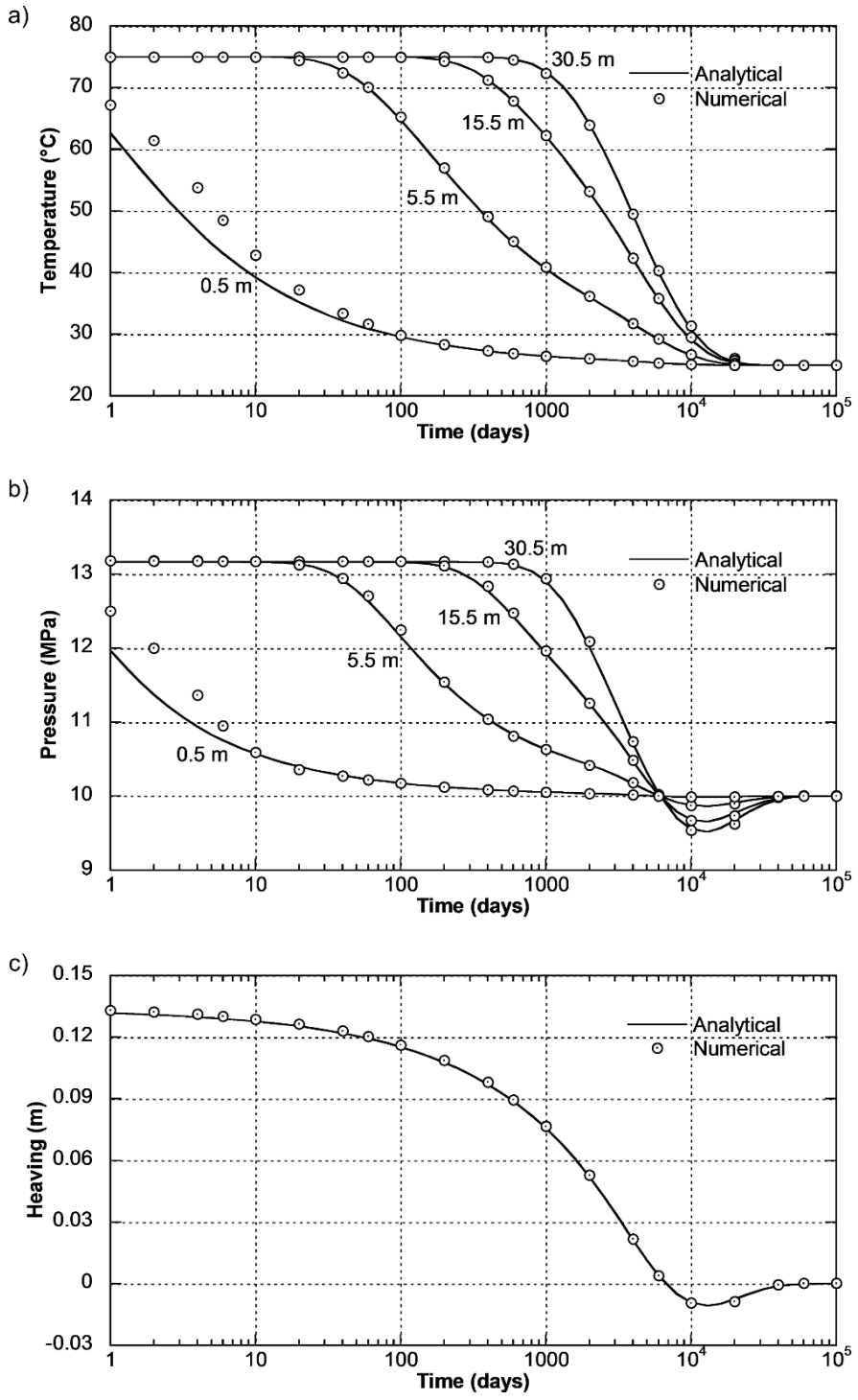

Figure 2.7—Comparison of analytical solution (Selvadurai & Suvorov 2016) and numerical results for the thermal consolidation case: a) temperature and b) pore pressure measurements at four monitoring points (0.5, 5.5, 10.5 and 30.5 meters depth); c) heaving at the top surface (x = 0 m).

The time-dependant response of the vertical displacement at the top surface is shown in Figure 2.7c. The results of the numerical simulation and the analytical solution are in good agreement; however, there are some differences in the temperature and pressure measurements observed at the early stages in the top monitoring point (x = 0.5m, in Figure 2.7). This local discrepancy comes from the installation of the measurement point at the same top element of the model where the three wells are perforated and does not exist for any other monitoring locations in the model.

2.4.2 Mandel's Problem

The Mandel's problem (Mandel 1953) has been frequently used as a benchmark to verify and validate numerical solutions of coupled poromechanical codes (Cui et al. 1996b; Kim et al. 2011; Castelletto et al. 2015; Blanco-Martín et al. 2017; Garipov et al. 2018; Borregales et al. 2019). This problem involves a layer of infinitely long material with rectangular cross-section, compressed between two rigid, impermeable and frictionless platens, loaded with a constant force.

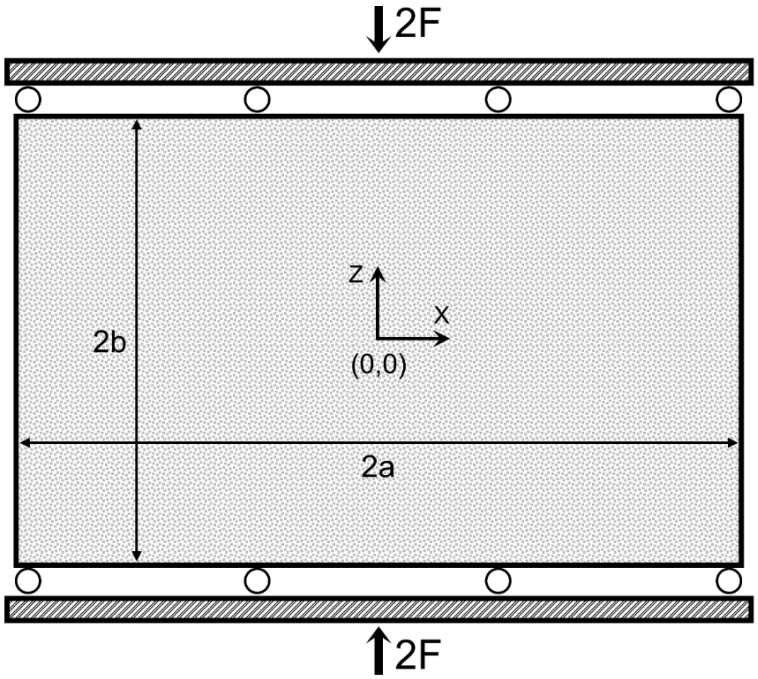

Figure 2.8—Schematic of the geometry and boundary conditions for Mandel's problem.

The layer is analyzed as a two-dimensional (2D) section under plane strain conditions, where the saturating fluid is allowed to flow out of the specimen through the lateral boundaries (Figure 2.8). In the classic problem, the porous material is considered isotropic with incompressible fluid and solid constituents; hence, the analytical solution has been extended to the fully poroelastic case (Cheng & Detournay 1988) and revisited to include transversely isotropic porous media (Abousleiman et al. 1996). This last solution is used here to verify the capability of the proposed numerical coupling scheme to simulate the poromechanical response of anisotropic materials.

For the following cases, a layer of square cross-section with dimensions 2a = 0.2 m × 2b = 0.2 m has been analyzed. The porous medium is considered homogeneous, transversely isotropic and saturated by a compressible fluid. The temperature is assumed constant, and the effect of gravity is neglected. Similar to the case analyzed in Abousleiman et al. (1996), the anisotropic material properties have been derived from the experimental data for the Trafalgar shale reported in Aoki et al. (1993). In this material, the solid phase is considered to be microscopically homogeneous and isotropic. Accordingly, the specimen has been modelled as an ideal porous medium (Gassmann 1951; Cheng 2016), in which the anisotropy arises at the macroscopic scale from the presence of structural features. These micromechanical assumptions allow to simplify the Biot tensor and Biot modulus, Eqs. (2.3) and (2.4), as (Cheng 1997):

$$b_{ij} = \delta_{ij} - \frac{1}{3K_s} C_{ijkl}\delta_{kl} \tag{2.19}$$

$$\frac{1}{M} = \frac{1}{K_s}\left(1 - \frac{1}{9K_s} C_{iikk}\right) - \phi\left(\frac{1}{K_s} - C_f\right) \tag{2.20}$$

where K_s is the bulk modulus of the solid matrix. The elastic constants in the plane of isotropy are calculated as: E = 20.6 GPa, ν = 0.189 and G = 8.66 GPa, and in the direction normal to the symmetry plane are: E' = 17.3 GPa, ν' = 0.246 and G' = 7.23 GPa. The bulk modulus of the solid constituent is, K_s = 48.2 GPa, and the Biot modulus is, M = 15.8 GPa. The calculated Biot tensor coefficient in the plane of isotropy is, b = 0.733 and in the normal direction, b' = 0.749. The porosity

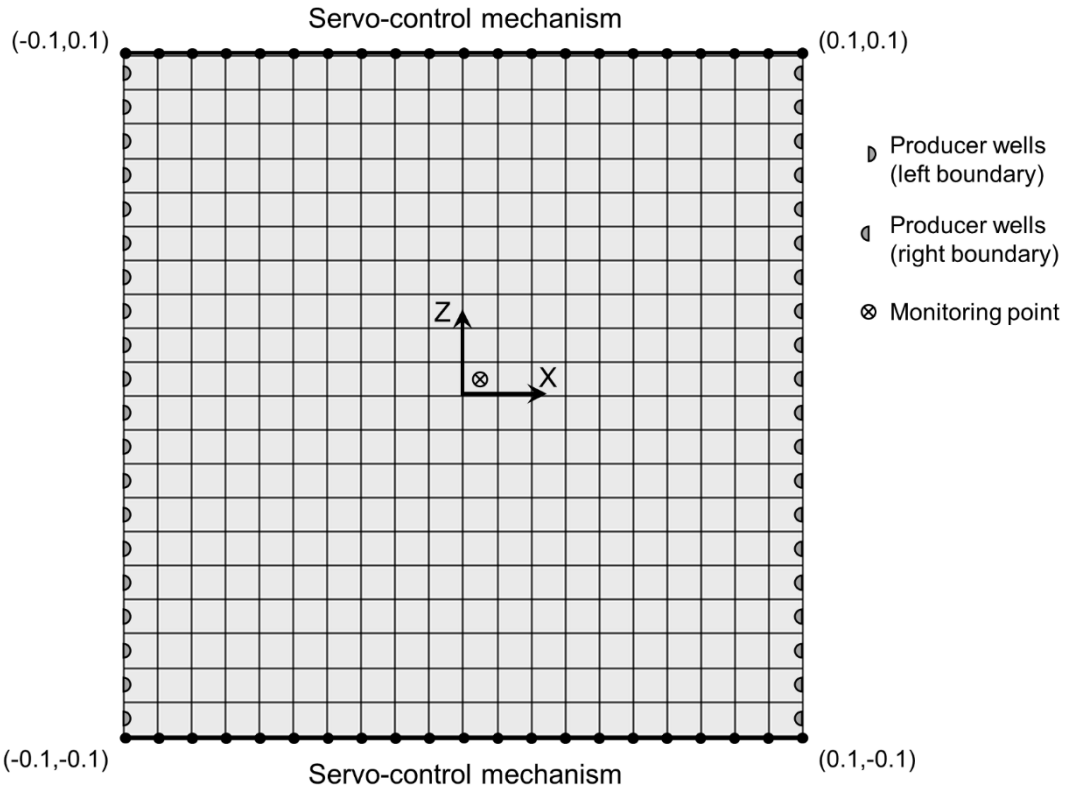

Figure 2.9—Domain discretization in 20 × 1 × 20 cubic elements of edge 0.01 m, for Mandel's problem simulations. Servo-control mechanism installed at the gridpoints of top and bottom boundaries; producer wells drilled at the lateral boundaries and; monitoring point at coordinates (x, z) = (0.005, 0.005) m.

is set to 11.5 %. The fluid compressibility is, $C_f = 0.435$ GPa^{-1}, and viscosity is, $\mu = 0.001$ Pa·s. The permeability is set equal in all directions, $k = 9.87 \cdot 10^{-20}$ m^2, to evaluate the material behaviour due only to mechanical anisotropy. The model domain is discretized in a three dimensional (3D) grid of 20 × 1 × 20 cubic elements (in the x, y and z directions), each with a 0.01 m edge length. All the elements located at the lateral boundaries of the STARS model are perforated with producer wells to allow for the fluid drainage. The rigid platens are simulated in the FLAC^{3D} model employing a numerical servo-control mechanism, whereby the vertical velocities of the gridpoints at the top and bottom boundaries of the mechanical grid are adjusted to maintain the specified load (Figure 2.9). This servomechanism has been coded in FISH and is based on the servo algorithm implemented in the particle flow code, PFC, developed by Itasca Consulting Group Inc., (Itasca 2008). The displacement in the out-of-plane direction (Y-axis) is constrained to zero to impose the plane strain condition.

The model is initially at equilibrium, free of total stresses with a pore pressure of 1 MPa. The producer wells are set to operate with a bottomhole pressure also of 1 MPa and initially closed. At the beginning of the first simulation stage, the servo-control is set to apply a constant force, F = 10^6 N per meter of layer in the out-of-plane direction, at the top and bottom boundaries. This suddenly applied force gives an average initial compressive stress of 10 MPa, which causes an instantaneous undrained pore pressure response. Then, the producer wells are opened to allow for the progressive dissipation of pore pressure as the fluid flows out of the layer. The simulation is conducted in several stages with two short-time iterations (n_u = 2) at the end of each time interval. Following this procedure, a model with the isotropic plane in the horizontal direction (X-Y) has been analyzed. In this simulation (Case 1), the elastic parameters are defined by, $E_x = E_y = E$; $E_z = E'$; $v_{xy} = v_{yx} = v$; $v_{zx} = v_{zy} = v'$; $G_{xy} = G$; $G_{yz} = G_{zx} = G'$ (note that $v_{zx} = v_{zy} \neq v_{xz} = v_{yz} =$ 0.293). The Biot tensor coefficients correspond with, $b_x = b_y = b$; and $b_z = b'$. Figure 2.10 shows the orientation of the symmetry plane for Case 1, including the drained compliance matrix of the skeleton (Appendix A) and the Biot tensor in column form. The analytical and numerical results of the pore pressure are measured at the monitoring point (x = 0.005 m, z = 0.005 m), the vertical displacement along the top boundary (x, z = 0.1 m), and the horizontal displacement of the right boundary (x = 0.1 m, z) (Figure 2.11). Two further scenarios have been simulated, in which the solid phase has been assumed incompressible in one case, $K_s^{\infty} \to \infty$, and with a stiffness half of K_s in the other case, $K_s^{50\%}$ = 24.1 GPa. For the incompressible solid scenario (Case 2), the Biot modulus and Biot tensor coefficients are calculated to: M = 20.0 GPa and $b_x = b_y = b_z = 1$; also, the drained compliance under plane strain conditions (Appendix A) is used to improve the solution convergence. In the case with 50% of the bulk modulus of the solid matrix, $K_s^{50\%}$ (Case 3), the Biot parameters are M = 15.4 GPa, $b_x = b_y = 0.468$ and $b_z = 0.499$. The remaining modelling parameters are equal to Case 1. The numerical and analytical solutions are also included in Figure 2.11. The simulation results are in perfect agreement with the analytical solution in Abousleiman et al. (1996).

Case 1 – Horizontal symmetry plane (X-Y)

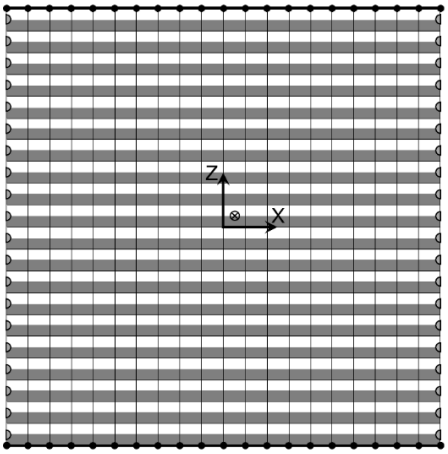

Drained compliance matrix (GPa^{-1})

$$S_{IJ} = \begin{pmatrix} 0.0485 & -0.0092 & -0.0142 & 0 & 0 & 0 \\ -0.0092 & 0.0485 & -0.0142 & 0 & 0 & 0 \\ -0.0142 & -0.0142 & 0.0578 & 0 & 0 & 0 \\ 0 & 0 & 0 & 0.1383 & 0 & 0 \\ 0 & 0 & 0 & 0 & 0.1383 & 0 \\ 0 & 0 & 0 & 0 & 0 & 0.1154 \end{pmatrix}$$

Biot tensor in column form

$$b_J = \left[0.733, 0.733, 0.749, 0, 0, 0 \right]^T$$

Case 4 – Vertical symmetry plane (Y-Z)

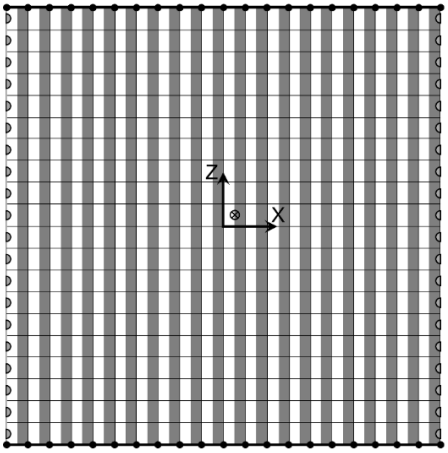

Drained compliance matrix (GPa^{-1})

$$S_{IJ} = \begin{pmatrix} 0.0578 & -0.0142 & -0.0142 & 0 & 0 & 0 \\ -0.0142 & 0.0485 & -0.0092 & 0 & 0 & 0 \\ -0.0142 & -0.0092 & 0.0485 & 0 & 0 & 0 \\ 0 & 0 & 0 & 0.1154 & 0 & 0 \\ 0 & 0 & 0 & 0 & 0.1383 & 0 \\ 0 & 0 & 0 & 0 & 0 & 0.1383 \end{pmatrix}$$

Biot tensor in column form

$$b_J = \left[0.749, 0.733, 0.733, 0, 0, 0 \right]^T$$

Case 5 – Symmetry plane (at 45° with X-Y)

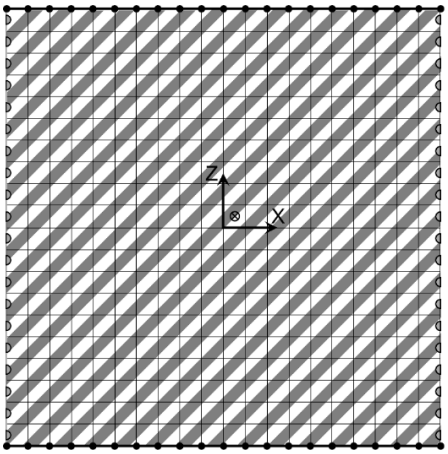

Drained compliance matrix (GPa^{-1})

$$S_{IJ} = \begin{pmatrix} 0.0541 & -0.0117 & -0.0151 & 0 & -0.0046 & 0 \\ -0.0117 & 0.0485 & -0.0117 & 0 & 0.0050 & 0 \\ -0.0151 & -0.0117 & 0.0541 & 0 & -0.0046 & 0 \\ 0 & 0 & 0 & 0.1269 & 0 & -0.0114 \\ -0.0046 & 0.0050 & -0.0046 & 0 & 0.1383 & 0 \\ 0 & 0 & 0 & -0.0114 & 0 & 0.1269 \end{pmatrix}$$

Biot tensor in column form

$$b_J = \left[0.741, 0.733, 0.741, 0, -0.008, 0 \right]^T$$

Figure 2.10—Isotropic plane orientation for Cases 1, 4 and 5 of the Mandel's problem; (Cases 2 and 3 have the same symmetry plane orientation as Case 1, but different Biot parameters). Each case includes the drained compliance matrix of the skeleton and the Biot tensor (where the superscript T denotes matrix transposition), both defined in the coordinate system (X, Y, Z).

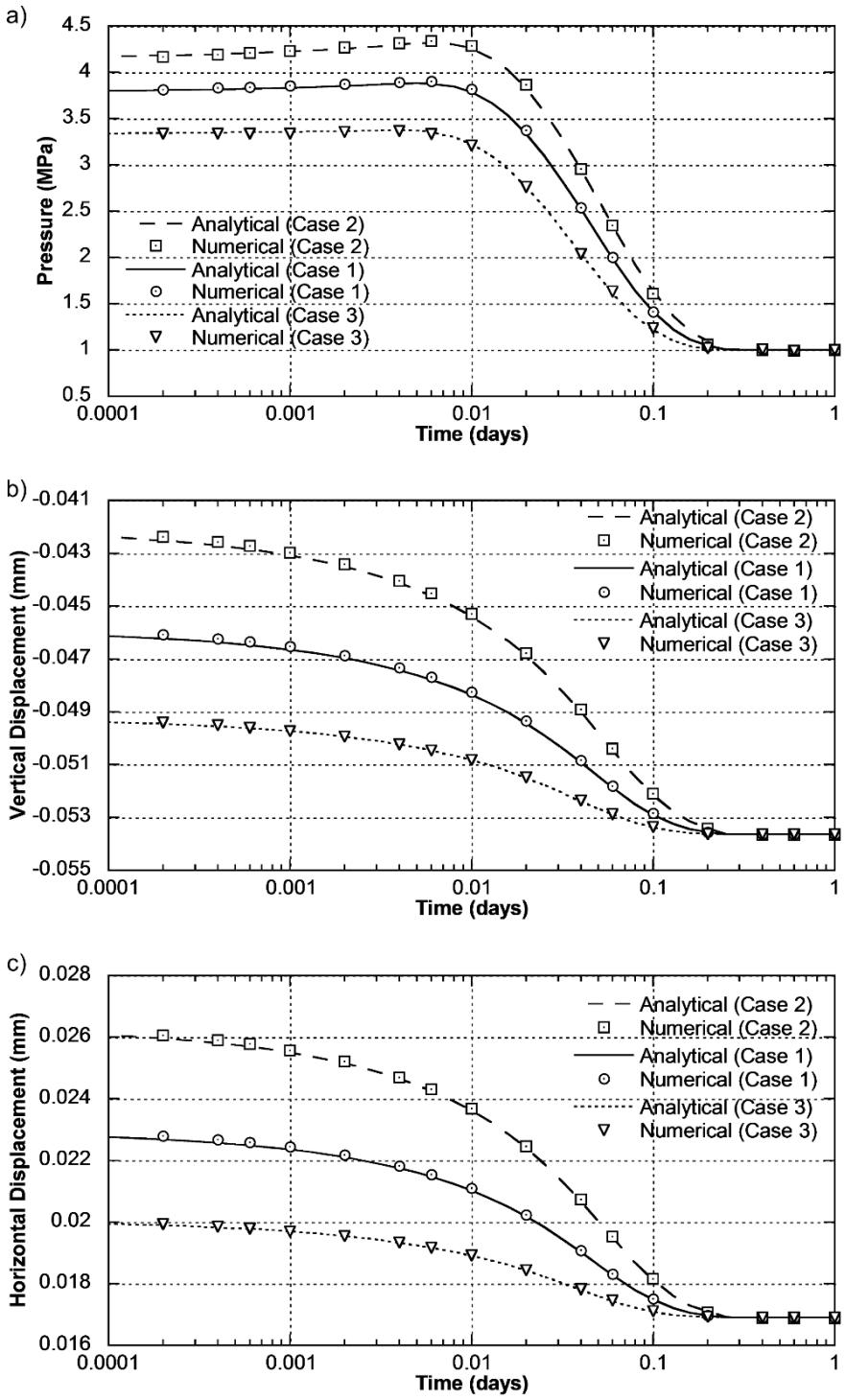

Figure 2.11—Comparison of numerical results and analytical solutions (Abousleiman et al. 1996) for Mandel's problem simulations with $K_s = 48.2$ GPa (Case 1); $K_s^{\infty} \to \infty$ (Case 2); and $K_s^{50\%} = 24.1$ GPa (Case 3). The horizontal plane (X-Y) is set as the plane of isotropy. The plots show: a) pore pressure measurement at monitoring point (0.005 m, 0.005 m); b) vertical displacements along the top boundary (x, z=0.1 m); and c) horizontal displacements of the right boundary (x=0.1 m, z).

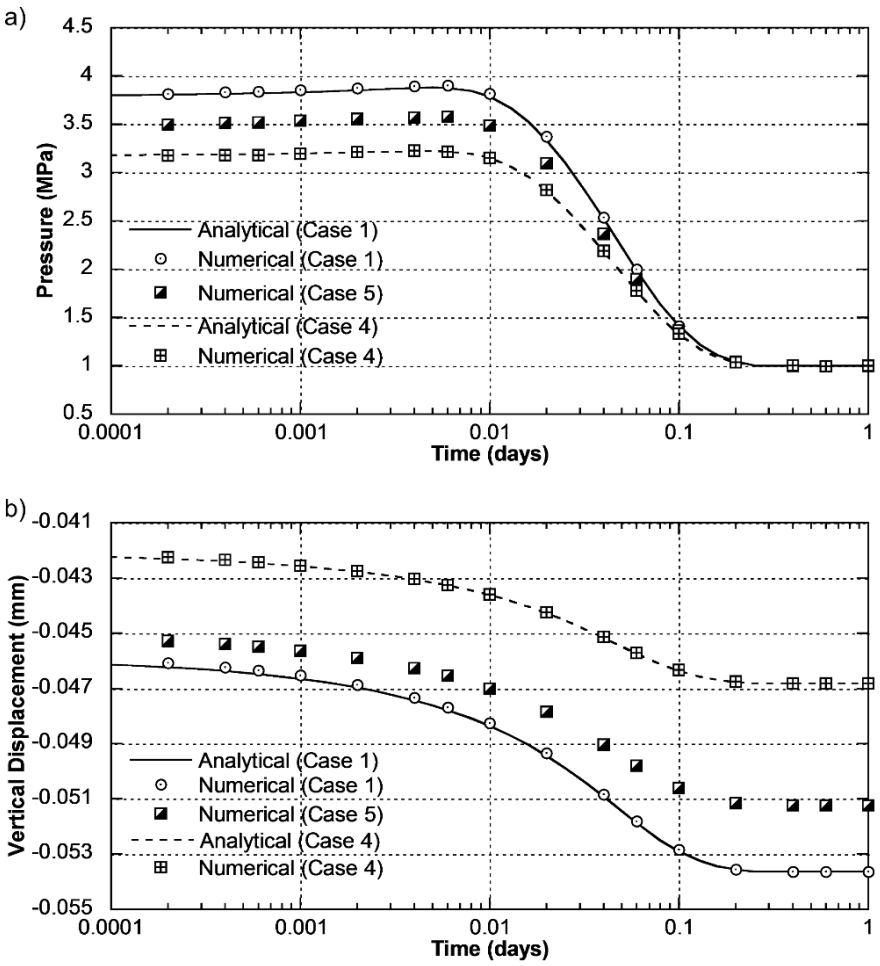

Figure 2.12—Numerical results and analytical solution (Abousleiman et al. 1996) for Mandel's problem with different isotropic plane orientations: horizontal plane (X-Y) for Case 1; vertical plane (Y-Z) for Case 4 and; at 45° with the horizontal for Case 5 (see Figure 2.10). The Case 5 cannot be solved with the analytical solution used here; therefore, only the numerical solution is included. The plots show: a) pore pressure measurement at monitoring point (0.005 m, 0.005 m) and; b) vertical displacements along the top boundary (x, z=0.1 m).

Two additional cases have been analyzed to assess the influence of the symmetry plane orientation on the poromechanical response of the specimen. Both simulations are modelled the same as Case 1, except for the isotropic plane direction. Since these cases represent 2D problems under plane strain conditions, the out-of-plane direction of the model must be a principal direction of material symmetry (Zienkiewicz et al. 2005); thus, the isotropic plane has been oriented containing the Y-axis in both cases. For the first extra model (Case 4), the plane of isotropy is

oriented in the vertical direction (Y-Z), giving the following elastic parameters, $E_y = E_z = E$; $E_x = E'$; $v_{yz} = v_{zy} = v$; $v_{xy} = v_{xz} = v'$; $G_{yz} = G$; $G_{zx} = G_{xy} = G'$; $b_y = b_z = b$; and $b_x = b'$. In the second extra model (Case 5), the specimen is rotated anticlockwise around the Y-axis until the isotropic plane forms an angle of 45° with the horizontal plane. Analogous to Case 1, the orientation of the symmetry plane for Case 4 and Case 5, as well as the drained compliance matrix and Biot tensor, are included in Figure 2.10. The evolution of the pore pressure at the monitoring point and the vertical displacement of the top boundary is illustrated in Figure 2.12.

The results of the numerical simulations are in excellent agreement with the analytical solution (only available for Case 1 and Case 4). The horizontal displacements have not been included in the results, since the lateral boundaries of the specimen in the Case 5 do not remain vertical during the simulation (i.e., the layer deforms in a rhombohedral shape).

2.5 Discussion

The verification cases have shown that there is a good match between the results of the analytical solutions and the numerical simulations conducted with the RGRG coupling platform, following the proposed sequentially coupled scheme. The effect of inducing mechanical anisotropy by changing the Poisson's ratio in the 1D consolidation problem can be identified, comparing Figure 2.5 with Figure 2.6. It was observed that the initial pore pressure rise is slightly lower in the anisotropic simulation than in the isotropic model; nevertheless, both solutions monotonically converge to the same value once the pressure increment was fully dissipated. In addition, the final settlement of the surface is substantially smaller in the anisotropic case. This poromechanical response is due to the lower oedometric compliance of the transversely isotropic material compared with the corresponding value of the isotropic column. The thermo-poroelastic behaviour developed in the thermal consolidation problem is illustrated in Figure 2.7. In this case, the temperature increment monotonically decreases along the column from 75°C until reaching the initial value of 25°C again. As the temperature dissipates, the excess of pore pressure eventually drops below the initial condition of 10 MPa to finally converge to that value. A similar

trend was observed in the vertical displacement of the surface, where the initial heaving due to the thermal expansion of the column is followed by a slight surface settlement, just before the model returns to the initial state of zero displacement. This analysis shows the capability of the coupling method to simulate the interaction between thermo-poromechanical coupled processes.

The influence of the solid phase stiffness on the poroelastic behaviour of the Mandel's problem, modelled with a transversely isotropic layer, is depicted in Figure 2.11. There, the pore pressure evolution measured at the monitoring point follows the conventional non-monotonic response known as the Mandel-Cryer effect (Schiffman et al. 1969; Detournay & Cheng 1993; Abousleiman et al. 1996; Cheng 2016), in which the initial excess of pore pressure at the center of the layer continues to increase before it begins to decline. This phenomenon, characteristic of the Mandel's problem, has been properly captured in the analyzed cases. The results of the simulations have revealed that the initial pore pressure increment is higher in the specimen with the incompressible solid (Case 2) and lower in the model with 50% bulk modulus of the solid matrix (Case 3), compared with the solution of the Case 1. Also, the initial vertical displacement at the top boundary of the model is smaller in Case 2 and larger in Case 3. Conversely, the initial lateral expansion, or horizontal displacement, measured at the right boundary has been found larger in Case 2 and smaller in Case 3. Although these cases show different initial undrained behaviours, the three solutions converge to the same results corresponding to the final drained state of the model. Moreover, during the transition from undrained to the drained response, the layer continues to consolidate even more in the vertical direction while it is laterally contracting as time evolves. It can be seen in the input properties for these simulations that the values of the Biot modulus and Biot tensor coefficients corresponding to the anisotropic porous material increase with the stiffness of the solid matrix. Consequently, increasing the Biot parameters leads to an initial undrained response with higher pore pressure rise, smaller vertical consolidation and larger horizontal expansion of the model.

The results of the Mandel's problem for each of the three proposed symmetry plane orientations are shown in Figure 2.12. As expected, the characteristic non-monotonic pore pressure

response at the center of the specimen can be observed in the three cases. The simulation with the horizontal plane defined as the plane of isotropy, Case 1, shows the highest excess of pore pressure, followed by the model with the symmetry plane oriented at 45° with the horizontal, Case 5, whereas the lowest value is obtained in the model with the isotropic plane oriented in the vertical direction, Case 4. It can be seen that the pore pressure response for Case 5 is equidistant from the other two solutions. As time progresses, these three different initial pore pressure increments converge to the same final value of 1 MPa, which corresponds to the initial pressure condition at the equilibrium state. Additionally, the vertical displacement measurements show the largest consolidation of the anisotropic layer in Case 1, and the smallest one in Case 4. The vertical displacement at the top boundary in Case 5 lies between the two previous solutions, but this time, it is closer to Case 1. Contrarily to the pore pressure response, the vertical consolidation of the specimen reaches different final values at the end of each simulation. This poroelastic behaviour arises from the change of material compliance in the vertical direction induced by rotating the specimen around the Y-axis (Figure 2.10). Since the platens are rigid, the vertical displacements are uniform along the horizontal direction of the model. Moreover, the lateral boundaries stay perpendicular to the platens during the simulation of Case 1 and Case 4; however, they do not remain vertical for Case 5 due to the inclined orientation of the symmetry plane, causing the rhombohedral deformation shape of the cross-section. For this reason, the horizontal displacements have not been compared in this analysis. Also, the analytical solution presented in Abousleiman et al. (1996) is intended to solve problems where the principal directions of material symmetry are aligned with the coordinate system of the model, such as in Case 1 and Case 4. Thus, only the numerical results corresponding to the pore pressure and vertical displacements are shown for Case 5. These cases illustrate the significant effect of the material symmetry orientation on the fluid flow and mechanical coupled simulations.

In this study, the change in permeability has not been included in the main coupling cycle; however, it can be updated during the simulation process through analytical or empirical relationships in those cases where the permeability is sensitive to geomechanical effects (Touhidi-

Baghini 1998; Li & Chalaturnyk 2006; Ben Abdallah et al. 2014). Also, the heat generation effect related to the geomechanical deformation is considered negligible in the coupling process. That is, the temperature change induced by the strain increment is not taken into account in the heat flow simulation, implying a one-way coupling scheme between heat transport and geomechanics (Kim et al. 2012; Kim 2018b). This assumption is suitable for many applications since the temperature field is not significantly affected by mechanical changes in most materials (Wang 2000; Cheng 2016). Nonetheless, the method should be used with caution in those problems where frictional processes leading to large heat generation effects may occur. The analytical and numerical examples presented here demonstrate the capability of the proposed coupling method to accurately solve thermo-poromechanical coupled problems involving anisotropic porous materials with the Biot effective stress coefficient defined in tensorial form. Although the formulation has been implemented in the RGRG coupling platform to sequentially couple STARS with FLAC^{3D}, this methodology can also be used to couple similar reservoir and geomechanical commercial simulators.

2.6 Conclusions

A sequentially coupled method has been developed to accurately model the thermo-poromechanical behaviour of anisotropic porous formations in complex reservoir geomechanical simulations. The sequential scheme has been implemented in a numerical platform developed by the reservoir geomechanics research group of the University of Alberta, in which the reservoir simulator STARS is coupled with the geomechanical code FLAC^{3D} through a porosity correction strategy based on the fixed stress split method. The generalized tensorial form of the Biot effective stress coefficient has been rigorously included in the thermo-poromechanical coupling formulation. The methodology presented here has been verified against the analytical solutions corresponding to the 1D consolidation of isotropic and anisotropic materials, to the thermal consolidation, as well as to the Mandel's problem for transversely isotropic porous media.

Several numerical simulations of the Mandel's problem have been conducted to evaluate the effect of the Biot elastic parameters and the orientation of the symmetry plane on the poromechanical behaviour of transversely isotropic materials. These models show that the excess pore pressure increases with increasing the Biot modulus and Biot tensor, whereas the undrained vertical consolidation of the specimen decreases. Regarding the isotropic plane orientation, the simulations with higher material compliance in the vertical direction result in higher undrained pore pressure responses and larger vertical consolidations. In particular, depending on the orientation of material symmetry, these vertical consolidations converge to different final drained values at the end of each simulation. These results demonstrate the importance of correctly modelling the effect of material anisotropy in thermo-poromechanical coupled simulations. Finally, the modular characteristic of the sequential coupling scheme allows easy inclusion of different simulators within the RGRG coupling platform, or even implement this formulation in another numerical interface developed to couple similar commercial codes for modelling thermo-poroelastic coupled processes in reservoir geomechanical simulations of anisotropic porous formations.

3 Virtual rock mass numerical laboratory for the anisotropic mechanical characterization of fractured rock formations

3.1 Summary

The mechanical characterization for large scale numerical simulations of rock masses containing complex fracture patterns with different geometrical and geomechanical parameters is not a simple task. In these cases, the fractured rock formation is often represented by an equivalent continuum that includes implicitly the average mechanical effect of all the fractures. The equivalent elastic properties are determined through homogenization or upscaling processes using analytical or numerical methods. However, the closed-form solutions usually neglect the fracture interaction effects, whereas the numerical solutions rely on the existence of a representative elementary volume (REV) which is not always granted, especially in rock masses with fractures of very different size. In this study, a numerical homogenization methodology is proposed for the anisotropic mechanical characterization of fractured rock formations with an embedded DFN, discretized in regions at the required scale for the purpose of the engineering analysis, independently of the REV size. The homogenization process of the discretization regions for the equivalent continuum model is managed by a virtual rock mass (VRM) numerical laboratory implemented in the three-dimensional distinct element code 3DEC. These homogenized regions are represented by an elastic material with orthotropic symmetry. The comparison of the VRM laboratory with the analytical Oda's crack tensor approach verifies the validity of this methodology. The results demonstrate that the VRM lab is able to capture with a great deal of fidelity the small-scale variability of the deformational response of the fractured rock formation.

3.2 Introduction

Rock mass formations generally occur in nature as complex systems of rock bodies containing and being delimited by discontinuities at different scales such as faults, veins, bedding planes, fractures, fissures and joints. The presence of discontinuities in the rock formation is the

main cause of the scale dependent mechanical behaviour characteristic of fractured rock masses. Although the mechanical characterization is an essential step in the analysis of rock engineering problems, the determination of accurate mechanical properties is not a simple task since discontinuities often form complicated fracture patterns with different geometrical and geomechanical parameters. The rock mass deformation modulus may be directly estimated through experimental *in situ* measurements from large-scale tests conducted in the field. However, these tests are usually expensive, time consuming and sometimes difficult to interpret (Bieniawski 1978; Hoek & Diederichs 2006). Empirical equations have been suggested by numerous authors as indirect methods for estimating the deformation modulus of rock masses (Kulatilake et al. 1993). The proposed equations are based on empirical correlations between the deformation modulus and rock mass classification schemes such as the rock mass rating (RMR) and the geological strength index (GSI) among others (Hoek & Diederichs 2006; Hoek & Brown 2019). The applicability of these correlations is limited to rock formations where the discontinuities are randomly oriented and their number is sufficiently large (Hoek & Brown 2019). In these cases, the rock mass can be assumed to behave as a homogeneous and isotropic material. However, this assumption may not be valid for rock formations containing systematic patterns of well-defined joint sets that frequently induce a clear anisotropic mechanical response in the rock mass.

An alternative method to estimate indirectly the rock mass deformation is by means of analytical expressions. Essentially, these equations determine the overall elastic properties of the fractured system, from the summation of the deformation responses of discontinuities and the intact rock. The intact rock and fracture properties are commonly obtained from separate laboratory tests on small size samples. In the analytical methods, the fractured rock mass is traditionally replaced by an equivalent continuum with properties determined through homogenization or upscaling techniques. In the homogenization processes, the equivalent properties are averaged over the volume of a particular size region, whereas, in the upscaling procedures, they are averaged at the representative elementary volume (REV) scale (Jing & Stephansson 2007). The REV can be defined as the minimum volume beyond which all the

equivalent parameters of interest remain virtually constant with increasing the region size (Salamon 1968; Bear 1972; Long et al. 1982; Oda 1988; Mas Ivars et al. 2001). During the past decades, several analytical solutions have been presented for determining the equivalent continuum properties of stratified rock formations (Salamon 1968; Gerrard 1982) and, rock masses containing systematic and persistent joint sets (Duncan & Goodman 1968; Amadei & Goodman 1983; Fossum 1985; Yoshinaka & Yamabe 1986; and Huang et al. 1995). Oda (1986, 1993) proposed a symmetric crack tensor to determine the equivalent elastic compliance tensor of fractured rock systems with non-persistent and randomly oriented joints. Analogous formulations have also been provided in the framework of geophysics (Sayers & Kachanov 1995; Schoenberg & Sayers 1995). Recently, a modified version of the Oda's crack tensor has been proposed by Cui et al. (2016) for rock masses with multiple persistent joint sets and extended to include non-persistent joints by Jiang et al. (2017). All of these solutions neglect the effect of fracture interactions that may be important in rock formations with multiple intersecting joints of finite size. Therefore, the analytical methods are more suited for rock masses containing simple and regular fracture geometries where the non-interaction approximation is assumed valid.

The use of numerical techniques in determining the equivalent mechanical properties of fractured rock formations has grown considerably over the years along with the improvement of computational capabilities. Contrary to the analytical solutions, the numerical methods are able to capture the fracture interaction effect and nonlinear deformation of the intact rock and joints. Although the finite element method (FEM) has been used for studying the mechanical behaviour of fractured media (Duncan & Goodman 1968; Kulatilake 1985; Pouya & Ghoreychi 2001; Chalhoub & Pouya 2008; Yang et al. 2014; Wu et al. 2019), the discrete element method (DEM), initially presented by Cundall (1971) for systems of polygonal blocks and assemblies of circular particles (Lemos 2018), has become a popular method for modelling discontinuum materials. The main advantage of the DEM is the capability to represent multiple intersecting discontinuities explicitly, allowing for large displacements and the total separation of discrete bodies while new contacts are created as the calculation progresses (Cundall & Hart 1992). Using an early version

of three-dimensional distinct element code 3DEC (Itasca 2016), Kulatilake et al. (1993) studied the REV size of a rock mass with non-persistent joint sets, including the relationship between the mechanical parameters and the Oda's crack tensor. Kulatilake et al. (1993) also proposed an orthotropic constitutive model that was later applied in a dam project to represent the equivalent elastic behaviour of the jointed rock mass (Wu & Kulatilake 2012). Min and Jing (2003) conducted a series of numerical simulations of fractured rock masses containing different realizations of discrete fracture networks (DFN), using the two-dimensional distinct element code UDEC (Itasca 2000), to determine the REV size and elastic properties of the equivalent continuum. Thoraval and Renaud (2004) proposed an upscaling approach to compute the equivalent stiffness matrix using 3DEC. Mas Ivars et al. (2011) presented the synthetic rock mass (SRM) approach for the three-dimensional mechanical characterization of fractured rock masses. The SRM method uses the particle flow code PFC^{3D} (Itasca 2008) to simulate the rock mass as an assembly of bonded spherical particles with an embedded DFN, allowing for the development of block deformations, fracture propagation and fragmentation processes. Later studies have used UDEC to investigate the effect of the fracture intensity (Khani et al. 2013a) and, the deformability and strength of fractured rock masses (Khani et al. 2013b; Noorian Bidgoli et al. 2013; Noorian Bidgoli & Jing 2014; Alshkane et al. 2017). Similarly, the DFN–DEM approach (Min & Jing 2003) has been used together with 3DEC to numerically estimate the corresponding deformability and strength parameters at the REV scale of three-dimensional fractured media (Laghaei et al. 2018; Mahboubi Niazmandi & Binesh 2020). These studies essentially rely on the existence of the REV to upscale the mechanical properties of the fractured rock. However, the REV may not exist in rock formations containing joint sets and fractures of very different size (Jing & Stephansson 2007). In these cases, a homogenization process may be more appropriate for determining the equivalent parameters at specific regions of the rock mass.

An analytical approach for estimating the continuum properties of a jointed rock mass independently of the REV scale was proposed by Pariseau (1993, 1995). In this non-representative volume element (NRVE) approach, the equivalent parameters are determined for every

discretization element of the continuum model representative of the fractured rock. Thus, the problem of smearing out the equivalent continuum properties over the model elements is prevented in those cases where the REV is larger than the smallest discretization zone (Pariseau 1993). Stietel et al. (1996) presented a homogenization procedure based on the Oda's crack tensor theory for the analysis of two-dimensional problems. Similarly, Rutqvist et al. (2013) also used the crack tensor approach to analytically derive the block-scale properties for all the equivalent continuum elements of a two-dimensional fractured system. These homogenization techniques are useful tools for estimating the equivalent properties of every element of the continuum model that represents the fractured formation. However, they are based on analytical solutions and, therefore, the interactions between fractures are not taken into account. In this study, a numerical homogenization approach is proposed for the anisotropic mechanical characterization of fractured rock formations with an embedded DFN. A virtual rock mass (VRM) laboratory is presented here to conduct numerical simulations using 3DEC for determining the equivalent elastic compliance tensor of specific fractured regions. That way, a fractured rock formation discretized in regions of different dimensions can be fully characterized and represented by an anisotropic continuum model that accounts for the fracture interaction effect.

3.3 Numerical homogenization methodology

The explicit inclusion of most of the existing discontinuities in large scale numerical simulations of fractured media is generally unfeasible in terms of computational time and model size. In these cases, the original discontinuum model may be replaced by an equivalent continuum that includes implicitly the average effect of the fractures contained in the rock formation. Usually, the equivalent continuum properties are averaged at the REV scale through upscaling processes. However, depending on the purpose of the engineering analysis, the discretization of the continuum model may include elements of different dimensions that should be equal or larger than the REV; otherwise, the scale dependent variability of the model may not be properly represented at smaller scales. In the homogenization methodology presented here, the anisotropic continuum parameters of the discretization elements are determined, independently of the REV scale, through

numerical simulations of their corresponding discontinuum models. These simulations are conducted in 3DEC and managed by the VRM laboratory during the homogenization process.

3.3.1 Anisotropic constitutive model for continuum materials

The definition of a constitutive model is an essential requirement in the mechanical characterization of continuum materials. Following the generalized Hooke's law, the stress-strain relationship of an anisotropic material can be expressed in tensor form as (Jayne & Suddarth 1966):

$$\varepsilon_{ij} = S_{ijkl}\sigma_{kl} \tag{3.1}$$

where ε_{ij}, σ_{kl} and S_{ijkl} are the strain, stress and compliance tensors, respectively, with each of the indices (*i, j, k, l*) ranging over the Cartesian coordinates of the three-dimensional space. In this study, the tensor contraction is implied over repeated indices only in those equations expressed in tensor form. The fourth-order elastic compliance tensor enjoys the full symmetry conditions $S_{ijkl} = S_{jikl} = S_{jilk} = S_{ijlk}$ and $S_{ijkl} = S_{klij}$ that come from enforcing the symmetry of the stress and strain tensors as well as the conservation of the complementary strain-energy density (Ting 1996; Nemeth 2011). As a result, the number of independent components of the compliance tensor is reduced to 21 elastic coefficients that are usually represented in matrix form using the Voigt notation. Thus, the Eq. (3.1) can be written in contracted form as (Min & Jing 2003; Jaeger et al. 2007):

$$\begin{pmatrix} \varepsilon_{xx} \\ \varepsilon_{yy} \\ \varepsilon_{zz} \\ \gamma_{yz} \\ \gamma_{xz} \\ \gamma_{xy} \end{pmatrix} = \begin{pmatrix} S_{11} & S_{12} & S_{13} & S_{14} & S_{15} & S_{16} \\ S_{21} & S_{22} & S_{23} & S_{24} & S_{25} & S_{26} \\ S_{31} & S_{32} & S_{33} & S_{34} & S_{35} & S_{36} \\ S_{41} & S_{42} & S_{43} & S_{44} & S_{45} & S_{46} \\ S_{51} & S_{52} & S_{53} & S_{54} & S_{55} & S_{56} \\ S_{61} & S_{62} & S_{63} & S_{64} & S_{65} & S_{66} \end{pmatrix} \begin{pmatrix} \sigma_{xx} \\ \sigma_{yy} \\ \sigma_{zz} \\ \tau_{yz} \\ \tau_{xz} \\ \tau_{xy} \end{pmatrix} \tag{3.2}$$

where ε_{ii} are the normal components of the strain tensor, γ_{ij} are the engineering shear strains defined as twice the shear components of the strain tensor (i.e., $\gamma_{ij} = \varepsilon_{ij} + \varepsilon_{ji} = 2\varepsilon_{ij}$) and, the σ_{ij} and τ_{ij} are the normal and shear components of the stress tensor. In Voigt notation, the subscripts (1,

2, 3, 4, 5, 6) represent the component directions (*xx, yy, zz, yz, xz, xy*), respectively. Furthermore, the relationships between the coefficients of the compliance matrix and the tensor components satisfy that the presence of a subscript with the value 4, 5 or 6 in any matrix coefficient requires the multiplication of its corresponding tensor component by 2, (e.g., $S_{33} = S_{zzzz}$; $S_{36} = 2S_{zzxy} = 2S_{xyzz} = S_{63}$; $S_{66} = 4S_{xyxy}$). It is important to note that the engineering shear strains are not components of the strain tensor; however, their definition in Eq. (3.2) makes the elastic compliance matrix symmetric (Ting 1996).

3.3.2 Virtual rock mass laboratory

In order to determine all the coefficients of the compliance matrix, at least six independent tests have to be conducted on the target specimen. The first column of the compliance matrix can be obtained from a compression test in the x-direction where only the component σ_{xx} of the stress tensor is increased while the rest of the components remain constant (i.e., $\Delta\sigma_{ij} = \left(\Delta\sigma_{xx}, 0, 0, 0, 0, 0\right)^T$ where superscript *T* denotes transposition). In this test, the coefficients of the first column are calculated from the resultant strain measurements divided by the stress increment applied in the x-direction. Similarly, the second and third columns are obtained from compression tests in the y- and z-directions. To determine the fourth column, a pure shear test can be conducted in the yz-plane by increasing only the shear component τ_{yz} of the stress tensor. Then, the coefficients are calculated from the relations between the applied shear stress increment and the measured strains. The last two columns can be obtained by performing pure shear tests in the xz- and xy-planes, respectively. Thus, the columns of the compliance matrix (Eq. (3.2)) can all be determined through compression and pure shear tests by applying the corresponding stress increments in the axial and shear directions of the coordinate system and measuring the resultant strains (Figure 3.1).

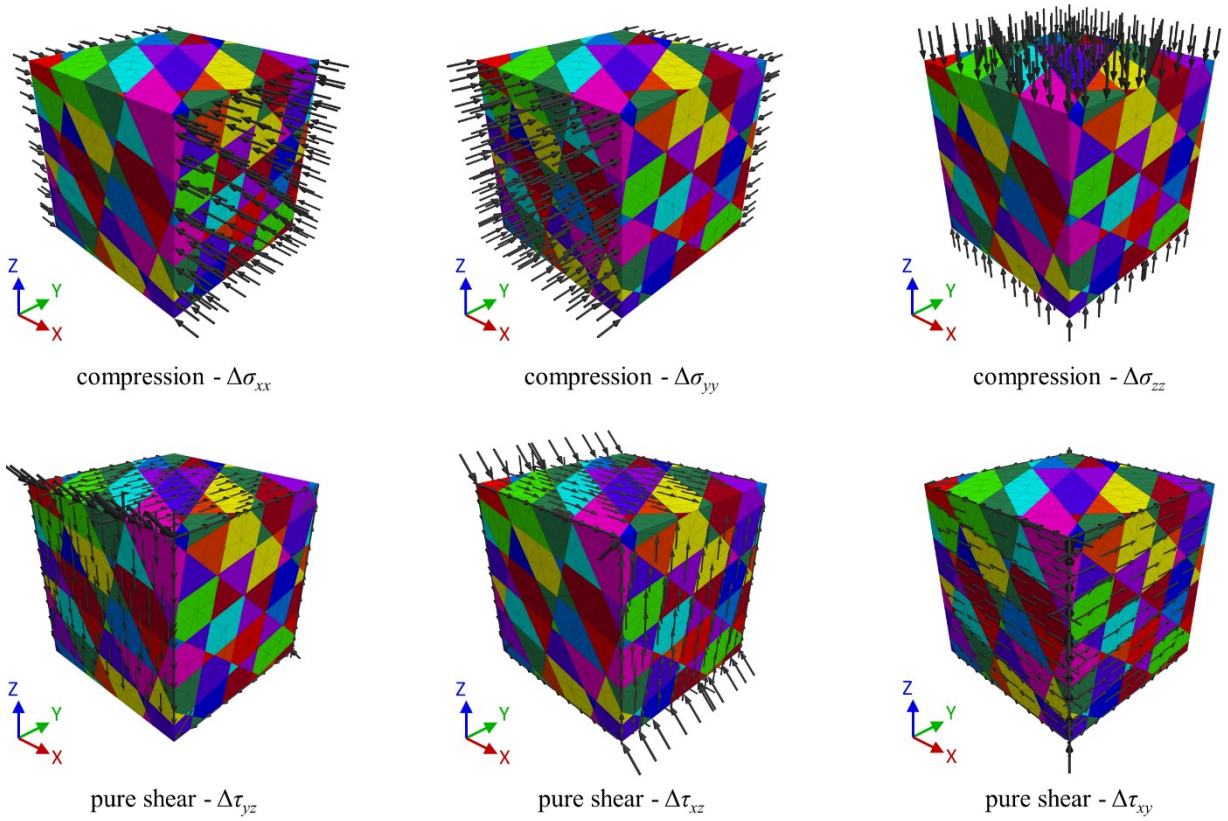

Figure 3.1—Compression and pure shear tests carried out with the VRM mechanical lab developed for 3DEC to determine the compliance matrix. The arrows show the directions of the loads corresponding to the stress increments applied as boundary conditions in each numerical test.

The VRM mechanical laboratory has been coded using the programing language FISH embedded in 3DEC, which allows for the definition of subroutines and functions for implementing new user-defined features and controlling the numerical simulation process (Itasca 2016). The main task of the VRM lab is to mount target fractured regions in 3DEC and automatically conduct the six numerical tests necessary for determining the equivalent compliance matrix. In the homogenization process, once the virtual discontinuum region is mounted, the current *in situ* stress field is installed and the simulation is brought to equilibrium. Then, the compression and pure shear tests are conducted by imposing the corresponding stress boundary conditions for each numerical test as depicted in Figure 3.1. During these numerical simulations, the stresses and strains are monitored at the boundaries of the model. After the compliance matrix is calculated,

the principal directions of material symmetry and the corresponding equivalent elastic parameters are also determined, assuming that the fractured region can be represented by an orthotropic continuum material. The process is repeated over the remaining target regions representing the fractured formation and all the orthotropic elastic parameters input for the equivalent continuum model are finally stored.

3.3.3 Measurements of stress and strain tensors

The quality of the stress and strain measurements within the VRM mechanical laboratory is crucial for determining an accurate equivalent compliance matrix. Conventionally, the stresses and displacements are measured at selected monitoring points equally distributed over the whole model domain in two-dimensional analyses (Min & Jing 2003; Noorian Bidgoli et al. 2013) or, on the boundary faces of the model for three-dimensional simulations (Kulatilake 1993; Wu & Kulatilake 2012; Cui et al. 2016; Laghaei et al. 2018; Mahboubi Niazmandi & Binesh 2020). The average values of the stresses and displacements measured at the monitoring points are considered as representative mean values of the mechanical behaviour of the model. These mean values are used for calculating the average stress and strain tensors which are required to determine the elastic compliance matrix. An important feature of the UDEC and 3DEC numerical codes is that the data queried at a monitoring point correspond to the values of the nearest object to that specified location (Itasca 2016). Thus, the stresses and displacements are actually measured at the zone and the gridpoint closest to the specific coordinates of the monitoring point. However, in the VRM lab, instead of measuring at monitoring point locations, the measurements are directly conducted over the zone faces and the gridpoints located at the boundary of the model domain (Figure 3.2). In addition, in order to increase the speed and efficiency of the measuring process, the memory addresses of the gridpoints and zone faces at the model boundary are stored in several linked-lists, similarly to the internal data structure of 3DEC.

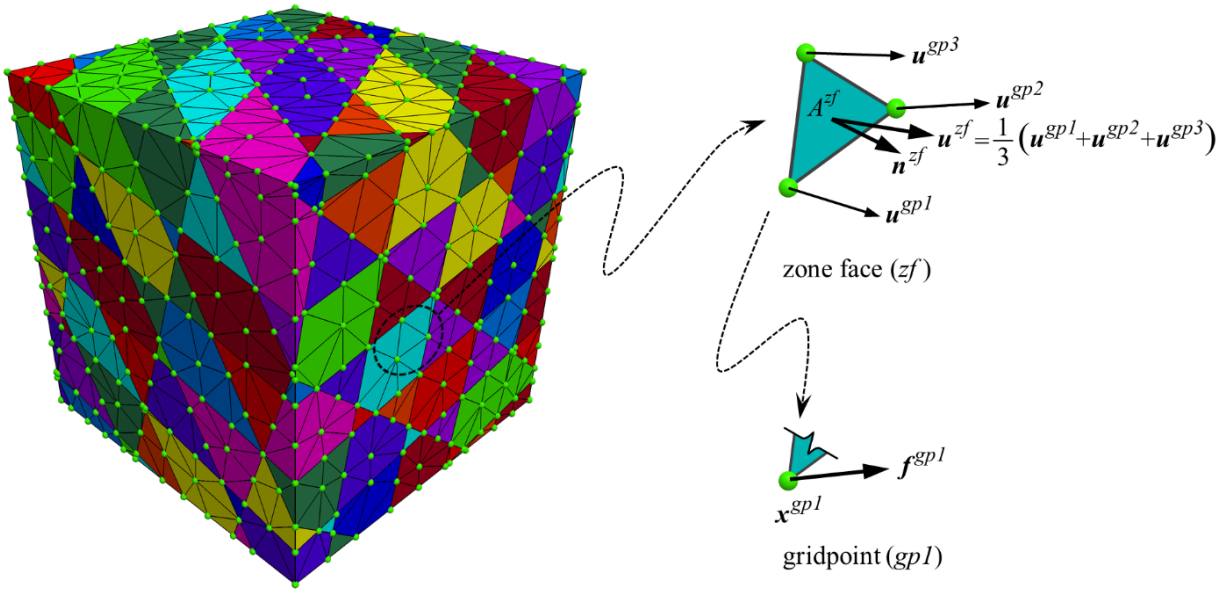

Figure 3.2—Gridpoints and zone faces at the boundary of the discontinuum model. Details of one gridpoint and a zone face showing the position, force, normal and displacement vectors used in the calculation of the stress and strain tensors.

The stress and strain tensors calculated in the VRM lab are based on the homogenization procedure proposed by Wellmann et al. (2008) for DEM models of granular materials, and the surface averaging-based approach for composites presented in Kushch (2013). The average stress tensor is then expressed in discrete form as:

$$\sigma_{ij} = \frac{1}{V}\sum_{gp=1}^{Ngp} f_i^{gp}\left(x_j^{gp} - x_j^c\right) \tag{3.3}$$

where V is the volume of the model, Ngp is the total number of gridpoints at the model boundary, f_i^{gp} is the force vector at the gridpoint gp, x_j^{gp} is the position vector of the gridpoint and, x_j^c is the position vector of the center of the model acting as a reference point. The strain tensor is calculated from measurements at the zone faces located on the model boundary by the following definition:

$$\varepsilon_{ij} = \frac{1}{2V}\sum_{zf=1}^{Nzf}\left(u_i^{zf} n_j^{zf} - n_i^{zf} u_j^{zf}\right) A^{zf} \tag{3.4}$$

where *Nzf* is the total number of zone faces at the model boundary, A^{zf} is the area of the zone face *zf*, n_j^{zf} is the outward normal vector to the zone face and, u_i^{zf} is the average of the displacement vectors of the three gridpoints at the zone face given by $u_i^{zf} = \frac{1}{3}\left(u_i^{gp1} + u_i^{gp2} + u_i^{gp3}\right)$, as shown in Figure 3.2. The subscripts *i, j* represent the vector components in the directions (*x, y, z*).

The stress and strain tensors in Eqs. (3.3) and (3.4) are derived under the assumption of small deformations, according to the infinitesimal strain theory. These surface averaging-based expressions have the main advantage of being suitable for the numerical homogenization of materials with imperfect interfaces, such as fractures and joints sets, in contrast to the conventional volume-averaging definitions based on the classic mean stress and strain theorems, which are more convenient for materials with perfectly bonded mechanical contacts (Kushch 2013).

3.3.4 Principal directions of anisotropy

The elastic compliance matrix calculated during the homogenization process usually has all of the coefficients with values different than zero. To reduce the number of anisotropic parameters input for the equivalent continuum model, the fractured region is assumed to behave as a continuum material with orthotropic symmetry. Thus, the resultant compliance matrix can be transformed to the principal axes of symmetry giving the following simplified form of the stress-strain constitutive relationship (Rand & Rovenski 2005):

$$\begin{pmatrix} \varepsilon_{11} \\ \varepsilon_{22} \\ \varepsilon_{33} \\ \gamma_{23} \\ \gamma_{13} \\ \gamma_{12} \end{pmatrix} = \begin{pmatrix} \frac{1}{E_{11}} & \frac{-\nu_{21}}{E_{22}} & \frac{-\nu_{31}}{E_{33}} & 0 & 0 & 0 \\ \frac{-\nu_{12}}{E_{11}} & \frac{1}{E_{22}} & \frac{-\nu_{32}}{E_{33}} & 0 & 0 & 0 \\ \frac{-\nu_{13}}{E_{11}} & \frac{-\nu_{23}}{E_{22}} & \frac{1}{E_{33}} & 0 & 0 & 0 \\ 0 & 0 & 0 & \frac{1}{G_{23}} & 0 & 0 \\ 0 & 0 & 0 & 0 & \frac{1}{G_{13}} & 0 \\ 0 & 0 & 0 & 0 & 0 & \frac{1}{G_{12}} \end{pmatrix} \begin{pmatrix} \sigma_{11} \\ \sigma_{22} \\ \sigma_{33} \\ \tau_{23} \\ \tau_{13} \\ \tau_{12} \end{pmatrix} \tag{3.5}$$

where E_{ii}, v_{ij} and G_{ij} are the Young's modulus, Poisson's ratio and shear modulus of the equivalent orthotropic material. The subscripts (1, 2, 3) represent the principal directions of material symmetry which correspond to the orientation of the local coordinate system $\{x', y', z'\}$. Here, the matrix coefficients with zero values are referred to the non-orthotropic components of the compliance tensor, whereas the remaining coefficients correspond to the orthotropic components.

The assumption of orthotropic symmetry allows for the characterization of the fractured rock through nine independent elastic parameters derived from the orthotropic coefficients shown in Eq. (3.5) and, three principal directions representing the orthogonal planes of symmetry. The approach used herein to identify the symmetry planes involves the solution of the eigenvalue problem for each of the two second-rank tensors, S_{ijkk} and S_{ikjk}, defined as the hydrostatic pressure modulus and the Reuss tensor, respectively (Cowin & Mehrabadi 1987; Cowin 1989; Ting 1996; Sevostianov & Kachanov 2008). These tensor contractions are defined in terms of the compliance matrix coefficients as (Cowin 1989):

$$S_{ijkk} = \frac{1}{2}\begin{pmatrix} 2\left(S_{11}+S_{12}+S_{13}\right) & S_{16}+S_{26}+S_{36} & S_{15}+S_{25}+S_{35} \\ S_{16}+S_{26}+S_{36} & 2\left(S_{12}+S_{22}+S_{23}\right) & S_{14}+S_{24}+S_{34} \\ S_{15}+S_{25}+S_{35} & S_{14}+S_{24}+S_{34} & 2\left(S_{13}+S_{23}+S_{33}\right) \end{pmatrix} \tag{3.6}$$

$$S_{ikjk} = \frac{1}{4}\begin{pmatrix} 4S_{11}+S_{55}+S_{66} & 2\left(S_{16}+S_{26}\right)+S_{45} & 2\left(S_{15}+S_{35}\right)+S_{46} \\ 2\left(S_{16}+S_{26}\right)+S_{45} & 4S_{22}+S_{44}+S_{66} & 2\left(S_{24}+S_{34}\right)+S_{56} \\ 2\left(S_{15}+S_{35}\right)+S_{46} & 2\left(S_{24}+S_{34}\right)+S_{56} & 4S_{33}+S_{44}+S_{55} \end{pmatrix} \tag{3.7}$$

Provided that the orthotropic symmetry holds, the eigenvectors calculated for both compliance contractions coincide and represent the normal vectors to the symmetry planes. Also, they define the rows of the transformation matrix whereby the compliance tensor can be rotated from the coordinate axes of the model to the local coordinate system that represents the principal directions of anisotropy. Adopting the convention used in 3DEC, the orientation of the orthogonal planes of symmetry can be defined with a dip-direction, dip and rotation angles which are estimated from the coordinate transformation matrix (see Appendix B). Once the symmetry planes

are identified, the compliance matrix can be rotated to the principal directions in the form of Eq. (3.5), following the matrix transformation operations shown in the Appendix C (Ting 1987; Tinder 2008). Thus, the nine orthotropic elastic parameters are finally determined from the compliance matrix coefficients corresponding to the principal directions.

Although the orthotropic behaviour is a reasonable assumption for fractured rocks, the compliance matrices obtained with the VRM lab may slightly differ from the exact orthotropic form. Therefore, the equivalent elastic parameters and principal directions determined during the homogenization process are considered here as the closest approximation to the perfect orthotropic symmetry. According to Sevostianov and Kachanov (2008), the approximation error can be estimated using the Euclidean norm through the following expression:

$$\delta = \sqrt{\frac{\left(S'_{ijkl} - \overline{S}'_{ijkl}\right)\left(S'_{ijkl} - \overline{S}'_{ijkl}\right)}{S'_{pqrs}S'_{pqrs}}} \tag{3.8}$$

where S'_{ijkl} is the compliance tensor rotated to the principal directions of symmetry and, $\overline{S}'_{ijkl}$ is the previous rotated tensor in which the non-orthotropic components are set to zero while the orthotropic components are kept the same. Hence, the error δ essentially depends on the non-orthotropic terms that remain different than zero after the rotational transformation of the compliance to the principal axes. In the case that the error of the orthotropic approximation is considerably large, the equivalent material should be characterized by a triclinic constitutive model with the 21 independent coefficients of the general anisotropic compliance matrix.

3.4 Numerical results

3.4.1 Verification of the methodology

To verify the proposed methodology, the elastic compliance matrix of a simple case has been determined through the numerical homogenization procedure of the VRM laboratory, and also analytically using the Oda's crack tensor approach (Oda 1986). In addition, the displacement

fields of the equivalent orthotropic continuum have been compared with the deformational behaviour of the underlying full discontinuum model.

3.4.1.1 Oda's crack tensor approach

In the Oda's theory, the compliance tensor of a fractured rock mass with circular joints is defined as the summation of the compliances of the fractures and the intact rock. For an isotropic material, the elastic compliance tensor can be expressed as:

$$S^{r}_{ijkl} = \frac{(1+\nu)\delta_{ik}\delta_{jl} - \nu\delta_{ij}\delta_{kl}}{E} \tag{3.9}$$

where E and ν are the Young's modulus and Poisson's ratio of the intact rock and, δ_{ij} is the Kronecker delta. Assuming the mechanical behaviour of every fracture is fully characterized with a normal stiffness k_n and a shear stiffness k_s (Goodman et al. 1968), the elastic compliance tensor corresponding to the fractures can be formulated as (Oda 1993; Rutqvist et al. 2013):

$$S^{f}_{ijkl} = \sum^{Nf}\left[\left(\frac{1}{k_n D} - \frac{1}{k_s D}\right)F_{ijkl} + \frac{1}{4k_s D}\left(\delta_{ik}F_{jl} + \delta_{jk}F_{il} + \delta_{il}F_{jk} + \delta_{jl}F_{ik}\right)\right] \tag{3.10}$$

where Nf is the total number of circular fractures, D is the fracture diameter. F_{ij} and F_{ijkl} are the second- and fourth-rank crack tensors which are defined for a single fracture as (Oda 1993):

$$F_{ij} = \frac{A}{V} D n_i n_j \tag{3.11}$$

$$F_{ijkl} = \frac{A}{V} D n_i n_j n_k n_l \tag{3.12}$$

where A is the fracture area, V is the total volume of the fractured region and, n_i is the i-component of the normal vector to the fracture plane, with indices (i, j, k, l) ranging over the coordinate axes $\{x, y, z\}$. Substituting the expressions of the crack tensors in the Eq. (3.10), the fracture diameters vanish and the fracture compliance tensor results in:

$$S_{ijkl}^{f} = \frac{1}{V}\sum^{Nf}\left[\left(\frac{1}{k_n}-\frac{1}{k_s}\right)A n_i n_j n_k n_l + \frac{1}{4k_s}A\left(\delta_{ik}n_j n_l + \delta_{jk}n_i n_l + \delta_{il}n_j n_k + \delta_{jl}n_i n_k\right)\right] \quad (3.13)$$

where the term between brackets is evaluated for every fracture of the discontinuum model during the summation. For a particular rock mass containing a single joint set having the fractures defined with the same orientation and mechanical properties, the fracture compliance tensor in Eq. (3.13) directly depends on the relation between the total sum of joint areas and the total volume of the fractured region. This relationship coincides with the fracture intensity measure P_{32} defined in Dershowitz and Herda (1992) and it is traditionally replaced by the joint spacing in the classic closed-from solutions (e.g. Amadei & Goodman 1983). The total elastic compliance tensor of the equivalent continuum representing the fractured rock mass is finally given by:

$$S_{ijkl} = S_{ijkl}^{r} + S_{ijkl}^{f} \quad (3.14)$$

where the total compliance tensor S_{ijkl} can also be expressed in matrix form as the sum of the compliance matrices corresponding to the fractures and the intact rock as shown in Appendix D.

3.4.1.2 Comparison of analytical and numerical compliance matrices

The verification case analyzed here consists of a cubic block model, with an edge length L of one meter, of an isotropic material with three non-orthogonal joint sets cutting through the entire model domain (Figure 3.3). The mechanical properties of the intact rock and fractures used in this case correspond to the shale formation reported in Rangriz Shokri et al. (2019). The input parameters for the intact material and joint sets of the model are summarized in Table 3.1. The principal stresses of the *in situ* stress field have been installed in the model with the values of $\sigma_1 = 66.32$ MPa, $\sigma_2 = 47.75$ MPa, $\sigma_3 = 34.48$ MPa and with the principal directions aligned with the coordinate axes. The stress increment used in each of the six tests conducted with the VRM lab is set to 6.63 MPa, which corresponds to the 10% of the maximum principal stress. As shown in Figure 3.3, the compliance matrix determined analytically using the Oda's approach is essentially equal to the matrix resultant from the numerical tests conducted with the VRM lab.

These results verify the capability of the VRM laboratory to accurately determine the elastic compliance coefficients for the equivalent continuum representative of the jointed rock model.

Table 3.1—Input parameters of the intact rock and joint sets for the verification case.

Parameter	**Value**
Young's modulus E , (GPa)	26
Poisson's ratio v , (-)	0.2
Normal stiffness (for all joint sets) k_n , (GPa/m)	18
Shear stiffness (for all joint sets) $k_s = 0.42k_n$, (GPa/m)	7.56
Fracture spacing (for all joint sets) , (m)	0.2
Dip/Dip-direction for joint set 1 , (°)	60/60
Dip/Dip-direction for joint set 2 , (°)	80/210
Dip/Dip-direction for joint set 3 , (°)	15/130

The additional compliance matrix in the Figure 3.3 has been calculated following the conventional method used in previous studies, in which the equivalent stress and strain tensors are computed from the averaged stresses and displacements on the boundary faces of the model. This matrix is included here to compare the conventional measurement strategy for estimating the elastic properties of the discontinuum model with the method implemented in the VRM lab. It is observed that the compliance matrix determined with the conventional method is similar to the analytical solution; however, even though the differences between both matrices can be neglected in this particular case, they are significantly larger than the discrepancies between the analytical and VRM lab results. Furthermore, the 36 compliance coefficients calculated with the VRM lab result in a symmetric matrix, whereas the compliance matrix calculated with the conventional method deviates from the perfect symmetric form. Therefore, the measuring process implemented in the VRM lab is expected to provide reliable estimations of the compliance matrix and, hence, the equivalent orthotropic parameters, for complex models of fractured rock formations.

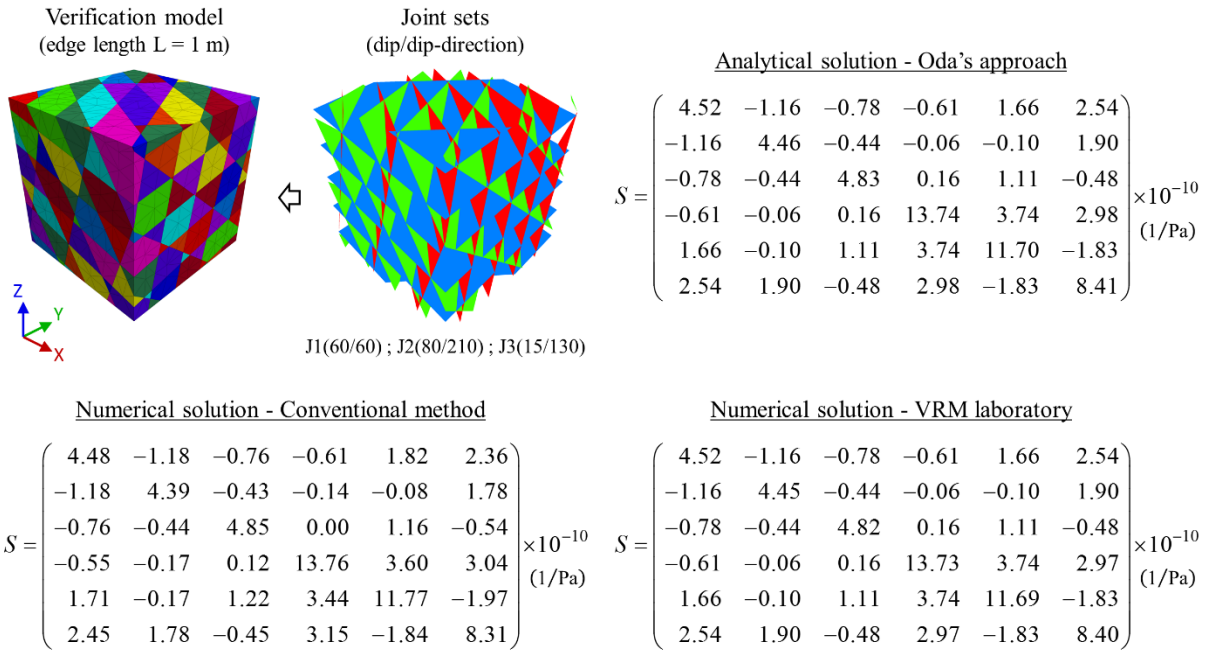

Figure 3.3—Geometry of the verification model with the three non-orthogonal joint sets (top-left figure) and the compliance matrices *S* calculated in the verification case by means of: the Oda's approach (top-right figure), the VRM laboratory (bottom-right figure) and, the conventional measurement method used in previous studies (bottom-left figure).

3.4.1.3 Equivalent continuum parameters

Typically, the anisotropic elastic properties for the equivalent continuum are determined through the compliance matrix coefficients measured in the coordinate system of the discontinuum model $\{x, y, z\}$, as shown in the following expressions:

$$E_{xx} = \frac{1}{S_{11}} \quad ; \quad E_{yy} = \frac{1}{S_{22}} \quad ; \quad E_{zz} = \frac{1}{S_{33}} \tag{3.15}$$

$$G_{yz} = \frac{1}{S_{44}} \quad ; \quad G_{xz} = \frac{1}{S_{55}} \quad ; \quad G_{xy} = \frac{1}{S_{66}} \tag{3.16}$$

$$v_{xy} = \frac{-S_{21}}{S_{11}} \quad ; \quad v_{zx} = \frac{-S_{13}}{S_{33}} \quad ; \quad v_{zy} = \frac{-S_{23}}{S_{33}} \tag{3.17}$$

$$v_{yx} = \frac{-S_{12}}{S_{22}} \quad ; \quad v_{xz} = \frac{-S_{31}}{S_{11}} \quad ; \quad v_{yz} = \frac{-S_{32}}{S_{22}} \tag{3.18}$$

where only three Poisson's ratios defined in Eq. (3.17) or Eq. (3.18) are necessary to complete the nine elastic parameters required for the mechanical characterization of the equivalent orthotropic material. That way, the coordinate axes of the model are assumed as the principal directions of material symmetry and, therefore, the non-orthotropic coefficients of the compliance matrix are neglected in the calculation of the anisotropic parameters. On the other hand, in the VRM lab, the compliance matrix is rotated to the principal directions of orthotropic symmetry to minimize the non-orthotropic coefficients before determining the equivalent continuum parameters. Thus, the equivalent properties can be calculated by substituting the rotated compliance matrix S' in Eqs. (3.15), (3.16), (3.17) and (3.18), e.g. $E_{x'x'} = 1/S'_{11}$, $v_{x'y'} = -S'_{21}/S'_{11}$, $G_{y'z'} = 1/S'_{44}$, where the orientation of the local coordinate system $\{x', y', z'\}$ represents the principal directions of material symmetry.

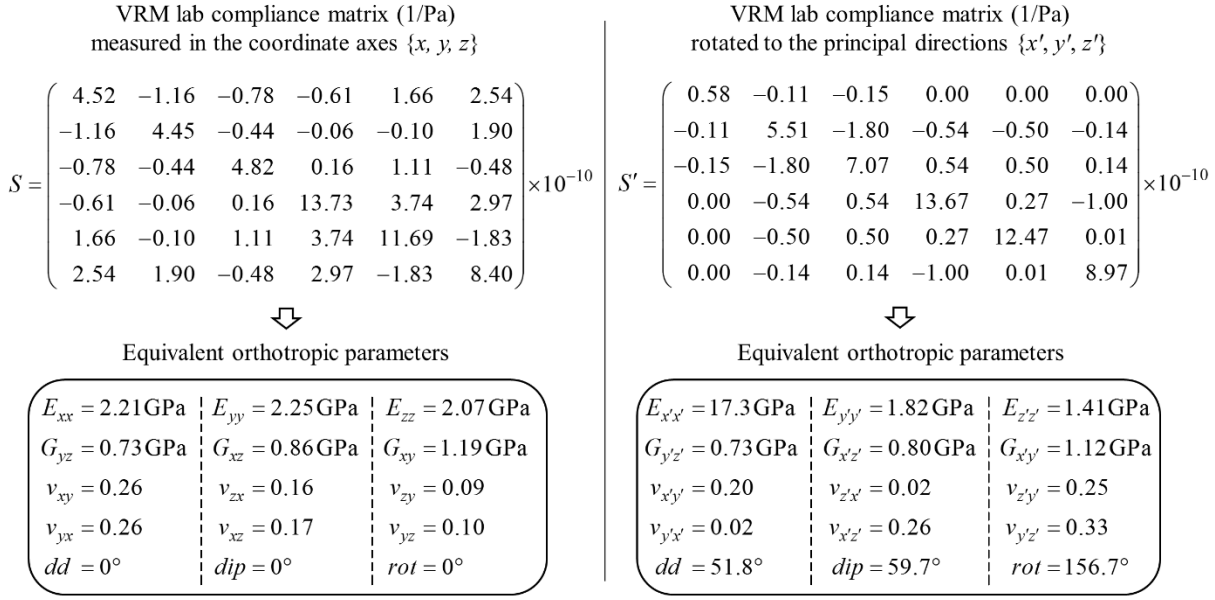

Figure 3.4—Compliance matrix and equivalent orthotropic parameters measured in the coordinate axes of the model {*x, y, z*} (left figure) and; rotated to the principal directions of orthotropic symmetry {*x′, y′, z′*} (right figure). These results have been obtained in the verification case by the VRM lab. Note that three Poisson's ratios are enough for the characterization of the orthotropic continuum material.

Figure 3.4 shows the compliance matrices and the equivalent orthotropic parameters determined with the VRM lab in the verification case. These results have been obtained in the orientation of the coordinate axes and, also, in the principal directions of material symmetry. It can be seen that the non-orthotropic coefficients have been considerably reduced in the rotated compliance matrix; however, some values are still different than zero implying a slight deviation from the perfect orthotropic form. This discrepancy is expected since the systematic joint sets in the verification case are fully persistent and non-orthogonal. The orthotropic approximation error defined in Eq. (3.8) has been calculated for the matrix oriented in the principal directions, resulting in $\delta = 0.092$; whereas, for the compliance matrix measured in the coordinate axes of the model, the calculated error is equal to $\delta = 0.378$, which is a substantially larger value. Consequently, the equivalent elastic parameters determined from the rotated compliance matrix are closer to the exact orthotropic form.

To illustrate the influence of the non-orthogonal components of the compliance matrix in the behaviour of the equivalent orthotropic material, two continuum models have been tested in the VRM lab (Figure 3.5). The two sets of equivalent orthotropic parameters input for each continuum model can be found in Figure 3.4. As shown in Figure 3.5, the displacement field of the continuum model with the input parameters determined in the principal directions of symmetry corresponds very well with the deformational behaviour of the discontinuum model in the six numerical tests conducted with the VRM lab. In contrast, the continuum case modelled with the equivalent elastic parameters measured in the coordinate axes shows displacement fields considerably different in comparison with the discontinuum simulation. These differences are found more evident in the pure shear tests. Thus, assuming the principal directions of material symmetry coincide with the coordinate axes of the model may yield in misleading elastic orthotropic parameters input for the equivalent continuum model.

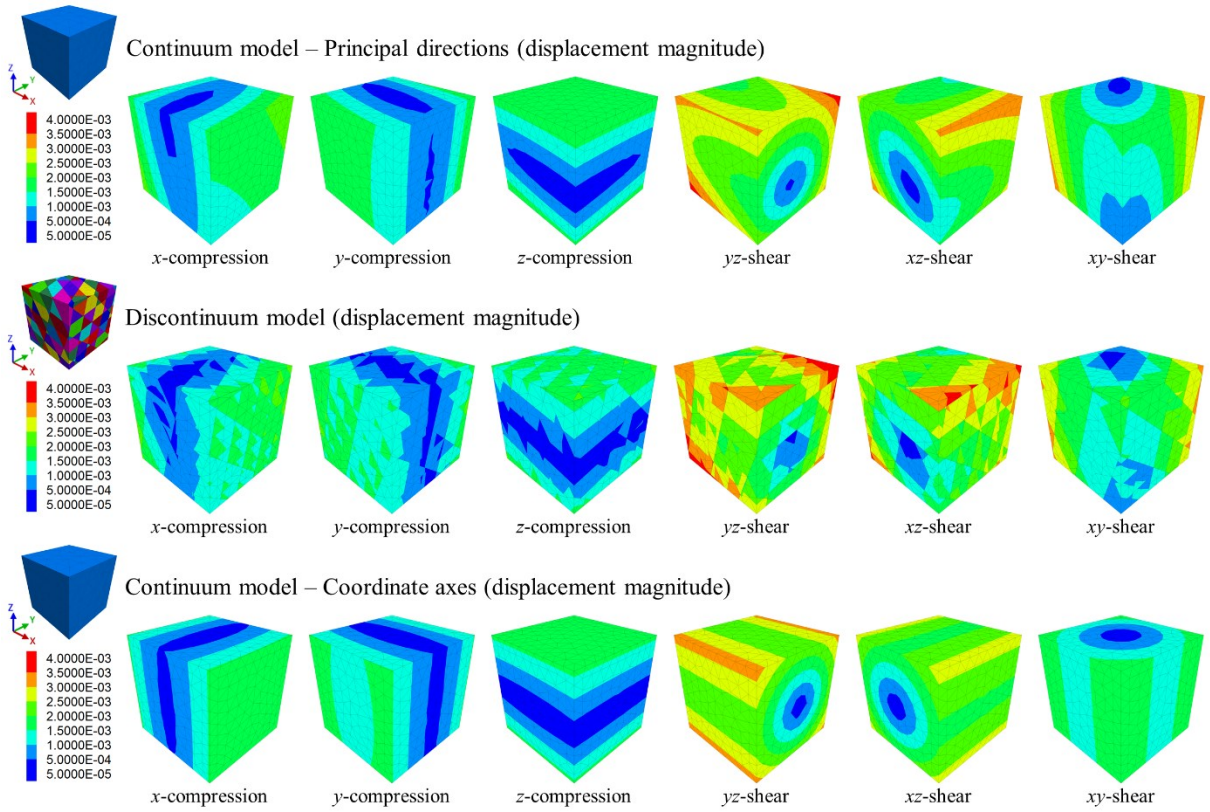

Figure 3.5—Displacement magnitudes for each of the six numerical tests conducted with the VRM laboratory in the verification case for: the discontinuum model (middle figure) and, the continuum models with the equivalent orthotropic parameters corresponding to the principal directions of symmetry (top figure) and the coordinate axes orientation (bottom figure).

3.4.2 Fracture rock formation with an embedded DFN.

The mechanical characterization of a fractured rock mass is frequently conducted through homogenization or upscaling procedures. In general, these homogenization techniques are often based on analytical methods to calculate the equivalent continuum properties; however, the close-form solutions usually disregard the fracture interaction effect in the overall behaviour of the fractured rock. In the upscaling schemes, the equivalent elastic parameters are averaged at the REV size; although, the variability of the fractured rock model may not be properly captured at smaller scales. To study the effect of fracture interactions and the REV scale, a fractured rock formation with an embedded DFN is analyzed here using the Oda's crack tensor approach and compared with the VRM laboratory results.

3.4.2.1 Discontinuum model generation.

The fractured rock is modelled by a cubic block of 20×20×20 m^3 of the same formation used in the verification case (Figure 3.6). In this model, the fractures embedded into the rock mass have been generated using the DFN module included in the 3DEC code (Itasca 2016). The DFN model contains three joint sets of circular fractures oriented with the dip and dip-direction angles following a Gaussian distribution and, with their locations uniformly distributed over the model domain. The fracture size is assumed to follow a power law distribution with a scaling exponent of 4 and the minimum and maximum diameters of 2 m and 40 m, respectively. Table 3.2 summarizes the parameters used for the DFN generation in 3DEC.

Table 3.2—Input parameters for the DFN generation.

DFN	**Orientation (Gaussian distribution)**		**Fracture size (power law distribution)**	
Joint set	**Dip angle (°) (Mean, SD)**	**Dip-direction (°) (Mean, SD)**	**Scaling exponent α**	**Fracture diameter (m) (Minimum - Maximum)**
J1	(60, 5)	(60, 10)	4	(2 - 20)
J2	(80, 5)	(210, 10)	4	(2 - 20)
J3	(15, 5)	(130, 10)	4	(2 - 40)

For the DFN realization, the joint sets are generated in a box of 40×40×40 m^3 encasing the whole model domain to ensure that the larger fractures are still created even if their centers fall outside the model extent (Min & Jing 2003, Itasca 2016). The discontinuum model has been populated with a total number of 1500 circular fractures from which 600 belong to the joint set J1, other 600 to the joint set J2 and the remaining 300 to the joint set J3 (Figure 3.6). The mechanical properties of the fractures (k_n and k_s) and the intact rock (E and ν) as well as the *in situ* stress field are assigned the same values of the verification case (Table 3.1).

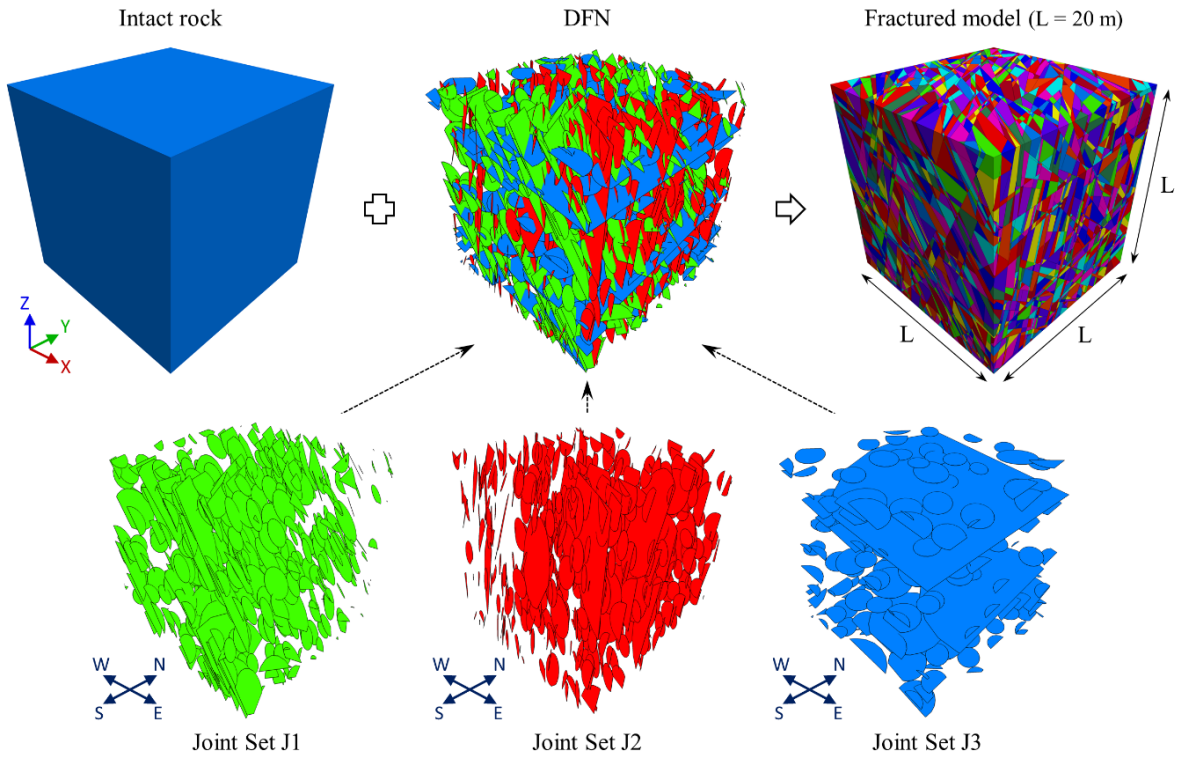

Figure 3.6—Geometry of the fractured rock model (edge length L = 20 m) and DFN joint sets used for the study of the REV scale and fracture interaction effects.

To create a fracture of finite size in 3DEC, the joint plane must cut through all the blocks containing the fracture. This condition is required to prevent the generation of block geometries with partial cuts, ensuring that the model is only formed by convex polyhedral blocks (Itasca 2016). The contact surfaces between adjacent blocks represent the discontinuities of the model. During the mesh generation process, each contact is automatically discretized into sub-contacts which can be assigned different constitutive models and mechanical properties. Thus, the circular fractures of the DFN can be represented in the model by the sub-contacts lying inside of the fracture area, whereas the sub-contacts lying outside of the circular fracture define the area of a fictitious joint (Figure 3.7). The fracture stiffnesses (Table 3.1) can be directly assigned to the sub-contacts representing the actual fractures. On the other hand, the input parameters of the fictitious joints should be such that their contribution to the overall deformability of the fractured rock model is negligible.

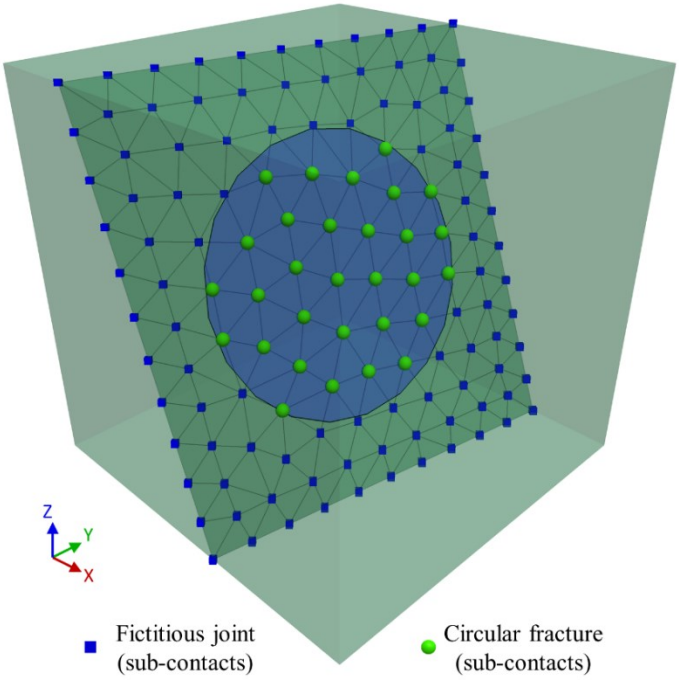

Figure 3.7—Contact surface discretization into sub-contacts representing a DFN circular fracture (spherical nodes) and the fictitious joint area (cubical nodes outside the circle). Different constitutive models and mechanical properties can be assigned at any sub-contact (after Itasca (2016)).

3.4.2.2 Elastic parameters for the fictitious joints.

According to Kulatilake et al. (1992), the elastic parameters for the fictitious joints can be chosen by satisfying the following conditions. First, the ratio between the shear modulus of the intact material and the shear stiffness of the fictitious joint G/k_s must be between 0.008 and 0.012 m. Second, the ratio between the normal and shear stiffnesses of the fictitious joint k_n/k_s must be between 2 and 3; where the most appropriate value in this range may correspond to the ratio between the Young's modulus and the shear modulus E/G of the intact material. These conditions are suggested for fictitious joints simulated with a plastic constitutive model with the same strength parameters as the intact rock. Furthermore, the fictitious joint stiffnesses are chosen independently of the total number of fractures which may have a significant impact in the deformability of the discontinuum model.

An alternative method based on the Oda's crack tensor theory is introduced here to determine the normal and shear stiffnesses for fictitious joints defined with an elastic constitutive model. Assuming that both stiffnesses are equal (i.e., $k_n^{Fict} = k_s^{Fict} = k^{Fict}$) and all the fictitious joints share the same values, the compliance tensor as defined in Eq. (3.13) can be simplified to:

$$S_{ijkl}^{Fict} = \frac{1}{4Vk^{Fict}} \sum^{Nf} \left[A^{Fict} \left(\delta_{ik} n_j n_l + \delta_{jk} n_i n_l + \delta_{il} n_j n_k + \delta_{jl} n_i n_k \right) \right] \tag{3.19}$$

where S_{ijkl}^{Fict}, A^{Fict} and k^{Fict} are the compliance tensor, the area and, the stiffness of the fictitious joints. Ideally, the fictitious joint stiffness should tend to infinity, so the total deformability of the numerical model is only due to the behaviour of the intact material. On the other hand, the timestep of the numerical cycles in 3DEC decreases with increasing the stiffness of the system. Thus, the stiffness k^{Fict} must be small enough to have reasonable computational times and, large enough such that the fictitious joints contribution to the overall deformability of the model becomes insignificant. Here, the stiffness of the fictitious joints is calculated by setting the largest values of the compliance matrix coefficients in Eq. (3.19) equal to a proportional value of their counterpart compliances corresponding to the intact rock. In general, the largest values in a compliance matrix coincide with the diagonal coefficients. Then, assuming the intact rock is isotropic, the diagonal coefficients of the compliance matrix of the fictitious joints are given by:

$$S_{II}^{Fict} = \lambda^{Fict} S_{II}^{r} = \lambda^{Fict} \frac{1}{E} \quad ; \quad S_{JJ}^{Fict} = \lambda^{Fict} S_{JJ}^{r} = \lambda^{Fict} \frac{2(1+v)}{E} = \lambda^{Fict} \frac{1}{G} \tag{3.20}$$

where λ^{Fict} is the proportionality factor of the compliances of the intact material and, the subscripts correspond to *II* = (11, 22, 33) and *JJ* = (44, 55, 66). Substituting the compliance matrix coefficients of the fictitious joints in Eq. (3.20) with those determined from Eq. (3.19) and rearranging, gives six alternative stiffnesses from which the maximum value is chosen as the fictitious joint stiffness; that is:

$$k^{Fict} = \max \left\{ \frac{E}{\lambda^{Fict} V} \sum^{Nf} \left[A^{Fict} n_i^2 \right] \quad ; \quad \frac{G}{\lambda^{Fict} V} \sum^{Nf} \left[A^{Fict} \left(1 - n_i^2 \right) \right] \right\} \tag{3.21}$$

where the index *i* ranges over the coordinate axes {*x, y, z*}. This method allows for limiting the deformation measurement error to a specific value proportional to the intact rock. For each discontinuum model analyzed here, the fictitious joint stiffness k^{Fict} is calculated by setting a proportionality factor of $\lambda^{Fict} = 0.001$, whereby the compliance measurement error is expected to be reduced to approximately 0.1% of the intact rock deformation.

3.4.2.3 Fracture interaction effect and REV scale.

The REV scale is studied through the homogenization of a series of cubic blocks carved from the center of the large fractured rock model of 20×20×20 m^3 volume (L20). The sequence of cubic models under study begins with a unit block, i.e. L = 1 m (L1), followed by nine cubic blocks with edge lengths increasing at intervals of 2 meters, from L=2 m (L2) to L=18 m (L18). The large block model L20 is also included in the analysis (Figure 3.8). Analogous to the verification case, the compliance matrices are determined with the VRM lab and calculated analytically using the Oda's crack tensor approach for each cubic model. Additionally, the compliance matrices rotated to the principal directions of orthotropic symmetry are also included.

For simplicity, Figure 3.9 and Figure 3.10 only show the compliance matrices of the cubic blocks L2, L12 and L20 measured in the coordinate axes of the model and rotated to the principal directions. It can be seen that all of the compliance matrices resultant from the VRM lab are virtually symmetric, even in the particular case of the small cubic model L2, which is partially cut by a few circular fractures (Figure 3.8). Moreover, in contrast with the verification case, the analytical results are different from the numerical solutions, since the joint sets of the DFN consist of non-persistent fractures and the analytical solution neglects the fracture interaction effects.

To determine the REV size, the equivalent orthotropic parameters are calculated numerically with the VRM lab and analytically by means of the Oda's crack tensor approach for each cubic model. These parameters are determined from the compliance matrices measured in the coordinate axes of the model {x, y, z} (Figure 3.11), and also in the principal directions of orthotropic symmetry {x', y', z'} (Figure 3.12). The equivalent Young's moduli and shear moduli

are normalized with the elastic parameters, E and G, of the intact material. As shown in Figure 3.11 and Figure 3.12, the variation of the equivalent elastic parameters is reduced with increasing the edge length of the cubic model. Furthermore, the orthotropic parameters are almost constant for the cubic models from L12 to L20. Thus, based on these results, the cubic model with the edge length of L = 12 m can be chosen as the REV for this analysis.

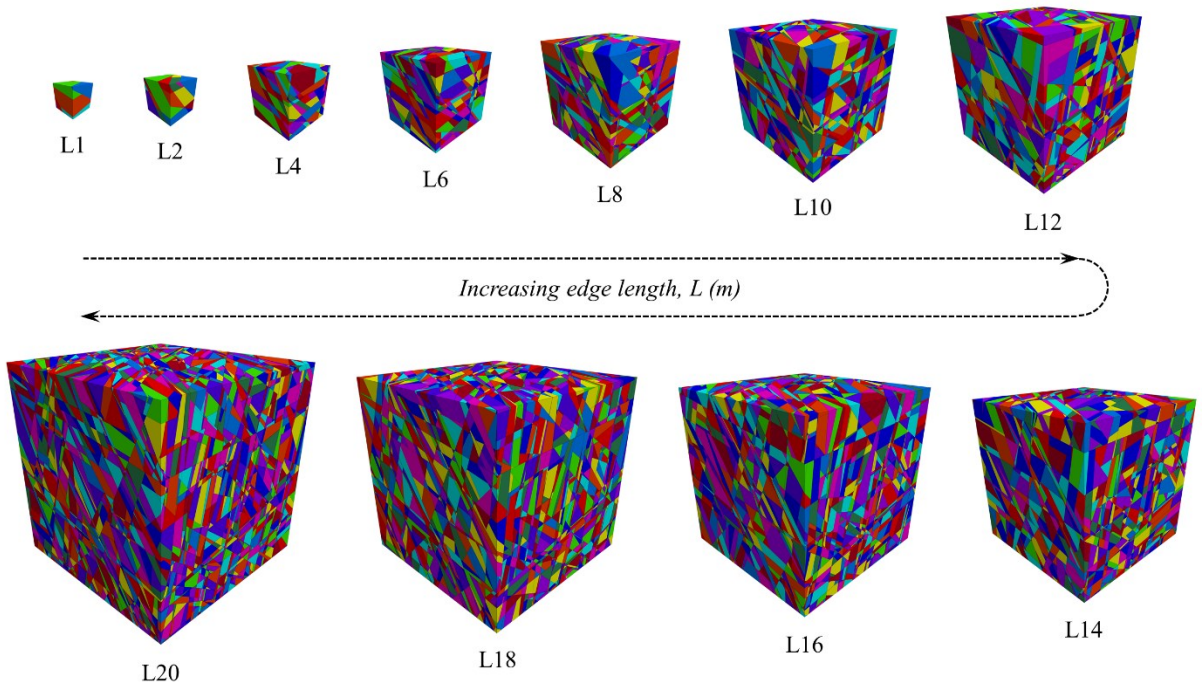

Figure 3.8—Sequence of cubic blocks with different edge lengths L tested to study the effect of fracture interactions and the REV scale. These cubes are carved from the center of the large block L=20 m (L20) by setting the edge length at intervals of 2 meters starting from L=2 m (L2) to L=18 m (L18). An extra block with L=1 m (L1) and the large block L20 have also been included in the analysis.

The comparison of the numerical and analytical results of the elastic parameters depicted in Figure 3.11 clearly shows the effect of fracture interactions. It is observed that the Young's moduli and shear moduli determined at the REV scale with the VRM lab for this particular case are around 17% stiffer than the analytical values calculated using the Oda's theory. Additionally, the six different Poisson's ratios measured with the VRM lab are less scattered compared to the analytical results. The stiffer mechanical response of the numerical solution can be attributed to

the different stress distribution over the circular fractures, where the stresses are generally low at the central areas while they are highly concentrated at the fracture tips. Hence, the fracture deformation is usually smaller at the center compared to the analytical solution, which assumes a uniform stress distribution on the fracture surfaces. Thus, the numerical response can be expected to be stiffer for the same far-field stress increment applied to the fractured model. This behaviour of stress shielding and amplification has also been observed by Grechka and Kachanov (2006) in the numerical homogenization of a fractured material with penny-shaped cracks.

In general, the degree of anisotropy of the fractured rock is commonly assessed through relationships between the equivalent elastic stiffnesses determined in the directions of the coordinate axes of the model (e.g. the ratio E_{yy}/E_{xx}). As shown in Figure 3.11a, the normalized Young's moduli obtained with the VRM lab at the REV scale are virtually the same in the three coordinate axes. On the other hand, the normalized shear moduli and Poisson's ratios, in Figure 3.11b and Figure 3.11c, show slightly different results in several directions; nevertheless, the scatter at the REV scale is small enough, so it may be considered negligible. The analytical solutions in Figure 3.11 show analogous results. These observations suggest that the REV of the fractured rock essentially behaves as an isotropic material. However, the three joint sets generated with the DFN model have well-defined orientations, suggesting an anisotropic material response instead of the observed isotropic behaviour. In fact, taking a close look at Figure 3.12, the equivalent elastic parameters determined in the principal directions reveal the actual anisotropic nature of the fractured rock, where the ratio of $E_{x'x'}$ to $E_{z'z'}$ at the REV size is about 1.73 and 2.06 for the numerical (Figure 3.12a) and analytical results (Figure 3.12d), respectively. The misleading isotropic mechanical response observed in Figure 3.11 comes from neglecting the non-orthotropic coefficients of the compliance matrix in the calculation of the elastic properties. However, this is not the case for the homogenization procedure conducted with the VRM lab, where the equivalent orthotropic parameters are determined from the compliance matrix rotated to the principal directions in which the non-orthotropic coefficients are minimized. Therefore, it is clear that the principal directions of symmetry and the non-orthotropic compliance coefficients play an

important role in estimating reliable equivalent continuum parameters to capture the actual anisotropic behaviour of the fractured rock.

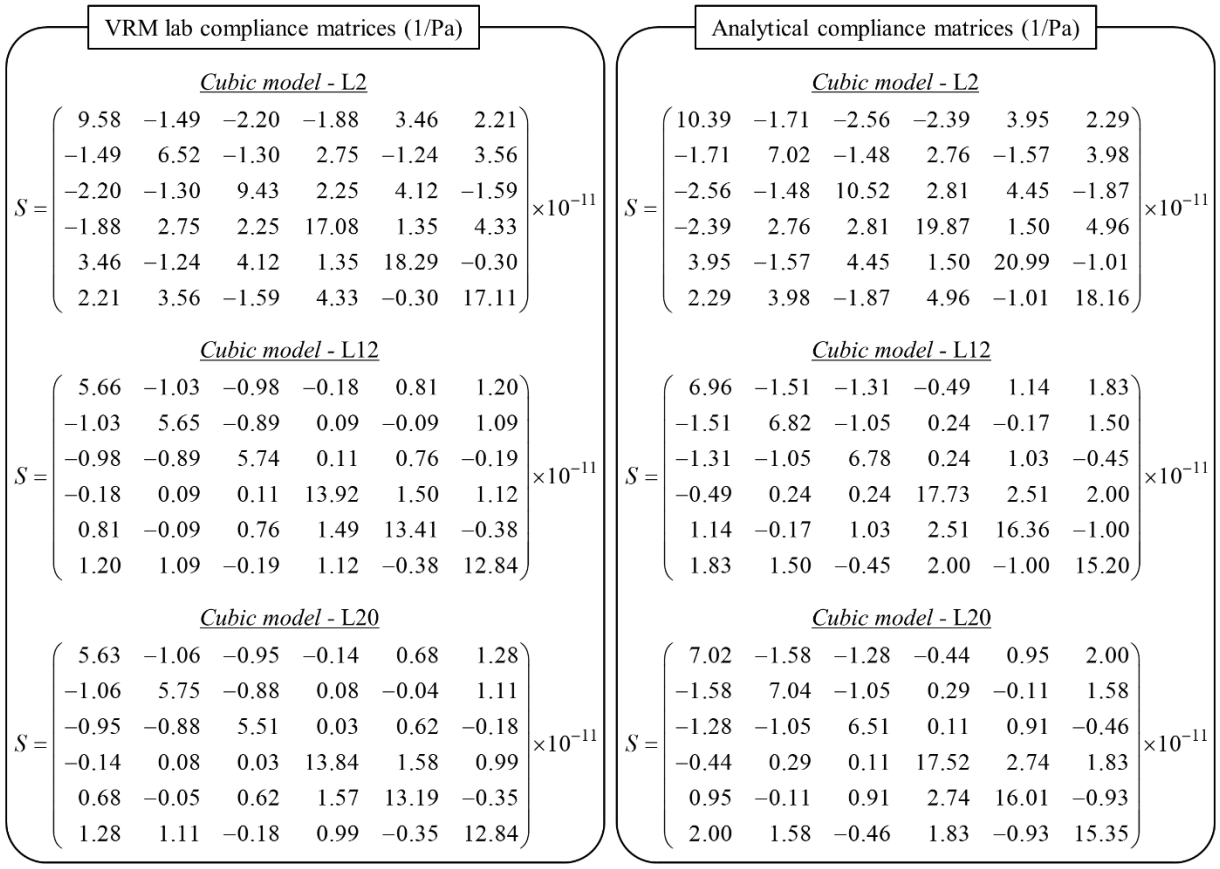

Figure 3.9—Compliance matrices corresponding to the cubic blocks L2, L12 and L20 obtained with the VRM lab (left figure) and calculated analytically by means of the Oda's crack tensor approach (right figure).

The principal directions of orthotropic symmetry obtained for the cubic models in the REV study have been projected and represented on the Schmidt net (Figure 3.13). The numerical and analytical results are depicted in Figure 3.13a and Figure 3.13b, respectively. Both solutions show similar evolutions of the principal directions. As expected, the change in orientation of the principal axes decreases with increasing the cubic model size. In addition, the small values of the approximation error δ for the VRM lab results show a very good correspondence with the orthotropic symmetry (Figure 3.10). These errors are slightly larger for the analytical solution.

Figure 3.13 shows that the principal directions remain constant with the same orientation at the L18 and L20 models, where the poles representing the symmetry planes overlap each other. Therefore, to account for the change in orientation of the principal axes of orthotropic symmetry, the previous REV scale should be revisited and finally stablished at the cubic model with L = 18 m edge length.

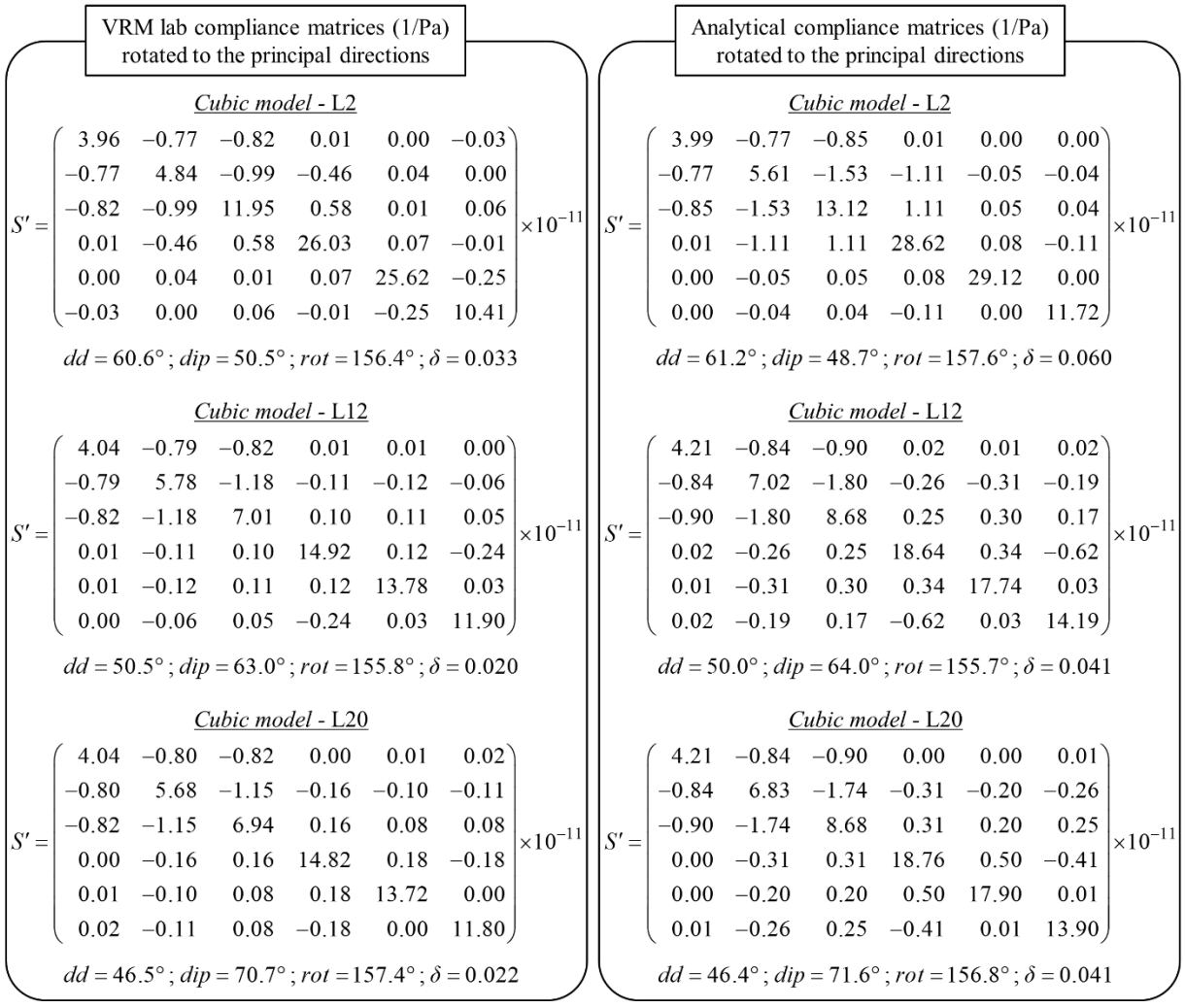

Figure 3.10—Compliance matrices rotated to the principal directions of orthotropic symmetry corresponding to the cubic blocks L2, L12 and L20. These matrices have been determined numerically with the VRM lab (left figure) and calculated analytically by means of the Oda's crack tensor approach (right figure). The rotational transformation angles (*dd, dip, rot*) have been included, as well as the orthotropic approximation errors (δ).

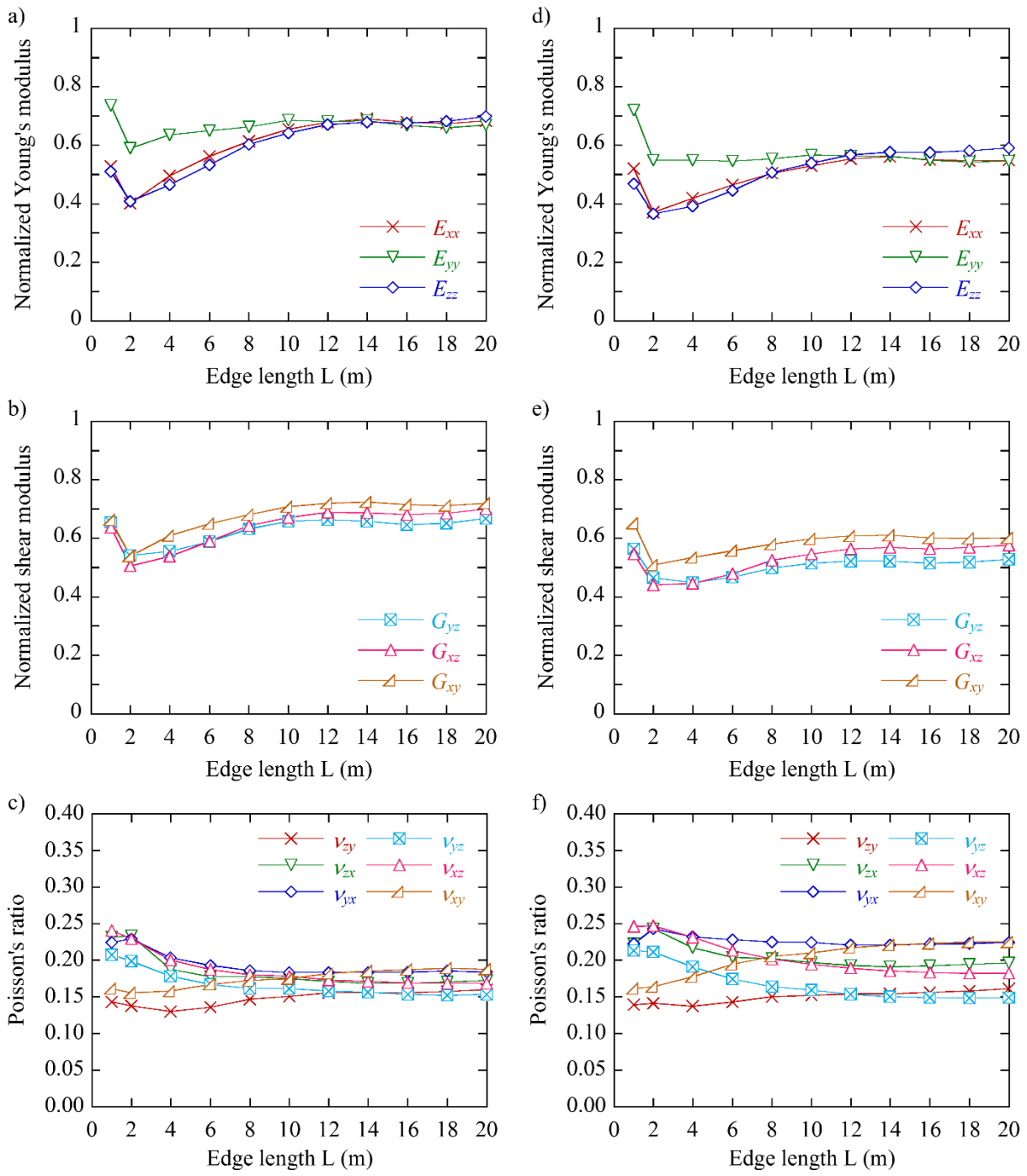

Figure 3.11—Equivalent orthotropic parameters measured in the coordinate axes of the model {x, y, z} with the VRM lab (left figures a), b) and c)) and calculated analytically by the Oda's crack tensor approach (right figures d), e) and f)), corresponding to the cubic models of the REV study. The Young's moduli (in a) and d)) and the shear moduli (in b) and e)) are normalized with the elastic parameters, *E* and *G*, of the intact material.

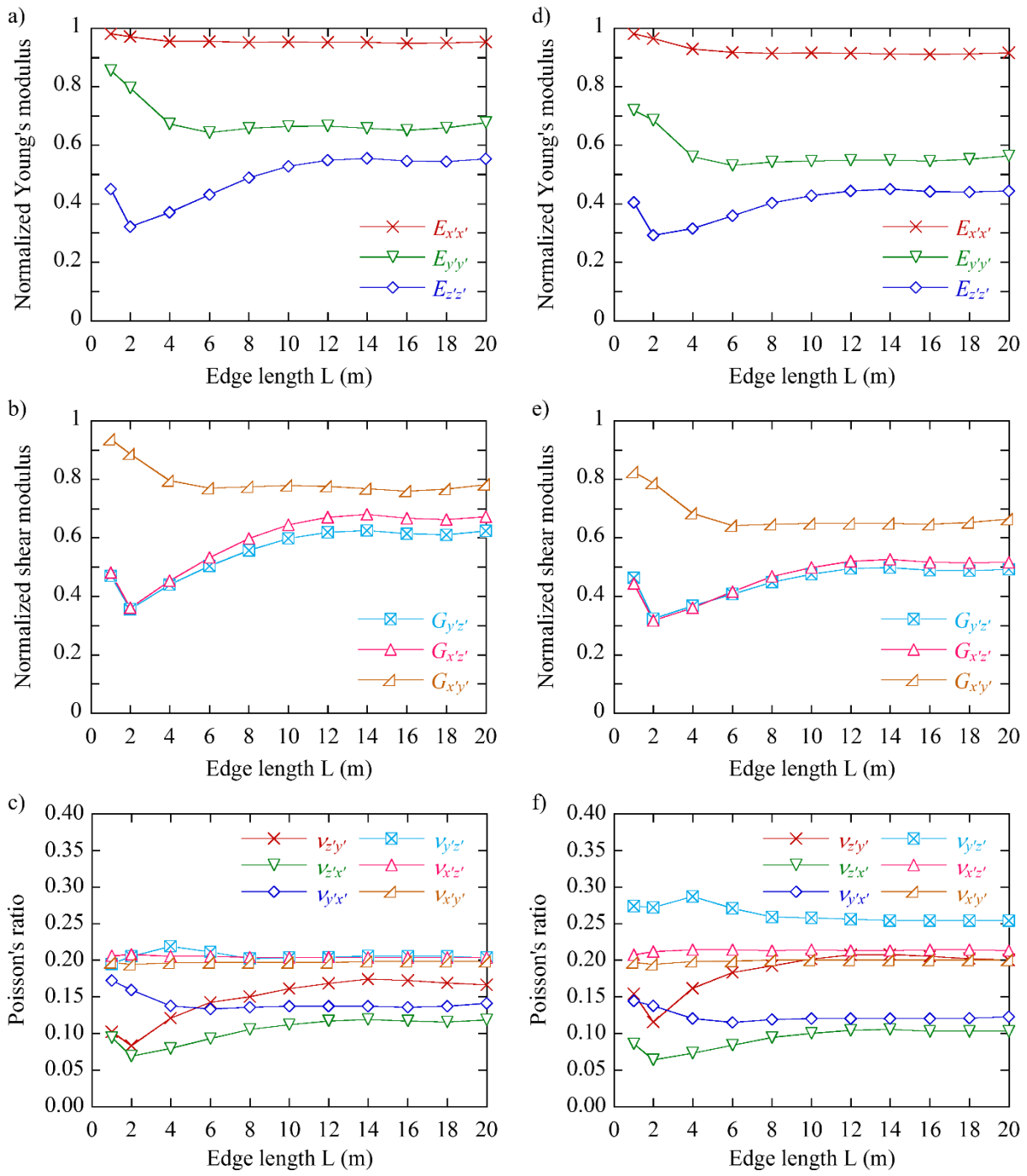

Figure 3.12—Equivalent orthotropic parameters determined in the principal directions of orthotropic symmetry $\{x', y', z'\}$ with the VRM lab (left figures a), b) and c)) and analytically by the Oda's crack tensor approach (right figures d), e) and f)), corresponding to the cubic models of the REV study. The Young's moduli (in a) and d)) and the shear moduli (in b) and e)) are normalized with the elastic parameters, E and G, of the intact material.

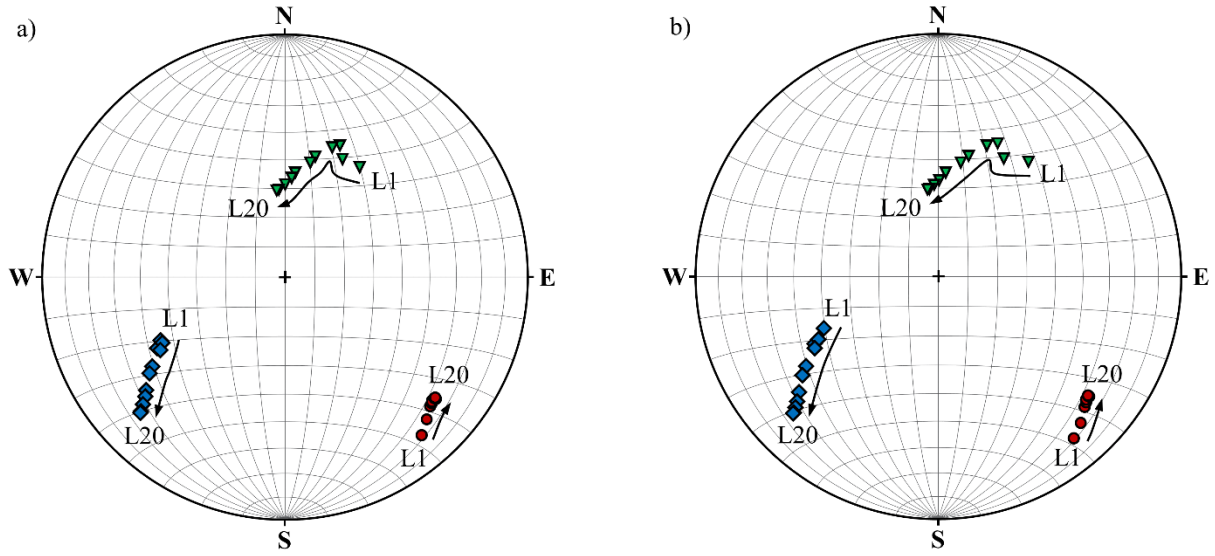

Figure 3.13—Projection on the Schmidt net of the principal directions of orthotropic symmetry determined for the cubic models of the REV study. These results correspond to: a) the VRM lab and, b) the analytical solution using the Oda's crack tensor approach. The arrows show the evolution of the principal directions of the cubic models from L1 to L20.

3.4.2.4 Numerical homogenization at different scales.

Although the VRM laboratory can be used to find the equivalent orthotropic parameters at the REV scale, its main objective is the numerical homogenization of a large fractured model, discretized in regions at the most suitable scale for the engineering purpose of the numerical simulation. To demonstrate the capabilities of the VRM lab for this case, the cubic model L20 is homogenized in two equivalent continuum models with discretization regions below the REV scale. In the first homogenization proposed, the large discontinuum model L20 is cut in 5×5×5 blocks of 4 m edge length, giving a total of 125 fractured cubic regions, each of which is tested in VRM lab to determine their orthotropic parameters. For the second continuum model, the block L20 is cut in a finer discretization of 10×10×10 cubes of 2 m edge length, which are homogenized with the VRM lab, resulting in 1000 sets of equivalent orthotropic parameters, one for each region. Once the homogenization process is complete, both equivalent continuum models are additionally tested, as a whole, in the VRM lab to compare their mechanical deformation behaviour with the large discontinuum model as well as with the continuum model assigned the input equivalent elastic parameters of the L20 model.

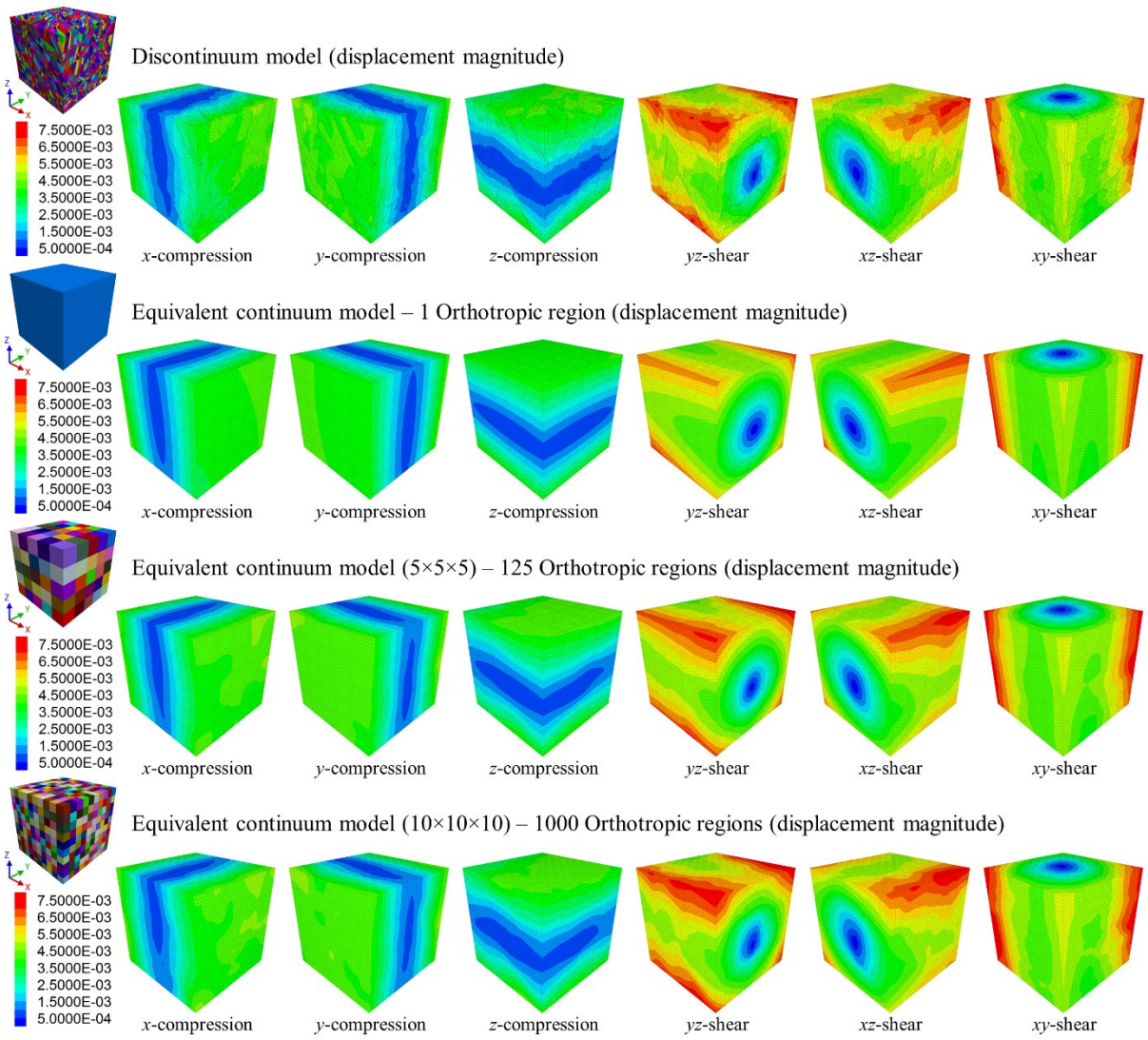

Figure 3.14—Displacement magnitudes for each of the six numerical tests conducted with the VRM laboratory for the discontinuum cubic model L20, and three equivalent continuum models with the orthotropic parameters corresponding to the homogenization of: 1 region of L = 20 m, 125 regions of L = 4 m and 1000 regions of L = 2 m.

As shown in Figure 3.14, the equivalent continuum model discretized in 1000 orthotropic regions of 2 m edge length (L2) captures with a great deal of fidelity, the small-scale variability of the displacement fields observed in the large discontinuum model. Moreover, the homogenization of the coarser discretization corresponding to the equivalent continuum with 125 regions still shows some details of the displacement field variability of the discontinuum simulation. However,

this variability is obviously lost in the continuum model that is simulated as one large homogeneous region with the equivalent orthotropic parameters representative of the large discontinuum block L20. These results show the versatility of the VRM lab to characterize fractured rock formations at specific scales that may be required in different engineering analyses.

3.5 Discussion and conclusion

In general, the numerical modelling of discontinuum media at large scale is computationally expensive, since large numbers of discrete blocks and explicit fractures result in impractical simulation times and large memory sizes. Traditionally, to speed up the numerical simulation and relaxing the memory requirements, the number of explicit fractures is reduced by modelling only the most relevant ones for the purpose of the engineering analysis. Also, the fractured rock formation is often represented as an equivalent continuum which includes implicitly the mechanical behaviour of all the fractures. The mechanical characterization of this equivalent continuum model is usually conducted through analytical solutions or numerical methods.

The closed-form solution based on the Oda's crack tensor theory is a common analytical method for estimating the equivalent elastic parameters of fractured rocks. In this study, the Oda's approach shows very accurate results corresponding to the elastic compliance matrix and equivalent orthotropic parameters determined for verification case, which consists of an isotropic material containing three non-orthogonal and fully persistent joint sets. However, for the case with the embedded DFN of finite circular fractures with different sizes and orientations, the analytical results differ from the numerical solution which provides stiffer Young's moduli and shear moduli. This difference essentially comes from the effect of fracture interactions that is neglected in the analytical solution. Thus, the Oda's crack tensor approach can be used with confidence in fractured rocks containing joint sets of infinite size with linear elastic behaviour, where the non-interaction approximation is assumed valid.

To account for fracture interaction effects and the nonlinear elastic behaviour of the fractures, the equivalent continuum properties must be determined by numerical methods. Usually, these equivalent elastic parameters are estimated at the REV scale. However, the existence of the REV is not always granted, especially in fractured rock formations with joint sets and fractures of very different size. Depending on the objective of the numerical analysis, the discretization of the equivalent continuum may include elements with sizes below the REV scale. Therefore, a numerical homogenization methodology is proposed here, for determining the equivalent continuum parameters of the fractured rock formation discretized in regions of certain size, independently of the REV scale. The homogenization process of the fractured regions for the equivalent continuum model is managed by a VRM numerical laboratory implemented in 3DEC. It is assumed that the fractured regions can be represented by an equivalent continuum material with orthotropic symmetry. In those cases where the error of the orthotropic approximation is large, the equivalent material must be characterized by a triclinic constitutive model with 21 independent coefficients. The methodology has been validated by the comparison of the analytical results of a simple verification case using the Oda's crack tensor approach with the numerical solution of the VRM lab. In addition, the measuring procedure used in the VRM lab for estimating the equivalent compliance matrix is compared with the conventional measurement technique used in previous studies. Contrary to the conventional method, the compliance matrix determined with the VRM lab is symmetric and virtually the same as the analytical solution.

The REV study conducted on the fractured rock formation with the embedded DFN has shown that assuming the principal directions of material symmetry coincide with the coordinate axes of the model or, in other words, disregarding the non-orthotropic coefficients of the compliance matrix in the calculation of the equivalent orthotropic parameters may yield misleading results. In this study, the similarities between the elastic moduli determined in the directions of the coordinate axes suggest the isotropic behaviour of the fractured rock; however, the equivalent orthotropic parameters calculated in the principal directions reveal the inherent anisotropic mechanical behaviour of the fractured material. Thus, the non-orthotropic compliance

coefficients and the principal directions of material symmetry must be taken into account in the mechanical characterization of fractured rock masses.

Traditionally, the REV scale is chosen as the model size beyond which the equivalent elastic properties remain virtually constant. However, the projection on the Schmidt net of the principal axes of orthotropic symmetry suggests that the change in orientation of the principal directions should also be considered to choose the REV size. Moreover, even though the analytical elastic parameters are more compliant than the numerical results, the REV study has confirmed that the Oda's crack tensor approach is an excellent method to estimate the REV scale.

The numerical homogenization of the large cubic model L20 analyzed in the REV study shows that only the equivalent continuum models discretized in 125 and 1000 orthotropic regions are able to capture the small-scale variability of the deformational response of the discontinuum model. Therefore, the VRM lab can be used with confidence to characterize the fractured rock formation at the specific scale that satisfy the requirements of the engineering analysis.

In this study, all the discontinuum models and regions homogenized with the VRM lab are cubic blocks. However, the VRM lab is developed to determine the equivalent orthotropic parameters of any rectangular parallelepiped representing a specific region of the fractured rock. Thus, the discretization of the equivalent continuum representative of the fractured material may comprise small regions in the important areas of the model and large regions in the outer domain. Also, all the fractures here are modelled as linear elastic; however, due to the numerical nature of the VRM laboratory, a nonlinear elastic constitutive model can be assigned to the fractures to capture the stress-dependent mechanical response of the fractured rock formation.

4 Modelling the anisotropic hydro-mechanical behaviour of discrete fracture networks in coupled reservoir geomechanical simulations

4.1 Summary

A coupling methodology has been proposed for the inclusion of the hydro-mechanical behavior of discrete fracture networks in reservoir geomechanical simulations of fractured porous formations through hydraulic and mechanical equivalent continuum parameters determined by the numerical homogenization of rock mass discretization regions using a VRM laboratory. The VRM hydraulic laboratory has been developed for the calculation of the full equivalent permeability tensor of discontinuum media with embedded DFN fractures of any shape and geometry and it has been verified against the analytical Oda's crack tensor approach. Also, a nonlinear elastic joint constitutive model has been implemented in the VRM lab to simulate fracture deformation behaviors closer to experimental observations. An initial mechanical analysis and hydro-mechanical coupled simulations have been studied. The results show that the equivalent continuum model with the VRM laboratory equivalent orthotropic parameters fairly captures the anisotropic deformation behavior of the explicitly fractured rock mass. Moreover, assuming the model axes as principal directions of material symmetry in the homogenization process results in misleading deformation orientations and behaviors of the fractured formation. The DFN fractures included in the coupled simulations have shown a mild impact on the deformability of the rock mass; however, they still show a significant effect on the equivalent permeability parameters obtained through the hydraulic homogenization process. Modelling the fractures as nonlinear elastic results in higher equivalent permeability and consequently leads to a faster build-up in pore pressure in the reservoir. The update of equivalent continuum parameters as well as the plastic fracture deformations slightly improve the permeability and pore pressure development throughout the rock formation.

4.2 Introduction

Natural reservoirs are often significantly fractured due to the action of different geological processes involving mechanical, thermal and chemical activities over millions of years. The presence of geological structures and discontinuities at different scales such as folds, veins, bedding planes, faults, fissures and joints generally affect the geomechanical and fluid flow behaviour of fractured porous formations, which, in turn, may have a significant impact on the formation performance. Consequently, an efficient reservoir management should assume all formations as fractured, unless any other treatment or assumption is proven more appropriate (Narr et al. 2006; Liu & Martinez 2012).

Discontinuities are commonly represented as implicit or explicit structural features in reservoir numerical simulations. Among the different modelling approaches, the discrete fracture model (DFM) is a conventional method to simulate complex fluid flow through porous media with explicit fractures (Karimi-Fard et al. 2004). In general, the DFM provides realistic representations of fractured reservoirs (Moinfar et al. 2014; Fumagalli et al. 2017; Rueda et al. 2021). However, modelling thousands of fractures with complex geometries and different orientations is impractical in terms of computational efficiency, since most of DFMs rely on unstructured meshes for the explicit representation of fractures (Moinfar et al. 2014; Berre et al. 2019; Olorode et al. 2020). To reduce the computational cost, the embedded discrete fracture model (EDFM) (Li & Lee 2008; Moinfar et al. 2014) follows the approach of discretizing the porous matrix in a structured grid, whereas the fractures are represented in the computational domain through additional discretization cells. In the EDFM, the fluid transfer is modeled proportional to the pressure difference between fracture and matrix cells with a transport index that accounts for the fracture geometry (Xu et al. 2016; Berre et al. 2019). Thus, the EDFM is able to handle complex fracture networks more efficiently, at the cost of evaluating transfer functions between the separate fracture and matrix domains. The equivalent continuum models (ECM) are traditionally used for the implicit representation of well-connected fracture networks and systematic joint sets in reservoir simulations. In the simplest ECM approach, the fractured formation is modeled through a single

porous medium with equivalent hydraulic properties that account implicitly for the effect of fractures on the fluid flow process. Thus, the single-continuum approach is very attractive in terms of computational efficiency and simplicity (Berre et al. 2019). On the other hand, multi-continuum models simulate the fractured reservoir as the superposition of several porous media representing different physical domains of the matrix and pore space. Analogous to the EDFMs, the flow exchange between continuum domains is modelled through transfer functions. However, the influence of fracture geometry is lost, since ECMs generally assume fractures as fully-persistent joint sets aligned with the coordinate system of the discretization grid. In reservoir engineering, the dual porosity model (Barenblatt et al. 1960; Warren & Root 1963) is the conventional dual-continuum model for the simulation of fractured formations, where the fluid flow is mainly controlled by regular systems of interconnected fractures (Rutqvist et al. 2013). Another relevant multi-continuum model is the multiple interacting continua (MINC) (Pruess & Narasimhan 1985), which was developed to improve the simulation of transient effects in tight formations with low fluid transfer rate between matrix and fractures (Berre et al. 2019; Olorode et al. 2020). Most of these methods were mainly developed for solving the fluid flow problem in fractured reservoir simulations, disregarding geomechanical deformations during the numerical solution.

The importance of coupling geomechanical processes with flow simulations in fractured porous media has received great attention in reservoir engineering during the past decades. This problem has been traditionally of interest for geoengineering applications in geothermal energy, oil and gas extraction, nuclear waste management and geologic carbon sequestration (Rutqvist & Stephansson 2003; Rutqvist et al. 2013). Along with the growth of computational capabilities, different numerical strategies and coupling methods have been proposed to account for the impact of geomechanical deformations in reservoir simulations. The fully coupled or monolithic approach has been traditionally used to model fractured porous media with explicit (Noorishad et al. 1982) or implicit fracture representations (Bai et al. 1993). Nevertheless, although fully coupled formulations have been recently proposed (Garipov et al. 2016; Rueda et al. 2021), the sequential coupling approach has been mostly used to couple geomechanics with reservoir simulators, since

it allows for the solution of the flow and mechanical sub-problems in separate numerical modules (Kim et al. 2012; Garipov & Hui 2019). Thus, different robust commercial codes can be easily incorporated in a sequential scheme (Settari & Mourits 1998) to satisfy the particular requirements of the reservoir analysis.

Rutqvist et al. (2002) developed the TOUGH-FLAC simulator by the sequential coupling of two widely used numerical codes: the multi-phase, multi-component flow simulator, TOUGH2 (Pruess 1991) and the commercial geomechanical modelling software, FLAC^{3D} (Itasca 1997). In their study, the changes in hydraulic properties of the rock mass were modelled through nonlinear empirical relationships dependent on the effective stress (Rutqvist et al. 2002). Gu and Chalaturnyk (2005, 2010) explicitly coupled the commercial code GEM, developed by Computer Modelling Group Ltd. (CMG 2002), with FLAC^{3D} for the simulation of methane recovery processes in coalbeds. The coal matrix and orthogonal cleats were modelled as an equivalent continuum elastic medium, with the principal directions of permeability and mechanical anisotropy aligned with the model grid. The porosity and permeability changes induced by the mechanical deformation of cleats were modelled using nonlinear analytical expressions. Bagheri (2006) developed a coupled geomechanical reservoir simulator to include the effect of fracture deformations in a dual porosity model. They used an empirical nonlinear elastic constitutive model for joints (Bandis et al. 1983) and an analytical formulation (Huang et al. 1995) to estimate the equivalent properties for the dual-continuum model. The formulation also includes a multi-point flux approximation technique (Aavatsmark 2002) to handle full permeability tensors. However, the coupled simulations are limited to fractured reservoirs with fully persistent joint sets with arbitrary orientation, where the fracture shear deformations are not taken into account. Rutqvist et al. (2013) implemented a linked multicontinuum and crack tensor approach (Oda 1986) in the TOUGH-FLAC simulator. This approach uses the MINC for simulating complex fluid flow and solute transport in the fractured rock, where the fractures are represented by a discrete fracture network (DFN). On a similar basis, Gan and Elsworth (2016) implemented the Oda's crack tensor approach in a coupled continuum simulator (introduced by Taron et al. 2009) for dual-porosity model simulations. Rueda et al.

(2021) recently presented a fully coupled hydromechanical formulation for dual-continuum models of fractured porous media with fully persistent joint sets, where the joint closure is also simulated with an empirical nonlinear elastic model and the equivalent continuum properties are analytically estimated.

The previous coupled reservoir-geomechanical simulators essentially rely on analytical methods to estimate and update the mechanical and hydraulic parameters of the equivalent continuum representative of the fractured porous formation. However, the analytical formulations, such as the Oda's crack tensor approach and other effective medium theories, are not able to accurately capture the effects of complex fracture interactions and fracture connectivity (Min et al. 2004b), often leading to the overestimation of the elastic compliance (see Chapter 3.4.2.3) and permeability properties. To avoid this limitation, several studies have proposed the determination of equivalent continuum properties from numerical simulations, using discrete element codes, UDEC (Itasca 2004) or 3DEC (Itasca 2016), and discrete fracture models as an alternative to the traditional analytical methods (Long et al. 1982; Min et al. 2003, 2004a, 2004b; Thoraval & Renaud 2004; Pouya & Fouché 2009; Lang et al. 2014; Chen et al. 2015, 2018).

In this study, a reservoir geomechanical coupling methodology has been developed to implicitly include the hydro-mechanical effect of fracture deformations in the numerical modelling of fractured porous formations where the fractures are represented by a DFN. In this methodology, the commercial codes STARS and FLAC^{3D} are sequentially coupled through a porosity correction strategy based on the fixed stress split method (see Chapter 2). The fractured formation is represented by a structured grid of discontinuum regions modelled as equivalent porous media, where the mechanical and hydraulic equivalent continuum properties are numerically determined, accounting for the influence of the current effective stress field, with a virtual rock mass (VRM) laboratory implemented in the commercial three-dimensional distinct element code 3DEC. That way, the hydro-mechanical effects induced by fracture deformations can be implicitly included in the numerical simulation. The VRM numerical laboratory is also linked to the sequential coupling scheme. Thus, the equivalent continuum properties may be updated during the sequential coupled

simulation by triggering the VRM lab at specific simulation stages, depending on changes in the effective stress field computed in the continuum geomechanical simulator. The coupled simulation scheme presented here is based on the envisioned reservoir geomechanics coupling approach proposed by Deisman et al. (2009) where several numerical simulators are linked together to model the complex processes found in fractured reservoirs.

4.3 Numerical characterization of the fractured formation

Ideally, the hydro-mechanical characterization of a fractured formation should be conducted through laboratory and *in situ* testing campaigns to capture the scale effect arising from the presence of structural features. However, performing *in situ* tests at large scale directly in the field is generally not possible (Lorig et al., 2010). On the other hand, the conventional analytical methods usually disregard the fracture connectivity and interaction effects. These shortcomings can be avoided by estimating the equivalent anisotropic continuum properties using numerical modelling techniques. In line with that approach, a VRM numerical laboratory is used here to determine the equivalent elastic compliance and permeability tensors of target regions, representing the discretization of the fractured porous formation, through numerical tests conducted in the 3DEC code. In the VRM laboratory, a nonlinear elastic joint constitutive model is implemented to simulate the mechanical closure of the DFN fractures. The Mohr Coulomb-slip constitutive model can also be assigned to the fractures to include the effect of plastic deformations in the computation of the equivalent permeability tensors.

4.3.1 Nonlinear elastic joint constitutive model implemented in VRM laboratory

Empirical observations usually show that the deformation of a fracture under a normal compressive stress is nonlinear (Goodman 1976). To account for this nonlinearity, Bandis et al. (1983) proposed a widely used hyperbolic empirical model to represent the relationship between the stress and fracture closure observed in laboratory experiments. Later, Malama and Kulatilake (2003) found that a generalized negative exponential function can be used to provide a better fit to experimental data. Based on this previous work, Kulatilake et al. (2016) introduced a simple

method to estimate in laboratory the normal and shear stiffnesses of joints through direct shear and uniaxial compression tests. They proposed the following exponential function to describe the nonlinear closure of a joint under compression:

$$\sigma = Ae^{Bu_J} \tag{4.1}$$

where σ is the normal compressive stress, u_J is the joint closure, A and B are empirical constants determined from the experimental data. The constant A can be defined as the seating load at zero joint closure, corresponding to the initial condition or reference for measuring the normal displacement during the compression test (Goodman 1976). Using the definition of joint normal stiffness k_n, as the rate of change of normal stress with respect to the normal displacement (Goodman 1970), and differentiating Eq. (4.1) with respect to σ gives:

$$k_n = B\sigma \tag{4.2}$$

This simple linear relationship between the joint normal stiffness and the compressive stress, introduced by Kulatilake et al. (2016), can be implemented in numerical methods to simulate the nonlinear behavior of joints. Following that approach, Mehranpour and Kulatilake (2017) applied this relationship in the particle flow code PFC (Itasca 2016) to update the normal stiffness at joint contacts between particles during the numerical simulation. They also proposed the use of a user-defined minimum joint normal stiffness $k_n^{\min}$ to avoid very low stiffnesses with values close to zero, which may result in large particle overlaps leading to numerical instabilities during the PFC simulations. Similarly, this empirical constitutive model proposed by Kulatilake et al. (2016) has been implemented, here, in the VRM numerical laboratory (see Chapter 3), to include the nonlinear normal deformation of the joints during the 3DEC simulations. That way, the joint normal stiffness is updated according to the relationship in Eq. (4.2) at each of the joint sub-contacts representing the circular fractures of the DFN (Figure 3.7).

In the VRM lab, the minimum joint normal stiffness $k_n^{\min}$ is assumed the same as the normal stiffness of an open crack embedded in an infinite elastic medium, which can be determined

from the expression of the average normal displacement induced by a uniform normal traction acting on the open crack (e.g., Rice 1979). According to Sevostianov and Kachanov (2013), the normal compliance of an open circular crack is given by:

$$B_N = \frac{16\left(1-\nu^2\right)r}{3\pi E} \tag{4.3}$$

where r is the radius, E and ν are the Young's modulus and Poisson's ratio of the infinite elastic material. Thus, the minimum joint normal stiffness is estimated here as the inverse of the crack normal compliance, that is:

$$k_n^{\min} = \frac{1}{B_N} = \frac{3\pi E}{16\left(1-\nu^2\right)r} \tag{4.4}$$

For simplicity, the elastic parameters of the intact rock are set as input for Eq. (4.4). However, assigning the elastic parameters of the rock mass surrounding the joint instead may be required in those cases where the density of joints is significant.

The minimum normal stiffness controls the elastic behavior of the joints under very low compressive normal stresses as well as in the tensile stress regime, preventing unrealistic low values of normal stiffness that may lead to numerical instabilities due to the excessive overlap between discretization blocks in the 3DEC simulation. In addition, a maximum limit to the normal stiffness $k_n^{\max}$ has also been included in the VRM lab, to prevent large stiffness values that will result in very small numerical timesteps, which usually leads to large computational times. The maximum joint normal stiffness is calculated here by substituting the area of the fictitious joints in Eq. (3.21) with the whole area of the fracture plane in 3DEC, A^{tot}, which includes the fictious and actual joint areas:

$$k_n^{\max} = \max\left\{\frac{E}{\lambda V}\sum^{Nf}\left[A^{tot}n_i^2\right] \;\; ; \;\; \frac{G}{\lambda V}\sum^{Nf}\left[A^{tot}\left(1-n_i^2\right)\right]\right\} \tag{4.5}$$

where λ is a proportionality factor that corresponds to λ^{Fict} in Eq. (3.21), V is the total volume of the fractured region, G is the shear modulus of the intact material, Nf is the total number of fractures, and n_i is the i-component of the normal vector to the fracture plane with the index i ranging over the coordinate axes $\{x, y, z\}$. Additionally, the maximum normal stiffness obtained for the nonlinear behaviour (Eq. (4.5)) is also assigned to the sub-contacts representing the fictitious joint area outside the circular fracture (Figure 3.7).

4.3.1.1 Verification of the nonlinear elastic joint constitutive model

A simple case of a block containing a horizontal joint has been modelled to illustrate and verify the nonlinear model implemented in the VRM numerical lab. The model consists of a cubic block with size 15×15×15 m^3 containing a horizontal circular fracture with a radius of 6.75 m. The intact rock represents a shale with a Young's modulus and Poisson's ratio of 26 GPa and 0.2 respectively. Substituting the previous data in Eq. (4.4) gives the minimum normal stiffness $k_n^{\min}$ of 2.4 GPa/m. The joint shear stiffness is set to $k_s = 7.56$ GPa/m. Kulatilake et al. (2016) conducted laboratory experiments to determine the parameter B of different rock types. They estimated the mean value of $B = 18.9$ (units of 1/mm) for the particular group of shale samples. The same value is used here as input for this case. Additionally, the seating load of the sample is assumed to 1 atm, i.e., $A = 101325$ Pa. A compressive stress of 40 MPa is applied in the vertical direction at the top and bottom boundaries of the model. The maximum normal stiffness is calculated in this case by assigning a proportionality factor of $\lambda = 0.001$ (see Chapter 3.4.2.2), which results in a value of $k_n^{\max} = 1733$ GPa/m. The normal compressive stress and joint closure have been monitored at the center of the fracture during the numerical simulation conducted in 3DEC through the VRM lab. The numerical results show very good agreement with the exponential function obtained by substituting the input data in Eq. (4.2) (Figure 4.1).

4.3.2 Determination of the equivalent mechanical parameters

The VRM laboratory includes a mechanical module that has been developed to determine the equivalent elastic compliance matrix of specific fractured regions of the porous formation (see

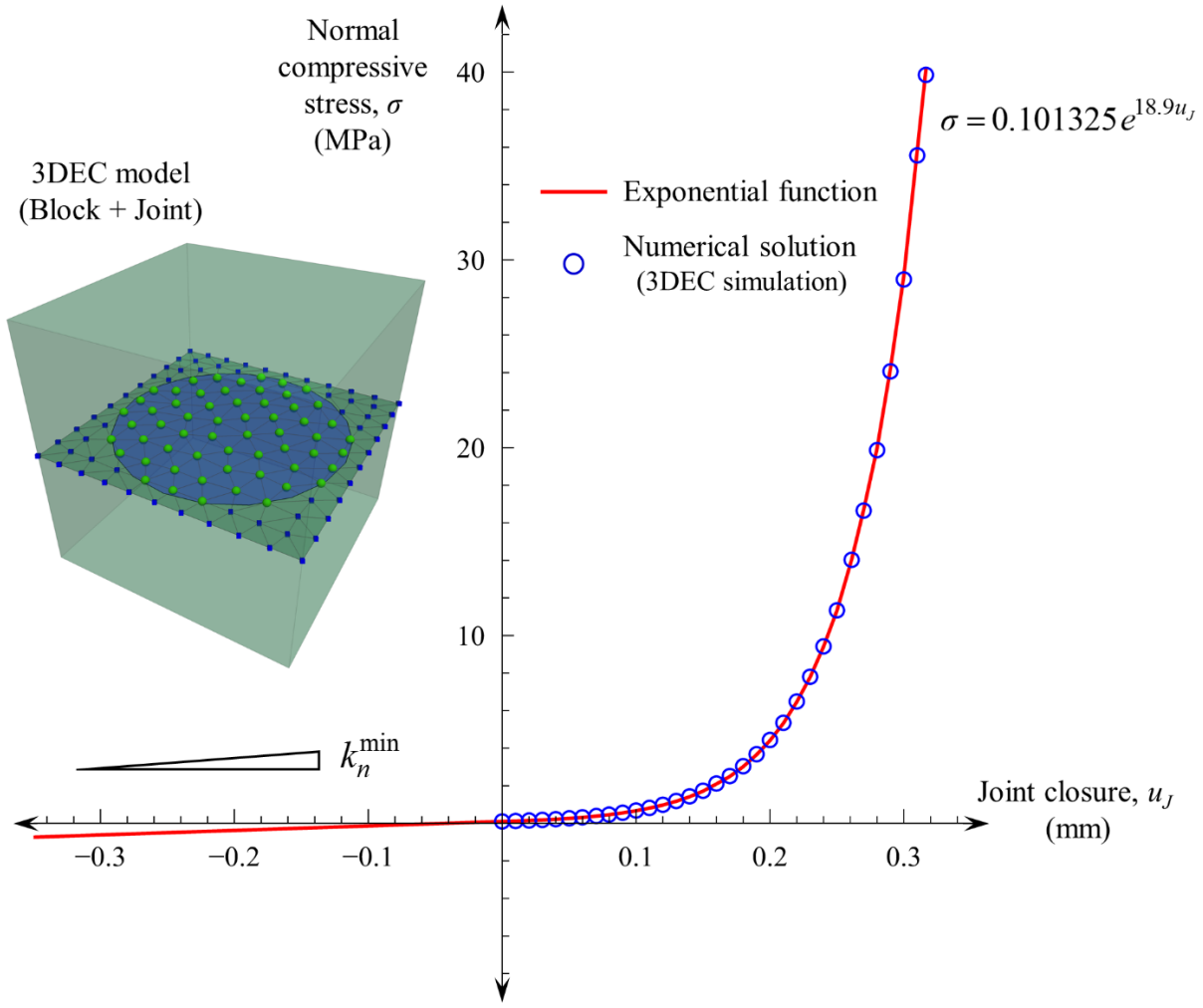

Figure 4.1—Verification case of the nonlinear joint constitutive model implemented in VRM lab. Comparison of the exponential function (solid line) and the numerical solution (open circles) measured at the center of the fracture in the 3DEC simulation. A detail of the 3DEC model is also included, showing the block containing the circular fracture with the fictitious and joint sub-contacts. The vertical compressive stress and joint closure are plotted as positive.

Chapter 3). That matrix is later used to calculate the orthotropic elastic properties for the equivalent continuum. To obtain the compliance matrix, the VRM lab mounts the target fractured region in 3DEC and conducts six independent numerical tests, compression and shear (Figure 3.1). During these tests, the joint normal stiffness at each sub-contact is set constant. However, before conducting those six tests, the current effective stress field is installed in the 3DEC model with the nonlinear elastic joint constitutive model active and the simulation is run to equilibrium. Therefore, the joint normal stiffness is updated only during the installation of the current effective stresses in

the model, following the relationship in Eq. (4.2), to account for the effect of the nonlinear elastic behavior of the joints. Once the stress field is successfully installed and the required initial equilibrium is reached, the last values of the updated normal stiffnesses are fixed and kept constant in the subsequent six numerical tests.

4.3.3 Determination of the anisotropic equivalent permeability tensor

The permeability of a fractured formation can be evaluated using analytical or numerical methods. Among the analytical methods, the Oda's crack tensor approach (Oda 1985, 1986) has been widely used to estimate the effective permeability tensor of fractured media, by relying only on the geometrical properties of the fractures. Nevertheless, the Oda's crack tensor theory is not suited to accurately take into account the connectivity and interactions of complex fracture networks (Barla et al. 2000; Min et al. 2004b). As an alternative to the analytical approach, several studies have proposed the use of numerical methods to determine the equivalent permeability tensor of rock formations with complex systems of fractures.

Long et al. (1982) used a finite element numerical code to estimate the equivalent permeability tensor and the representative elementary volume (REV) size of two-dimensional (2D) models populated with random fracture networks. In their numerical tests, a linear pressure gradient is imposed in the model by applying two constant pressure heads at the boundaries normal to the gradient and a linearly varying pressure at the boundaries parallel to the gradient. The matrix is modelled impermeable and the cubic law (Snow 1969) is assumed valid. Additionally, the mechanical deformation effect is disregarded in the numerical analysis. The permeability tensor is estimated using the Darcy's law with the measurements of the steady-state flow rate in two numerical simulations; one with a horizontal pressure gradient and the other one with a vertical gradient. Following a similar approach, Min et al. (2004a) used the two-dimensional distinct element code UDEC (Itasca 2000) to find the REV size and calculate the anisotropic permeability tensor of rock masses with multiple realizations of discrete fracture networks (DFN), which were modelled with constant hydraulic apertures. At the same time, they also studied the effect of the

nonlinear normal deformation and shear dilation of fractures in the stress-dependent permeability of rock masses under several load conditions (Min et al. 2004b). In their study, they found significant channeling effects of the fluid flow in fractures with high mobilization of shear dilation. Similarly, Thoraval et al. (2003) used the 3DEC code to determine the equivalent permeability of three-dimensional (3D) fractured rocks at different scales. Later, Baghbanan and Jing (2008) studied the influence of the correlation of fracture aperture with the trace length on the permeability and fluid flow in 2D simulations using the UDEC code.

Pouya and Fouché (2009) presented a double definition of the equivalent permeability for heterogeneous media, involving two symmetric and positive definite tensors that result from applying the boundary conditions of constant flux or linear pressure gradient in numerical models. They also introduced a method to estimate the equivalent permeability tensor of a 3D fractured medium, from 2D permeability tensors measured in several cross-sections of the rock mass cut in different orientations. Subsequently, Lang et al. (2014) proposed an averaging method to determine the full equivalent permeability tensor from the volume-averaged values of flux and pressure gradient computed in 3D finite element simulations, where the matrix is modelled as permeable and the mechanical deformations are neglected. In their study, they compared the permeability tensor estimated in a 3D model with the results of several cross-sections, showing that the equivalent permeability measured in the 2D simulations underestimate the permeability computed in the 3D simulation. Chen et al. (2015), developed a multiple boundary upscaling method for the estimation of the equivalent permeability of 2D fractured porous media using discrete fracture models. In the numerical simulations, a linear pressure gradient is imposed in the 2D model and the vector components of the flow rate are measured at the boundaries to calculate the permeability tensor. Also, the mechanical deformations are disregarded and the matrix is assumed permeable. In their method, instead of measuring only the flow rate in the normal direction to the model boundaries, all the components of the flow rate vectors measured at multiple boundaries are taken into consideration to compute the total flow rate through the volumetric domain. They showed that the multiple boundary method gives better estimates of the equivalent

permeability tensor than the methods based on the classic flow rate measurement (e.g., Long et al 1982 among others). Chen et al. (2018) extended the multiple boundary method for 3D models with fractured networks. However, this last method is limited to fractures that are parallel, at least, to one axis of the model; otherwise the equivalent permeability may be overestimated by a factor of two (Chen et al. 2018). This issue does not exist in 2D models, since all fractures are assumed parallel to the model axis in the out-of-plane direction.

These studies have shown the capability of different modelling techniques to numerically determine the equivalent permeability of fractured media. Thus, according to the numerical approach, a module has been developed in the VRM lab for the hydraulic characterization of fractured porous formations with an embedded DFN; and, this way, including the effect of mechanical deformations and fracture interactions in the estimation of the equivalent permeability tensor.

4.3.3.1 Virtual rock mass hydraulic laboratory

The hydraulic module of the VRM laboratory has been developed to conduct fluid flow simulations on target regions of the fractured formation with the 3DEC code. This module has been coded using the FISH scripting language embedded in the Itasca software (Itasca 2016). The equivalent permeability tensor of the fractured region is determined by measuring the flow rate at the boundary of the model after reaching the steady-state solution in three independent numerical experiments. Similarly to Long et al. (1982), each of these tests is modelled with a linear pressure gradient applied at the boundary conditions in the direction of one of the three coordinate axes of the model (Figure 4.2). In these simulations, the matrix is assumed deformable and impermeable to reduce the computational time. Thus, the fluid is allowed to flow only through the fractures, which are represented in 3DEC with a parallel plate model obeying the cubic law (Itasca 2016).

The mechanical deformations are disregarded during the numerical solution of each of the three steady-state flow problems. However, the deformation of fractures and matrix is taken into account during the installation of the current effective stress field, in the process of reaching the

required initial equilibrium state in the jointed region before running the flow tests. During the effective stress field installation, the change in hydraulic aperture in the fractures is assumed herein the same as the fracture closure, which follows the nonlinear elastic joint constitutive model implemented in the VRM lab. In addition, the hydraulic aperture is bound by a residual value a_{res} and a maximum aperture a_{max} for computational efficiency during the simulation (Figure 4.3).

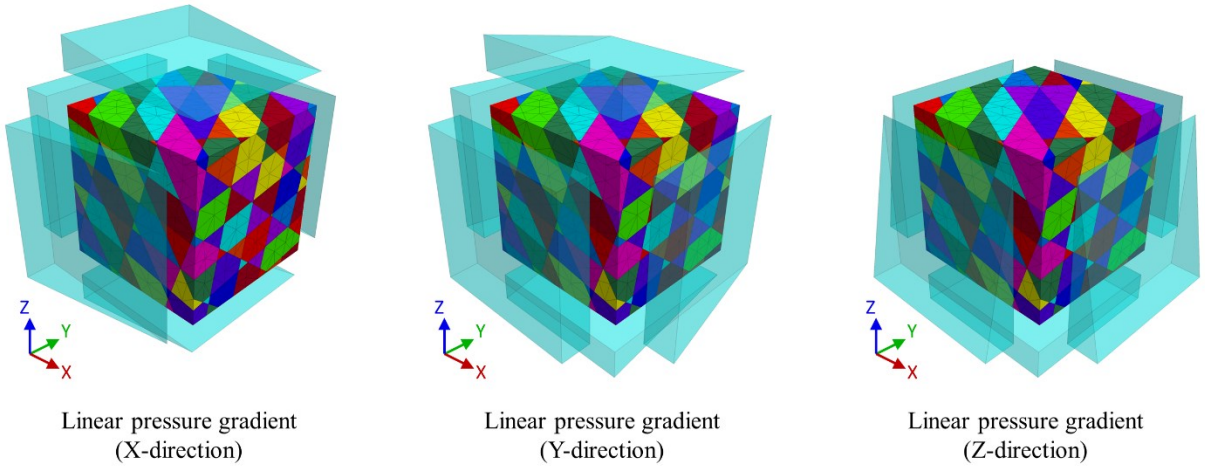

Figure 4.2—Steady-state flow tests under three different linear pressure gradients conducted with the VRM hydraulic lab developed for 3DEC to determine the equivalent permeability tensor (where the light blue volumes represent fluid pressure with a linear pressure drop Δp).

Assuming the validity of the Darcy's law, the equivalent permeability tensor can be determined using the generalized expression for anisotropic porous media (Bear 1972):

$$q_i = -\frac{k_{ij}}{\mu}\frac{\partial p}{\partial x_j} \tag{4.6}$$

where q_i is the specific discharge, μ is the dynamic viscosity, $\partial p/\partial x_j$ is the pressure gradient, and k_{ij} is the permeability tensor, with indices (i, j) ranging over the Cartesian coordinates of the 3D space $\{x, y, z\}$. Here, the summation is implied over repeated indices.

In the VRM hydraulic lab, each of the three steady-state flow tests is conducted to determine one column of the permeability tensor, analogous to the compliance matrix determined

with the mechanical module (see Chapter 3.3.2). Thus, for a rectangular parallelepiped with dimensions $L_x \times L_y \times L_z$ m^3 representing a specific region of the fractured rock, the equivalent permeability tensor can be calculated by the following expression of the Eq. (4.6) in matrix form:

$$\begin{pmatrix} k_{xx} & k_{xy} & k_{xz} \\ k_{yx} & k_{yy} & k_{yz} \\ k_{zx} & k_{zy} & k_{zz} \end{pmatrix} = \frac{\mu}{\Delta p} \begin{pmatrix} q_x L_x & q_x L_y & q_x L_z \\ q_y L_x & q_y L_y & q_y L_z \\ q_z L_x & q_z L_y & q_z L_z \end{pmatrix} \tag{4.7}$$

where Δp is the linear pressure drop applied in the numerical model, and the specific discharges q_i are the required unknowns to be measured in the three flow simulations.

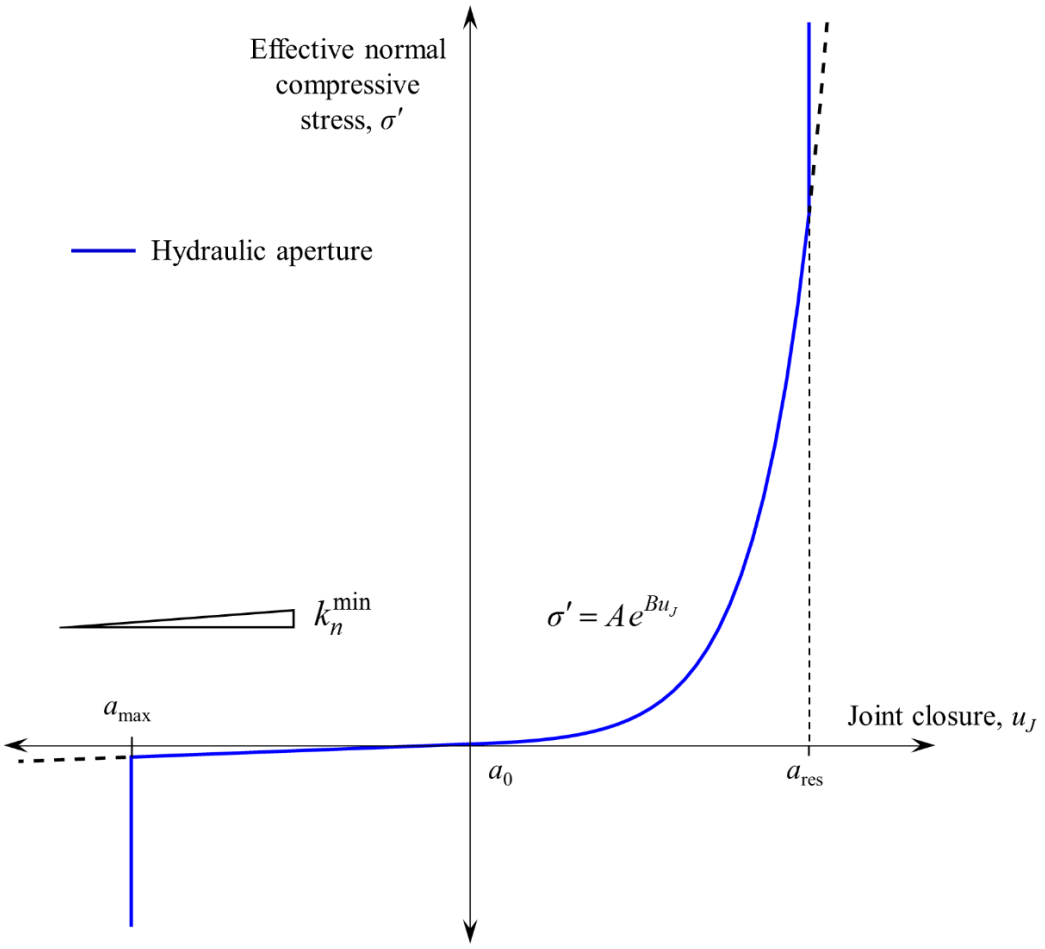

Figure 4.3—Hydraulic aperture behaviour of a joint under a normal effective stress, compressive or tensile, following the nonlinear joint constitutive model implemented in VRM lab with the residual a_{res} and maximum $a_{\max}$ bounds. The a_0 corresponds to the initial hydraulic aperture under the seating load A.

The total equivalent permeability of the fractured target region is determined following the approach presented in Oda (1985), where the permeability tensor of the intact rock matrix is added to the permeability tensor induced by the network of fractures (Eq. (4.7), provided that the total volume of the fractures is negligible with respect to the volume of the region.

4.3.3.2 Measurement of specific discharges in the 3DEC model

To determine the specific discharges over the target discontinuum region after solving the steady-state flow problem, the VRM hydraulic lab integrates the flow rate measurements at the center of the joint trace segments (*jts*) located at the boundary of the model (Figure 4.4). Similar to the mechanical module of the VRM lab and with the aim of improving the speed and efficiency of the measuring process, several linked-list are created to store the memory addresses of the flow knots located at the model boundary and their associated flow plane zones (*fpz*). The flow knots correspond to the discretization nodes of the flow elements (i.e., flow plane zones) of the 3DEC model (Itasca 2016). The location of the centers of the joint trace segments and their trace length defined by the flow knots at the boundary are also stored in the linked-lists.

The method implemented in the VRM hydraulic laboratory to determine the specific discharges through the discontinuum model in 3DEC is based on the definition of the mean flux (measured at the region frontier) presented in Pouya and Fouché (2009) and the surface averaging-based approach presented in Kushch (2013) for the homogenization of the thermal conductivity in composites. According to these two previous studies, the mean flux determined from the flow rate values at the boundary $\partial\Omega$ of the target domain Ω can be expressed as:

$$\langle \boldsymbol{q} \rangle = \frac{1}{V} \int_{\partial\Omega} (\boldsymbol{q} \cdot \boldsymbol{n})\, \boldsymbol{x}\, dS \tag{4.8}$$

where $\langle \boldsymbol{q} \rangle$ is the mean flux vector, V is the volume of the target domain Ω, $\boldsymbol{q}$ is the flow rate vector through the element area dS associated to one point of the boundary $\partial\Omega$, $\boldsymbol{n}$ is the unit normal vector to the boundary element dS, and $\boldsymbol{x}$ is the position vector for each of the boundary points.

Integrating the Eq. (4.8) over the areas, A^{jts}, associated to the joint trace segments at the boundary of the 3DEC model gives the expression, in discrete form, to determine the surface-averaged specific discharges q_i as follows:

$$q_i = \frac{1}{V} \sum_{jts=1}^{Njts} \left(q_k^{jts} n_k^{jts} \right) \left(x_i^{jts} - x_i^c \right) A^{jts} \tag{4.9}$$

where V is the volume of the model, $Njts$ is the total number of joint trace segments at the model boundary, q_k^{jts} and n_k^{jts} are the k-components of the flow rate and unit normal vectors, respectively, corresponding to the joint trace segment jts, x_i^{jts} is the i-component of the position vector of the trace segment center, x_i^c is the i-component of the position vector of the center of the model acting as a reference point and, A^{jts} is the cross-sectional area associated to the joint trace segment that is defined by the intersection of the model boundary with the volume represented by the flow plane zone and its hydraulic aperture. Assuming a parallelepided region oriented in the cartesian coordinates, it is calculated by:

$$A^{jts} = \frac{l^{jts} a^{fpz}}{\sqrt{1 - \left(n_i^{fpz} \right)^2}} \tag{4.10}$$

where l^{jts} is the joint trace segment length, a^{fpz} is the current hydraulic aperture of the flow plane zone fpz and, n_i^{fpz} is the i-component of the unit normal vector to the flow plane zone (Figure 4.4). The subscripts (i, k) represent the vector components in the directions $\{x, y, z\}$. Note that the summation is implied over the repeated k-index in the Eq. (4.9). On the other hand, the whole expression of the area A^{jts} in Eq. (4.10) is deliberately not included in the Eq. (4.9) to avoid the otherwise implied summation over the i-index. Once the specific discharges are measured in the three steady-state flow tests according to the Eq. (4.9), they can be substituted in the Eq. (4.7) to finally determine the full equivalent permeability tensor of the target fractured region.

The main advantage of the surface averaging-based measurement of the specific discharge presented here, over the conventional volume averaging method, is that the former is valid for

materials with imperfect interfaces while the later requires perfect contacts between the constituents of the discontinuum material (Kushch 2013).

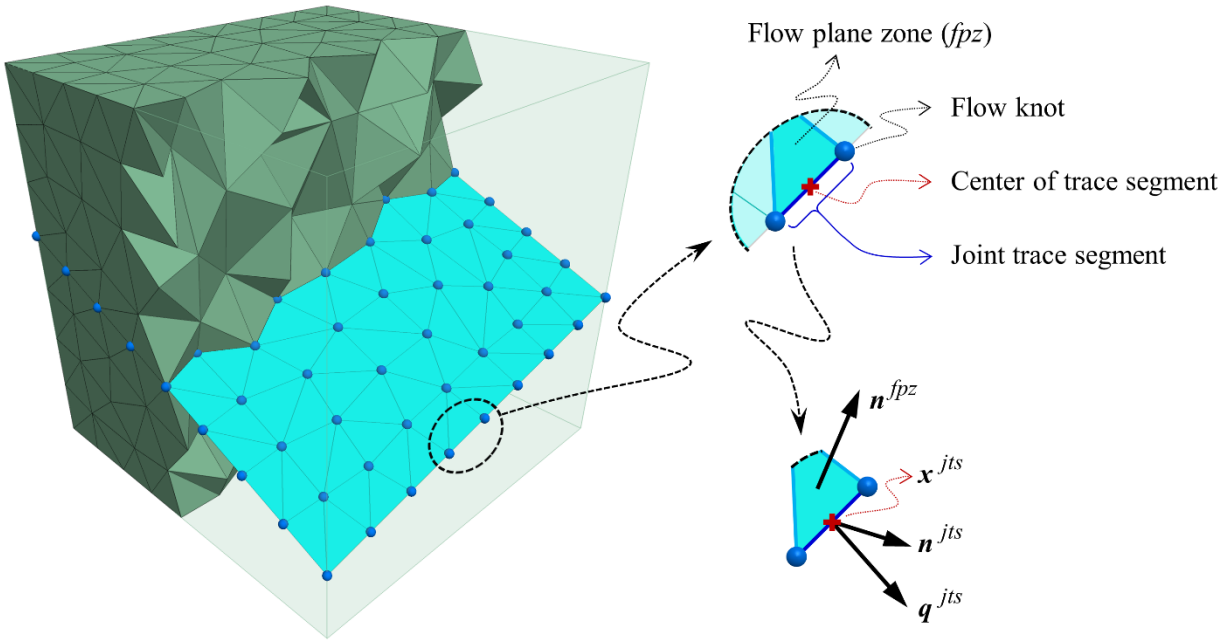

Figure 4.4—Flow knots and flow plane zones (*fpz*) corresponding to the discretization of the flow model in 3DEC. Details of one flow plane zone and the corresponding joint trace segment (*jts*) at the boundary of the model showing the unit normal vector ($\boldsymbol{n}^{fpz}$) to the flow plane zone, the position vector of the joint trace segment center ($\boldsymbol{x}^{jts}$), the unit normal ($\boldsymbol{n}^{jts}$) vector to the boundary and the flow rate vector ($\boldsymbol{q}^{jts}$) used in the computation of the specific discharges for calculating the equivalent permeability tensor.

4.3.3.3 Verification of the VRM hydraulic laboratory

To verify the proposed methodology for measuring the equivalent permeability tensor implemented in the VRM hydraulic lab, the numerical solutions of several cases of a block containing a single fracture with different orientations (Figure 4.5) have been compared with the analytical results obtained using the Oda's crack tensor approach (Oda 1985, 1986).

In the Oda's theory, the fractured formation is considered as an intact rock matrix with an embedded network of circular joints. The permeability tensor due to the presence of the system of fractures is calculated by means of a crack tensor, which takes only into account the geometrical

features of the discontinuities (Oda 1985). Thus, the expression to calculate the permeability tensor can be formulated as (Oda 1985; Rutqvist et al. 2013):

$$k_{ij} = \sum^{Nf} \frac{1}{12}\left(P_{kk}\delta_{ij} - P_{ij}\right) \tag{4.11}$$

where *Nf* is the total number of circular fractures, δ_{ij} is the Kronecker delta and, P_{ij} is the second-order crack tensor, which is defined for a single fracture as:

$$P_{ij} = \frac{A}{V} a^3 n_i n_j \tag{4.12}$$

where *V* is the total volume of the fractured region, *A* is the fracture area, *a* is the hydraulic aperture, and, n_i is the *i*-component of the normal vector to the fracture plane, with indices (*i, j*) ranging over the coordinate axes {*x, y, z*}. Substituting Eq. (4.12) into Eq. (4.11) and representing the tensors in matrix form gives the following expression for the equivalent permeability:

$$\begin{pmatrix} k_{xx} & k_{xy} & k_{xz} \\ k_{yx} & k_{yy} & k_{yz} \\ k_{zx} & k_{zy} & k_{zz} \end{pmatrix} = \frac{1}{12V} \sum^{Nf} Aa^3 \begin{pmatrix} 1-n_x^2 & -n_x n_y & -n_x n_z \\ -n_y n_x & 1-n_y^2 & -n_y n_z \\ -n_z n_x & -n_z n_y & 1-n_z^2 \end{pmatrix} \tag{4.13}$$

where the summation terms are evaluated for every fracture of the discontinuum model. The Eq. (4.13) clearly shows the symmetry of the permeability tensor determined through the Oda's crack tensor approach.

The verification cases studied here consist of a cubic block of dimension 1×1×1 m^3 cut through its center by one fully persistent fracture, which is rotated at several intervals a total of 180° around the horizontal. Eight cases have been modeled with the following dip and dip direction angles (i.e., dip/dip-dir.): 0/120, 30/120, 45/120, 60/120, 90/300, 60/300, 45/300 and 30/300 (Figure 4.5). This way, the fracture plane will be totally oblique to the axes of the model in the six verification cases where the dip angle is different than 0° or 90°. The hydraulic aperture is assumed constant with a value of 1 mm in the simulations and the dynamic viscosity is set to 0.001 Pa·s. A

linear pressure drop of $\Delta p = 10^5$ Pa is applied at the model boundary in each of the numerical steady-state flow tests (Figure 4.2).

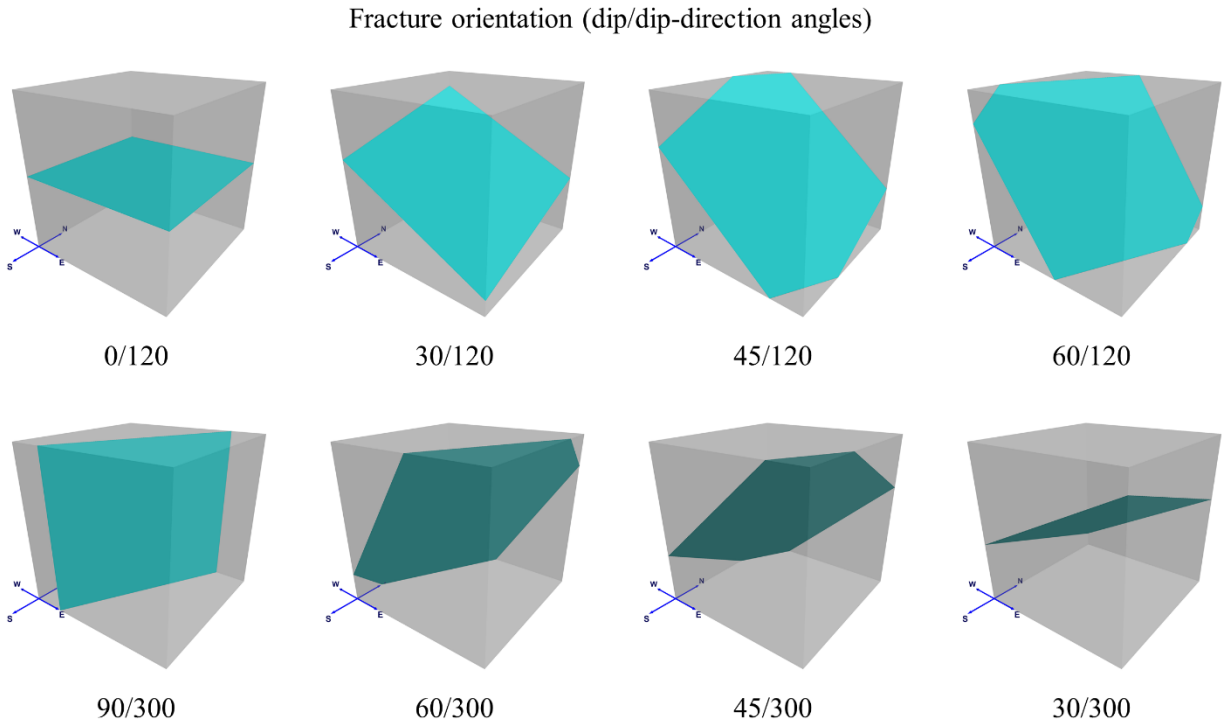

Figure 4.5—Verification cases of the methodology for measuring the equivalent permeability tensor implemented in the VRM hydraulic lab, showing the different dip and dip-direction angles of the fracture in each of the eight analyzed cases.

As shown in Figure 4.6, the normal components (k_{xx}, k_{yy}, k_{zz}) and the shear components (k_{xy}, k_{xz}, k_{yz}) of the equivalent permeability tensor determined analytically using the Oda's crack tensor approach for the eight verification cases are equal to the corresponding numerical results of the tests conducted with the VRM hydraulic lab, demonstrating its capability to accurately determine the equivalent permeability tensor of the fractured region.

The measurement methodology implemented in the hydraulic module of the VRM lab takes into account the vector components of the flow rate measured at all the boundary faces of the model, analogous to the multiple boundary method proposed by Chen et al. (2018). However, contrary to this last method which is limited to certain fracture orientations, VRM hydraulic lab is able to accurately compute the equivalent permeability tensor of 3D discontinuum models with

fractures totally oblique to the model coordinate system, as it is shown in the results of the verification cases with fracture dip angles different than 0° and 90° (Figure 4.6).

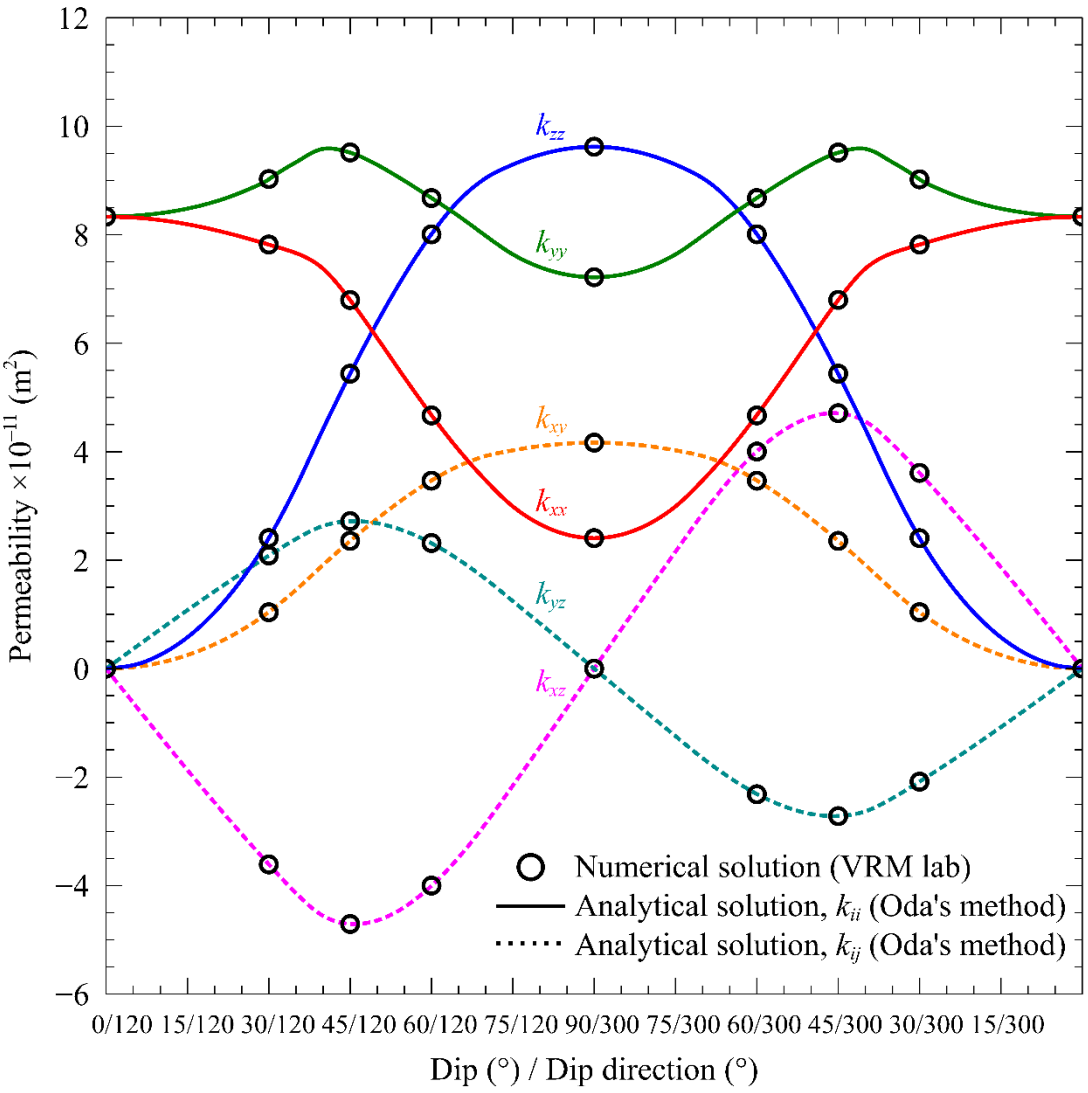

Figure 4.6—Comparison of the components of the equivalent permeability tensor determined numerically with the VRM hydraulic lab (in circles) and analytically through the Oda's crack tensor approach (normal components k_{ii} in solid line and shear components k_{ij} in dotted line), for each of the verification cases.

4.3.4 Plastic behavior of DFN joints

To include the effect of the plastic deformation of fractures in the computation of the equivalent permeability tensor, the joints in the VRM hydraulic lab are modelled with the Mohr

Coulomb-slip joint constitutive model (MC) implemented and embedded in the 3DEC code (Itasca 2016). As in the case of the nonlinear elastic behavior of the joints, the plastic deformations of the discontinuities are taken into account during the installation of the current effective stress field in the model, to establish the required initial equilibrium state before running the three flow simulations. In this process, the 3DEC model is generated with the addition of a buffer that is enclosing the target region, where both, buffer and region, are modelled with the same mechanical properties. Based on the observations presented in Gao and Lei (2018), the buffer is modelled with a thickness no less of 20% of the length of the model to minimize the influence of the applied boundary conditions on the stress field dispersion in the fractured region (Figure 4.7).

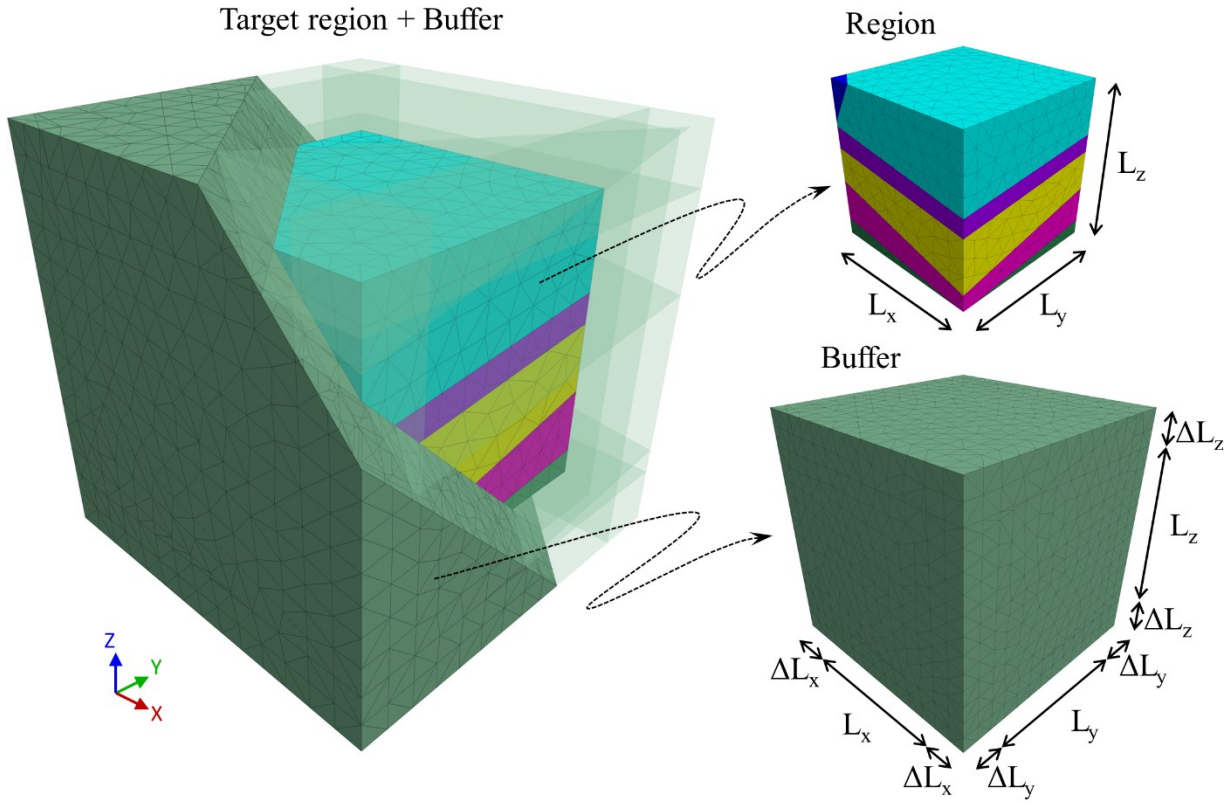

Figure 4.7—Buffer enclosing the target region generated in the VRM hydraulic lab. The buffer thickness in this case corresponds to the 20% of the model length (i.e., $\Delta L_i = 0.2L_i$).

After the model generation, the effective stress field is installed in the 3DEC model with the joints modelled as nonlinear elastic by setting their strength properties to large values. Once

the initial elastic equilibrium state is reached, the boundary faces of the model are fixed, the actual strength parameters of the Mohr Coulomb-slip constitutive model are assigned to the joints and the numerical model is run again until equilibrium. This procedure is necessary to avoid possible numerical simulation instabilities during the effective stress installation, in those cases where the 3DEC numerical model is totally cut through a large joint that may be at failure mode, developing a deformation state of continuous plastic flow. Once the equilibrium state is achieved with the plastic constitutive model assigned to the joints, the buffer is deleted and the three numerical flow simulations are finally conducted to compute the equivalent permeability of the fractured region.

4.4 Coupling strategy and methodology

The coupling of the complex flow and mechanical processes induced during the reservoir operations is conducted through a numerical platform developed at the University of Alberta by the reservoir geomechanics research group (RGRG). In this coupling platform, two widely used commercial software, STARS and FLAC^{3D}, are linked together following an explicit sequential coupled scheme. The reservoir simulator STARS developed by Computer Modelling Group Ltd. (CMG 2018) is used to capture the complex thermal and fluid flow processes. The reservoir deformations and effective stress changes are computed with the continuum geomechanical simulator FLAC^{3D} developed by Itasca Consulting Group Inc. (Itasca 2013). Both simulators are sequentially coupled through a porosity correction strategy based on the fixed stress split method, where the thermo-poromechanical formulation accounts for the generalized Biot effective stress coefficient in tensorial form (see Chapter 2). Analogous to the envisioned reservoir geomechanical coupling approach proposed by Deisman et al. (2009) for simulations of fractured reservoirs sensitive to stress changes, where several numerical simulators are linked together, the VRM laboratory is also linked to the explicit sequential coupled scheme built into the RGRG platform to implicitly include the hydro-mechanical behaviour induced by the presence of fractures in the numerical simulation (Figure 4.8). Thus, the target discontinuum regions representing the discretization of the fractured porous formation are modelled as equivalent porous media with

anisotropic continuum properties determined through the mechanical and hydraulic modules of the VRM laboratory.

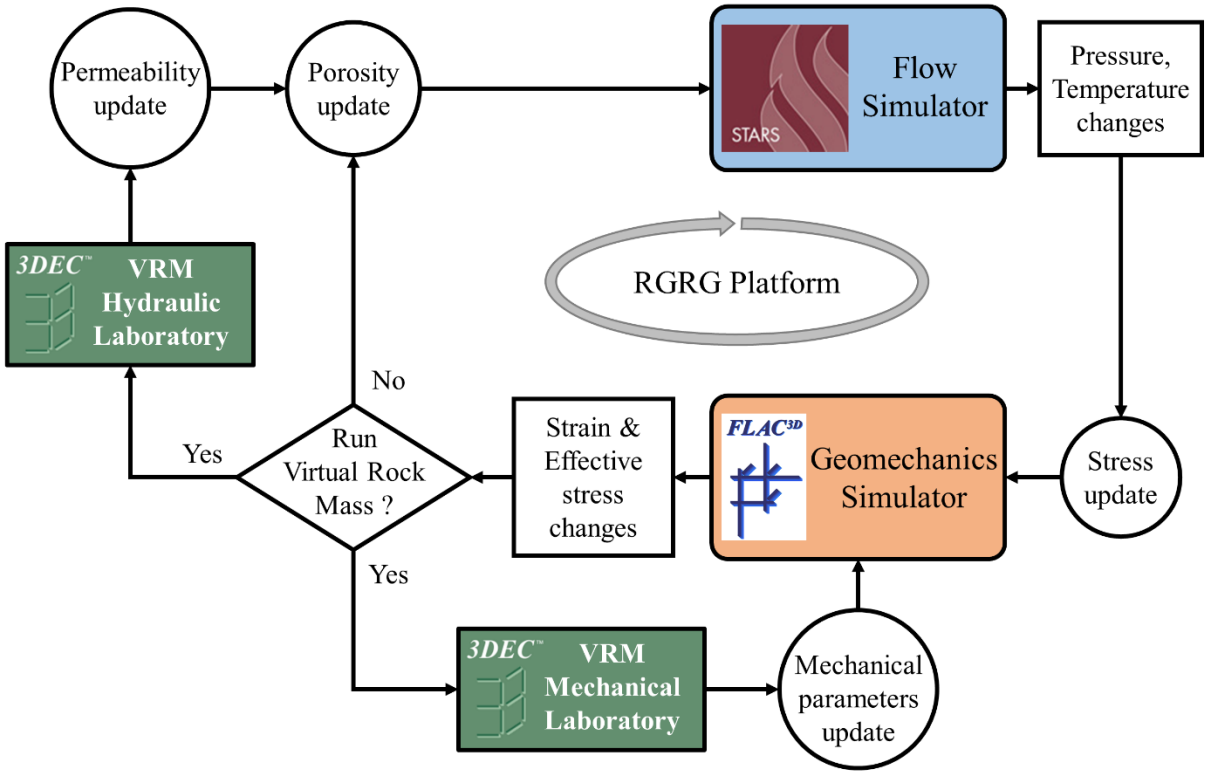

Figure 4.8—Diagram of the sequential coupling scheme between STARS and FLAC^{3D} controlled by the RGRG coupling platform, including the hydraulic and mechanical modules of the VRM laboratory. The coupling cycle starts with the flow simulator, according to the fixed stress split method. (Note that this figure corresponds to an expanded version of Figure 2.1).

The coupling process begins with the generation of the numerical grids for the flow and mechanical models by the RGRG coupling platform, which also populates the simulators with the input data and controls the exchange, update and storage of coupling parameters throughout the sequential simulation. Both numerical grids, that represent the discretization regions of the fractured reservoir, are compatible with each other and structured as in a box of sugar cubes. After the structured numerical grids are created, the initial mechanical problem is solved in FLAC^{3D} to establish the initial equilibrium state and determining the resultant effective stress field for each reservoir region. Then, the mechanical and hydraulic modules of the VRM laboratory are executed

to compute the equivalent continuum parameters under the current effective stresses for each region partially or totally cut by fractures, corresponding to a DFN previously generated with the 3DEC code (or imported into the VRM lab from another DFN alternative source). Thus, the equivalent anisotropic permeability and orthotropic parameters calculated in the VRM lab are ready to be updated in the reservoir simulator STARS and also in the continuum geomechanical simulator FLAC^{3D}, respectively. In addition, the Biot effective stress coefficient tensor can also be updated using the new elastic parameters. Once the mechanical and hydraulic equivalent continuum parameters are updated in the numerical simulators, the sequential coupling scheme is started through the RGRG coupling platform and carried out until the last reservoir simulation stage is reached (according to the procedure introduced in Chapter 2). During the coupled reservoir geomechanical simulation, the equivalent anisotropic parameters can be updated at specific simulation stages in all the fractured reservoir regions or only in those where the change in the effective stress field reaches a certain tolerance.

The coupling strategy and methodology implemented in the RGRG coupling platform is described in the following steps:

1. Generation of numerical grids for flow and mechanical simulators by the RGRG coupling platform, which also populates both models with the required input data. Run the geomechanical simulator until equilibrium to establish the initial effective stress field.

2. The equivalent continuum parameters of the discretization regions representative of the fractured reservoir are computed using the mechanical and hydraulic modules of the VRM numerical laboratory. The current effective stress field is installed during the required initial equilibrium of the VRM lab models to account for the nonlinear behavior of the DFN fractures.

3. The equivalent permeability and orthotropic parameters are updated in the reservoir simulator STARS and in the continuum geomechanical simulator FLAC^{3D}. The orthotropic

parameters are used to update the Biot effective stress coefficient tensor as required. The RGRG coupling platform starts the sequential coupling scheme (see Chapter 2).

4. The thermal and fluid flow problem is solved by STARS. The changes in pore pressure and temperature obtained in the reservoir model are stored in the RGRG platform. The stress increment induced by these changes is calculated and added to the stress in the FLAC^{3D} model.

5. The mechanical problem is solved by FLAC^{3D} and the resulting stress and strain increment tensors are stored. The pore compressibility, volumetric thermal expansion coefficient and porosity change corresponding to the correction parameters of the porosity function in the STARS model are calculated and updated through the RGRG platform.

6. The VRM lab can be run at specific simulation stages to compute the equivalent permeability and orthotropic parameters of all reservoir regions or at those regions where the change in the mean effective stress (i.e., $\sigma'_{kk}/3$) becomes greater than a user defined effective stress tolerance. These new parameters are updated in their corresponding simulators. The sequential scheme is resumed from step 3 and a new coupling cycle is started again.

The previous coupling sequence from step 3 to step 6 is repeated until the last reservoir geomechanical simulation stage is computed.

4.5 Numerical cases and results

4.5.1 Initial mechanical analysis

A mechanical analysis is conducted to assess the capability of the proposed methodology implemented in the RGRG coupling platform for modelling and capturing the deformation behavior of a fractured rock mass through equivalent continuum orthotropic parameters.

4.5.1.1 Model geometry, conditions and parameters

The numerical case presented here studies the deformation of a hypothetical fractured caprock due to the change in pore pressure induced by a steam chamber developed in a fictitious reservoir. The dimensions of the model are 200 m long, 25 m wide and 40 m height in the x, y and z directions, respectively. The model domain is discretized in cubes of 5 m side, resulting in a grid of 40×5×8 cubic regions. The six intermediate layers from the total eight of the discretization are used for modelling the caprock, which is represented as a constant horizontal layer of 30 m height with the upper and lower limits at -150 m and -180 m depths (Figure 4.9). For simplicity, a non-uniform change in pore pressure is directly assigned to the bottom layer to simulate the impact of

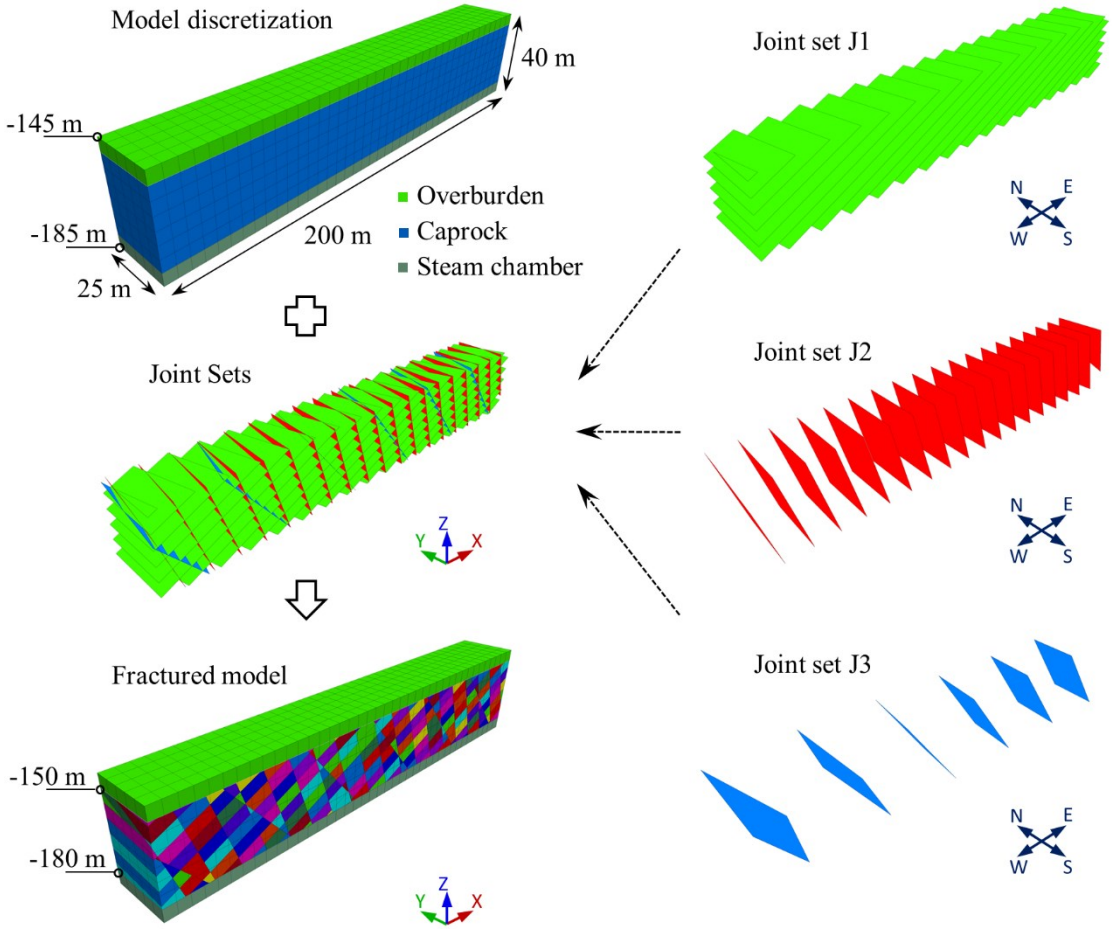

Figure 4.9—Model geometry and joint sets used for the initial mechanical case.

the steam chamber on the deformation behavior of the caprock. A density of 64200 kg/m^3 is assigned to the 5 meters height top layer of the model discretization to simulate the equivalent gravitational load corresponding to 150 m height of overburden with density 2140 kg/m^3. This last density is assigned to the bottom and caprock layers. The gravity is set to 9.81 m/s^2. The initial vertical stresses result from the gravitational loads following a 21 kPa/m gradient. The initial horizontal stresses and their increase with depth are set in the model with the gradients of 24 kPa/m for the stresses in the x-direction and 29 kPa/m for those in the y-direction. The initial stresses oriented in the coordinate axes of the model are assumed as principal stresses. The displacements of the vertical boundaries are only constrained in their normal directions (i.e., roller boundaries). Moreover, the displacements are fixed in all directions in the bottom boundary, while the top boundary is totally unconstrained.

In the model, the caprock is considered fractured by a DFN, consisting of three fully persistent joint sets as shown in Figure 4.9. The intact material is modelled as isotropic and linear elastic with Poisson's ratio of 0.35 and Young's modulus of 500 MPa. Table 4.1 shows the assumed geometry, orientation and mechanical parameters corresponding to each of the three joint sets, which are assigned a linear elastic joint constitutive model. To simulate the impact of the changes in pore pressure developed in the steam chamber, the stresses in the bottom layer are increased after reaching the initial equilibrium by adding pressure increments up to 10 MPa, following a non-uniform load profile in the x-direction (Figure 4.10).

Table 4.1—Input parameters of the joint sets for the initial mechanical case.

Parameter	**J1**	**J2**	**J3**
Dip angle , (°)	25	70	50
Dip-direction , (°)	260	100	110
Normal stiffness k_n , (MPa/m)	100	50	50
Shear stiffness k_s , (MPa/m)	10	20	20
Fracture spacing , (m)	5	10	25

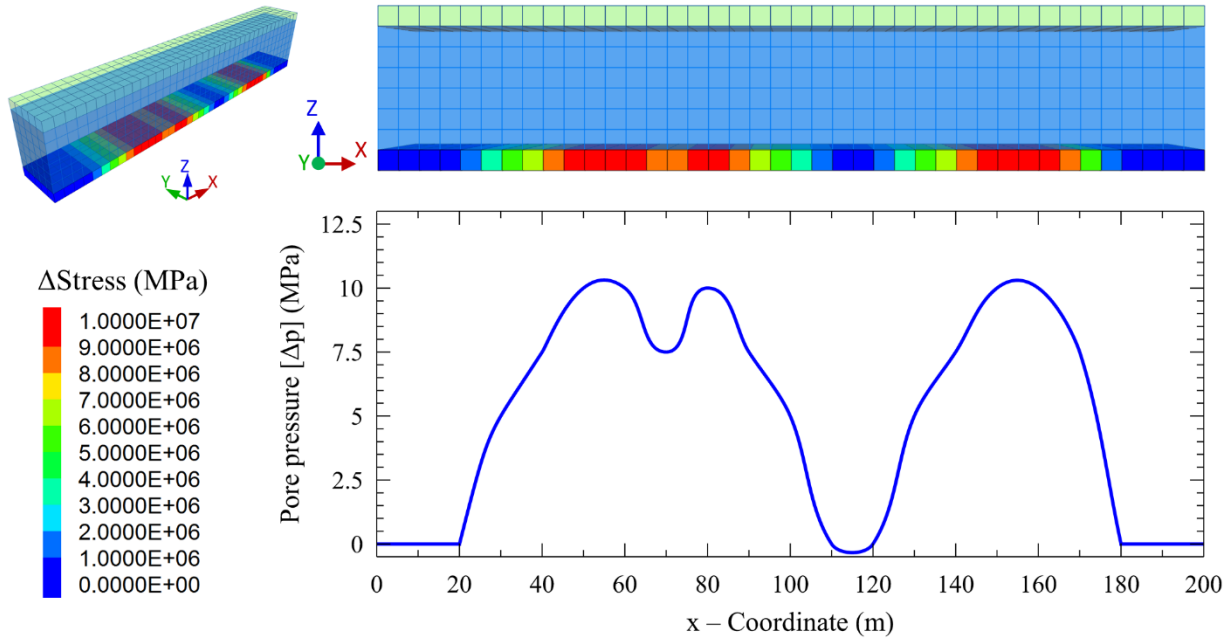

Figure 4.10—Pressure increments applied at the bottom layer to simulate the impact of the pore pressure changes developed in the steam chamber, following a non-uniform load profile in the x-direction. Note that the pressure increments are applied uniformly along the y-direction (see the model in perspective view at the top-left corner).

4.5.1.2 Equivalent continuum and discontinuum scenarios

To evaluate the presented methodology, three simulation scenarios are considered. A discontinuum model with explicit joint sets is analyzed first using the 3DEC code. The obtained results are compared with a continuum FLAC^{3D} simulation, which is assigned the equivalent orthotropic parameters determined for each cubic fractured region of the model discretization using the VRM laboratory. During the homogenization process, the orientations of the orthogonal planes of symmetry are determined and the equivalent orthotropic parameters are calculated from the compliance matrix rotated to the principal directions of material symmetry. That way, the influence of the non-orthogonal components of the compliance matrix (i.e., the off-diagonal matrix coefficients, excluding those in the top-left 3×3 submatrix which involve the Poisson's ratios) is taken into account (see Chapter 3.4.1.3). On the other hand, it is customary to calculate the equivalent continuum parameters from the compliance matrix directly obtained in the coordinate axes of the model or, in the case of analytical homogenization methods, in the Cartesian coordinate system, where the contribution of the non-orthogonal components is totally neglected. Thus, to

assess the impact of the non-orthogonal components on the deformation behavior of the caprock, another FLAC^{3D} continuum model is analyzed, assuming the principal directions of anisotropy oriented in the model axes direction, with the equivalent parameters determined from the compliance matrix directly measured in the coordinate system of the model.

4.5.1.3 Numerical analysis results

The vertical displacement fields developed in the caprock obtained in the simulations of the three analyzed scenarios, discontinuum and continuum models, are plotted in Figure 4.11. As expected, the deformation behavior of the caprock observed in the 3DEC discontinuum model is clearly anisotropic due to the influence of the three explicit joints sets. This behaviour is also captured in the FLAC^{3D} continuum model with equivalent orthotropic parameters determined after

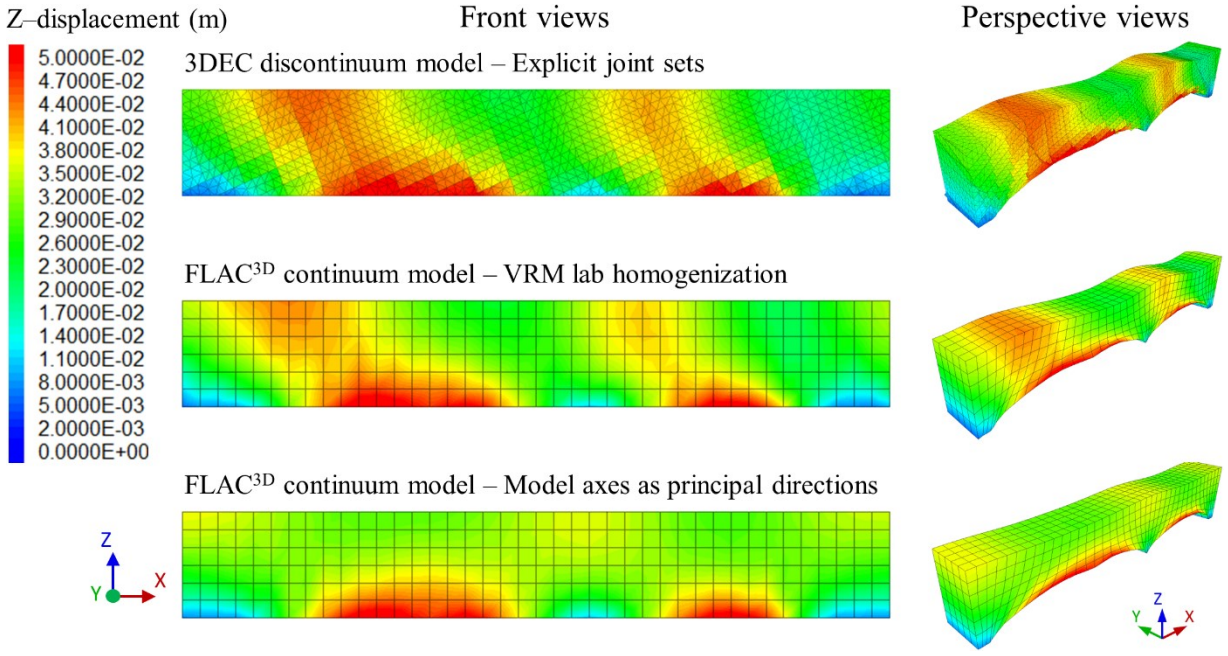

Figure 4.11—Vertical displacement fields developed in the caprock corresponding to the three analyzed simulation scenarios, the 3DEC discontinuum model and the two FLAC^{3D} continuum models, one with the VRM laboratory equivalent orthotropic parameters and the other with the parameters determined from the non-rotated matrix assuming the model axes as principal directions of material symmetry. Note that the displacement contours are plotted in 1 mm increments and the perspective views show magnified deformations.

the homogenization process using the VRM laboratory. Conversely, the anisotropic deformation is not observed in the continuum model with the orthotropic parameters calculated directly from the non-rotated compliance matrix, neglecting the non-orthogonal components. Furthermore, the displacement orientation and magnitudes are in good agreement between the discontinuum simulation and the continuum model with VRM laboratory equivalent parameters, where the largest discrepancies in the observed displacement magnitudes are lower than 4% (i.e., smaller than 2 mm difference in 50 mm magnitudes). However, only the vertical displacement magnitude is fairly captured just over the steam chamber at the bottom of the continuum model that assumes the model axes as principal directions of material symmetry, disregarding the non-orthogonal components of the compliance matrix.

4.5.2 Hydro-Mechanical coupled analysis of a fractured formation with a DFN

A fractured rock formation with an embedded DFN is analyzed here, using the proposed coupling methodology, to study the effect of the hydro-mechanical behavior of fractures implicitly included in reservoir geomechanical coupled simulations.

4.5.2.1 Geometry and properties for the flow and geomechanical models

The modelled reservoir formation consists in a volume of 200×100×100 m^3 (in the coordinate directions x, y and z) which is discretized for the flow simulator in a grid of 20×10×10 cubic elements. For the geomechanical simulator, the formation is extended by the addition of a top layer of zones of 10 m height, an overburden of 50 m, an underburden of 50 m and sideburdens of 50 m each, giving a model of 300×200×210 m^3 discretized in 30×20×21 cubic elements or zones (of 10 m^3 each). Disregarding the top layer of zones in the geomechanical grid, both models are centered at the origin in the horizontal directions and at a depth of -2600 m in the vertical direction (Figure 4.12). The parameters of the fluid and intact material used in the coupled simulations are summarized in Table 4.2. The properties for the mechanical and flow models are based on the reservoir formation reported in Rangriz Shokri et al. (2019).

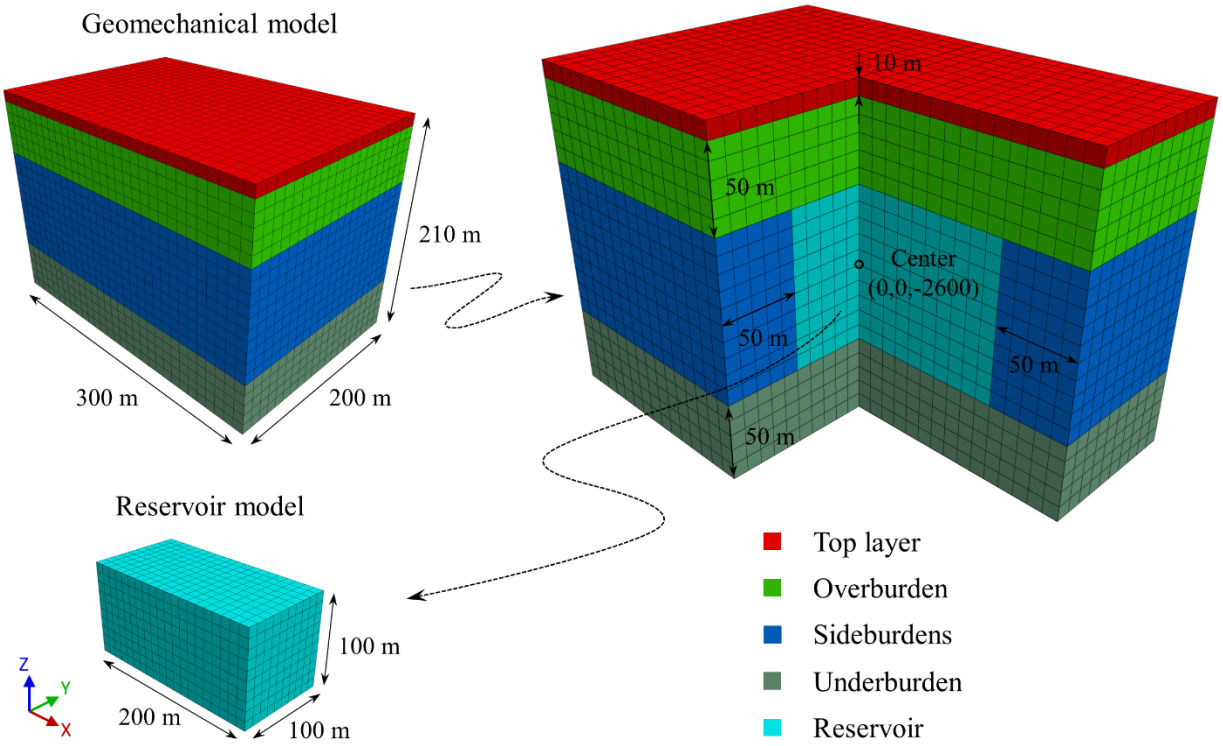

Figure 4.12—Model domain implemented in the RGRG platform for the numerical grid generation of the rock formation in the geomechanical and the reservoir simulators. The right side of the picture shows the dimensions of the top layer, overburden, underburden and sideburdens of the geomechanical model enclosing the reservoir model.

4.5.2.2 Initial and boundary conditions

All the reservoir boundaries are set to impermeable in the flow simulator. The vertical boundaries of the geomechanical model are fixed in their normal direction (i.e., roller boundaries) and the bottom boundary is totally fixed in all directions; conversely, the top boundary is free to move in any direction. The gravitational loads are included in the simulations by setting a gravity of 9.81 m/s^2. In the geomechanical grid, the zones of the top layer just above depth -2500 m are set with a density of 650000 kg/m^3 to simulate the equivalent load of an overburden of 2500 m height and density 2600 kg/m^3 on the level -2500 m. The initial *in situ* stress field has been installed in the model assuming the principal stresses aligned with the coordinate axes, where the maximum, intermediate and minimum stresses are oriented in the Z, X and Y axes, respectively. In the model, the principal stresses increase with depth due to the gravitational gradient. The vertical stresses result from the load of the top layer of high density zones and the gravitational load of the

remaining zones, which are modeled with a bulk density of 2552 kg/m^3 (see Table 4.2). The ratio between the maximum horizontal to vertical stress is set to 0.72 (in the x-direction), while the minimum horizontal to vertical stress ratio is set to 0.52 (in the y-direction). Thus, the stresses at the center of the model, at -2600 m depth, result in $\sigma_z = \sigma_v = 66.3$ MPa, $\sigma_x = \sigma_H = 47.7$ MPa, $\sigma_y = \sigma_h = 34.5$ MPa. Additionally, the initial pore pressure increases gradually with depth in the model, following the pressure gradient of 9.81 kPa/m. The pore pressure calculated at the center of the model is $p = 25.5$ MPa, assuming fully saturated conditions.

Table 4.2—Intact material and fluid properties.

Property	**Value**
Young's modulus E , (GPa)	26
Poisson's ratio v , (-)	0.2
Porosity ϕ , (%)	3
Biot's coefficient b , (-)	0.75
Fluid bulk modulus K_f , (GPa)	2.3
Fluid viscosity μ , (Pa·s)	0.001
Permeability k , (m^2)	$1.974 \cdot 10^{-18}$
Solid density ρ_s , (kg/m^3)	2600
Fluid density ρ_f , (kg/m^3)	1000
Bulk density * ρ_b , (kg/m^3)	2552
* The bulk density is calculated as: $\rho_b = \rho_s (1-\phi) + \rho_f \phi$	

4.5.2.3 Embedded fracture network in the rock formation

The system of fractures embedded in the rock formation is modeled using the DFN module of the 3DEC code (Itasca 2016). The fractures are considered as circular structural features and arranged in three joint sets. In the DFN model, the circular fractures of the joint sets are assumed uniformly distributed over the model domain. They are oriented with the dip and dip-direction angles following a Gaussian distribution. A power law distribution with a scaling exponent of 4 is used for modelling the fracture size. The minimum and maximum fracture diameters in the model are 5 m and 150 m, respectively. The fractures are generated so that the reservoir volume domain

contains a total of 1800 embedded fractures, where 700 fractures correspond to joint set J1, 600 fractures to joint set J2 and 500 to joint set J3 (Figure 4.13). After fracture generation, the average diameter length considering all fractures resulted in 13.5 m. A summary of the parameters used for the DFN generation in 3DEC is shown in Table 4.3.

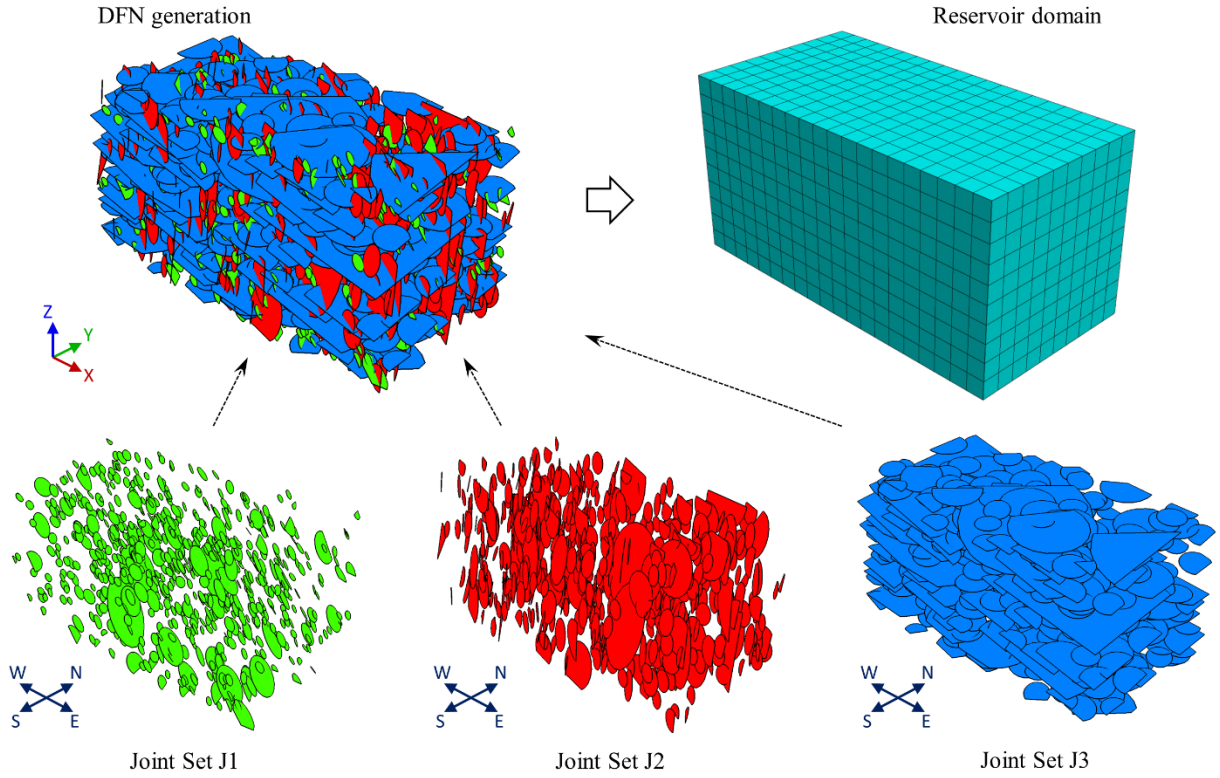

Figure 4.13—Generation of the circular fractures embedded in the reservoir volume domain and single plots of the three DFN joint sets.

Table 4.3—Input parameters for the generation in the 3DEC DFN module of the joint sets embedded in the rock formation.

DFN		**Orientation (Gaussian distribution)**		**Fracture size (power law distribution)**	
Joint set	**Number of joints**	**Dip angle (°) (Mean, SD)**	**Dip-direction (°) (Mean, SD)**	**Scaling exponent α**	**Fracture diameter (m) (Minimum - Maximum)**
J1	700	(60, 5)	(60, 10)	4	(5 - 50)
J2	600	(80, 5)	(210, 10)	4	(10 - 100)
J3	500	(15, 5)	(130, 10)	4	(15 - 150)

4.5.2.4 Analyzed coupled cases

Based on the analyses presented in Rangriz Shokri et al. (2019), for the numerical cases investigated here, a fluid injection is simulated close to the center of the reservoir flow model. The injection point of the horizontal well is located at the zone with centroid coordinates at x = -5 m, y = -5 m and z = -2605 m depth (Figure 4.14). A bottomhole pressure of 38.5 MPa is assigned to the injector well of 10 cm diameter, leaving a pore pressure increment of 13 MPa between the injection point and the fractured formation. The injector well is kept opened during the whole flow simulation.

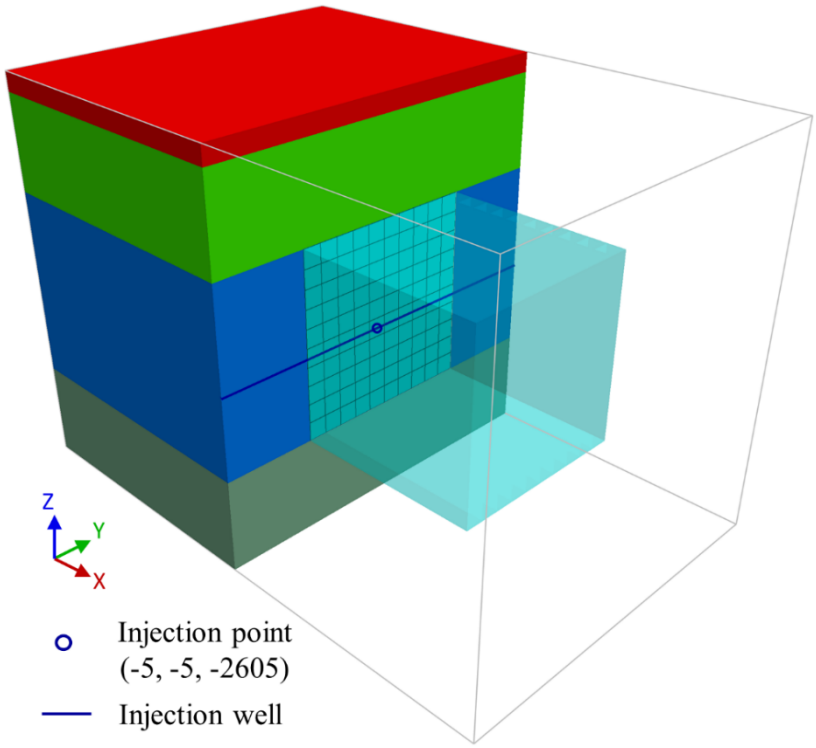

Figure 4.14—Geomechanical and reservoir domains showing the injection well perforated in the flow model and the injection point location with the coordinate units given in meters.

To analyze several simulation scenarios, different parameters have been assigned to the joint constitutive model of the fractures during the homogenization process in the mechanical and flow modules of the VRM lab. The first simulation case (Case 1) assumes the fracture mechanical

behavior as linear elastic (LE) with a constant joint shear stiffness of $k_s = 7.56$ GPa/m and normal stiffness of $k_n = 18$ GPa/m, where the minimum normal stiffness governing the normal deformability behavior of fractures under tensile stresses are determined through Eq. (4.4). A proportionality factor of $\lambda = 0.001$ is used in Eq. (4.5) to determine the maximum normal stiffnesses. For simplicity, the average fracture radius length of the DFN fractures is used to calculate the minimum normal stiffness $k_n^{\min}$ for all the fractures. Using the intact rock elastic parameters in Table 4.2 and the average radius of 6.75 m (from the measured average diameter length of 13.5 m) results in a $k_n^{\min}$ of 2.4 GPa/m. For modelling the fluid flow through the fractures, the change in mechanical aperture is considered the same as the change in hydraulic aperture. The initial hydraulic aperture a_0 is set to 0.4 mm in all the DFN fractures and the seating load *A* at zero joint closure is set to 101325 Pa (that is, 1 atm). The hydraulic aperture bounds for computational efficiency during the simulation (Figure 4.3), i.e., the residual value a_{res} and a maximum aperture $a_{\max}$ are set to 0.1 mm and 3 mm, respectively.

For the second simulation case (Case 2), a nonlinear elastic (NonLE) joint constitutive model is assigned to the normal deformation behavior of the fractures under effective compressive stresses. Setting the *B* parameter in Eq. (4.2) to 18.9 (1/mm) gives the following linear relationship $k_n = 18.9\,\sigma'$ between the joint normal stiffness and the effective compressive stress, and consequently the exponential expression $\sigma' = 0.101325\, e^{18.9 u_j}$ that describes the nonlinear joint closure under compression (Eq. (4.1)). Note that the stresses in the previous expressions correspond to effective stresses, since the RGRG platform sends the effective stresses determined in the geomechanical simulator (FLAC^{3D}) as input for the VRM lab. The rest of the mechanical and fluid flow parameters are the same as in the previous LE Case 1. Figure 4.15 shows the joint constitutive models assigned to both simulation cases and the initial hydraulic aperture at zero closure under 1 atm normal load. Observe that since the maximum bound is 3 mm, only the residual hydraulic aperture limit is shown in the plot due to the scale of the joint closure axis.

A third case (Case 3) is modelled with the same parameters as the previous NonLE Case 2; however, in this case the mechanical and flow parameters are updated during the simulation.

Additionally, to assess the effect of the plastic deformation of the DFN fracture, two extra cases, 4 and 5, have been analyzed. These cases are modelled with the same parameters and properties as the second and third cases, respectively; however, the Mohr Coulomb-slip joint model (MC) available in 3DEC is assigned to the DFN joints. The plastic parameters of the MC joint constitutive model are summarized in Table 4.4 (see Itasca 2016 for details of the MC joint model). The residual properties are assumed the same as the initial input properties.

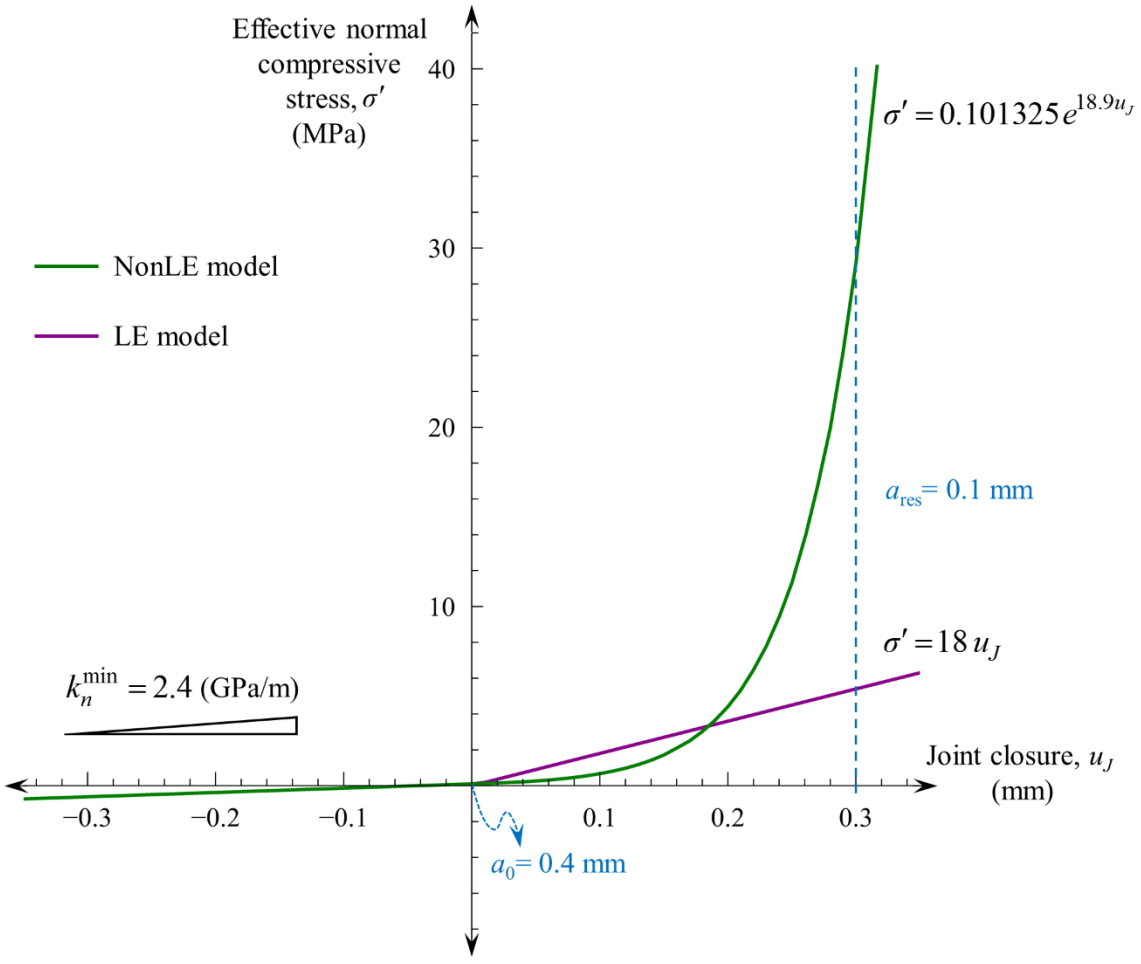

Figure 4.15—Joint constitutive models for the normal deformation behavior of fractures in the first (LE) and second (NonLE) simulation cases. The minimum joint stiffness of 2.4 GPa/m is the considered the same in both cases. The initial a_0 and residual a_{res} hydraulic apertures are shown at 0.0 mm and 0.3 mm joint closure, respectively. Note that the maximum hydraulic aperture $a_{max} = 3$ mm is omited since it is out of scale with respect to the joint closure axis.

Table 4.4—Plastic parameters for the Mohr Coulomb-slip joint model (MC) assigned to all the DFN joints in the Case 4 and Case 5.

Joint parameter	**Value**
Friction angle** φ , (°)	25
Cohesion c , (MPa)	0.5
Tensile strength σ_t , (MPa)	0.1
Dilation angle ψ , (°)	5
Zdilation * u_{cs} , (mm)	3

* Maximum shear displacement limit (Zdilation) after which the dilation angle is set to zero (Itasca 2016).

** Corresponds to the peak friction angle.

4.5.2.5 Simulation results

The development of pore pressure changes during the simulation at the injection point is shown in Figure 4.16 for the cases: linear elastic (LE), nonlinear elastic (NonLE) and nonlinear elastic with updated parameters (NonLE Updated). The results corresponding to Case 4 and Case 5 are not explicitly plotted in the previous figure, since they show virtually the same results of Case 2 (NonLE) and Case 3 (NonLE Updated) respectively. The equivalent hydro-mechanical continuum parameters are updated in the Case 3 for all the discretization fractured regions at the simulation stages of 40 and 200 hours of fluid injection. For the Case 1, the results show an earlier build-up in pore pressure at the injection point during the initial stages of the simulation; however, the final bottomhole pressure of 38.5 MPa is reached roughly 200 hours later than the other cases. The cases 2 and 3 show the same results at the initial stages, while the pore pressure is developed slightly earlier at the stages were the parameters are updated in Case 3 compared to Case 2. Figure 4.17 shows the cross-sectional views of the XZ-plane cutting through the injection point representing the pore pressure development after 10 hours for the cases 1, 2 and 4 (cases 3 and 5 are excluded, since the first parameters update is conducted in the simulations after 40 h of fluid injection). It can be seen that the build-up in pore pressure in the Case 1 is developed through the reservoir later than in the other cases. In addition, the Case 4 result is the same as the Case 2,

showing that the reservoir behaves as elastic at this simulation stage. The cross-sectional views of the build-up in pore pressure after 100 hours of fluid injection are presented for all the cases in Figure 4.18. There, the pore pressure is developed earlier in Case 3, following the Case 2 and later in the Case 1, which is in agreement with the results in Figure 4.16. Moreover, the cases 4 and 5 show a pore pressure build-up slightly earlier than case 2 and 3 respectively.

The displacements measured at three points located at coordinates (50,0,-2600), (0,50,-2600), (0,0,-2550), that is, at +50 m from the model center (0,0,-2600) in the x, y and z directions are shown in Figure 4.19, Figure 4.20 and Figure 4.21. In those figures, the vertical displacements (roughly 20 mm) are larger than the horizontal displacements. Also, the displacements in the x-direction (about 2.3 mm) are smaller than those in the y-direction (approximately 7.5 mm). Moreover, the horizontal displacements in the Case 1 are slightly larger than in cases 2 and 3. However, the vertical displacements are considerably larger in the Case 1 than in the other cases.

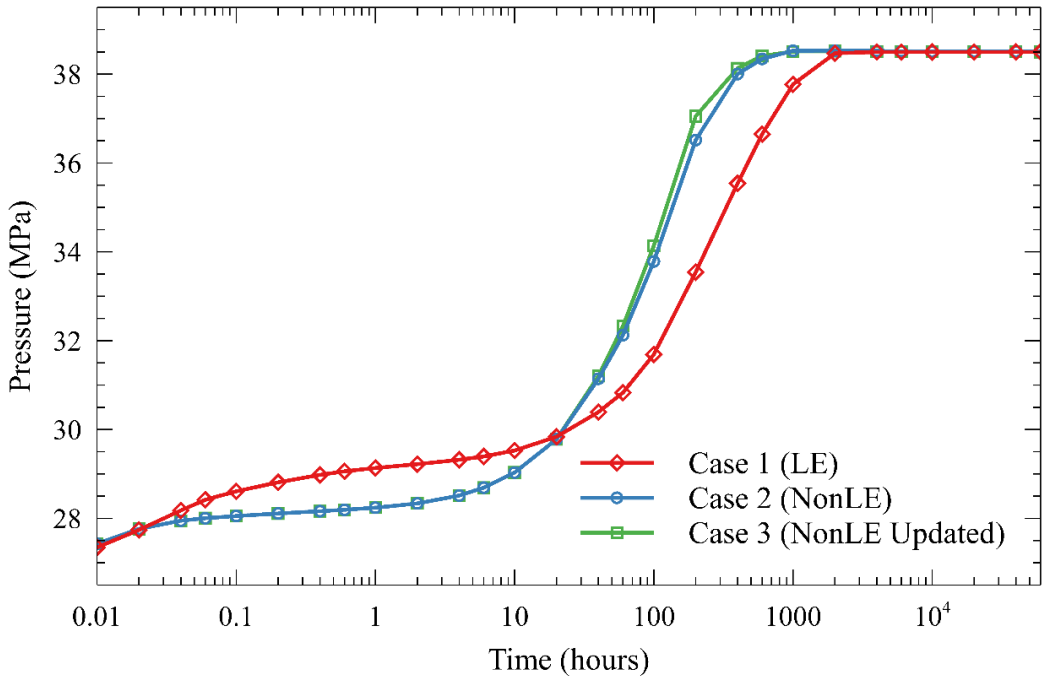

Figure 4.16—Evolution of the pore pressure measurements at the injection point (-5,-5,-2605) during the simulation for the linear elastic (LE) Case 1, the nonlinear elastic (NonLE) Case 2 and the nonlinear elastic with updated parameters (NonLE Updated) Case 3.

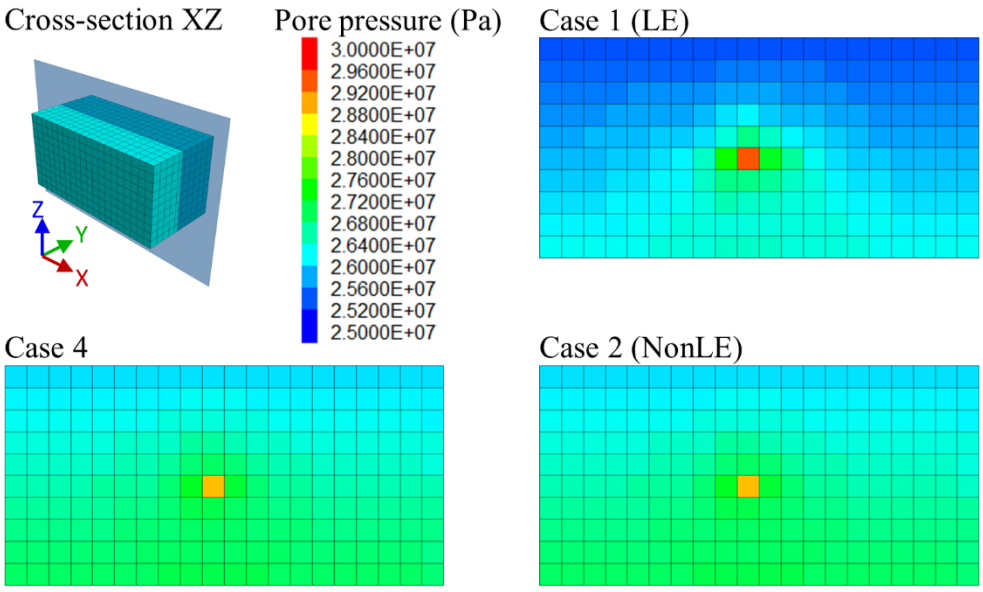

Figure 4.17—Cross-sectional views at XZ-plane of the pore pressure changes developed after 10 hours of fluid injection in Case 1, Case 2 and Case 4.

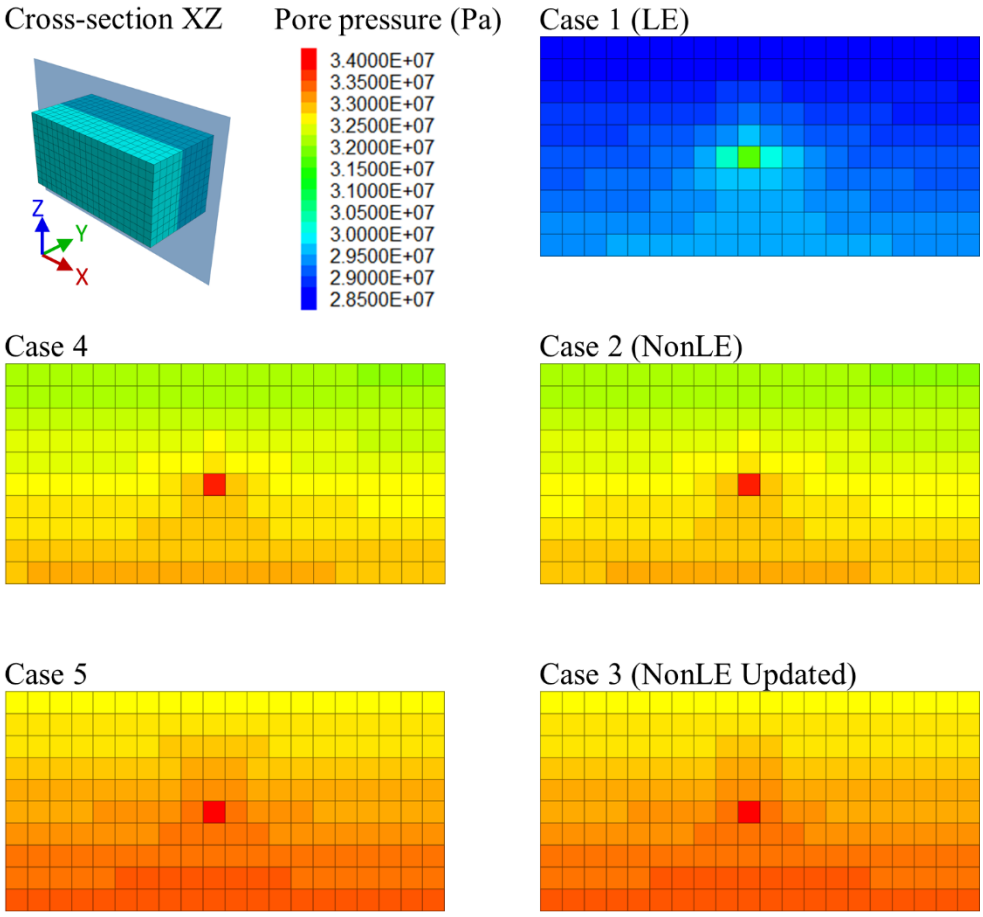

Figure 4.18—Cross-sectional views at XZ-plane of the pore pressure changes developed after 100 hours of fluid injection in all the analyzed cases.

To study the influence of the orientation of the principal directions of material symmetry on the deformation behavior of the fractured formation, several cross-sectional views of the reservoir displacement fields resulting after 2000 hours of fluid injection are shown in Figure 4.22, Figure 4.23 and Figure 4.24. The anisotropic deformation is clearly not aligned with the model coordinates in the displacement field in the x-direction of the Case 1 (Figure 4.22), but less evident in the y-direction (Figure 4.23) and vertical displacements (Figure 4.24). On the other hand, the displacements field in cases 2 and 3 are virtually oriented in the coordinate system of the model.

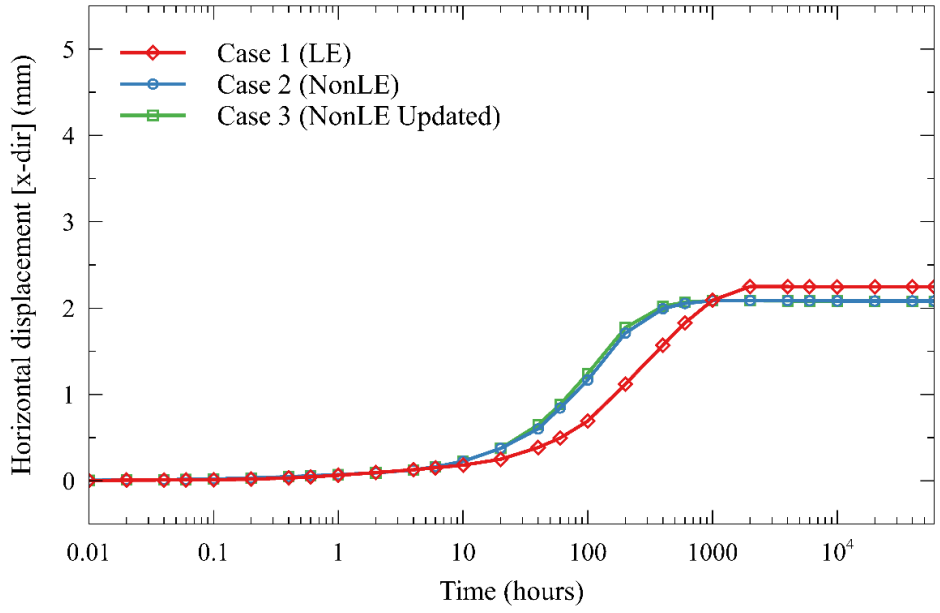

Figure 4.19—Evolution of horizontal displacements in the x-direction at the point located at coordinates (50,0,-2600), i.e., at x=50m from the model center, for Case 1 (LE), Case 2 (NonLE) and Case 3 (NonLE Updated).

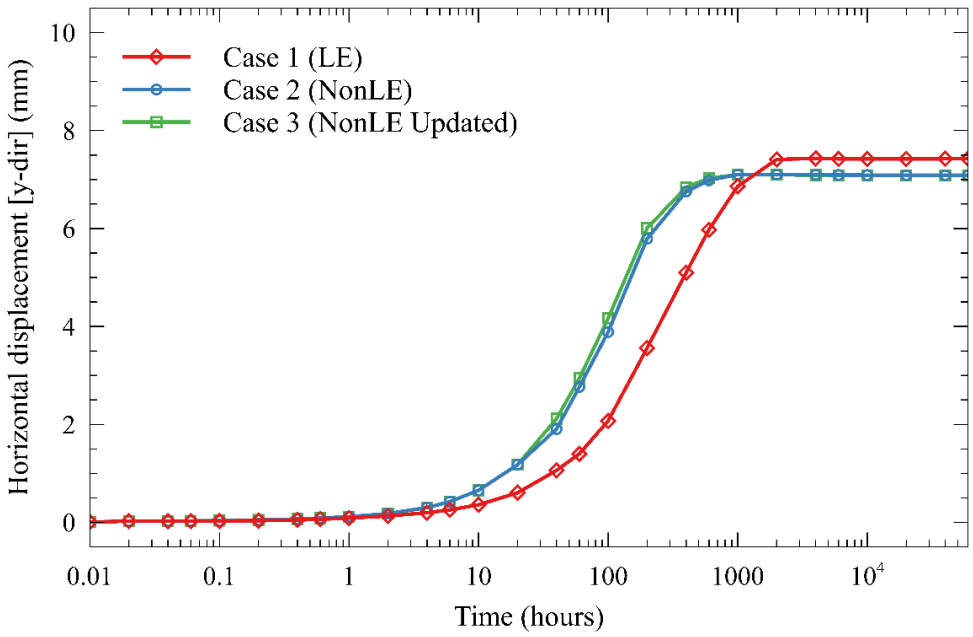

Figure 4.20—Evolution of horizontal displacements in the y-direction at the point located at coordinates (0,50,-2600), i.e., at y=50m from the model center, for Case 1 (LE), Case 2 (NonLE) and Case 3 (NonLE Updated).

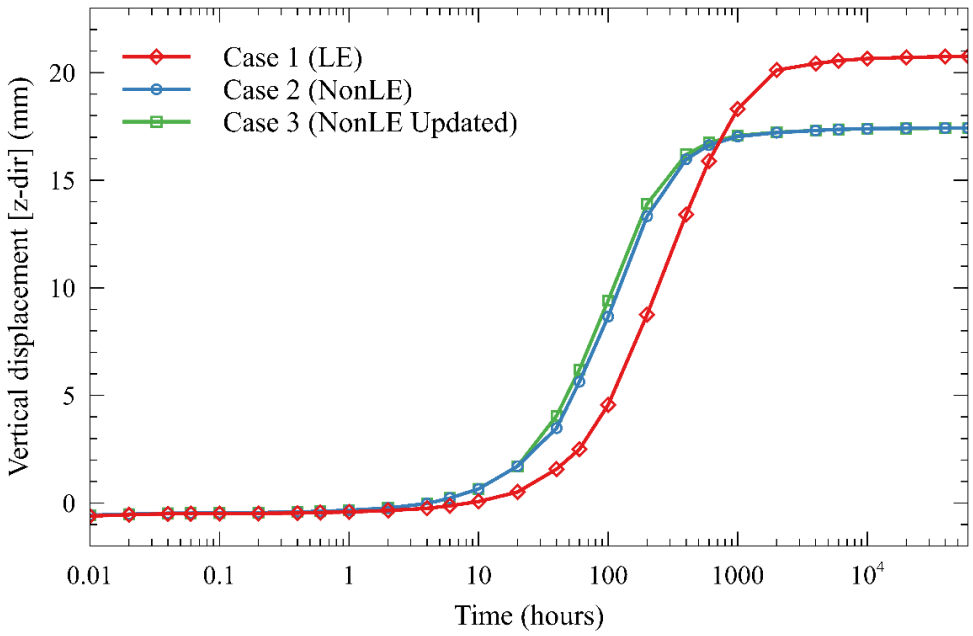

Figure 4.21—Evolution of vertical displacements (z-direction) at the point located at coordinates (0,0,-2550), i.e., at 50m in the z-direction from the model center, for Case 1 (LE), Case 2 (NonLE) and Case 3 (NonLE Updated).

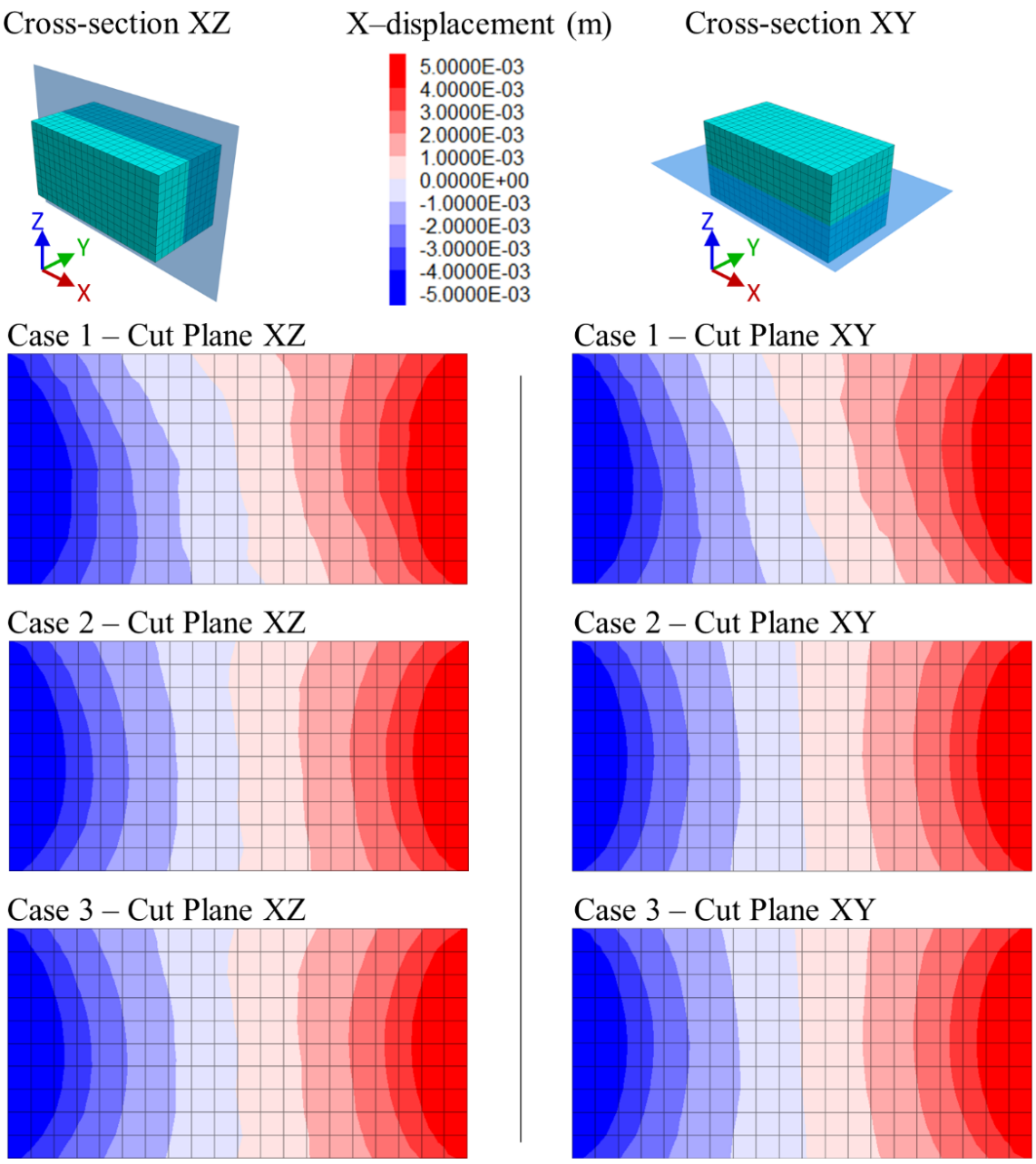

Figure 4.22—Cross-sectional views of the horizontal displacement fields in the x-direction developed after 2000 hours of fluid injection in Case 1, Case 2 and Case 3.

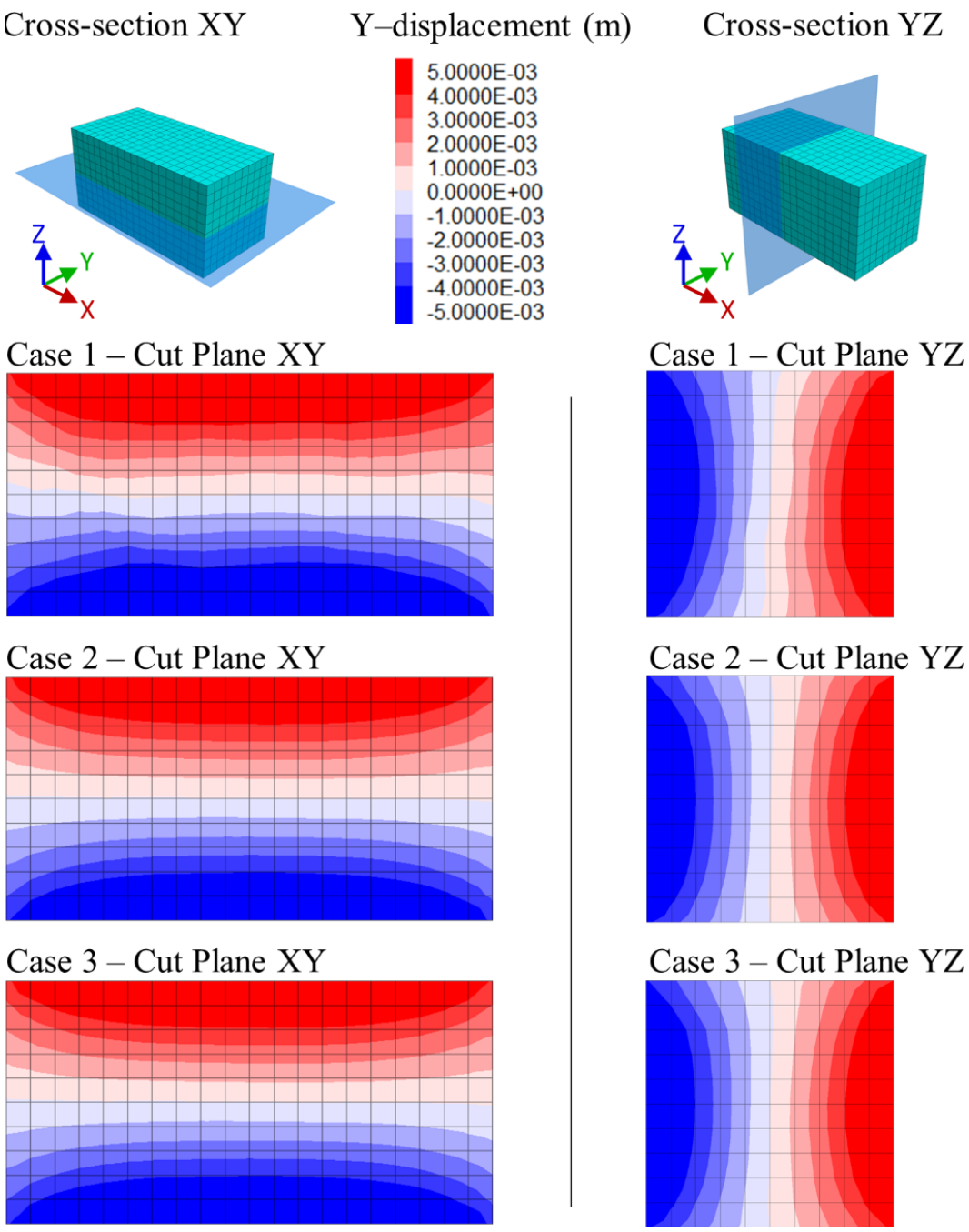

Figure 4.23—Cross-sectional views of the horizontal displacement fields in the y-direction developed after 2000 hours of fluid injection in Case 1, Case 2 and Case 3.

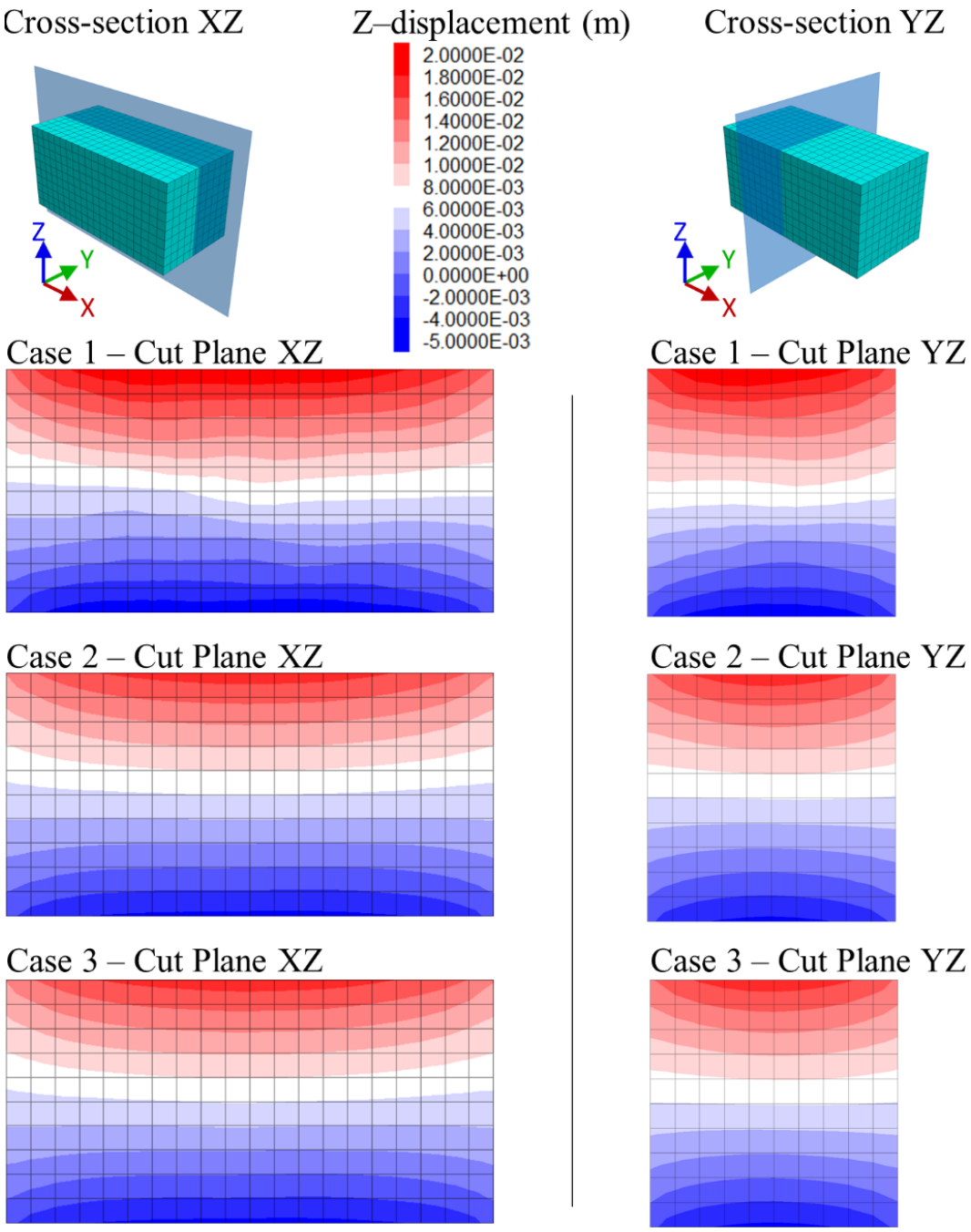

Figure 4.24—Cross-sectional views of the vertical displacement fields developed after 2000 hours of fluid injection in Case 1, Case 2 and Case 3.

4.6 Discussion and limitations

The influence of the three joint sets in the deformability of the rock mass in the initial mechanical analysis is revealed in the notable anisotropic behavior observed during the 3DEC discontinuum simulation. Moreover, the orientation of the resultant anisotropic deformation is not aligned with the coordinate system of the model, even though the displacements are constrained in the normal direction to the vertical boundaries. The results of the displacement fields obtained in the FLAC^{3D} continuum model with the VRM laboratory equivalent orthotropic parameters fairly capture the displacement magnitudes and clearly reflect the anisotropic deformation of the 3DEC model. Furthermore, the vertical displacement fields observed in the three analyzed scenarios (Figure 4.11) also show that disregarding the non-orthogonal components of the compliance matrix —as customary— by assuming the model axes as principal directions of material symmetry, results in misleading deformation orientations and behaviors of the fractured rock formation. These results show the capability of the proposed methodology implemented in the RGRG coupling platform for modelling and capturing the deformation behavior of a fractured rock mass through equivalent continuum orthotropic parameters.

The evolution of displacements obtained at the three measurement points in the hydro-mechanical coupled cases (Figure 4.19, Figure 4.20 and Figure 4.21) shows that the smallest deformations are oriented in the x-direction, followed by those in the y-direction, whereas the largest deformations are found in the z-direction. The observed large vertical displacements are due to the presence of the large-size sub-horizontal fractures corresponding to the joint set J3 (Figure 4.13; Table 4.3); while, the intermediate-size circular fractures of the sub-vertical joint set J2 are responsible of the moderate y-displacements, since their joint plane orientations are closer to the ZX-plane. The low-size inclined fractures of the joint set J1 are oriented in a way that their contribution to the deformability mainly affects the vertical and x-displacements. Consequently, the overall deformation response of the equivalent orthotropic discretization regions in the geomechanical simulator is more compliant in the vertical direction and stiffer in the x-direction.

The effect of the non-linear fracture deformability is also observed in the displacement evolutions, where the linear elastic Case 1 shows the largest displacements after 2000 hours of fluid injection compared to the other cases that present virtually the same final displacements. This behavior is due to the constant normal stiffness of 18 GPa/m assigned to the fractures during the determination of the equivalent continuum parameters with the VRM laboratory for the LE Case 1. Furthermore, the joint normal stiffnesses assigned to the fractures in the nonlinear cases are significantly stiffer, since, according to Figure 4.15, the effective stress fields input to the VRM lab result in effective normal compressive stress levels (acting on the fractures) lying on the steeper side of the exponential curve. Note that the effective normal stress level required to obtain the normal stiffness of 18 GPa/m (as in the Case 1) in the nonlinear exponential function used in the cases 2 and 3 is roughly about 1 MPa; while the minimum principal effective stress at initial conditions and model center is considerably much larger (approximately 15 MPa, accounting for the initial stress field, pore pressure and Biot effective stress coefficient). In addition, since the pore pressure increases during the simulation, the effective stresses decrease, leading to joint normal stiffnesses during the parameters updated in the NonLE Updated Case 3 slightly lower than those in the NonLE Case 2. These differences in joint normal stiffnesses imply equivalent continuum parameters more compliant in the Case 1 and stiffer in the cases 2 and 3. Also, the deformability parameters of the equivalent continuum regions are found closer to the intact rock properties, since the number and size of DFN fractures included in the simulations have a mild influence in the rock mass deformation. Thus, the fracture influence on the update of the Biot's effective stress coefficient tensor is found negligible. As consequence of the stiffness differences between the linear elastic and nonlinear elastic cases, the cross-sectional views of the reservoir displacement fields resulting after 2000 hours of fluid injection (Figure 4.22, Figure 4.23 and Figure 4.24) show a clear anisotropic deformation behavior which is oriented in the coordinate system of the model for the stiffer Case 2 and Case 3, while it is not aligned with the model axes for the more compliant Case 1.

The different deformability behaviors of the DFN fractures have an important influence in the equivalent permeability parameters and therefore in the pore pressure development throughout the reservoir in the analyzed cases. In general, large joint normal stiffnesses prevent significant joint closures, and at the same time avoid large changes in hydraulic apertures. In the Case 1, the DFN fractures are virtually closed under the initial effective stress field; and thus, all of them reach the residual hydraulic aperture limit of 0.1 mm (Figure 4.15). On the other hand, the hydraulic apertures of the fractures in the nonlinear elastic cases have values close but different to the residual aperture due to the high joint normal stiffnesses resultant from the effective stress field. The hydraulic apertures in the nonlinear cases with the updated parameters are slightly larger than the apertures in the other nonlinear cases, since the fractures are slightly more compliant during the parameters update due to the decrease of effective stresses (as already discussed above). The different changes in hydraulic aperture in the studied cases lead to lower equivalent permeability parameters determined in the VRM lab for the Case 1 and larger permeability parameters in the nonlinear elastic cases, where those cases with the permeability update show the largest values.

The effect of different equivalent permeability parameters can be observed in Figure 4.16, where the pore pressure at the injection point is developed slightly earlier in the NonLE Updated Case 3 than in the NonLE Case 2, followed by a significantly later build-up in pore pressure in the least permeable Case 1. Also, in agreement with the permeability parameters determined for the analyzed cases using the VRM laboratory, the cross-sectional views of the pore pressure build up throughout the reservoir (Figure 4.18) show a later pore pressure development in the Case 1, followed by the Case 2 and an earlier development in the Case 3. Additionally, the pore pressure build-up is slightly earlier in the Case 4 than in the Case 2. Similarly, the same observation applies for the Case 5 and Case 3. This response is explained by the fracture plastic deformation observed only in a small number of fractured regions during the hydraulic homogenization process conducted using the VRM lab. The small number of discretization regions with fractures at failure regime is due to the DFN fractures planes which are not critically oriented with respect to the effective stress field. The critical fracture orientation corresponds to the plane with zero (or 180

degrees) dip direction and 32.5 degrees dip angle for the initial effective stress field and the parameters of the Mohr Coulomb-slip joint model (Table 4.4). However, as the pore pressure evolves throughout the model the effective stresses decrease, increasing the number of fractures at failure regime during the permeability update in the Case 5. This is observed in the Figure 4.18 comparing the differences in pore pressure development between cases 5 and 3. The cases studied here show that even though the DFN fractures have a lower impact on the deformability of the rock mass, compared to the initial mechanical analysis, they can have an important effect on the equivalent permeability parameters and thus a significant impact in the hydraulic behavior of the fractured rock formation.

Although the hydraulic module of the VRM lab determines the full permeability tensor during the hydraulic homogenization process, the coupling methodology presented here disregards the off-diagonal components of the permeability tensor, since the flow simulator only allows to input the permeability components in the directions of the coordinate system of the model. The impact of this limitation on the hydraulic behavior of a fractured formation was observed by Rutqvist et al. (2013) during the analysis of a continuum model with homogenized parameters using the analytical Oda's crack tensor approach. They compared the continuum model results with alternative DFN model simulations and found that the flow rate measured in their continuum model was about 70% of the DFN model results when the homogenized regions contain few fractures; nevertheless, this discrepancy decreases with the increase in number of fractures. To overcome this limitation, the multi-point flux approximation technique (Aavatsmark 2002) can be implemented in the RGRG coupling platform.

The mechanical module of the VRM lab implemented in the coupling methodology presented here is developed for the homogenization of discontinuum regions assuming the intact rock and fractures are elastic, while the capability to include the effect of plastic fracture deformations is only implemented in the VRM lab hydraulic module. Thus, the continuum geomechanical simulator is limited to model the fractured formation through an equivalent orthotropic elastic material. This limitation is due to the challenging and time-consuming process

of determining the plastic failure characteristics such as defining a suitable anisotropic yield envelope and plastic potential in compression and tensile regimes for each discontinuum discretization region.

4.7 Summary and conclusion

A coupling strategy and methodology have been presented here for the inclusion of the hydro-mechanical behavior of discrete fracture networks in reservoir geomechanical simulations of fractured porous formations through numerical homogenization of rock mass discontinuum regions using a VRM laboratory. A nonlinear elastic joint constitutive model has been implemented in the VRM lab to simulate a deformation behavior of the DFN fractures closer to experimental observations and it has been verified against the analytical solution. The VRM hydraulic lab has been introduced and validated here against the analytical Oda's crack tensor approach, showing its ability for accurately determining the full equivalent permeability tensor of discontinuum models with embedded DFN fractures totally oblique to the coordinate system of the model.

A mechanical analysis has been conducted to assess the capability of the proposed methodology for modelling and capturing the deformation behavior of a fractured rock mass through equivalent continuum orthotropic parameters. The results show that the geomechanical continuum model with the VRM laboratory equivalent orthotropic parameters fairly captures the anisotropic deformation response of the fractured rock mass. Moreover, assuming the model axes as principal directions of material symmetry and therefore disregarding the non-orthogonal components of the compliance matrix, results in misleading deformation orientations and behaviors of the fractured formation.

The importance of modelling the DFN fractures as nonlinear elastic has been observed in the hydro-mechanical coupled simulations. The analyzed cases show that assigning a linear elastic constitutive model to the fractures results in larger mechanical joint closures and smaller hydraulic

apertures, since the fractures are assigned joint normal stiffnesses lower than those obtained in the nonlinear cases that take into account the impact of the effective confinement on the fracture normal deformation behavior. Therefore, modelling fractures as nonlinear elastic results in higher equivalent permeability parameters obtained through the hydraulic homogenization process and consequently leads to a faster build-up in pore pressure in the reservoir model. The update of equivalent continuum parameters as well as the plastic fracture deformations slightly improve the permeability and pore pressure development throughout the rock formation. Additionally, the DFN fractures included in the coupled simulations show a lower impact on the deformability of the rock mass compared to the initial mechanical analysis. As consequence, the fracture influence on the update of the Biot's effective stress coefficient tensor has been found negligible in these cases. Besides, the fractured reservoir shows a clear anisotropic deformation, which is oriented in the coordinate system of the model in the nonlinear cases while is not aligned with the model axes in the linear elastic case.

The reservoir geomechanical coupling methodology presented here involves a VRM laboratory for the numerical characterization of the mechanical and hydraulic equivalent continuum properties of fractured porous media. The VRM lab has been proposed as a numerical alternative to the traditional homogenization or upscaling processes using analytical methods, such as the Oda's crack tensor approach, which usually disregard the effect of fracture interactions and nonlinear fracture deformations. Finally, the VRM lab is capable of determining the equivalent continuum parameters of a fractured region including not only circular joints, but also fractures of any geometry and shape.

5 Conclusions

5.1 Summary

An explicit sequential coupling scheme has been presented for accurately modelling the thermo-poromechanical behaviour of anisotropic porous formations in complex reservoir geomechanical simulations. The scheme has been implemented in a numerical coupling platform developed at the University of Alberta by the reservoir geomechanics research group, RGRG. In this coupling platform two widely used commercial software, the reservoir simulator CMG – STARS and the continuum geomechanical simulator Itasca – FLAC^{3D}, are coupled together through a porosity correction strategy based on the fixed stress split method, which enjoys excellent stability and convergence properties. The generalized tensorial form of the Biot effective stress coefficient, disregarded in most numerical coupling methods, is rigorously included in the thermo-poromechanical coupling formulation. The explicit sequential coupling scheme implemented in the RGRG coupling platform has been successfully verified against analytical solutions of the mechanical and thermal consolidation problems for isotropic and anisotropic materials, as well as the Mandel's problem for transversely isotropic porous media, where the anisotropic effect of the Biot tensor and the symmetry plane orientation has been assessed.

The explicit inclusion in large reservoir geomechanical coupled simulations of all the structural features present in a fractured porous media usually leads to prohibitive simulation times, high demanding computational power and large memory requirements. To overcome these limitations, the fractured rock is often replaced by an equivalent continuum that implicitly includes the hydraulic and mechanical behaviour of the fracture network. Traditionally, upscaling or homogenization procedures based on analytical methods are used for the hydro-mechanical characterization of the equivalent continuum model; however the analytical approach usually disregards the effect of fracture interactions and nonlinear fracture deformations, as well as it is generally restricted to fractures of particular shape and geometry. Also, the analytical characterization usually relies on the existence of a representative elementary volume, REV, which

is not always granted particularly in rock formations with large disparity of fracture sizes. Therefore, a virtual rock mass numerical laboratory, VRM lab, has been presented here to determine the hydro-mechanical equivalent continuum parameters of the discontinuum regions corresponding to a suitable discretization of the fractured rock formation for the purpose of the engineering analysis, independently of the REV scale.

The VRM lab has been developed for the numerical homogenization process of all the discretization fractured regions using the commercial discontinuum geomechanical simulator Itasca – 3DEC. A mechanical module as well as a hydraulic module have been included in the VRM lab. The VRM mechanical laboratory is able to determine numerically the equivalent orthotropic parameters of any rectangular parallelepiped representing a specific region of the fractured rock, assuming the fractured regions can be represented by an equivalent continuum material with orthotropic symmetry. On the other hand, the VRM hydraulic laboratory is developed to determine the full equivalent permeability tensor of fractured regions, even with embedded fractures totally oblique to the coordinate system of the discontinuum model. Besides the linear elastic model, the fractures in the VRM lab can be assigned a nonlinear elastic joint constitutive model that has been added to the VRM lab for simulating fracture deformation behaviors closer to experimental observations. This nonlinear elastic constitutive model has been verified against the analytical solution. To account for nonlinear fracture deformations in the homogenization process conducted in the VRM lab, the fractured regions are tested after the effective in situ stress field is installed in the numerical discontinuum model. Additionally, plastic fracture deformations are only accounted for the equivalent permeability in the VRM hydraulic lab. Both modules of the VRM lab, the mechanical and hydraulic, have been successfully validated against the analytical Oda's crack tensor approach. During the development of the VRM lab, special attention has been given to the accuracy of the measurements.

To implicitly include the hydro-mechanical behaviour induced by the presence of discrete fracture networks in coupled reservoir geomechanical simulations of fractured porous formations, the VRM laboratory has been added to the explicit sequential coupling scheme implemented in the

RGRG coupling platform. Thus, the discontinuum regions representing the discretization of the fractured formation are modelled as equivalent porous media with anisotropic continuum properties determined through the mechanical and hydraulic modules of the VRM laboratory. In this reservoir geomechanical coupling strategy and methodology, the equivalent permeability, anisotropic elastic parameters as well as the Biot effective stress coefficient tensor can be updated at specific simulation stages in all the fractured reservoir regions or only in those where the change in the effective stress field reaches a certain tolerance.

5.2 Concluding remarks

The following conclusions may be drawn from this study:

- The explicit sequential coupling scheme implemented in the RGRG coupling platform has been successfully verified against analytical solutions. The mechanical consolidation cases show substantially smaller surface settlement in the anisotropic case compared to the isotropic case. The capability of the coupling method to simulate the interaction between thermo-poromechanical coupled processes has been shown in the thermal consolidation case.

- The numerical simulations of the Mandel's problem with a transversely isotropic material show that by increasing the Biot's elastic parameters, that is Biot modulus and Biot tensor coefficients, the excess pore pressure increases whereas the undrained vertical consolidation of the anisotropic porous formation decreases. Also, changing the isotropic plane orientation entails different undrained pore pressure responses and final drained vertical consolidations.

- The previous observations demonstrate the importance of properly modelling the effect of material anisotropy in thermo-poromechanical coupled simulations. Moreover, the methodology presented here is required to correctly model stress-sensitive reservoirs involving anisotropic porous formations.

- The mechanical and hydraulic modules of the VRM lab have been successfully validated against the analytical Oda's crack tensor approach. It has been found that the Oda's method can be used with confidence in fractured rocks with embedded fully persistent joint sets with linear elastic behaviour, where the non-interaction approximation is assumed valid. However, the Oda's crack tensor approach generally overestimates the equivalent elastic compliance of fractured formations with intersecting finite circular fractures with different sizes and orientations.

- The measuring procedure implemented in the VRM mechanical lab for determining the equivalent compliance matrix gives more accurate results than the traditional measurement techniques used in previous studies which usually yield non-symmetric compliance matrix.

- The VRM mechanical lab is able to capture with a great deal of fidelity the small-scale variability of the deformational response of fractured rock formations with a fine-scale discretization.

- The VRM hydraulic laboratory has the capability to determine the full equivalent permeability tensor of fractured regions, even with embedded fractures totally oblique to the coordinate system of the discontinuum model.

- Additionally, the VRM lab is not restricted to the homogenization of fractured regions but it could also be used to determine the REV scale and upscaling the equivalent continuum properties of the fractured porous formation.

- Disregarding the non-orthotropic coefficients of the compliance matrix in the calculation of the equivalent orthotropic parameters by assuming the model axes as principal directions of material symmetry usually yield misleading results. Moreover, neglecting the non-orthotropic coefficients may lead to similar elastic moduli suggesting the isotropic behaviour of the fractured rock, while the real

mechanical behaviour may be anisotropic. Thus, the non-orthotropic compliance coefficients and the principal directions of material symmetry must be taken into account in the mechanical characterization of fractured rock masses.

- A coupling strategy and methodology have been presented here for the inclusion of the hydro-mechanical behavior of discrete fracture networks in reservoir geomechanical simulations of fractured porous formations through hydraulic and mechanical equivalent continuum parameters determined by the numerical homogenization of rock mass discontinuum regions using a VRM laboratory. The capability of the proposed methodology implemented in the RGRG coupling platform for modelling and capturing the deformation behavior of a fractured rock mass through equivalent continuum orthotropic parameters has been demonstrated in the initial mechanical analysis.

- The conducted hydro-mechanical coupled simulations show that modelling fractures as nonlinear elastic results in higher equivalent permeability parameters and pore pressure build-up, since linear elastic fractures are usually more compliant allowing large joint closures and giving smaller hydraulic apertures. Also, updating the equivalent continuum parameters as well as the plastic fracture deformations slightly improve the permeability and pore pressure development throughout the rock formation.

- The fractured reservoir shows a clear anisotropic deformation, which is oriented in the coordinate system of the model in the nonlinear cases while is not aligned with the model axes in the linear elastic case. In addition, the fracture influence on the update of the Biot's effective stress coefficient tensor has been found negligible in the coupled simulations since the fractures show a lower impact on the deformability of the rock mass.

- Due to the challenging and time-consuming process of determining the plastic failure characteristics such as defining a suitable anisotropic yield envelope and plastic potential in compression and tensile regimes for each discontinuum discretization region, the continuum geomechanical simulator has been restricted to model the fractured formation through an equivalent orthotropic elastic material.

- The full analytical compliance matrix based on the Oda's theory has been presented in Appendix D.

5.3 Recommendations for future research

As previously mentioned above, in the reservoir geomechanical coupling methodology presented here the continuum geomechanical simulator is limited to model the fractured formation through an equivalent orthotropic elastic material. Therefore, further research would be necessary to improve the presented coupling scheme by including a fully anisotropic failure criteria to capture the plastic behavior in compression and tensile regimes of the fractured rock formation.

In this study, the hydraulic behavior of the fractured rock is represented by an equivalent continuum media; however, since the VRM hydraulic lab assumes the intact rock material as impervious, the resultant measured permeability is only due to the discrete fracture network. Therefore, the dual porosity model could be implemented in the sequential scheme of the RGRG coupling platform.

A thermal module could be implemented in the VRM laboratory for numerically determining the thermal expansion coefficient tensor of fractured regions to include the thermal effect of discrete fracture networks in reservoir geomechanical simulations.

The VRM laboratory can be combine with machine learning techniques to improve the efficiency of the homogenization process for prediction of the hydro-mechanical equivalent parameters of fractured porous formations.

References

Aavatsmark, I. (2002). An introduction to multipoint flux approximations for quadrilateral grids. *Computational Geosciences, 6*, 405–432. https://doi.org/10.1023/A:1021291114475

Abousleiman, Y., Cheng, A. D., Cui, L., Detournay, E., & Roegiers, J. C. (1996). Mandel's problem revisited. *Geotechnique, 46*(2), 187-195. https://doi.org/10.1680/geot.1996.46.2.187

Almani, T., Kumar, K., Dogru, A., Singh, G., & Wheeler, M. F. (2016). Convergence analysis of multirate fixed-stress split iterative schemes for coupling flow with geomechanics. *Computer Methods in Applied Mechanics and Engineering, 311*, 180-207. https://doi.org/10.1016/j.cma.2016.07.036

Alshkane, Y. M., Marshall, A. M., & Stace, L. R. (2017). Prediction of strength and deformability of an interlocked blocky rock mass using UDEC. *Journal of Rock Mechanics and Geotechnical Engineering, 9*(3), 531–542. https://doi.org/10.1016/j.jrmge.2017.01.002

Amadei, B., & Goodman, R. E. (1983). A 3-D constitutive relation for fractured rock masses. *Rock anisotropy and the theory of stress measurements, Lecture Notes in Engineering, 2*, 267–286. https://doi.org/10.1007/978-3-642-82040-3

Aoki, T., Tan, C. P., & Bamford, W. E. (1993). Effects of deformation and strength anisotropy on borehole failures in saturated shales. *International Journal of Rock Mechanics and Mining Sciences & Geomechanics Abstracts, 30*(7), 1031-1034. https://doi.org/10.1016/0148-9062(93)90067-n

Baghbanan, A., & Jing, L. (2008). Stress effects on permeability in a fractured rock mass with correlated fracture length and aperture. *International Journal of Rock Mechanics and Mining Sciences, 45*(8), 1320–1334. https://doi.org/10.1016/j.ijrmms.2008.01.015

Bagheri, M. A. (2006). *Modeling geomechanical effects on the flow properties of fractured reservoirs* (Ph.D. thesis). University of Calgary, Calgary, Alberta, 250. https://doi.org/10.11575/PRISM/255

Bai, M., Elsworth, D., & Roegiers, J.-C. (1993). Modeling of naturally fractured reservoirs using deformation dependent flow mechanism. *International Journal of Rock Mechanics and*

Mining Sciences & Geomechanics Abstracts, 30(7), 1185–1191. https://doi.org/10.1016/0148-9062(93)90092-r

Bandis, S. C., Lumsden, A. C., & Barton, N. R. (1983). Fundamentals of rock joint deformation. *International Journal of Rock Mechanics and Mining Sciences & Geomechanics Abstracts, 20*(6), 249–268. https://doi.org/10.1016/0148-9062(83)90595-8

Barenblatt, G. I., Zheltov, Iu. P., & Kochina, I. N. (1960). Basic concepts in the theory of seepage of homogeneous liquids in fissured rocks [strata]. *Journal of Applied Mathematics and Mechanics, 24*(5), 1286–1303. https://doi.org/10.1016/0021-8928(60)90107-6

Barla, G. (1974). Rock anisotropy; theory and laboratory testing. *Courses and Lectures - International Centre For Mechanical Sciences, 165*, 131–169. https://doi.org/10.1007/978-3-7091-4109-0_8

Barla, G., Cravero, M., & Fidelibus, C. (2000). Comparing methods for the determination of the hydrological parameters of a 2D equivalent porous medium. *International Journal of Rock Mechanics and Mining Sciences, 37*(7), 1133–1141. https://doi.org/10.1016/s1365-1609(00)00033-2

Bear, J. (1972). *Dynamics of fluids in porous media*. New York, USA: American Elsevier.

Ben Abdallah, K., Hamoud, M. T., & Chalaturnyk, R. J. (2014). Experimental studies: shear induced in single phase permeability. *SPE Heavy Oil Conference-Canada*. https://doi.org/10.2118/170136-ms

Berre, I., Doster, F., & Keilegavlen, E. (2018). Flow in fractured porous media: A review of conceptual models and discretization approaches. *Transport in Porous Media, 130*(1), 215–236. https://doi.org/10.1007/s11242-018-1171-6

Bieniawski, Z. T. (1978). Determining rock mass deformability: experience from case histories. *International Journal of Rock Mechanics and Mining Sciences & Geomechanics Abstracts, 15*(5), 237–247. https://doi.org/10.1016/0148-9062(78)90956-7

Biot, M. A. (1941). General theory of three dimensional consolidation. *Journal of Applied Physics, 12*(2), 155-164. https://doi.org/10.1063/1.1712886

Biot, M. A. (1955). Theory of elasticity and consolidation for a porous anisotropic solid. *Journal of Applied Physics, 26*(2), 182-185. https://doi.org/10.1063/1.1721956

Biot, M. A. (1956a). Theory of deformation of a porous viscoelastic anisotropic solid. *Journal of Applied Physics, 27*(5), 459-467. https://doi.org/10.1063/1.1722402

Biot, M. A. (1956b). Thermoelasticity and irreversible thermodynamics. *Journal of Applied Physics, 27*(3), 240-253. https://doi.org/10.1063/1.1722351

Biot, M. A. (1962). Generalized theory of acoustic propagation in porous dissipative media. *The Journal of the Acoustical Society of America, 34*(9A), 1254-1264. https://doi.org/10.1121/1.1918315

Biot, M. A. (1973). Nonlinear and semilunar rheology of porous solids. *Journal of Geophysical Research, 78*(23), 4924-4937. https://doi.org/10.1029/JB078i023p04924

Biot, M. A., & Willis, D. G. (1957). The elastic coefficients of the theory of consolidation. *Journal of Applied Mechanics, 24*(1957), 594-601

Blanco-Martín, L., Rutqvist, J., & Birkholzer, J. T. (2017). Extension of TOUGH-FLAC to the finite strain framework. *Computers & Geosciences, 108*, 64-71, https://doi.org/10.1016/j.cageo.2016.10.015

Borregales M., Kumar, K., Radu, F. A., Rodrigo, C., & Gaspar, F. J. (2019). A partially parallel-in-time fixed-stress splitting method for Biot's consolidation model. *Computers & Mathematics with Applications, 77*(6), 1466-1478. https://doi.org/10.1016/j.camwa.2018.09.005

Both, J., Borregales, M., Nordbotten, J., Kumar, K. & Radu, F. (2017). Robust fixed stress splitting for Biot's equations in heterogeneous media. *Applied Mathematics Letters, 68*, 101-108. https://doi.org/10.1016/j.aml.2016.12.019

Brady, B. H. G, & Brown, E. T. (2004). *Rock mechanics: for underground mining.* (3rd ed.). Dordrecht: Kluwer Academic Publishers. https://doi.org/10.1007/978-1-4020-2116-9

Carroll, M. M. (1979). An effective stress law for anisotropic elastic deformation. *Journal of Geophysical Research: Solid Earth, 84*(B13), 7510–7512. https://doi.org/10.1029/jb084ib13p07510

Castelletto, N., White, J. A., & Tchelepi, H. A. (2015). Accuracy and convergence properties of the fixed-stress iterative solution of two-way coupled poromechanics. *International Journal for Numerical and Analytical Methods in Geomechanics, 39*, 1593-1618. https://doi.org/10.1002/nag.2400

Chalhoub, M., & Pouya, A. (2008). Numerical homogenization of a fractured rock mass: a geometrical approach to determine the mechanical representative elementary volume. *Electronic Journal of Geotechnical Engineering, 13*(K), 1–12. http://www.ejge.com/2008/JourTOC13K.htm

Chen, T., Clauser, C., Marquart, G., Willbrand, K., & Hiller, T. (2018). Upscaling permeability for three-dimensional fractured porous rocks with the multiple boundary method. *Hydrogeology Journal, 26*(6), 1903–1916. https://doi.org/10.1007/s10040-018-1744-z

Chen, T., Clauser, C., Marquart, G., Willbrand, K., & Mottaghy, D. (2015). A new upscaling method for fractured porous media. *Advances in Water Resources, 80*, 60–68. https://doi.org/10.1016/j.advwatres.2015.03.009

Cheng, A. H.-D. (1997). Material coefficients of anisotropic poroelasticity. *International Journal of Rock Mechanics and Mining Sciences, 34*(2), 199-205. https://doi.org/10.1016/s0148-9062(96)00055-1

Cheng, A. H.-D. (2016). *Poroelasticity*. Theory and applications of transport in porous media (Vol. 27). Cham, Switzerland: Springer International Publishing. https://doi.org/10.1007/978-3-319-25202-5

Cheng, A. H.-D., & Detournay, E. (1988). A direct boundary element method for plane strain poroelasticity. *International Journal for Numerical and Analytical Methods in Geomechanics, 12*(5), 551-572. https://doi.org/10.1002/nag.1610120508.

Computer Modelling Group Ltd. (2002). *GEM Users guide.* Calgary, Alberta, Canada: CMG.

Computer Modelling Group Ltd. (2018). *STARS Users guide: Thermal & advance processes simulator*. Calgary, Alberta, Canada: CMG.

Coussy, O. (1995). *Mechanics of Porous Media*. Chichester, England: John Wiley & Sons.

Coussy, O. (2004). *Poromechanics*. Chichester, England: John Wiley & Sons. https://doi.org/10.1002/0470092718

Coussy, O. (2010). *Mechanics and physics of porous solids*. Chichester, England: John Wiley & Sons. https://doi.org/10.1002/9780470710388

Cowin, S. C. (1989). Properties of the anisotropic elasticity tensor. *The Quarterly Journal of Mechanics and Applied Mathematics, 42*(2), 249–266. https://doi.org/10.1093/qjmam/42.2.249

Cowin, S. C., & Mehrabadi, M. M. (1987). On the identification of material symmetry for anisotropic elastic materials. *The Quarterly Journal of Mechanics and Applied Mathematics, 40*(4), 451–476. https://doi.org/10.1093/qjmam/40.4.451

Cui, L., Abousleiman, Y., Cheng, A. H.-D., & Roegiers, J. C. (1996a). Anisotropy effect on one-dimensional consolidation. In Y. K. Lin & T. C. Su (Eds.), *11th ASCE Engineering Mechanics Conference, 1,* (pp. 471–474). Fort Lauderdale, Florida, 20-22 May.

Cui, L., Cheng, A. H. D., Kaliakin, V. N., Abousleiman, Y., & Roegiers, J. C. (1996b). Finite element analyses of anisotropic poroelasticity: A generalized Mandel's problem and an inclined borehole problem. *International Journal for Numerical and Analytical Methods in Geomechanics, 20*(6), 381–401. https://doi.org/10.1002/(sici)1096-9853(199606)20:6<381::aid-nag826>3.0.co;2-y

Cui, J., Jiang, Q., Feng, X., Li, S., Gao, H., & Li, S. (2016). Equivalent elastic compliance tensor for rock mass with multiple persistent joint sets: Exact derivation via modified crack tensor. *Journal of Central South University*, *23*(6), 1486–1507. https://doi.org/10.1007/s11771-016-3201-2

Cundall, P. A. (1971). A computer model for simulating progressive large-scale movements in blocky rock systems. *Proceedings of the Symposium of the International Society for Rock Mechanics*, France, II-8.

Cundall, P. A., & Hart, R. D. (1992). Numerical modeling of discontinua. *Engineering Computations, 9*(2), 101–113. https://doi.org/10.1108/eb023851

Dana, S., Ganis, B., & Wheeler, M. F. (2018). A multiscale fixed stress split iterative scheme for coupled flow and poromechanics in deep subsurface reservoirs. *Journal of Computational Physics, 352*, 1–22. https://doi.org/10.1016/j.jcp.2017.09.049

Dana, S., & Wheeler, M. F. (2018). Convergence analysis of fixed stress split iterative scheme for anisotropic poroelasticity with tensor Biot parameter. *Computational Geosciences, 22*(5), 1219-1230. https://doi.org/10.1007/s10596-018-9748-2

de Boer, R. (2000). *Theory of porous media. Highlights in historical development and current state*. Berlin Heidelberg, Germany: Springer-Verlag. https://doi.org/10.1007/978-3-642-59637-7

Dean, R. H., Gai, X., Stone, C. M., & Minkoff, S. E. (2006). A comparison of techniques for coupling porous flow and geomechanics. *SPE Journal, 11*(01), 132–140. https://doi.org/10.2118/79709-pa

Deisman, N., Mas Ivars, D., & Chalaturnyk, R. J. (2009). An adaptive continuum/discontinuum coupled reservoir geomechanics simulation approach for fractured reservoirs. *SPE Reservoir Simulation Symposium*, The Woodlands, Texas, 2-4 February. SPE-119254-MS. https://doi.org/10.2118/119254-ms

Delgado, P. M., Kotteda, V. M. K., & Kumar, V. (2019). Hybrid fixed-point fixed-stress splitting method for linear poroelasticity. *Geosciences, 9*(2), 29. https://doi.org/10.3390/geosciences9010029

Dershowitz, W. S., & Herda, H. H. (1992). Interpretation of fracture spacing and intensity. In Tillerson & Wawersik (Eds.), *33rd U.S. Symposium on Rock Mechanics (USRMS), Santa Fe, New Mexico* (pp. 757–766). Rotterdam: Balkema.

Detournay, E., & Cheng, A. H.-D. (1993). Fundamentals of poroelasticity. In C. Fairhurst (Ed.), *Analysis and design methods* (pp. 113–171). Pergamon. https://doi.org/10.1016/B978-0-08-040615-2.50011-3

Duncan, J. M., & Goodman, R. E. (1968). *Finite element analysis of slopes in jointed rock*. Final report to US Army Corps of Engineers, Vicksburg, Mississippi, Report S-68-3.

Felippa, C. A., & Park, K. C. (1980). Staggered transient analysis procedures for coupled mechanical systems: Formulation. *Computer Methods in Applied Mechanics and Engineering, 24*(1), 61-111. https://doi.org/10.1016/0045-7825(80)90040-7

Fossum, A. F. (1985). Effective elastic properties for a random jointed rock mass. *International Journal of Rock Mechanics and Mining Sciences & Geomechanics Abstracts, 22*(6), 467–470. https://doi.org/10.1016/0148-9062(85)90011-7

Fumagalli, A., Zonca, S., & Formaggia, L. (2017). Advances in computation of local problems for a flow-based upscaling in fractured reservoirs. *Mathematics and Computers in Simulation, 137*, 299–324. https://doi.org/10.1016/j.matcom.2017.01.007

Gan, Q., & Elsworth, D. (2016). A continuum model for coupled stress and fluid flow in discrete fracture networks. *Geomechanics and Geophysics for Geo-Energy and Geo-Resources, 2*(1), 43–61. https://doi.org/10.1007/s40948-015-0020-0

Gao, K., & Lei, Q. (2018). Influence of boundary constraints on stress heterogeneity modelling. *Computers and Geotechnics, 99*, 130–136. https://doi.org/10.1016/j.compgeo.2018.03.003

Gao, Y., Liu, Z., Zhuang, Z., & Hwang, K. C. (2017). A reexamination of the equations of anisotropic poroelasticity. *Journal of Applied Mechanics, 84*(5), 051008. https://doi.org/10.1115/1.4036194

Garipov, T. T., & Hui, M. H. (2019). Discrete Fracture Modeling approach for simulating coupled thermo-hydro-mechanical effects in fractured reservoirs. *International Journal of Rock Mechanics and Mining Sciences, 122*, 104075. https://doi.org/10.1016/j.ijrmms.2019.104075

Garipov, T. T., Karimi-Fard, M., & Tchelepi, H. A. (2016). Discrete fracture model for coupled flow and geomechanics. *Computational Geosciences, 20*(1), 149–160. https://doi.org/10.1007/s10596-015-9554-z

Garipov, T. T., Tomin, P., Rin, R., Voskov, D. V., & Tchelepi, H. A. (2018). Unified thermo-compositional-mechanical framework for reservoir simulation. *Computational Geosciences, 22*(4), 1039-1057. https://doi.org/10.1007/s10596-018-9737-5

Gaspar, F. J., & Rodrigo, C. (2018). On the fixed-stress split scheme as smoother in multigrid methods for coupling flow and geomechanics. *Computer Methods in Applied Mechanics and Engineering, 326*, 526-540. https://doi.org/10.1016/j.cma.2017.08.025

Gassmann, F. (1951). Uber die elastizitat poroser medien (On elasticity of porous media). *Veirteljahrsschrift der Naturforschenden Gesellschaft in Zurich 96*, 1-23

Geertsma, J. (1957). The effect of fluid pressure decline on volumetric changes of porous rocks. *Society of Petroleum Engineers: Petroleum Transactions, AIME, 210*, 331-340. SPE-728-G

Gerrard, C. M. (1982). Equivalent elastic moduli of a rock mass consisting of orthorhombic layers. *International Journal of Rock Mechanics &Mining Sciences, 19*(1), 9–14. https://doi.org/10.1016/0148-9062(82)90705-7

Giot, R., Granet, S., Faivre, M., Massoussi, N., & Huang, J. (2018). A transversely isotropic thermo-poroelastic model for claystone: parameter identification and application to a 3D underground structure. *Geomechanics and Geoengineering, 13*(4), 246-263. https://doi.org/10.1080/17486025.2018.1445874

Goodman, R. E. (1970). The deformability of joints. *Determination of the In Situ Modulus of Deformation of Rock, ASTM STP477-EB,* 174–196. https://doi.org/10.1520/STP29147S

Goodman, R. E. (1796). *Methods of geological engineering in discontinuous rocks*. St. Paul, USA: West Publishing Co.

Goodman, R. E., Taylor, R. L. & Brekke, T. L. (1968). A model for the mechanics of jointed rock. *Journal of the Soil Mechanics and Foundations Division, 94*(3), 637-659.

Goulet, G. C., Coombe, D., Tran, D., Martinuzzi, R. J., & Zernicke, R. F. (2009). Validation and application of iterative coupling to poroelastic problems in bone fluid flow. *Bulletin of Applied Mechanics, 5*(17), 6-17.

Grechka, V., & Kachanov, M. (2006). Effective elasticity of fractured rocks: A snapshot of the work in progress. *GEOPHYSICS, 71*(6), W45–W58. https://doi.org/10.1190/1.2360212

Gu, F., & Chalaturnyk, J. (2005). Analysis of coalbed methane production by reservoir and geomechanical coupling simulation. *Journal of Canadian Petroleum Technology, 44*(10), 33-42. https://doi.org/10.2118/05-10-03

Gu, F., & Chalaturnyk, R. (2010). Permeability and porosity models considering anisotropy and discontinuity of coalbeds and application in coupled simulation. *Journal of Petroleum Science and Engineering, 74*(3-4), 113–131. https://doi.org/10.1016/j.petrol.2010.09.002

Gutierrez, M. & Lewis, M. (1998). The role of geomechanics in reservoir simulation. *SPE/ISRM Eurock'98*, Trondheim, Norway, 8-10 July, 439-448. https://doi.org/10.2118/47392-ms

Hart, R. D. (1993). An Introduction to Distinct Element Modeling for Rock Engineering. In *Comprehensive Rock Engineering, 2,* (pp. 245–261). Oxford: Pergamon Press, Ltd. https://doi.org/10.1016/b978-0-08-040615-2.50016-2

Hoang, S. K., & Abousleiman, Y. N. (2012). Correspondence principle between anisotropic poroviscoelasticity and poroelasticity using micromechanics and application to compression of orthotropic rectangular strips. *Journal of Applied Physics, 112*(4), 044907. https://doi.org/10.1063/1.4748293

Hoek, E., & Diederichs, M. S. (2006). Empirical estimation of rock mass modulus. *International Journal of Rock Mechanics and Mining Sciences, 43*(2), 203–215. https://doi.org/10.1016/j.ijrmms.2005.06.005

Hoek, E., & Brown, E. T. (2019). The Hoek–Brown failure criterion and GSI – 2018 edition. *Journal of Rock Mechanics and Geotechnical Engineering, 11*(3), 445–463. https://doi.org/10.1016/j.jrmge.2018.08.001

Huang, T. H., Chang, C. S., & Yang, Z. Y. (1995). Elastic moduli for fractured rock mass. *Rock Mechanics and Rock Engineering, 28*(3), 135–144. https://doi.org/10.1007/bf01020148

Hudson, J., & Harrison, J. P. (1997). *Engineering rock mechanics: an introduction to the principles.* Oxford: Pergamon.

Itasca Consulting Group, Inc. (1997). *FLAC3D — Fast Lagrangian Analysis of Continua in Three-Dimensions, Ver. 2.0*. Minneapolis: Itasca.

Itasca Consulting Group, Inc. (2000). *UDEC — Universal Distinct Element Code, Ver. 3.1*. Minneapolis: Itasca.

Itasca Consulting Group, Inc. (2008). *PFC — Particle Flow Code, Ver. 4.0.* Minneapolis: Itasca.

Itasca Consulting Group, Inc. (2011). *FLAC — Fast Lagrangian Analysis of Continua, Ver. 7.0.* Minneapolis: Itasca.

Itasca Consulting Group, Inc. (2013). *FLAC3D — Fast Lagrangian Analysis of Continua in Three-Dimensions, Ver. 5.01*. Minneapolis: Itasca.

Itasca Consulting Group, Inc. (2016). *3DEC — Three-Dimensional Distinct Element Code, Ver. 5.2*. Minneapolis: Itasca.

Itasca Consulting Group, Inc. (2016). *PFC — Particle Flow Code, Ver. 5.0.* Minneapolis: Itasca.

Itasca Consulting Group, Inc. (2017). *FLAC3D — Fast Lagrangian Analysis of Continua in Three-Dimensions, Ver. 6.0*. Minneapolis: Itasca.

Jaeger, J. C., Cook, N. G.W., & Zimmerman, R. W. (2007). *Fundamentals of rock mechanics.* (4th ed.). Oxford: Wiley Blackwell.

Jayne, B. A., & Suddarth, S. K. (1966). Matrix-tensor mathematics in orthotropic elasticity. *Orientation Effects in the Mechanical Behavior of Anisotropic Structural Materials, ASTM STP 405*, 39–58. https://doi.org/10.1520/stp45150s

Jiang, Q., Cui, J., Feng, X., Zhang, Y., Zhang, M., Zhong, S., & Ran, S. (2017). Demonstration of spatial anisotropic deformation properties for jointed rock mass by an analytical deformation tensor. *Computers and Geotechnics, 88*, 111–128. https://doi.org/10.1016/j.compgeo.2017.03.009

Jin, L., & Zoback, M. D. (2017). Fully coupled nonlinear fluid flow and poroelasticity in arbitrarily fractured porous media: A hybrid-dimensional computational model. *Journal Geophysical Research: Solid Earth, 122*, 7626–7658. https://doi.org/10.1002/2017JB014892

Jing, L., & Hudson, J. A. (2002). Numerical methods in rock mechanics. *International Journal of Rock Mechanics & Mining Sciences, 39*(4), 409-427. https://doi.org/10.1016/s1365-1609(02)00065-5

Jing, L., & Stephansson, O. (2007). *Fundamentals of discrete element methods for rock engineering: theory and applications*. Elsevier. https://doi.org/10.1016/s0165-1250(07)x8500-6

Karimi-Fard, M., Durlofsky, L. J., & Aziz, K. (2004). An efficient discrete-fracture model applicable for general-purpose reservoir simulators. *SPE Journal, 9*(02), 227–236. https://doi.org/10.2118/88812-pa

Khani, A., Baghbanan, A., & Hashemolhosseini, H. (2013a). Numerical investigation of the effect of fracture intensity on deformability and REV of fractured rock masses. *International Journal of Rock Mechanics and Mining Sciences, 63*, 104–112. https://doi.org/10.1016/j.ijrmms.2013.08.006

Khani, A., Baghbanan, A., Norouzi, S., & Hashemolhosseini, H. (2013b). Effects of fracture geometry and stress on the strength of a fractured rock mass. *International Journal of Rock Mechanics and Mining Sciences, 60*, 345–352. https://doi.org/10.1016/j.ijrmms.2013.01.011

Kim, J. (2010). *Sequential methods for coupled geomechanics and multiphase flow* (Ph.D. Thesis) Department of Energy Resources Engineering. Stanford University, California, 264.

Kim, J., Tchelepi, H. A., & Juanes, R. (2011). Stability, accuracy, and efficiency of sequential methods for coupled flow and geomechanics. *SPE Journal, 16*(2), 249-262. https://doi.org/10.2118/119084-pa

Kim, J., Moridis, G., Yang, D., & Rutqvist, J. (2012). Numerical studies on two-way coupled fluid flow and geomechanics in hydrate deposits. *SPE Journal, 17*(02), 485-501. https://doi.org/10.2118/141304-pa

Kim, J., Tchelepi, H. A., & Juanes, R. (2013). Rigorous coupling of geomechanics and multiphase flow with strong capillarity. *SPE Journal, 18*(06), 1123-1139. https://doi.org/10.2118/141268-pa

Kim, J., Sonnenthal, E., & Rutqvist, J. (2015). A sequential implicit algorithm of chemo-thermo-poro-mechanics for fractured geothermal reservoirs. *Computers & Geosciences, 76*, 59-71. https://doi.org/10.1016/j.cageo.2014.11.009

Kim, J. (2018a). A new numerically stable sequential algorithm for coupled finite-strain elastoplastic geomechanics and flow. *Computer Methods in Applied Mechanics and Engineering, 335*, 538-562. https://doi.org/10.1016/j.cma.2018.02.024

Kim, J. (2018b). Unconditionally stable sequential schemes for all-way coupled thermoporomechanics: Undrained-adiabatic and extended fixed-stress splits. *Computer Methods in Applied Mechanics and Engineering, 341*, 93-112. https://doi.org/10.1016/j.cma.2018.06.030

Kulatilake, P. H. S. W. (1985). Estimating elastic constants and strength of discontinuous rock. *Journal of Geotechnical Engineering, 111*(7), 847–864. https://doi.org/10.1061/(asce)0733-9410(1985)111:7(847)

Kulatilake, P. H. S. W., Shreedharan, S., Sherizadeh, T., Shu, B., Xing, Y., & He, P. (2016). Laboratory estimation of rock joint stiffness and frictional parameters. *Geotechnical and Geological Engineering, 34*(6), 1723–1735. . https://doi.org/10.1007/s10706-016-9984-y

Kulatilake, P. H. S. W., Ucpirti, H., Wang, S., Radberg, G., & Stephansson, O. (1992). Use of the distinct element method to perform stress analysis in rock with non-persistent joints and to study the effect of joint geometry parameters on the strength and deformability of rock masses. *Rock Mechanics and Rock Engineering, 25*(4), 253–274. https://doi.org/10.1007/bf01041807

Kulatilake, P. H. S. W., Wang, S., & Stephansson, O. (1993). Effect of finite size joints on the deformability of jointed rock in three dimensions. *International Journal of Rock Mechanics and Mining Sciences & Geomechanics Abstracts, 30*(5), 479–501. https://doi.org/10.1016/0148-9062(93)92216-d

Kushch, V. I. (2013). Multipole expansion method in micromechanics of composites. In M. Kachanov & I. Sevostianov (Eds.), *Effective properties of heterogeneous materials, Solid mechanics and its applications, 193,* (pp. 97–197). Dordrecht: Springer. https://doi.org/10.1007/978-94-007-5715-8_2

Laghaei, M., Baghbanan, A., Hashemolhosseini, H., & Dehghanipoodeh, M. (2018). Numerical determination of deformability and strength of 3D fractured rock mass. *International*

Journal of Rock Mechanics and Mining Sciences, 110, 246–256. https://doi.org/10.1016/j.ijrmms.2018.07.015

Lang, P. S., Paluszny, A., & Zimmerman, R. W. (2014). Permeability tensor of three-dimensional fractured porous rock and a comparison to trace map predictions. *Journal of Geophysical Research: Solid Earth, 119*(8), 6288–6307. https://doi.org/10.1002/2014jb011027

Lekhnitskii, S. G. (1981). *Theory of Elasticity of an Anisotropic Body*. Moscow: Mir Publishers.

Lemos, J. V. (2018). Rock failure analysis with discrete elements. In: Cardoso et al. (Eds.), *Numerical Methods in Geotechnical Engineering IX, Volume 1: Proceedings of the 9th European Conference on Numerical Methods in Geotechnical Engineering, June 25-27, 2018, Porto, Portugal* (pp. 13–22). London: Taylor & Francis Group.

Li, P., & Chalaturnyk, R. J. (2006). Permeability variations associated with shearing and isotropic unloading during the SAGD process. *Journal of Canadian Petroleum Technology, 45*(1), 54-61. https://doi.org/10.2118/06-01-05

Li, L., & Lee, S. H. (2008). Efficient field-scale simulation of black oil in a naturally fractured reservoir through discrete fracture networks and homogenized media. *SPE Reservoir Evaluation & Engineering, 11*(04), 750–758. https://doi.org/10.2118/103901-pa

Liu, E., & Martinez, A. (2012). *Seismic fracture characterization: Concepts and practical applications* (EET 8). Houten, Netherlands: EAGE Publications.

Long, J. S., Remer, J. S., Wilson, C. R., & Witherspoon, P. A. (1982). Porous media equivalents for networks of discontinuous fractures. *Water Resources Research*, *18*(3), 645–658. https://doi.org/10.1029/wr018i003p00645

Lorig, L. J., Cundall, P. A., Damjanac, B., & Emam, S. (2010). A three-dimensional model for rock slopes based on micromechanics. *44th US Rock Mechanics Symposium and 5th US-Canada Rock Mechanics Symposium*, Salt Lake City, UT, 27–30 June. ARMA 10-163.

Mahboubi Niazmandi, M., & Binesh, S. M. (2020). A DFN–DEM approach to study the influence of confinement on the REV size of fractured rock masses. *Iranian Journal of Science and Technology, Transactions of Civil Engineering.* https://doi.org/10.1007/s40996-020-00348-2

Mainguy, M., & Longuemare, P. (2002). Coupling fluid flow and rock mechanics: formulations of the partial coupling between reservoir and geomechanical simulators. *Oil & Gas Science and Technology, 57*(4), 355-367. https://doi.org/10.2516/ogst:2002023

Malama, B., & Kulatilake, P. H. S. W. (2003). Models for normal fracture deformation under compressive loading. *International Journal of Rock Mechanics and Mining Sciences, 40*(6), 893–901. https://doi.org/10.1016/s1365-1609(03)00071-6

Mandel, J. (1953). Consolidation des sols (étude mathématique). *Géotechnique, 3*(7), 287-299. https://doi.org/10.1680/geot.1953.3.7.287.

Mas Ivars, D., Min, K. B., & Jing, L. (2001). Homogenization of mechanical properties of fracture rocks by DEM modeling. In: S. Wang, B. Fu & Z. Li, (Eds.), *Frontiers of rock mechanics and sustainable development in 21st century. Proceedings of the Second Asia Rock Mechanics Symposium, Beijing, China* (pp. 311–314). Rotterdam: Balkema.

Mas Ivars, D., Pierce, M. E., Darcel, C., Reyes-Montes, J., Potyondy, D. O., Paul Young, R., & Cundall, P. A. (2011). The synthetic rock mass approach for jointed rock mass modelling. *International Journal of Rock Mechanics and Mining Sciences, 48*(2), 219–244. https://doi.org/10.1016/j.ijrmms.2010.11.014

Mehranpour, M. H., & Kulatilake, P. H. S. W. (2017). Improvements for the smooth joint contact model of the particle flow code and its applications. *Computers and Geotechnics, 87*, 163–177. https://doi.org/10.1016/j.compgeo.2017.02.012

Mikelić, A., & Wheeler, M. F. (2012). Convergence of iterative coupling for coupled flow and geomechanics. *Computational Geosciences, 17*(3), 455-461. https://doi.org/10.1007/s10596-012-9318-y

Min, K.-B., & Jing, L. (2003). Numerical determination of the equivalent elastic compliance tensor for fractured rock masses using the distinct element method. *International Journal of Rock Mechanics and Mining Sciences, 40*(6), 795–816. https://doi.org/10.1016/s1365-1609(03)00038-8

Min, K.-B., Jing, L., & Stephansson, O. (2004a). Determining the equivalent permeability tensor for fractured rock masses using a stochastic REV approach: Method and application to the

field data from Sellafield, UK. *Hydrogeology Journal, 12*(5), 497–510. https://doi.org/10.1007/s10040-004-0331-7

Min, K.-B., Rutqvist, J., Tsang, C.-F., & Jing, L. (2004b). Stress-dependent permeability of fractured rock masses: a numerical study. *International Journal of Rock Mechanics and Mining Sciences, 41*(7), 1191–1210. https://doi.org/10.1016/j.ijrmms.2004.05.005

Min, K. B., & Thoraval, A. (2012). Comparison of two- and three-dimensional approaches for the numerical determination of equivalent mechanical properties of fractured rock masses. *Tunnel & Underground Space, 22*(2), 93–105. https://doi.org/10.7474/tus.2012.22.2.093

Moinfar, A., Varavei, A., Sepehrnoori, K., & Johns, R. T. (2014). Development of an efficient embedded discrete fracture model for 3D compositional reservoir simulation in fractured reservoirs. *SPE Journal, 19*(02), 289–303. https://doi.org/10.2118/154246-pa

Moon, H. (1987). Elastic moduli of well-jointed rock masses (Ph.D. thesis). University of Utah: Salt Lake City, UT, United States.

Narr, W., Schechter, D. S., & Thompson, L. B. (2006). *Naturally fractured reservoir characterization*. Richardson, USA: SPE Publications.

Nemeth, M. P. (2011) An in-depth tutorial on constitutive equations for elastic anisotropic materials. *NASA Technical Reports Server (NTRS)*, NASA/TM-2011-217314. Hampton, VA, USA: NASA. https://ntrs.nasa.gov/search.jsp?R=20110023650

Noorian Bidgoli, M., Zhao, Z., & Jing, L. (2013). Numerical evaluation of strength and deformability of fractured rocks. *Journal of Rock Mechanics and Geotechnical Engineering, 5*(6), 419–430. https://doi.org/10.1016/j.jrmge.2013.09.002

Noorian Bidgoli, M., & Jing, L. (2014). Anisotropy of strength and deformability of fractured rocks. *Journal of Rock Mechanics and Geotechnical Engineering, 6*(2), 156–164. https://doi.org/10.1016/j.jrmge.2014.01.009

Noorishad, J., Ayatollahi, M. S., & Witherspoon, P. A. (1982). A finite-element method for coupled stress and fluid flow analysis in fractured rock masses. *International Journal of Rock Mechanics and Mining Sciences & Geomechanics Abstracts, 19*(4), 185–193. https://doi.org/10.1016/0148-9062(82)90888-9

Nur, A., & Byerlee, J. D. (1971). An exact effective stress law for elastic deformation of rock with fluids. *Journal of Geophysical Research, 76*(26), 6414–6419. https://doi.org/10.1029/jb076i026p06414

Oda, M. (1982). Fabric tensor for discontinuous geological materials. *Soils and Foundations, 22*(4), 96–108. https://doi.org/10.3208/sandf1972.22.4_96

Oda, M. (1985). Permeability tensor for discontinuous rock masses. *Géotechnique, 35*(4), 483–495. https://doi.org/10.1680/geot.1985.35.4.483

Oda, M. (1986). An equivalent continuum model for coupled stress and fluid flow analysis in jointed rock masses. *Water Resources Research, 22*(13), 1845–1856. https://doi.org/10.1029/wr022i013p01845

Oda, M. (1988). A method for evaluating the representative elementary volume based on joint survey of rock masses. *Canadian Geotechnical Journal, 25*(3), 440–447. https://doi.org/10.1139/t88-049

Oda, M., Yamabe, T., Ishizuka, Y., Kumasaka, H., Tada, H., & Kimura, K. (1993). Elastic stress and strain in jointed rock masses by means of crack tensor analysis. *Rock Mechanics and Rock Engineering, 26*(2), 89–112. https://doi.org/10.1007/bf01023618

Olorode, O., Wang, B., & Rashid, H. U. (2020). Three-dimensional projection-based embedded discrete-fracture model for compositional simulation of fractured reservoirs. *SPE Journal, 25*(04), 2143–2161. https://doi.org/10.2118/201243-pa

Pariseau, W. G. (1993). Equivalent properties of a jointed Biot material. *International Journal of Rock Mechanics and Mining Sciences & Geomechanics Abstracts, 30*(7), 1151–1157. https://doi.org/10.1016/0148-9062(93)90085-r

Pariseau, W. G. (1995). Non-representative volume element modeling of equivalent jointed rock mass properties. In Rossmanith (Ed.), *Mechanics of jointed and faulted rock* (pp. 563–568). Rotterdam: Balkema.

Pariseau, W. G., & Moon, H. (1988). Elastic moduli of well-jointed rock masses. *Numerical Methods in Geomechanics, 6*, 815–822.

Peng, S., & Zhang, J. (2007). *Engineering geology for underground rocks.* Berlin: Springer. https://doi.org/10.1007/978-3-540-73295-2

Pierce, M., Cundall, P., Potyondy, D., & Mas Ivars, D. (2007). A synthetic rock mass model for jointed rock. *Proceedings of The 1St Canada-US Rock Mechanics Symposium - Rock Mechanics Meeting Society's Challenges and Demands*, *1*, 341-349. https://doi.org/10.1201/noe0415444019-c42

Pouya, A., & Fouché, O. (2009). Permeability of 3D discontinuity networks: New tensors from boundary-conditioned homogenisation. *Advances in Water Resources, 32*(3), 303–314. https://doi.org/10.1016/j.advwatres.2008.08.004

Pouya, A., & Ghoreychi, M. (2001). Determination of rock mass strength properties by homogenization. *International Journal for Numerical and Analytical Methods in Geomechanics, 25*(13), 1285–1303. https://doi.org/10.1002/nag.176

Pruess, K. (1991). TOUGH2: *A general-purpose numerical simulator for multiphase fluid and heat flow*. https://doi.org/10.2172/5212064

Pruess, K. & Narasimhan, T. N. (1985). A practical method for modeling fluid and heat flow in fractured porous media. *Society of Petroleum Engineers Journal, 25*(01), 14–26. https://doi.org/10.2118/10509-pa

Rand, O., & Rovenski, V. (2005). *Analytical methods in anisotropic elasticity: with symbolic computational tools*. Boston: Birkhäuser. https://doi.org/10.1007/b138765

Rangriz Shokri, A., Chalaturnyk, R. J., & Bearinger, D. (2019). Deployment of pressure hit catalogues to optimize multi-stage hydraulic stimulation treatments and future re-fracturing designs of horizontal wells in horn river shale basin. *Society of Petroleum Engineers, Annual Technical Conference and Exhibition.* https://doi.org/10.2118/196221-ms

Rice, J. R. (1979). Theory of precursory processes in the inception of earthquake rupture. *Gerlands Beiträge zur Geophysik, 88*, 91–127

Rice, J. R., & Cleary, M. P. (1976). Some basic stress diffusion solutions for fluid-saturated elastic porous media with compressible constituents. *Reviews of Geophysics, 14*(2), 227-241. https://doi.org/10.1029/rg014i002p00227

Roe, R. (1965). Description of crystallite orientation in polycrystalline materials. III. General solution to pole figure inversion. *Journal of Applied Physics, 36*(6), 2024–2031. https://doi.org/10.1063/1.1714396

Rueda, J., Mejia, C., Noreña, N., & Roehl, D. (2021). A three-dimensional enhanced dual-porosity and dual-permeability approach for hydromechanical modeling of naturally fractured rocks. *International Journal for Numerical Methods in Engineering, 122*(7), 1663–1686. https://doi.org/10.1002/nme.6594

Rutqvist, J. (2017). An overview of TOUGH-based geomechanics models. *Computers & Geosciences, 108*, 56-63. https://doi.org/10.1016/j.cageo.2016.09.007

Rutqvist, J., Leung, C., Hoch, A., Wang, Y., & Wang, Z. (2013). Linked multicontinuum and crack tensor approach for modeling of coupled geomechanics, fluid flow and transport in fractured rock. *Journal of Rock Mechanics and Geotechnical Engineering*, *5*(1), 18–31. https://doi.org/10.1016/j.jrmge.2012.08.001

Rutqvist, J., & Stephansson, O. (2003). The role of hydromechanical coupling in fractured rock engineering. *Hydrogeology Journal, 11*(1), 7–40. https://doi.org/10.1007/s10040-002-0241-5

Rutqvist, J., Wu, Y.-S., Tsang, C.-F., & Bodvarsson, G. (2002). A modeling approach for analysis of coupled multiphase fluid flow, heat transfer, and deformation in fractured porous rock. *International Journal of Rock Mechanics and Mining Sciences, 39*(4), 429–442. https://doi.org/10.1016/s1365-1609(02)00022-9

Salamon, M. D. G. (1968). Elastic moduli of a stratified rock mass. *International Journal of Rock Mechanics and Mining Sciences & Geomechanics Abstracts, 5*(6), 519–527. https://doi.org/10.1016/0148-9062(68)90039-9

Sangnimnuan, A., Li, J., & Wu, K. (2018). Development of efficiently coupled fluid-flow/geomechanics model to predict stress evolution in unconventional reservoirs with complex-fracture geometry. *SPE Journal, 23*(03), 640-660. https://doi.org/10.2118/189452-pa

Sayers, C. M., & Kachanov, M. (1995). Microcrack-induced elastic wave anisotropy of brittle rocks. *Journal of Geophysical Research: Solid Earth, 100*(B3), 4149–4156. https://doi.org/10.1029/94jb03134

Schiffman, R. L., Chen, A. T.-H., & Jordan, J. C. (1969). An analysis of consolidation theories. *Journal of Soil Mechanics & Foundations Division ASCE 95*(1), 285–312

Schoenberg, M., & Sayers, C. M. (1995). Seismic anisotropy of fractured rock. *GEOPHYSICS, 60*(1), 204–211. https://doi.org/10.1190/1.1443748

Selvadurai, A., & Suvorov, A. (2016). *Thermo-Poroelasticity and Geomechanics*. Cambridge: Cambridge University Press. https://doi.org/10.1017/cbo9781316543832

Settari, A., & Mourits, F. M. (1994). Coupling of geomechanics and reservoir simulation models. In H. J. Siriwardane & M. M. Zaman (Eds.), *Computer methods and advances in geomechanics, 3,* (pp. 2151–2158). Rotterdam, Netherlands: A.A. Balkema.

Settari, A., & Mourits, F. M. (1998). A Coupled Reservoir and Geomechanical Simulation System. *SPE Journal, 3*(03), 219-226. https://doi.org/10.2118/50939-pa

Sevostianov, I., & Kachanov, M. (2008). On approximate symmetries of the elastic properties and elliptic orthotropy. *International Journal of Engineering Science, 46*(3), 211–223. https://doi.org/10.1016/j.ijengsci.2007.11.003

Sevostianov, I., & Kachanov, M. (2013). Non-interaction approximation in the problem of effective properties. In M. Kachanov & I. Sevostianov (Eds.), *Effective properties of heterogeneous materials, Solid mechanics and its applications, 193,* (pp. 1–95). Dordrecht: Springer. https://doi.org/10.1007/978-94-007-5715-8_1

Snow, D. T. (1969). Anisotropic permeability of fractured media. *Water Resources Research, 5*(6), 1273–1289. https://doi.org/10.1029/wr005i006p01273

Stietel, A., Millard, A., Treille, E., Vuillod, E., Thoraval, A., & Ababou, R. (1996). Continuum representation of coupled hydromechanic processes of fractured media: Homogenisation and parameter identification. In O. Stephansson, L. Jing & C.-F. Tsang (Eds.), *Coupled Thermo-Hydro-Mechanical processes of fractured media, Developments in geotechnical engineering, 79*, (pp. 135–164). Amsterdam: Elsevier B.V. https://doi.org/10.1016/s0165-1250(96)80024-1

Taron, J., Elsworth, D., & Min, K.-B. (2009). Numerical simulation of thermal-hydrologic-mechanical-chemical processes in deformable, fractured porous media. *International Journal of Rock Mechanics and Mining Sciences, 46*(5), 842–854. https://doi.org/10.1016/j.ijrmms.2009.01.008

Terzaghi, K. (1923). Die Berechnung der Durchlassigkeitsziffer des Tones aus dem Verlauf der Hydrodynamischen Spannungerscheinungen. *Sitzungsberichte der Akademie der Wissenschaften in Wien, mathematisch-naturwissen-schaftliche Klasse, Abteilung IIa 132*(3/4), 125-138

Terzaghi, K. (1925). *Erdbaumechanik auf bodenphysikalischer grundlage*. Vienna, Austria: Franz Deuticke.

Thompson, M., & Willis, J. R. (1991). A reformation of the equations of anisotropic poroelasticity. *Journal of Applied Mechanics, 58*(3), 612-616. https://doi.org/10.1115/1.2897239

Thoraval, A., & Renaud, V. (2004). Hydro-mechanical upscaling of a fractured rockmass using a 3D numerical approach. *Elsevier Geo-Engineering Book Series*, *2*, 275–280. https://doi.org/10.1016/s1571-9960(04)80053-3

Tinder, R. F. (2008). *Tensor properties of solids: Phenomenological development of the tensor properties of crystals.* San Rafael, Calif.: Morgan & Claypool Publishers

Ting, T. C. T. (1987). Invariants of anisotropic elastic constants. *The Quarterly Journal of Mechanics and Applied Mathematics, 40*(3), 431–448. https://doi.org/10.1093/qjmam/40.3.431

Ting, T. C. T. (1996). *Anisotropic elasticity: theory and applications*. The Oxford engineering science series (No. 45). New York: Oxford University Press.

Touhidi-Baghini, A. (1998). *Absolute permeability of McMurray formation oil sands at low confining stresses* (Ph.D. Thesis) Department of Civil Engineering, University of Alberta, 339. https://doi.org/10.7939/R3Z31P07M

Tran, D., Nghiem, L., & Buchanan, L. (2009). Aspects of coupling between petroleum reservoir flow and geomechanics. *43rd US Rock Mechanics Symposium & 4th US-Canada Rock Mechanics Symposium*, Asheville, North Carolina, 28 June-1 July. ARMA 09-89

Tran, D., Settari, A., & Nghiem, L. (2004). New iterative coupling between a reservoir simulator and a geomechanics module. *SPE Journal, 9*(03), 362-369. https://doi.org/10.2118/88989-pa

Tsang, C. F. (1991). Coupled hydromechanical-thermochemical processes in rock fractures. *Reviews of Geophysics, 29*(4), 537–551. https://doi.org/10.1029/91rg01832

Verruijt, A. (1969). Elastic storage of aquifers. In R. D. Wiest (Ed.), *Flow through porous media* (pp. 331–376). New York: Academic Press

Wang, H. F. (2000). *Theory of Linear Poroelasticity with Applications to Geomechanics and Hydrogeology*. Princeton University Press. https://doi.org/10.1515/9781400885688

Warren, J. E., & Root, P. J. (1963). The behavior of naturally fractured reservoirs. *Society of Petroleum Engineers Journal, 3*(03), 245–255. https://doi.org/10.2118/426-pa

Wellmann, C., Lillie, C., & Wriggers, P. (2008). Homogenization of granular material modeled by a three-dimensional discrete element method. *Computers and Geotechnics, 35*(3), 394–405.

Wu, N., Liang, Z., Li, Y., Li, H., Li, W., & Zhang, M. (2019). Stress-dependent anisotropy index of strength and deformability of jointed rock mass: insights from a numerical study. *Bulletin of Engineering Geology and the Environment, 78*(8), 5905–5917. https://doi.org/10.1007/s10064-019-01483-5

Wu, Q., & Kulatilake, P. H. S. W. (2012). REV and its properties on fracture system and mechanical properties, and an orthotropic constitutive model for a jointed rock mass in a dam site in China. *Computers and Geotechnics, 43*, 124–142. https://doi.org/10.1016/j.compgeo.2012.02.010

Xu, Y., Cavalcante Filho, J. S. A., Yu, W. & Sepehrnoori, K. (2016). Discrete-fracture modeling of complex hydraulic-fracture geometries in reservoir simulators. *SPE Reservoir Evaluation & Engineering, 20*(02), 403–422. https://doi.org/10.2118/183647-pa

Yang, J.-P., Chen, W.-Z., Dai, Y., & Yu, H.-D. (2014). Numerical determination of elastic compliance tensor of fractured rock masses by finite element modeling. *International Journal of Rock Mechanics and Mining Sciences, 70*, 474–482. https://doi.org/10.1016/j.ijrmms.2014.06.007

Yoshinaka, R., & Yamabe, T. (1986). Joint stiffness and the deformation behaviour of discontinuous rock. *International Journal of Rock Mechanics and Mining Sciences & Geomechanics Abstracts, 23*(1), 19–28. https://doi.org/10.1016/0148-9062(86)91663-3

Zandarin, M. T. (2010). *Thermo-hydro-mechanical analysis of joints a theoretical and experimental study* (Ph.D. thesis). Polytechnic University of Catalonia, Spain, 183.

Zandi, S., Renard, G., Nauroy, J. F., Guy, N., & Tijani, M. (2010). Numerical Coupling of Geomechanics and Fluid Flow during Steam Injection in SAGD. *SPE Improved Oil Recovery Symposium*. https://doi.org/10.2118/129739-ms

Zienkiewicz, O. C., Taylor, R. L., & Zhu, J. Z. (2005). *The finite element method: its basis and fundamentals*. Elsevier.

Zimmerman, R. W., Somerton, W. H., & King, M. S. (1986). Compressibility of porous rocks. *Journal of Geophysical Research: Solid Earth, 91*(B12), 12765-12777. https://doi.org/10.1029/jb091ib12p12765

Appendix A – Plane strain and oedometric conditions for anisotropic materials.

This section shows the reduced form of the compliance matrix and thermal expansion tensor for anisotropic materials under plane strain and oedometric conditions.

Orthotropic Materials:

An orthotropic material has three orthogonal planes of symmetry, and it is fully defined by nine independent material constitutive constants. Adopting the Voigt's notation, the fourth order compliance tensor, S_{ijkl}, is usually represented in the following matrix form (Lekhnitskii 1981; Ting 1996):

$$S_{IJ} = \begin{pmatrix} S_{11} & S_{12} & S_{13} & 0 & 0 & 0 \\ S_{21} & S_{22} & S_{23} & 0 & 0 & 0 \\ S_{31} & S_{32} & S_{33} & 0 & 0 & 0 \\ 0 & 0 & 0 & S_{44} & 0 & 0 \\ 0 & 0 & 0 & 0 & S_{55} & 0 \\ 0 & 0 & 0 & 0 & 0 & S_{66} \end{pmatrix} \tag{A-1}$$

where the coordinate system (1, 2, 3) defines the principal directions of material symmetry. The elastic compliance matrix must be symmetric, then: $S_{12} = S_{21}$; $S_{13} = S_{31}$; and $S_{23} = S_{32}$. It is commonly expressed in terms of Young's modulus, Poisson's ratio and shear modulus as:

$$S_{IJ} = \begin{pmatrix} 1/E_x & -\nu_{yx}/E_y & -\nu_{zx}/E_z & 0 & 0 & 0 \\ -\nu_{xy}/E_x & 1/E_y & -\nu_{zy}/E_z & 0 & 0 & 0 \\ -\nu_{xz}/E_x & -\nu_{yz}/E_y & 1/E_z & 0 & 0 & 0 \\ 0 & 0 & 0 & 1/G_{yz} & 0 & 0 \\ 0 & 0 & 0 & 0 & 1/G_{zx} & 0 \\ 0 & 0 & 0 & 0 & 0 & 1/G_{xy} \end{pmatrix} \tag{A-2}$$

where the coordinate axes X, Y and Z are aligned with the principal directions. The shear compliances have been defined considering that the shear strain components in the stress-strain constitutive formulation correspond to the shear engineering strains: $\gamma_{yz} = \varepsilon_{yz} + \varepsilon_{zy} = 2\varepsilon_{yz}$; $\gamma_{zx} = \varepsilon_{zx} + \varepsilon_{xz} = 2\varepsilon_{zx}$; and $\gamma_{xy} = \varepsilon_{xy} + \varepsilon_{yx} = 2\varepsilon_{xy}$ (Lekhnitskii 1981). It should be noted that the six Poisson's ratios are all different, i.e., $\nu_{ij} \neq \nu_{ji}$, in materials with orthotropic symmetry.

For unconstrained cases, the expression of the stress-strain relationship in contracted notation including thermal effects is: $\varepsilon_I = S_{IJ}\sigma_J + \alpha_I \Delta T$; where the strains, stresses and linear thermal expansion are written in column form: $\varepsilon_I = [\varepsilon_1, \varepsilon_2, \varepsilon_3, \gamma_4, \gamma_5, \gamma_6]^T$; $\sigma_J = [\sigma_1, \sigma_2, \sigma_3, \sigma_4, \sigma_5, \sigma_6]^T$; and $\alpha_I = [\alpha_1, \alpha_2, \alpha_3, 0, 0, 0]^T$; with *I* and *J* {1,2,3,4,5,6} representing the compliance tensor indices, *ij* and *kl* {11,22,33,23,31,12}.

For two-dimensional models representing the cross-section of an infinitely long body, the constitutive equation can be reduced by assuming plane deformations. In these problems, the normal direction to the cross-section must be a principal direction of material symmetry (Zienkiewicz et al. 2005). Thus, assuming axis 1 to be the out-of-plane direction of the model, the stress-strain relation in plane strain conditions ($\varepsilon_1 = \gamma_5 = \gamma_6 = 0$), including thermal effects is:

$$\begin{pmatrix} \varepsilon_2 \\ \varepsilon_3 \\ \gamma_4 \end{pmatrix} = \begin{pmatrix} S_{22}^{ps} & S_{23}^{ps} & 0 \\ S_{32}^{ps} & S_{33}^{ps} & 0 \\ 0 & 0 & S_{44}^{ps} \end{pmatrix} \begin{pmatrix} \sigma_2 \\ \sigma_3 \\ \sigma_4 \end{pmatrix} + \begin{pmatrix} \alpha_2^{ps} \\ \alpha_3^{ps} \\ 0 \end{pmatrix} \Delta T \tag{A-3}$$

where the S_{IJ}^{ps} and α_I^{ps} are the reduced compliance and thermal expansion coefficients in plane strain conditions:

$$S_{22}^{ps} = S_{22} - \frac{S_{21}S_{12}}{S_{11}} \quad ; \quad S_{33}^{ps} = S_{33} - \frac{S_{31}S_{13}}{S_{11}}$$

$$S_{23}^{ps} = S_{32}^{ps} = S_{23} - \frac{S_{21}S_{13}}{S_{11}} \quad ; \quad S_{44}^{ps} = S_{44}$$

$$\alpha_2^{ps} = \alpha_2 - \frac{S_{21}\alpha_1}{S_{11}} \quad ; \quad \alpha_3^{ps} = \alpha_3 - \frac{S_{31}\alpha_1}{S_{11}}$$

or in index notation:

$$S_{IJ}^{ps} = S_{IJ} - \frac{S_{I1}S_{1J}}{S_{11}} \quad ; \quad \alpha_I^{ps} = \alpha_I - \frac{S_{I1}\alpha_1}{S_{11}} \tag{A-4}$$

Analogous reduced stress-strain expressions for the out-of-plane in the direction of axis 2 and 3 can be obtained through index permutation.

For one-dimensional problems, the system of coordinates must be aligned with the principal directions of material symmetry. Then, the stress-strain law with thermal effects for the oedometric condition along the coordinate axes 1, 2 and 3 have the following expressions:

$$\varepsilon_1 = \frac{\begin{vmatrix} S_{11} & S_{12} & S_{13} \\ S_{21} & S_{22} & S_{23} \\ S_{31} & S_{32} & S_{33} \end{vmatrix}}{\begin{vmatrix} S_{22} & S_{23} \\ S_{32} & S_{33} \end{vmatrix}} \sigma_1 + \frac{\begin{vmatrix} \alpha_1 & S_{12} & S_{13} \\ \alpha_2 & S_{22} & S_{23} \\ \alpha_3 & S_{32} & S_{33} \end{vmatrix}}{\begin{vmatrix} S_{22} & S_{23} \\ S_{32} & S_{33} \end{vmatrix}} \Delta T \tag{A-5}$$

$$\varepsilon_2 = \frac{\begin{vmatrix} S_{11} & S_{12} & S_{13} \\ S_{21} & S_{22} & S_{23} \\ S_{31} & S_{32} & S_{33} \end{vmatrix}}{\begin{vmatrix} S_{11} & S_{13} \\ S_{31} & S_{33} \end{vmatrix}} \sigma_2 + \frac{\begin{vmatrix} S_{11} & \alpha_1 & S_{13} \\ S_{21} & \alpha_2 & S_{23} \\ S_{31} & \alpha_3 & S_{33} \end{vmatrix}}{\begin{vmatrix} S_{11} & S_{13} \\ S_{31} & S_{33} \end{vmatrix}} \Delta T \tag{A-6}$$

$$\varepsilon_3 = \frac{\begin{vmatrix} S_{11} & S_{12} & S_{13} \\ S_{21} & S_{22} & S_{23} \\ S_{31} & S_{32} & S_{33} \end{vmatrix}}{\begin{vmatrix} S_{11} & S_{12} \\ S_{21} & S_{22} \end{vmatrix}} \sigma_3 + \frac{\begin{vmatrix} S_{11} & S_{12} & \alpha_1 \\ S_{21} & S_{22} & \alpha_2 \\ S_{31} & S_{32} & \alpha_3 \end{vmatrix}}{\begin{vmatrix} S_{11} & S_{12} \\ S_{21} & S_{22} \end{vmatrix}} \Delta T \tag{A-7}$$

where the terms associated with the stress and temperature are the compliance and thermal expansion coefficients in oedometric conditions, respectively.

Transversely Isotropic Materials:

A transversely isotropic material is characterized by five independent material constitutive constants and a plane of isotropy. Similarly to the orthotropic case, the elastic compliance matrix can be expressed in terms of elastic coefficients in the principal directions. Setting the normal to the plane of isotropy in the direction of axis 1:

$$S_{IJ} = \begin{pmatrix} 1/E' & -\nu'/E' & -\nu'/E' & 0 & 0 & 0 \\ -\nu'/E' & 1/E & -\nu/E & 0 & 0 & 0 \\ -\nu'/E' & -\nu/E & 1/E & 0 & 0 & 0 \\ 0 & 0 & 0 & 1/G & 0 & 0 \\ 0 & 0 & 0 & 0 & 1/G' & 0 \\ 0 & 0 & 0 & 0 & 0 & 1/G' \end{pmatrix} \tag{A-8}$$

where E', ν' and G' are Young's modulus, Poisson's ratio and shear modulus involving the normal direction (axis 1) to the symmetry plane; E, ν and G are the elastic constants in the plane of isotropy (2-3 in this case), with $G = E/(2+2\nu)$. The shear modulus G' is an independent elastic parameter that should be determined through experimental tests; however, it can be estimated with the approximate formula (Lekhnitskii 1981):

$$G' = \frac{EE'}{E(1+2\nu') + E'} \tag{A-9}$$

The reduced strain-stress laws, including thermal effects for plane strain and oedometric conditions (2D and 1D problems), can be obtained by substituting the transversely isotropic compliance matrix in the previous orthotropic formulation.

Appendix B – Orthogonal planes of symmetry

The principal axes of anisotropy are prescribed in 3DEC by the dip-direction, dip and rotation angles that define the orientation of the three orthogonal planes of symmetry for the orthotropic elastic model (Itasca, 2016). Analogous to the Roe convention (Roe, 1965), the transformation matrix can be obtained through successive rotational transformations of the coordinate system until reaching the local orientation of the principal directions of symmetry. These sequence starts with the rotation of the dip-direction angle around the z-axis followed by the dip angle around the new rotated x-axis and finishing with the rotation angle around the final z-axis. Then, the coordinate transformation matrix is calculated by the expression:

$$a_{ij} = \begin{pmatrix} \cos rot & -\sin rot & 0 \\ \sin rot & \cos rot & 0 \\ 0 & 0 & 1 \end{pmatrix} \begin{pmatrix} 1 & 0 & 0 \\ 0 & \cos dip & -\sin dip \\ 0 & \sin dip & \cos dip \end{pmatrix} \begin{pmatrix} \cos dd & -\sin dd & 0 \\ \sin dd & \cos dd & 0 \\ 0 & 0 & 1 \end{pmatrix} \quad \text{(B-1)}$$

which results in:

$$a_{ij} = \begin{pmatrix} \cos dd \cos rot - \sin dd \cos dip \sin rot & -\sin dd \cos rot - \cos dd \cos dip \sin rot & \sin dip \sin rot \\ \cos dd \sin rot + \sin dd \cos dip \cos rot & -\sin dd \sin rot + \cos dd \cos dip \cos rot & -\sin dip \cos rot \\ \sin dd \sin dip & \cos dd \sin dip & \cos dip \end{pmatrix} \quad \text{(B-2)}$$

where *dd*, *dip* and *rot* are the dip-direction, dip and rotation angles, respectively, according to the 3DEC convention. Next, the transformation matrix resultant from the eigenvalue problem of the compliance contractions, Eqs. (3.6) and (3.7), can be defined as:

$$a_{ij} = \begin{pmatrix} a_{11} & a_{12} & a_{13} \\ a_{21} & a_{22} & a_{23} \\ a_{31} & a_{32} & a_{33} \end{pmatrix} \quad \text{(B-3)}$$

where the term a_{ij} corresponds to the *j*-component of the *i*-eigenvector. Then, the three angles can be determined with the following equations derived from the comparison of both expressions of the transformation matrix:

$$dip = \arccos\left(a_{33}\right) \quad ; \quad dd = \arctan2\left(a_{31}, a_{32}\right) \quad ; \quad rot = \arctan2\left(a_{13}, -a_{23}\right) \quad \text{(B-4)}$$

In the particular case of *dip* = 0, the angle *rot* can be set to 0 and the *dd* can be calculated as:

$$dd = \arctan2\left(-a_{12}, a_{22}\right) \tag{B-5}$$

The function $\arctan2\left(y, x\right)$ it is usually known as the 2-argument arctangent (or atan2) in programing languages. It is equivalent to $\arctan\left(y/x\right)$ where the argument *x* may be zero and the signs of the two arguments $\left(y, x\right)$ are used to define the correct quadrant of the resultant angle, (e.g. $\arctan2\left(1,1\right) = \pi/4$ and $\arctan2\left(-1,-1\right) = -3\pi/4$).

Appendix C – Compliance matrix transformation

The rotational transformation of the compliance matrix from the global coordinate axes {*x, y, z*} of the model to the local system {*x', y', z'*} of the principal directions of anisotropy is expressed as (Ting, 1987):

$$S' = Q^{-T} S Q^{-1} \tag{C-1}$$

consequently,

$$S = Q^{T} S' Q \tag{C-2}$$

where S is the compliance matrix in the global coordinate system as shown in Eq. (3.2), S' is the transformed compliance matrix rotated to the principal directions of symmetry as in Eq. (3.5) and, Q is the quadratic form of the coordinate transformation matrix a_{ij}. The superscript $-T$ denotes transposition of the inverse matrix. The quadratic transformation matrix is defined as (Ting, 1987; Tinder, 2008):

$$Q = \left(\begin{array}{ccc:ccc} a_{11}^2 & a_{12}^2 & a_{13}^2 & 2a_{12}a_{13} & 2a_{13}a_{11} & 2a_{11}a_{12} \\ a_{21}^2 & a_{22}^2 & a_{23}^2 & 2a_{22}a_{23} & 2a_{23}a_{21} & 2a_{21}a_{22} \\ a_{31}^2 & a_{32}^2 & a_{33}^2 & 2a_{32}a_{33} & 2a_{33}a_{31} & 2a_{31}a_{32} \\ \hdashline a_{21}a_{31} & a_{22}a_{32} & a_{23}a_{33} & a_{22}a_{33}+a_{23}a_{32} & a_{21}a_{33}+a_{23}a_{31} & a_{21}a_{32}+a_{22}a_{31} \\ a_{31}a_{11} & a_{32}a_{12} & a_{33}a_{13} & a_{12}a_{33}+a_{13}a_{32} & a_{11}a_{33}+a_{13}a_{31} & a_{11}a_{32}+a_{12}a_{31} \\ a_{11}a_{21} & a_{12}a_{22} & a_{13}a_{23} & a_{12}a_{23}+a_{13}a_{22} & a_{11}a_{23}+a_{13}a_{21} & a_{11}a_{22}+a_{12}a_{21} \end{array}\right) \tag{C-3}$$

with the corresponding inverse matrix expressed as:

$$Q^{-1} = \left(\begin{array}{ccc:ccc} a_{11}^2 & a_{21}^2 & a_{31}^2 & 2a_{21}a_{31} & 2a_{31}a_{11} & 2a_{11}a_{21} \\ a_{12}^2 & a_{22}^2 & a_{32}^2 & 2a_{22}a_{32} & 2a_{32}a_{12} & 2a_{12}a_{22} \\ a_{13}^2 & a_{23}^2 & a_{33}^2 & 2a_{23}a_{33} & 2a_{33}a_{13} & 2a_{13}a_{23} \\ \hdashline a_{12}a_{13} & a_{22}a_{23} & a_{32}a_{33} & a_{22}a_{33}+a_{23}a_{32} & a_{12}a_{33}+a_{13}a_{32} & a_{12}a_{23}+a_{13}a_{22} \\ a_{13}a_{11} & a_{23}a_{21} & a_{33}a_{31} & a_{21}a_{33}+a_{23}a_{31} & a_{11}a_{33}+a_{13}a_{31} & a_{11}a_{23}+a_{13}a_{21} \\ a_{11}a_{12} & a_{21}a_{22} & a_{31}a_{32} & a_{21}a_{32}+a_{22}a_{31} & a_{11}a_{32}+a_{12}a_{31} & a_{11}a_{22}+a_{12}a_{21} \end{array}\right) \tag{C-4}$$

where a_{ij} are the coefficients of the coordinate transformation matrix from the global coordinate system to local principal axes of anisotropy.

Appendix D – Analytical compliance matrix based on the Oda's theory

The total elastic compliance tensor S_{ijkl} derived in Eq. (3.14) using the Oda's crack tensor approach can be expressed in matrix form through the summation of the symmetric compliance matrices from the intact rock and the fractures. The definition of the compliance matrix for the isotropic intact rock is:

$$S_{IJ}^{r} = \left(\begin{array}{ccc:ccc} S_{11}^{r} & S_{12}^{r} & S_{12}^{r} & 0 & 0 & 0 \\ S_{12}^{r} & S_{11}^{r} & S_{12}^{r} & 0 & 0 & 0 \\ S_{12}^{r} & S_{12}^{r} & S_{11}^{r} & 0 & 0 & 0 \\ \hdashline 0 & 0 & 0 & S_{44}^{r} & 0 & 0 \\ 0 & 0 & 0 & 0 & S_{44}^{r} & 0 \\ 0 & 0 & 0 & 0 & 0 & S_{44}^{r} \end{array}\right) \tag{D-1}$$

where

$$S_{11}^{r} = \frac{1}{E} \quad ; \quad S_{12}^{r} = \frac{-v}{E} \quad ; \quad S_{44}^{r} = \frac{2(1+v)}{E}$$

are the matrix coefficients in terms of the elastic parameters of the intact material. On the other hand, the symmetric compliance matrix corresponding to the fractures can be defined as:

$$S_{IJ}^{f} = \left(\begin{array}{ccc:ccc} S_{11}^{f} & S_{12}^{f} & S_{13}^{f} & S_{14}^{f} & S_{15}^{f} & S_{16}^{f} \\ S_{12}^{f} & S_{22}^{f} & S_{23}^{f} & S_{24}^{f} & S_{25}^{f} & S_{26}^{f} \\ S_{13}^{f} & S_{23}^{f} & S_{33}^{f} & S_{34}^{f} & S_{35}^{f} & S_{36}^{f} \\ \hdashline S_{14}^{f} & S_{24}^{f} & S_{34}^{f} & S_{44}^{f} & S_{45}^{f} & S_{46}^{f} \\ S_{15}^{f} & S_{25}^{f} & S_{35}^{f} & S_{45}^{f} & S_{55}^{f} & S_{56}^{f} \\ S_{16}^{f} & S_{26}^{f} & S_{36}^{f} & S_{46}^{f} & S_{56}^{f} & S_{66}^{f} \end{array}\right) \tag{D-2}$$

where the 21 matrix coefficients are determined from the tensor components defined in Eq. (3.13) as follows:

$$
\begin{aligned}
S_{11}^f = S_{xxxx}^f &= \frac{1}{V}\sum^{Nf}\left[\left(\frac{1}{k_n}-\frac{1}{k_s}\right)A n_x^4 + \frac{1}{k_s}A n_x^2\right] \\
S_{22}^f = S_{yyyy}^f &= \frac{1}{V}\sum^{Nf}\left[\left(\frac{1}{k_n}-\frac{1}{k_s}\right)A n_y^4 + \frac{1}{k_s}A n_y^2\right] \\
S_{33}^f = S_{zzzz}^f &= \frac{1}{V}\sum^{Nf}\left[\left(\frac{1}{k_n}-\frac{1}{k_s}\right)A n_z^4 + \frac{1}{k_s}A n_z^2\right]
\end{aligned}
\tag{D-3}
$$

$$
\begin{aligned}
S_{12}^f = S_{xxyy}^f &= \frac{1}{V}\sum^{Nf}\left[\left(\frac{1}{k_n}-\frac{1}{k_s}\right)A n_x^2 n_y^2\right] \\
S_{13}^f = S_{xxzz}^f &= \frac{1}{V}\sum^{Nf}\left[\left(\frac{1}{k_n}-\frac{1}{k_s}\right)A n_x^2 n_z^2\right] \\
S_{23}^f = S_{yyzz}^f &= \frac{1}{V}\sum^{Nf}\left[\left(\frac{1}{k_n}-\frac{1}{k_s}\right)A n_y^2 n_z^2\right]
\end{aligned}
\tag{D-4}
$$

$$
\begin{aligned}
S_{14}^f = 2S_{xxyz}^f &= \frac{2}{V}\sum^{Nf}\left[\left(\frac{1}{k_n}-\frac{1}{k_s}\right)A n_x^2 n_y n_z\right] \\
S_{25}^f = 2S_{yyxz}^f &= \frac{2}{V}\sum^{Nf}\left[\left(\frac{1}{k_n}-\frac{1}{k_s}\right)A n_x n_y^2 n_z\right] \\
S_{36}^f = 2S_{zzxy}^f &= \frac{2}{V}\sum^{Nf}\left[\left(\frac{1}{k_n}-\frac{1}{k_s}\right)A n_x n_y n_z^2\right]
\end{aligned}
\tag{D-5}
$$

$$
\begin{aligned}
S_{15}^f = 2S_{xxxz}^f &= \frac{2}{V}\sum^{Nf}\left[\left(\frac{1}{k_n}-\frac{1}{k_s}\right)A n_x^3 n_z + \frac{1}{2k_s}A n_x n_z\right] \\
S_{16}^f = 2S_{xxxy}^f &= \frac{2}{V}\sum^{Nf}\left[\left(\frac{1}{k_n}-\frac{1}{k_s}\right)A n_x^3 n_y + \frac{1}{2k_s}A n_x n_y\right] \\
S_{24}^f = 2S_{yyyz}^f &= \frac{2}{V}\sum^{Nf}\left[\left(\frac{1}{k_n}-\frac{1}{k_s}\right)A n_y^3 n_z + \frac{1}{2k_s}A n_y n_z\right]
\end{aligned}
\tag{D-6}
$$

$$S_{26}^f = 2S_{yyxy}^f = \frac{2}{V}\sum^{Nf}\left[\left(\frac{1}{k_n}-\frac{1}{k_s}\right)A\,n_x n_y^3 + \frac{1}{2k_s}A\,n_x n_y\right]$$
$$S_{34}^f = 2S_{zzyz}^f = \frac{2}{V}\sum^{Nf}\left[\left(\frac{1}{k_n}-\frac{1}{k_s}\right)A\,n_y n_z^3 + \frac{1}{2k_s}A\,n_y n_z\right] \qquad \text{(D-7)}$$
$$S_{35}^f = 2S_{zzxz}^f = \frac{2}{V}\sum^{Nf}\left[\left(\frac{1}{k_n}-\frac{1}{k_s}\right)A\,n_x n_z^3 + \frac{1}{2k_s}A\,n_x n_z\right]$$

$$S_{44}^f = 4S_{yzyz}^f = \frac{4}{V}\sum^{Nf}\left[\left(\frac{1}{k_n}-\frac{1}{k_s}\right)A\,n_y^2 n_z^2 + \frac{1}{4k_s}A\left(n_y^2+n_z^2\right)\right]$$
$$S_{55}^f = 4S_{xzxz}^f = \frac{4}{V}\sum^{Nf}\left[\left(\frac{1}{k_n}-\frac{1}{k_s}\right)A\,n_x^2 n_z^2 + \frac{1}{4k_s}A\left(n_x^2+n_z^2\right)\right] \qquad \text{(D-8)}$$
$$S_{66}^f = 4S_{xyxy}^f = \frac{4}{V}\sum^{Nf}\left[\left(\frac{1}{k_n}-\frac{1}{k_s}\right)A\,n_x^2 n_y^2 + \frac{1}{4k_s}A\left(n_x^2+n_y^2\right)\right]$$

$$S_{45}^f = 4S_{yzxz}^f = \frac{4}{V}\sum^{Nf}\left[\left(\frac{1}{k_n}-\frac{1}{k_s}\right)A\,n_x n_y n_z^2 + \frac{1}{4k_s}A\,n_x n_y\right]$$
$$S_{46}^f = 4S_{yzxy}^f = \frac{4}{V}\sum^{Nf}\left[\left(\frac{1}{k_n}-\frac{1}{k_s}\right)A\,n_x n_y^2 n_z + \frac{1}{4k_s}A\,n_x n_z\right] \qquad \text{(D-9)}$$
$$S_{56}^f = 4S_{xzxy}^f = \frac{4}{V}\sum^{Nf}\left[\left(\frac{1}{k_n}-\frac{1}{k_s}\right)A\,n_x^2 n_y n_z + \frac{1}{4k_s}A\,n_y n_z\right]$$

where the terms between brackets are evaluated for every fracture with their particular parameters during the summation. The n_x, n_y and n_z are the components of the normal vector to the fracture plane. Traditionally, these components are defined in terms of the direction cosines of the angles α, β, γ between the normal vector and the coordinate axes $\{x, y, z\}$ as:

$$n_1 = n_x = \cos\alpha \quad ; \quad n_2 = n_y = \cos\beta \quad ; \quad n_3 = n_z = \cos\gamma \qquad \text{(D-10)}$$

By adding the compliance matrices of the intact rock and fractures defined in Eqs. (D-1) and (D-2) and, also substituting the components of the normal vectors with the direction cosines, the total elastic compliance matrix S can be expressed in the following block matrix form:

$$S = \left(\begin{array}{c|c} A_{3\times3} & B_{3\times3} \\ \hline B_{3\times3}^{T} & C_{3\times3} \end{array} \right) \tag{D-11}$$

where $B_{3\times3}^{T}$ is the transpose of $B_{3\times3}$ and, $A_{3\times3}$ and $C_{3\times3}$ are both symmetric. These blocks or submatrices are given by:

$$A_{3\times3} = \begin{pmatrix} \frac{1}{E} + \frac{1}{V}\sum^{Nf}\left[\left(\frac{\cos^2\alpha}{k_n} + \frac{\sin^2\alpha}{k_s}\right)A\cos^2\alpha\right] & \frac{-v}{E} + \frac{1}{V}\sum^{Nf}\left[\left(\frac{1}{k_n} - \frac{1}{k_s}\right)A\cos^2\alpha\cos^2\beta\right] & \frac{-v}{E} + \frac{1}{V}\sum^{Nf}\left[\left(\frac{1}{k_n} - \frac{1}{k_s}\right)A\cos^2\alpha\cos^2\gamma\right] \\ \frac{-v}{E} + \frac{1}{V}\sum^{Nf}\left[\left(\frac{1}{k_n} - \frac{1}{k_s}\right)A\cos^2\alpha\cos^2\beta\right] & \frac{1}{E} + \frac{1}{V}\sum^{Nf}\left[\left(\frac{\cos^2\beta}{k_n} + \frac{\sin^2\beta}{k_s}\right)A\cos^2\beta\right] & \frac{-v}{E} + \frac{1}{V}\sum^{Nf}\left[\left(\frac{1}{k_n} - \frac{1}{k_s}\right)A\cos^2\beta\cos^2\gamma\right] \\ \frac{-v}{E} + \frac{1}{V}\sum^{Nf}\left[\left(\frac{1}{k_n} - \frac{1}{k_s}\right)A\cos^2\alpha\cos^2\gamma\right] & \frac{-v}{E} + \frac{1}{V}\sum^{Nf}\left[\left(\frac{1}{k_n} - \frac{1}{k_s}\right)A\cos^2\beta\cos^2\gamma\right] & \frac{1}{E} + \frac{1}{V}\sum^{Nf}\left[\left(\frac{\cos^2\gamma}{k_n} + \frac{\sin^2\gamma}{k_s}\right)A\cos^2\gamma\right] \end{pmatrix}$$

$$B_{3\times3} = \begin{pmatrix} \frac{2}{V}\sum^{Nf}\left[\left(\frac{1}{k_n} - \frac{1}{k_s}\right)A\cos^2\alpha\cos\beta\cos\gamma\right] & \frac{2}{V}\sum^{Nf}\left[\left(\frac{\cos^2\alpha}{k_n} - \frac{\cos(2\alpha)}{2k_s}\right)A\cos\alpha\cos\gamma\right] & \frac{2}{V}\sum^{Nf}\left[\left(\frac{\cos^2\alpha}{k_n} - \frac{\cos(2\alpha)}{2k_s}\right)A\cos\alpha\cos\beta\right] \\ \frac{2}{V}\sum^{Nf}\left[\left(\frac{\cos^2\beta}{k_n} - \frac{\cos(2\beta)}{2k_s}\right)A\cos\beta\cos\gamma\right] & \frac{2}{V}\sum^{Nf}\left[\left(\frac{1}{k_n} - \frac{1}{k_s}\right)A\cos\alpha\cos^2\beta\cos\gamma\right] & \frac{2}{V}\sum^{Nf}\left[\left(\frac{\cos^2\beta}{k_n} - \frac{\cos(2\beta)}{2k_s}\right)A\cos\alpha\cos\beta\right] \\ \frac{2}{V}\sum^{Nf}\left[\left(\frac{\cos^2\gamma}{k_n} - \frac{\cos(2\gamma)}{2k_s}\right)A\cos\beta\cos\gamma\right] & \frac{2}{V}\sum^{Nf}\left[\left(\frac{\cos^2\gamma}{k_n} - \frac{\cos(2\gamma)}{2k_s}\right)A\cos\alpha\cos\gamma\right] & \frac{2}{V}\sum^{Nf}\left[\left(\frac{1}{k_n} - \frac{1}{k_s}\right)A\cos\alpha\cos\beta\cos^2\gamma\right] \end{pmatrix}$$

$$C_{3\times3} = \begin{pmatrix} \frac{2(1+v)}{E} + \frac{4}{V}\sum^{Nf}\left[\left(\frac{1}{k_n} - \frac{1}{k_s}\right)A\cos^2\beta\cos^2\gamma + \frac{1}{4k_s}A\sin^2\alpha\right] & \frac{4}{V}\sum^{Nf}\left[\left(\frac{\cos^2\gamma}{k_n} - \frac{1+2\cos(2\gamma)}{4k_s}\right)A\cos\alpha\cos\beta\right] & \frac{4}{V}\sum^{Nf}\left[\left(\frac{\cos^2\beta}{k_n} - \frac{1+2\cos(2\beta)}{4k_s}\right)A\cos\alpha\cos\gamma\right] \\ \frac{4}{V}\sum^{Nf}\left[\left(\frac{\cos^2\gamma}{k_n} - \frac{1+2\cos(2\gamma)}{4k_s}\right)A\cos\alpha\cos\beta\right] & \frac{2(1+v)}{E} + \frac{4}{V}\sum^{Nf}\left[\left(\frac{1}{k_n} - \frac{1}{k_s}\right)A\cos^2\alpha\cos^2\gamma + \frac{1}{4k_s}A\sin^2\beta\right] & \frac{4}{V}\sum^{Nf}\left[\left(\frac{\cos^2\alpha}{k_n} - \frac{1+2\cos(2\alpha)}{4k_s}\right)A\cos\beta\cos\gamma\right] \\ \frac{4}{V}\sum^{Nf}\left[\left(\frac{\cos^2\beta}{k_n} - \frac{1+2\cos(2\beta)}{4k_s}\right)A\cos\alpha\cos\gamma\right] & \frac{4}{V}\sum^{Nf}\left[\left(\frac{\cos^2\alpha}{k_n} - \frac{1+2\cos(2\alpha)}{4k_s}\right)A\cos\beta\cos\gamma\right] & \frac{2(1+v)}{E} + \frac{4}{V}\sum^{Nf}\left[\left(\frac{1}{k_n} - \frac{1}{k_s}\right)A\cos^2\alpha\cos^2\beta + \frac{1}{4k_s}A\sin^2\gamma\right] \end{pmatrix}$$

For the particular case of an isotropic intact rock with three orthogonal joint sets oriented in the coordinate axes, the analytical compliance matrix defined above is reduced to the analytical solution presented in Amadei and Goodman (1983) by replacing the relation between fracture area and total volume with the fracture spacing of each joint set.